Fakultät für Naturwissenschaften
Institut für Theoretische Chemie

Research on Interphases in Multivalent Batteries by Reflection Anisotropy Spectroscopy and Electrochemical Impedance Spectroscopy

Kumulative Dissertation

zur Erlangung des Doktorgrades Dr. rer. nat.

der Fakultät für Naturwissenschaften der Universität Ulm

Vorgelegt von:

Mario Löw

aus Laichingen

Ulm, 2026

Dekan: Prof. Dr. Kay Gottschalk

1. Gutachter: Dr. Matthias M. May

2. Gutachter: PD Dr. Joachim Bansmann

Tag der Promotion: 09.05.2025

© 2026 Mario Löw

Satz: PDF-LaTeX 2$_\varepsilon$

Contents

1 Abstract **1**

2 Introduction **3**

3 Background **9**

3.1 Fundamentals of Batteries 9

3.1.1 Electrochemical Fundamentals 10

3.1.2 Interphases in Batteries 12

Double-Layer Concepts 12

Solid Electrolyte Interphase Formation 14

Stripping and Plating 15

Techniques to Investigate the Interphase of Batteries 19

3.2 Multivalent Batteries 20

3.2.1 Magnesium Batteries 20

3.2.2 Aluminium Batteries 22

3.3 Photoelectrochemical Water Splitting 26

3.3.1 Fundamentals of Semiconductors 26

3.3.2 Semiconductor-Metal and Semiconductor-Electrolyte Interfaces 29

Semiconductor-Metal Contact 29

Semiconductor-Electrolyte Contact 31

3.3.3 Challenges in PEC Water Splitting 32

4 Characterization Techniques **35**

4.1 Reflection Anisotropy Spectroscopy 35

Historic Development 37

EC-RAS Set-up 39

4.2 Electrochemical Impedance Spectroscopy 40
4.2.1 The Cation Transference Number (t_+) 42
Determination of the Cation Transference Number by EIS . . 43
Determination of the Cation Transference Number by Galvanostatic Polarization 44
4.3 Cyclic Voltammetry 45
4.4 Chronoamperometry 48
4.5 Scanning Electron Microscopy 49
Energy Dispersive X-ray Spectroscopy 51

5 Results and Discussion **52**
5.1 The Interfacial Structure of InP(100) in Contact with HCl and H_2SO_4 Studied by Reflection Anisotropy Spectroscopy 52
5.2 In situ Monitoring of the Al(110)-[EMImCl]:$AlCl_3$ Interface by Reflection Anisotropy Spectroscopy 63
5.3 Operando Investigation of Al Plating Regimes on HOPG in [EMImCl]:$AlCl_3$ by Electrochemical Reflection Anisotropy Spectroscopy 74
5.4 Magnesium and Aluminum in Contact with Liquid Battery Electrolytes: Ion Transport through Interphases and in the Bulk 85
5.5 Investigation of the Surface of a Mg Anode in Contact with a Grignard Electrolyte and a Boron-Base Electrolyte with and without Additive by Electrochemical Reflection Anisotropy Spectroscopy 94
RA-Spectra of Magnesium 94
Operando Investigation of Mg in a Grignard Electrolyte 95
Operando Investigation of Mg in $Mg[B(HFIP)_4]_2$ Electrolyte with and without Additive 98
Polishing Routine of Mg 99
Conclusion 103

6 Conclusion **104**

7 Acknowledgment **107**

8 List of Symbols and Abbreviations **108**

9 List of Publications and Conferences Contributions **113**

Bibliography **119**

Curriculum Vitae **130**

Appendix **133**

1 Abstract

The significant decrease in solar and wind power costs over the past decade has made them competitive options in the energy market. However, due to their fluctuating supply, the energy they generate must be stored. Two possible systems that could be utilized for this purpose are rechargeable multivalent batteries and hydrogen. Rechargeable multivalent batteries are expected to replace state-of-the-art lithium-ion batteries in the future due to their higher capacity and the higher availability of their raw materials. Photoelectrochemical water splitting is projected to become a cost-effective method for producing hydrogen.

In both systems, the interface between the electrode and the electrolyte is a critical factor which needs further investigation under in-situ and operando conditions. In order to change this, this thesis uses reflection anisotropy spectroscopy (RAS) and electrochemical impedance spectroscopy (EIS) to investigate these interfaces under in-situ and operando conditions. Here, RAS examines the dynamic evolution of optical properties at interfaces, which can help detect adsorption phenomena or surface reconstruction. In contrast, EIS investigates the formation of solid electrolyte interphase (SEI) and cationic transference numbers, an essential electrolyte property for addressing potential dendrite formation.

In the context of solar-water splitting, the interface of InP in an acidic solution is examined using RAS to identify potential-dependent surface corrosion and the formation of a passivation layer. Here a low acid concentration of 10 mM leads to a reversible process of the reduction of the surface oxide at cathodic potential and its reformation close to open-circuit voltage. In contrast, a high acid concentration (0.5 N) leads to initial surface corrosion. The research also delves into multivalent batteries, particularly aluminium and magnesium batteries. For instance, the interaction of Grignard, one of the first electrolytes for rechargeable magnesium batteries, was examined using RAS and EIS. Here, the liquid pathway through the SEI

dominates after prolonged contact with the electrolyte. Further, the addition of stabilized THF (tetrahydrofuran) to the Grignards results in an unordered passivation layer on top of the surface and should, therefore, be avoided.

Similarly, the interaction between the promising boron-based $Mg[B(HFIP)_4]_2$ and the magnesium anode was studied using RAS, where a partially ordered structure was observed in the pure electrolyte. At the same time, the addition of tris(trimethylsilyl) borate (TMSB) leads to a more isotropic surface.

For rechargeable aluminium batteries, the surface corrosion of the aluminium anode when in contact with the commonly used but corrosive electrolyte [EMImCl]:$AlCl_3$ was investigated using RAS and EIS. The prolonged contact with the electrolyte turned the initially dense native oxide layer into an SEI with predominant liquid pathways. Simultaneously, the roughness of the surface increases. During electrochemical cycling, changes in the surface anisotropy were detected, which could be correlated with the stripping and plating of aluminium.

Finally, the same electrolyte was utilized to monitor the electrodeposition of aluminium onto highly ordered pyrolytic graphite (HOPG). This investigation shows that the morphology of the deposited aluminium is dependent on the applied cathodic potential, with a rough island-like deposition at less cathodic potentials. In comparison, a smooth layer covering the whole sample is observed at more cathodic potentials. Further, the investigation shows that the initial nucleation contains a step in which ordered nuclei are formed. The investigation in the anodic potential range shows the formation of a SEI as well as the irreversible swelling of the topmost graphite layer due to the intercalation of $AlCl_4^-$.

2 Introduction

The last decade saw a substantial decline in prices for lithium-ion batteries (LIBs) as well as solar and wind power.[1,2] The first enabled the widespread of key technologies like small portable electronic devices and electric vehicles, whereas the latter made these forms of energy competitive with the currently used energy sources like coal or natural gas. However, these technologies have some drawbacks. The due to their long cycle life and high energy density successful LiBs,[3,4] approach their theoretical energy limit and use expensive and critical raw materials.[5,6] Solar and wind have the issue of fluctuations in their energy production due to the availability of sunlight and wind. Therefore, storage is required to compensate for the discontinuous flow of energy.[7] These challenges require the development of new forms of energy storage since the worldwide energy demand is expected to rise by 28% in 2040 compared to 2017,[8] due to economic growth, rapid worldwide urbanisation and increasing digitalisation. Two possible solutions for this issue could be multivalent batteries and carbon-free fuels like hydrogen. Multivalent batteries have the potential for short- and medium-term energy storage, whereas hydrogen has the potential for long-term energy storage.[9]

The two most promising multivalent batteries are magnesium and aluminium, which tackle the two most relevant issues of LIBs: the limited and globally uneven distribution of its raw materials and the approach of its theoretical limits.[5] The lithium used in LIBs has a scarce abundance in the earth's crust of only 65 ppm[10], with the overwhelming resources being located in South America (Chile and Argentina), China and Western Australia.[11–13] This could lead to problems in the supply of Li when the demand for LIBs increases.[11,14]. Further on, the extraction methods for lithium are questionable regarding environmental aspects, leading to moral, social and ecological issues.[5,11] For example, to gain 1 ton of Li ore, 250 tons of minerals need to be handled, and 750 tons of brine is used.[5] Regarding environmental friendliness, it is also worth noting that it takes 400 kWh of energy to produce a LIB with 1 kWh.

Thereby, 75 kg of CO_2 is exhausted, the equivalent of burning 351 l of gasoline.[5] This means that a battery only becomes environmentally friendly after many cycles. A large part of this energy is used to mine the ore from which the battery compartments will be produced.[5] Figure 2.1 shows the worldwide geographical distribution of mineral resources for battery production and battery manufacturing companies. Contrary, Mg and Al have a high abundance in the earth's crust, with 23300 ppm for Mg and 82000 ppm for Al, and are more equally distributed globally.[15] This is also reflected in the price of the metal itself, with Li being six times more expensive than Mg or Al.[15]

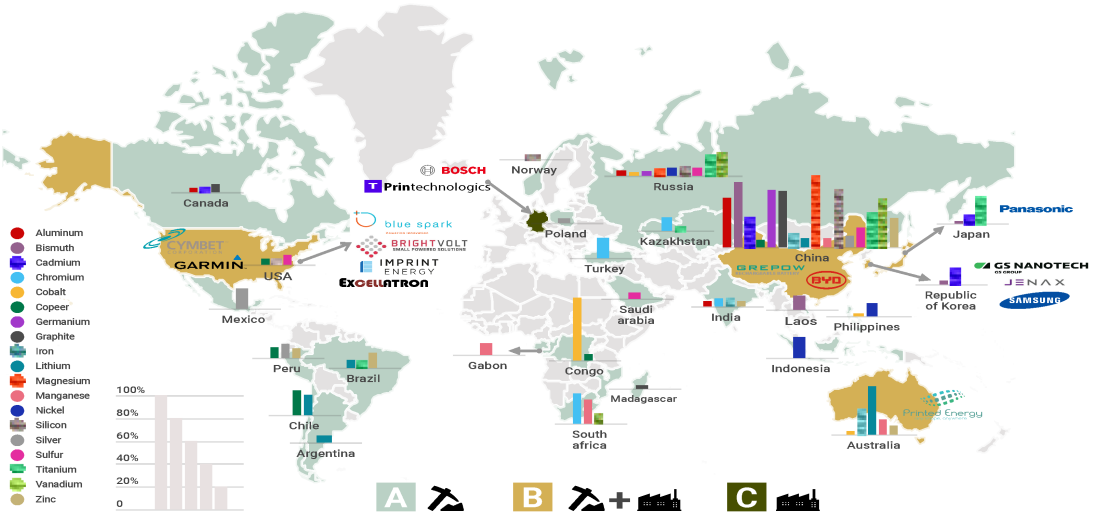

Figure 2.1: Geographical distribution of mineral resources vs. battery manufacturing companies. (A) Countries with mineral resources, (B) countries with mineral resources and manufacturing companies, and (C) manufacturing countries. Note: The bar length indicates the relative fraction of the total production. Data from US Geological Survey, Mineral Commodity Summaries 2020. Taken from [13]. Figure licensed under CC BY 4.0, `https://creativecommons.org/licenses/by/4.0/`

The second advantage of rechargeable Mg and Al batteries is that they can be used as metal anodes. This provides them with high theoretical gravimetric and volumetric capacities of 2205 mAh g^{-1} and 3868 mAh cm^{-3} for Mg and 2980 mAh g^{-1} and 8046 mAh cm^{-3} for Al. For Al, this is a factor of ten higher compared to the currently used LIBs with a volumetric capacity of only 760 mAh cm^{-3} and a gravimetric capacity of just 372 mAh g^{-1}, due the use of graphite as anode material.[16]

The usage of lithium metal as anode material would, in principle, also be possible. However, lithium is prone to the formation of dendrites already at low current densities, increasing the risk of cell damage.[17] However, a challenge with Mg and Al is that the cell voltage of Mg (-2.37 V vs. Standard Hydrogen Electrode (SHE)) and Al (1.66 V vs. SHE) is lower compared to the one of LIBs (-3.042 V vs. SHE).[15] Since multivalent batteries have such significant advantages over LIBs, why are they not commercially available? There are two reasons: the first one is that there is no suitable cathode material yet, and the second one, which this thesis tries to elucidate, is that the electrode-electrolyte interphase is not fully understood yet, especially under operation conditions.

Another suitable energy carrier is hydrogen, which can be used for long-term storage. However, the issue with hydrogen as an energy carrier is that it is only present in nature in its elementary form in a tiny amount,[18]; therefore, it must first be produced to be used as a fuel.[19] A possible way to do this is by photoelectrochemical (PEC) water splitting. Here, the photoelectrode is directly in contact with the aqueous electrolyte, and the front surface of the absorber is decorated with a catalyst. The advantage of PEC water splitting is that it is independent of fossil fuels, which are currently used to produce hydrogen via steam reforming.[20] Furthermore, the harvesting of photons and the evolution of hydrogen are combined, leading to a more compact design than a connected photovoltaic cell and an electrolyser, making the set-up ultimately more cost-efficient. However, the price of cell production is currently too high.[21,22]

One semiconductor which has been intensively studied for its use as photocathode[23,24] but also as a main component in photoelectrochemical multi-junction solarcells[25,26] is indium phosphide (InP). The advantage of InP is that it allows an efficient carrier transport across the semiconductor–electrolyte interface due to surface recombination velocities as low as 170 $cm\,s^{-1}$.[27,28] However, the major challenge when using InP in photoelectrochemical devices is the corrosion of its surface and instability in aqueous solution.[27] From simple systems like InP, knowledge transfer is possible to more complex ternary compounds used in PEC water splitting.[25,29] Further advantage of hydrogen produced by solar-water-splitting is its high purity. This means that there is no catalyst contamination in a later used fuel cell, as it would happen with hydrogen produced from hydrocarbons, which most of the time contains CO, which is a severe catalyst poison for the most common Pt-based cat-

alysts.[30]. Despite energy storage, another area where hydrogen is also needed is the production of fertiliser.[9] For PEC water splitting, a meticulous design of the solid-liquid interface is required for efficient and stable operation. However, operating in an aqueous environment leads to corrosion, lowering the efficiency and lifespan of the cell. Therefore, an investigation of the interface of the photocathode is necessary to understand the chemical processes going on at the surface and under applied potential to find a solution reducing and ultimately preventing corrosion.

This thesis deals with in-situ and operando measurements. Both terms come from Latin, with 'in-situ' meaning 'on side' in opposition to 'ex-situ'. In-situ measurement probes a reaction under natural conditions but with no time dependence.[31] An example of this would be the optical investigation of an electrode inside an electrolyte or investigating a cell after the cycling is stopped. Operando, on the other hand, means 'under operation'; here, a reaction is continuously monitored under operating conditions, ideally providing real-time operation information.[31] An example of this would be the optical investigation of an electrode inside an electrolyte while it is electrochemically cycled. A powerful tool for the in-situ / operando investigation of surfaces inside the electrolyte under applied potential is reflection anisotropy spectroscopy (RAS). RAS enables investigations of the surface chemistry and surface structure changes parallel to electrochemical measurements, with a high surface sensitivity of up to one monolayer and a time resolution of up to 10 ms.[32] However, a challenge of RAS is that single crystals are required for this investigation. Nevertheless, well-defined single-crystal surfaces enable the study of the surface structures and their physico-chemical properties in different environments, leading to a better understanding of the mechanisms taking place. The advantage of operando measurements with RAS is that they can detect surface changes that can only occur once a potential is applied and vanishes after it is set back to open-circuit potential (OCP). This can be seen in Figure 2.2, where chronoamperometry measurements were done with InP in an acidic medium. The simultaneously recorded transients show gradual changes once a potential is applied, showing the formation of a surface layer on top of the InP. Once the potential is set back to OCP, a drastic change is observed, with the transient returning to the value it had before applying the potential. This means the surface formed under the applied potential is unstable when turned off. This means that such a surface can only be investigated with opernado techniques.

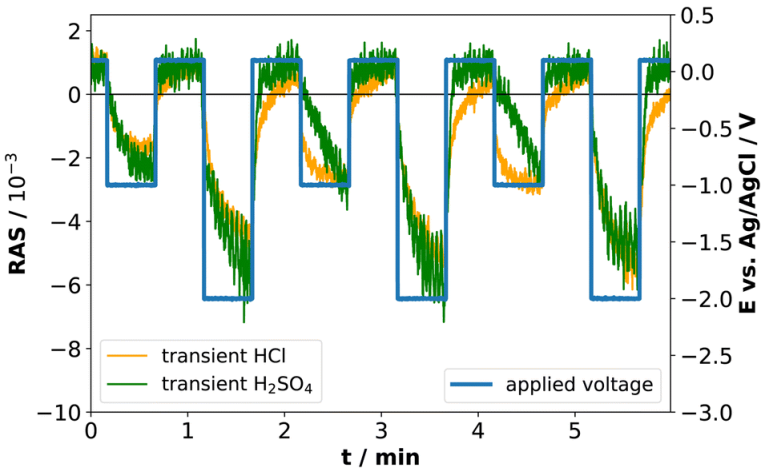

Figure 2.2: Potential-step and transient measurements at 2.25 eV of InP(100) in 0.01 M HCl and in 0.01 M H_2SO_4. Taken from [33]. Figure licensed under CC BY 3.0, https://creativecommons.org/licenses/by/3.0/

A second tool for the investigation of the electrode-electrolyte interface is electrochemical impedance spectroscopy (EIS). This technique enables the in-situ decoupling of different electrochemical transport properties, the evolution of the solid electrolyte interphase (SEI), and the determination of the cationic transference number of the electrolyte. To achieve this, the impedance of a system is measured by applying an alternating voltage over an extensive frequency range from megahertz to millihertz.[34,35]

This thesis will examine several topics in which RAS or EIS are used to investigate solid-liquid interfaces close to open-circuit potential or under applied potential.

1. InP in an acidic environment for the initial study of the corrosion of semiconductors, which is relevant for more complex devices in PEC water splitting.
2. Interfaces of Al batteries in a corrosive ionic liquid electrolyte.
3. Stripping and plating of Al on HOPG, as well as the formation of an SEI during the intercalation of $AlCl_4^-$.
4. The surface development and the transference number of Al in contact with an ionic liquid electrolyte and Mg in contact with a Grignard electrolyte.
5. EC-RAS investigation of Mg-metal anodes with Grignard electrolytes and the

$Mg[B(HFIP)_4]_2$ electrolyte with and without additives.

3 Background

Before introducing batteries and solar-water splitting, it is crucial to elucidate the meaning of two words used within this context: interface and interphase. An interface is a sharp two-dimensional boundary between two phases, as seen in the case of the Helmholtz layer of a surface in an electrolyte. On the contrary, an interphase is the transition zone between two phases in a system. An example would be the solid electrolyte interphase in a battery, where various compounds form a several nanometer thick layer between the anode and the electrolyte.

The background section will now provide an overview of the two topics covered in this thesis: the interphases of batteries and the interphases for photoelectrochemical water-splitting devices. The battery section commences with an introduction to batteries and their electrochemistry before the interphases of batteries, with the formation of the solid-electrolyte interphase and the electrodeposition of metals elucidated. Subsequently, an overview of the two post-lithium batteries, rechargeable magnesium and aluminium batteries, which are investigated in this thesis, is presented. The section about PEC water splitting contains an introduction to semiconductors, a material class most often used for these devices. It then covers the interface of semiconductors in various environments before highlighting the significant challenges that need to be addressed in PEC water splitting.

3.1 Fundamentals of Batteries

A battery is a free, independent, and self-contained electrochemical energy source containing one or several galvanic cells, directly converting chemical energy on demand into electrical energy. A galvanic cell is an electrochemical cell that consists of a cathode, an anode and an electrolyte, where an electric current is generated

from a spontaneous redox reaction. The anode is the electrode at which, during discharge, the oxidation (the release of electrons) happens, whereas at the cathode, the reduction (the absorption of electrons) takes place during discharge. Generally, there are two classes of batteries: primary batteries, which are discharged once and then disposed, and secondary/rechargeable batteries, which can be recharged by reversing the current flow through the cell.[36–38]

Rechargeable batteries can have different operation mechanisms. One of them is the rocking chair mechanism found in LIBs. In rocking chair batteries, the charge carriers shuttle back and forth between the cathode and the anode, not deteriorating the electrolyte.[39] A schematic drawing of a LIB rocking-chair battery is displayed in Figure 3.1. During 'charging', Li^+-ions are deintercalated from the cathode, mostly lithium-nickel-mangan-cobalt-oxide (NMC) or lithium iron phosphate (LFP)[40] and migrate through the electrolyte and the separator to the anode, where they are intercalated into a graphite structure. Simultaneously, as electricity carriers, the electrons migrate from the cathode via an outer electrical circle to the anode. This process is reversed during 'discharging', where Li^+ migrates from the anode through the electrolyte and the separator to the cathode. The electrons migrate again via an outer electric circle back to the cathode. In comparison to LIBs, rechargeable magnesium batteries (RMBs) and rechargeable aluminium batteries (RABs) use their respective metal as anodes. It is, in principle, also possible to build a rechargeable lithium battery with metallic lithium as anode. However, lithium metal is prone to dendrite formation even at low current densities, imposing the risk of battery failure.[41] For a battery with a metal anode, the respective ions are not intercalated as in the case of graphite but deposited on the metal anode. During discharging, the metal ions are stripped off the metal anode's surface.

3.1.1 Electrochemical Fundamentals

An electrochemical reaction is any process that is either caused or accompanied by the passage of an electric current and involves the transfer of electrons between two substances, such as redox reactions, galvanic processes, and electrolysis. A galvanic process is a spontaneous reaction between two externally connected electrodes in a cell.[38] In the state of thermodynamic equilibrium, the electrode potential E is determined by the Nernst equation:

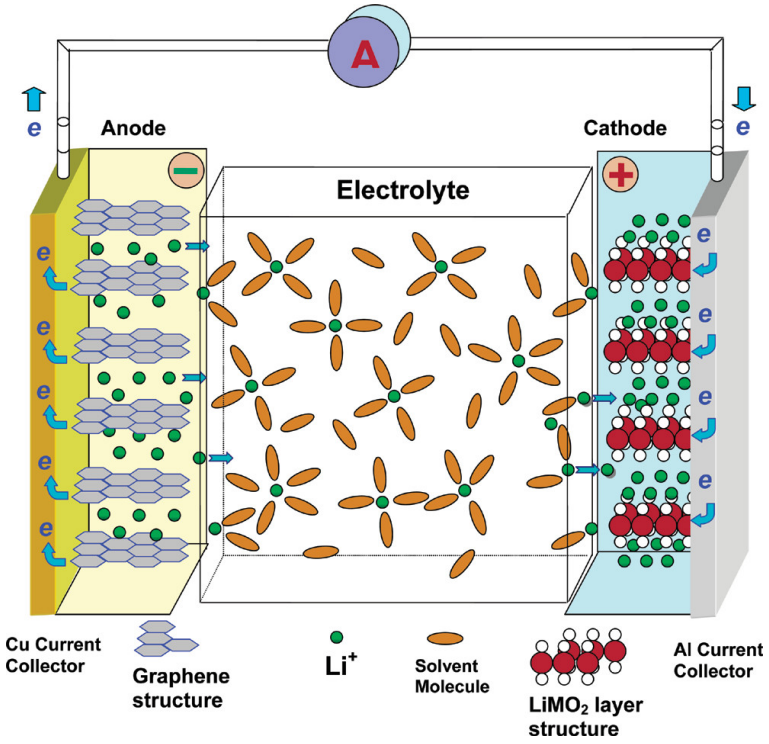

Figure 3.1: Schematic description of a "(lithium ion) rocking-chair" cell that employs graphitic carbon as anode and transition metal oxide as cathode. The undergoing electrochemical process is lithium ion deintercalation from the graphene structure of the anode and simultaneous intercalation into the layered structure of the metal oxide cathode. For the cell, this process is discharge, since the reaction is spontaneous. Reprinted (adapted) with permission from Chem. Rev. 2004, 104, 10, 4303–4418. Copyright 2004 American Chemical Society.[42]

$$E = E^0 + \frac{RT}{nF} \cdot \ln \frac{[a_{ox}]}{[a_{Red}]} \tag{3.1}$$

Here, E^0 is the standard potential of a species. a_{Ox} and a_{Red} are the activity of the oxidized (O) and reduced (R) electrolyte in the system at equilibrium, F is Faraday's constant, R is the universal gas constant, n is the number of electrons, and T is the temperature.[37]

In an electrochemical full cell, the measured potential ΔE at equilibrium is the difference between the positive electrode potential $E_{cathode}$ and the negative electrode

potential E_{anode} and is called open circuit potential (OCP).[37]

$$\Delta E = E_{cathode} - E_{anode} \tag{3.2}$$

Once a current is flowing, there is a deviation from the equilibrium potential ΔE. This deviation is caused by the so-called overvoltage η, which originates from polarization effects. These effects can be divided into three main contributions: Ohmic polarization, kinetic polarization, and mass transfer polarization.[37]

$$\eta = \eta_{Ohmic} + \eta_{kinetic} + \eta_{masstransfer} \tag{3.3}$$

The Ohmic polarization is caused by the IR-drop, which originates from the current I flowing through the cell and the cell's resistance R. Kinetic polarization arises from the activation barrier of the chemical reaction, such as the charge transfer at the electrode-electrolyte interface. Mass transfer polarization is caused by mass transport through the battery, mainly through migration and diffusion.[37]

3.1.2 Interphases in Batteries

The electrode-electrolyte interphase is a crucial area within a battery. Here, two critical phenomena occur; the first one is the formation of a SEI, which is influenced by the presence of a non-passivating or ion-blocking interphase on the metal anode. The second phenomenon is the electrodeposition (stripping and plating) of metals on the anode. The challenges with electrodeposition are the growth of dendrites leading to short circuits, increased cell resistance and electronically disconnected parts of the metal electrode.[43]

Double-Layer Concepts

To understand the interphase of batteries, one must first understand the concept of electrochemical double layers (EDL). Three different types of double-layer models are used in electrochemistry. The simplest and oldest model is the Helmholtz double layer.[44] In the Helmholtz model, ions of one type are close to an electrode's

surface. This layer is called the outer Helmholtz plane (OHP), which, together with the electrode, acts as a capacitor. Therefore, a linear drop of the potential across the double layer is assumed. The Helmholtz model can be used for very dilute solutions. However, it does not consider the ions' thermal movement or the solvent.[45] The movement of the solvated ions is considered in the Gouy-Chapman double-layer model. It assumes that the thermal movement leads to a diffuse layer that is more extensive than a molecular layer. A statistical distribution of the ions is considered, which leads to an exponential drop in the potential within this diffuse double layer. However, ions with no spherical expansion are assumed, so this model can only be used in dilute solutions.[45] This limitation is eliminated in the Stern double-layer model. It combines the two models mentioned above. Further, it also assumes that the ions have a finite extent. In the Stern model, the potential drops linearly in the rigid layer and exponentially in the diffuse layer. Additionally, it assumes that ions can also directly adsorb on the surface without their solvation shell, forming the inner Helmholtz plane (IHP); this means that the ion radius is the highest possible approximation of the ions to the electrode. The inner and outer Helmholtz double layer forms close to the electrode, and the Gouy-Chapman double layer is further away.[45] The three EDL models are schematically presented in Figure 3.2.

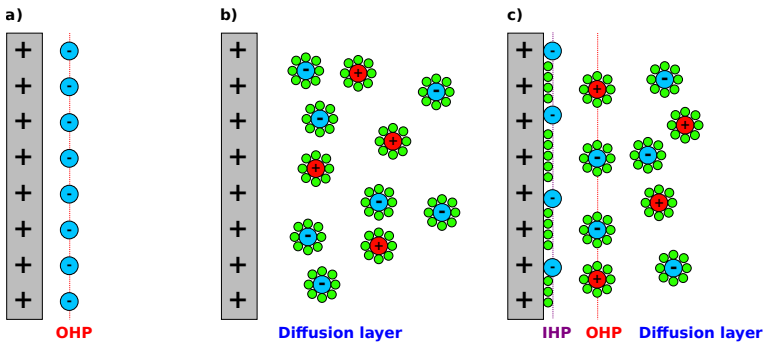

Figure 3.2: Models of the electrical double layer at a positively charged metal surface: a) the Helmholtz model, b) the Gouy–Chapman model, and c) the Stern model. The green circles represent solvent molecules. Inspired by [46, 47].

In the case of batteries, the EDL manifests itself in the following formation process. First, there is the selective adsorption of ions on the electrode after immersion in the electrolyte, a process facilitated by applying an external voltage. Here, a two-

layered structure with alternating electrical charges on the electrode, consisting of OHP, IHP, and a diffusion layer, is created. The IHP contains a single layer of specific adsorbed ions and solvent molecules, whereas the OHP has mainly solvated ions. A diffusion layer with solvated ions is formed due to the thermal motion of ions in the solvent. The specific adsorption of ions in IHP depends on the properties of the electrode material and electrolyte, irrespective of the charged nature of the electrode, which can be positive or negative.[48] For the performance of batteries, it is now important that the specific adsorbed ions of the IHP influence the major composition and initial formation process of the SEI, while the subsequent formation process of the SEI is affected by the solvation structures in the OHP.[48]

Solid Electrolyte Interphase Formation

For the formation of a Solid Electrolyte Interphase (SEI) on metal anodes, it is crucial to know that the metals used for batteries, like magnesium and aluminium, have a native surface oxide. These native oxides originate from the reaction of hydrocarbons, CO_2, water or oxygen from the air with the metal and contain oxides, hydroxides and carbonate components. These reactions even happen when the metal is stored in an inert glovebox and is freshly prepared before usage.[43] The Pilling–Bedworth ratio (P–B ratio), which is the ratio of the volume of the elementary cell of a metal oxide to the volume of the elementary cell of the metal from which the oxide is formed, determines if the native oxide layer is porous nor not. For R_{PB} smaller than one, the oxide coating layer is too thin, likely broken, leading to a porous native oxide and therefore does not provide a protective effect. This is the case for Li (0.567) and Mg (0.81). For R_{PB} bigger than two, the oxide coating chips off and provides no protective effect. For a R_{PB} between one and two, the oxide coating is passivating and provides a protecting effect against further surface oxidation. This is the case for Al (1.28).[49–51]

When the metal is brought in contact with a liquid electrolyte's salt, solvent, additive, or impurities, an SEI starts to form. The formation of the SEI can happen chemically during corrosion while calendar ageing or electrochemically when a current or voltage perturbation is applied.[43] Here, it is crucial that adsorbed ions already exist on the surface prior to electrochemical cycling. The specific adsorption thereby depends on the properties of the electrode material and the electrolyte. During elec-

trochemical cycling (applying a potential to the anode), solvated ions are attracted to the electrode. The solvent molecules obtain electrons from the electrode and are reduced. This happens once the potential of electrolyte reduction is more negative than the Fermi level of the anode.[52] This leads to the formation of a pristine SEI. This cycle continues until the formed SEI is so thick that the electrons from the electrode cannot tunnel through the SEI to reach the adsorbed solvent molecules.[48] The formed SEI can be several hundred nanometers thick and consist of a mosaic structure containing organic and inorganic components. It effectively protects the electrode surface from the continuous decomposition of electrolytes and enables rapid ion transport towards the interface due to its porosity.[43]

The thermodynamics of ion transport within the SEI is represented by ionic conductivity (σ), which can be described as

$$\sigma = |z| \cdot F \cdot c \cdot u \tag{3.4}$$

where z is a charge number, F is the Faraday constant, c is the ion concentration and u is mobility. The ionic conductivity follows the Arrhenius equation.

$$\sigma T = A \cdot \exp\left\{-\frac{E_a}{k_B T}\right\} \tag{3.5}$$

where E_a is the activation energy for ion transport, A is the Arrhenius prefactor at infinite temperature, and k_B is the Boltzmann constant.[35]

Stripping and Plating

The stripping and plating of metals onto a surface strongly depends on the substrate's morphology. Because inherent dislocations, ridges, cracks, and striations on the native surfaces of metal electrodes lead to energetically different electrodeposition areas.[53] These different surface morphology also increase the likelihood of dendrite formations, which are also influenced by high applied current, low salt diffusion coefficients and electrolytes with a low cationic transference number.[54]

In general, the metal deposition follows a simple mechanism. First, the ions lose parts of their solvation shell; then, they are transferred to the metal surface while

the charge is transferred. Afterwards, they diffuse on the surface to either agglomerate with other atoms to form a stable cluster, be incorporated into the electrode, whereby step edges and kink sites are energetically favoured or desorb from the surface again.[46,55] This process is schematically shown in Figure 3.3.

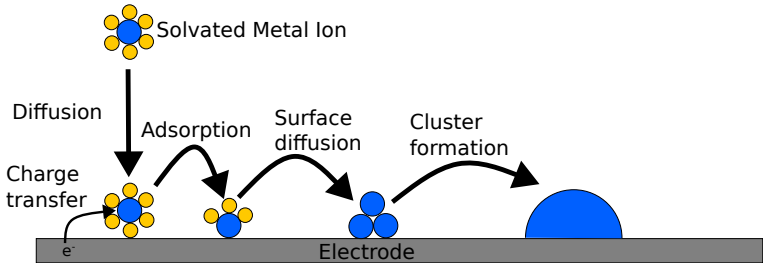

Figure 3.3: Simplified scheme showing the steps involved in the electrocrystallization of a metal on a foreign substrate. Inspired by [46].

However, a single adsorbed atom is energetically unstable. The amount of atoms needed to form a stable cluster can be calculated using the energy of formation. A simple model leads to the following formula.[55]

The first step is the surface area of the three-dimensional cluster with N atoms:

$$S = aN^{2/3} \tag{3.6}$$

Here, a is a constant depending on the particle density n and the cluster's shape. For a hemispherical cluster with the radius r, the number of particles is:

$$N = \frac{2}{3}\pi r^3 n \tag{3.7}$$

This results in:

$$a = (2\pi)^{1/3} \left(\frac{3}{n}\right)^{2/3} \tag{3.8}$$

The surface energy of a cluster is $\gamma \cdot S$, where γ is the surface energy per unit area. Now, the surface contribution of the electrochemical potential is calculated concerning N.

$$\tilde{\mu} = \tilde{\mu}_\infty + \frac{2}{3}\gamma a N^{-1/3} \tag{3.9}$$

Here, $\tilde{\mu_\infty}$ is the electrochemical potential of an atom in an infinite crystal. Now, the Gibbs free energy for the formation of a cluster can be calculated:

$$\Delta G(N) = N\left(\tilde{\mu}_\infty - \tilde{\mu}_s\right) + \gamma a N^{2/3} \tag{3.10}$$

$\tilde{\mu}_s$ is the electrochemical potential of the metal ion in the solution.

At equilibrium, the two electrochemical potentials are equal; therefore, when applying an overpotential η, the charge ze_0 of the metal ion is used.

$$\Delta G(N) = N z e_0 \eta + \gamma a N^{2/3} \tag{3.11}$$

In 3.11, the first term describes the formation of N adatoms on the surface. The second term describes the surface energy, which increases by creating a new surface. Equation 3.11 is graphically displayed in Figure 3.4.

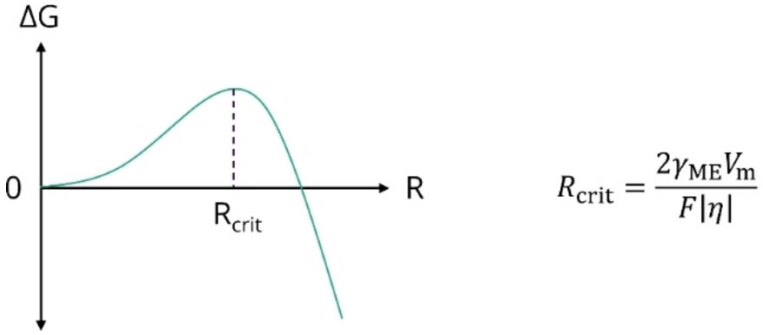

Figure 3.4: Left, impact of radius on change in Gibbs free energy, R_{crit} marks the peak and the critical nucleus radius. Right, formula to calculate R_{crit}. Taken from [56]. Figure licensed under CC BY-NC 4.0, `https://creativecommons.org/licenses/by-nc/4.0/`

Metal deposition can only occur when the overpotential η is negative. In Figure 3.4 R_{crit} marks the critical cluster size. When the cluster has more atoms than R_{crit}, it is more likely that the cluster will grow bigger, whereas when the cluster size is smaller than R_{crit}, it is more likely to disappear again. Nevertheless, there is a

certain probability that subcritical clusters will grow and supercritical clusters will disappear again since cluster formation and growth are stochastic processes.[55]

There are three different mechanisms for the morphology of the deposited metal, which depends strongly on the properties of the substrate S and the metal M. In the first case, the interaction of the atoms M with each other is stronger than with the substrate S. In this case, three-dimensional clusters are formed. This type of growth mechanism is called Volmer-Weber growth or island growth. In the second case, the interaction of the metal M is stronger with the substrate S than with each other; in his case, a monolayer of metal is deposited on the substrate. In this case, it is now important to consider the mismatch of the crystallographic structures between the metal and the substrate. In case of a small mismatch, further layers of the metal are deposited on the metal monolayer. This growth mechanism is called Frank-van-der-Merwe or layer-by-layer growth. In the case where there is a large mismatch in the crystallographic structures of metal and substrate, the metal continues to grow as a three-dimensional island. This growth mechanism is called Stranski-Krstanov growth. A possible fourth option is that the metal atoms and the atoms of the substrate radially exchange place and form a surface alloy.[55] The three growth models are schematically shown in Figure 3.5.

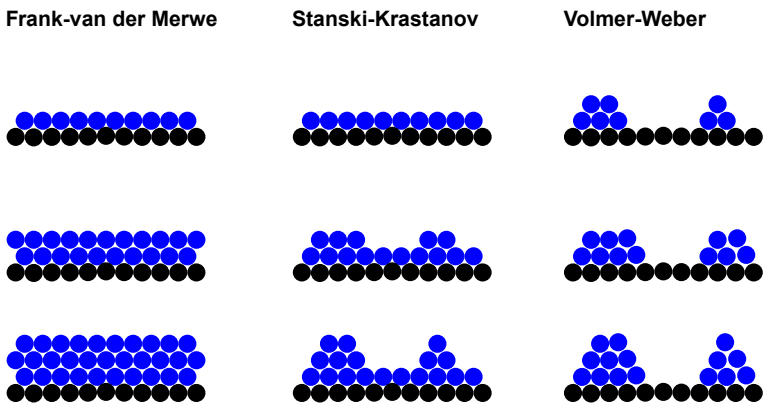

Figure 3.5: Schematic representation of the three different heteroepitaxial growth modes, namely Volmer-Weber, Frank-van der Merwe, and Stranski-Krastanov. Inspired by [55, 57].

The deposited metal's morphology depends not only on its interaction with the substrate but also on the applied overpotential. At low overpotentials, the energy for nucleation is small; therefore, the formation of new nuclei happens very rarely. Dur-

ing growth, large crystals are formed with a morphology of layers and blocks. At high overpotentials, a large number of crystal grains are formed, leading to a morphology of small nuclei and fine-grained deposits.[46]

Techniques to Investigate the Interphase of Batteries

Various techniques can be used when investigating the interface of batteries, depending on the specific properties of interest.[58] Electrochemical impedance spectroscopy (EIS) is commonly used to study transport properties. At the same time, the thickness of the SEI can be determined using focused ion beam scanning electron microscopy (FIB-SEM) and EIS. Techniques such as Fourier-transform infrared spectroscopy (FT-IR), X-ray photoelectron spectroscopy (XPS), and time-of-flight secondary ion mass spectrometry (TOF-SIMS) can be square millimetre, allowing for general compound identification. Information about the morphology, particle size and porosity can be gained by scanning electron microscopy (SEM) and transmission electron microscopy (TEM). Atomic force microscopy (AFM) can be used to investigate mechanical properties. Potential gas formation (which can occur during SEI formation) can be studied using gas chromatography coupled with mass spectrometry (GC-MS). X-ray absorption spectroscopy (XAS) can be used to determine the oxidation states of elements.[35,59]

Using in-situ and operando techniques for interface investigation is generally beneficial, as the sample is already in the desired environment. Ex-situ measurements may lead to removing potential surface compounds upon washing the electrode to eliminate salt and electrolyte remains. Additionally, ex-situ measurements require the sample to be kept under an inert atmosphere to prevent contamination with oxygen or moisture, which could alter the interface.[35]

A newly emerged technique to investigate the interface of batteries operando is near ambient pressure X-ray photoelectron spectroscopy (NAPXPS).[59] In this technique, the sample is dipped into the electrolyte and then pulled out, creating a meniscus of the electrolyte of only a few nanometers. As the mean free path of electrons, which are emitted during XPS, is only in the nanometer range, such low electrolyte thicknesses are needed. Since many emitted electrons are still scattered in the electrolyte, the signal-to-noise ratio is relatively low. Additionally, due to the small electrolyte layer, performing electrochemistry in parallel is challenging. Be-

cause of this and the fact that the technique is still relatively new and expensive, only a limited number of operando NAPXPS experiments have been performed.[59–61]

3.2 Multivalent Batteries

3.2.1 Magnesium Batteries

Rechargeable magnesium batteries have many advantages, such as a high abundance of raw material and a small likelihood of forming dendrites. Further, due to their doubly charged ions, they have a much higher theoretical volumetric capacity of 3.833 mAh cm^{-3}, compared to monovalent ions like lithium or sodium. However, one of the major hindrances to the improvement of RMBs is the electrode-electrolyte interphase; here, three essential challenges occur. Firstly, there is the poor reversibility of Mg stripping and plating, which reduces the battery performance. Secondly, the uneven stripping and plating of Mg can lead to dendrite formation, short circuits, and damage to the battery. Thirdly is the high reactivity of magnesium, causing the formation of a passivation layer when in contact with most electrolytes, primarily due to moisture in the electrolyte.[62]

The latter is due to the low anode potential of -2.67 V vs. SHE, which reduces most of the solvents. Lithium, however, also has a low anode potential; here, the formation of this passivation surface film is no problem because the Li^+-ions can diffuse through the passivation film.[63] However, due to the magnesium cation's high charge density, this is difficult, leading to sluggish migration and high dissolution energy barriers.[64] Nevertheless, a few electrolytes can be used in Mg-batteries, e.g. certain ethers, such as glymes and tetrahydrofuran (THF). For them, the challenge is that they have to be highly pure due to trace amounts of contamination like water, CO_2, protic solvents, or oxygen, leading to the formation of the blocking surface layer.[65] The first electrolytes discovered to work with RMB are Grignard electrolytes. They have the general term RMgX (R = alkyl or aryl group, X = halogen). Grignard reagents have the advantage of high reductive stability and sufficient oxidation stability, enabling reversible Mg deposition and dissolution.[66] Grignard reagents undergo the following equilibrium reactions:[67–69]

Schlenk equilibrium:

$$2\,\mathrm{RMgX} \rightleftharpoons \mathrm{R_2Mg} + \mathrm{MgX_2} \tag{3.12}$$

Ionization equilibrium:

$$2\,\mathrm{RMgX} \rightleftharpoons \mathrm{RMg^+} + \mathrm{RMgX_2} \tag{3.13}$$

During deposition, Mg is not directly reduced from Mg-ions but from the adsorbed RMg^+:

$$2\,\mathrm{RMg^+} \rightleftharpoons \mathrm{Mg} + \mathrm{R_2Mg} \tag{3.14}$$

The magnesium dihalides are reduced via dialkyl magnesium, hindering the development of a passivation layer.

$$\mathrm{R_2Mg} + 2\,\mathrm{MgX_2} \rightleftharpoons \mathrm{Mg} + 2\,\mathrm{RMgX_2} \tag{3.15}$$

During the electrochemical cycling of Grignards, no passivation layer is formed on the Mg surface. However, due to the adsorption of RMg^+, $2\,RMg\cdot$, R^- and $RMgX^{2-}$ on the surface, confirmed by in-situ Fourier transform infrared spectroscopy (FTIR), the interface impedance is relatively high.[68,70–73] These adsorbates have a considerable influence on the stripping and plating of the Mg by shaping the morphology of the Mg-deposition layer, especially when $AlCl_3$ is added to the electrolyte.[68] The morphology also follows a two-step mechanism, where a porous Mg layer is initially formed in which solution species may be trapped. With ongoing Mg deposition proceeds, the Mg layer becomes compact and crystalline, and the nature of the electrolyte used attenuates its morphology.[68] However, Grignards face the challenge of being nucleophilic and therefore unsuitable for most cathode materials and possess a low oxidative stability of around 1.5 V (vs. Mg/Mg^{2+}). Because of this, the electrolytes used for RMBs have improved further in the upcoming years.

One of the most prominent electrolytes is the boron-based $Mg[B(HFIP)_4]_2$ (HFIP= $-OCH(CF_3)_2$) developed by Zhao-Karger et al. in 2017.[74] They discovered that $Mg[B(HFIP)_4]_2$ has an anodic stability of up to 4.3 V (vs. Mg/Mg^{2+}) on stainless

steel and aluminium, a columbic efficiency of 98%, and also an ionic conductivity of 11 mS cm^{-1}. Furthermore, the $Mg[B(HFIP)_4]_2$·DME salt is air- and water-insensitive.[74,75] Further research has shown that this electrolyte needs preconditioning cycles to achieve a better performance.[76] The electrolyte was further improved by additives. The addition of $Mg(BH_4)_2$ facilitates the preconditioning by removing the native oxide layer and promotes the formation of an SEI.[77] By adding bismuth triflate ($Bi(Otf)_3$), a surface layer of Bi/Mg_3Bi_2 forms. This reduces the adsorption of inactive species and alleviates the surface passivation, increasing the charge transfer.[78], A recent study on the morphology of Mg electrodeposition from $Mg[B(HFIP)_4]_2$ does not show any formation of dendrites; however, the deposition was not smooth, either.[79]

A further advantage of magnesium is that the formation of dendrites on a pure metal anode is less likely due to its deposition either in a hemispherical or cauliflower-like morphology.[80] This is also proposed by theoretical calculations, which show that the migrating barrier between the Li(001) and the Mg(0001) is 120 meV and therefore, relatively large, resulting in dendrite formation for Li but not for Mg.[81,82] However, these findings are highly debatable since other theoretical calculations propose that the difference in the migrating barrier between the Li(001) and the Mg(0001) is only 30 meV and, therefore, too small to make a difference in the dendrite formation behaviour between Li and Mg.[83] Further investigations also show that for the most commonly observed surface orientation, $(101\bar{1})$, the surface diffusion energy is 0.29 eV and therefore too small, leading to the formation of dendrites.[84] Experimental results show Mg-dendrites formation in the Grignard electrolytes at high current density.[85,86] Operando X-ray imaging in Grignard electrolyte further shows that spherical deposits are formed at 2 mA cm^{-2}, but branched dendritic Mg are formed at 10 mA cm^{-2}.[87] The current density at which Li dendrite formation is observed below 1 mA cm^{-2}. However, spherical deposited Mg can also penetrate the separator and form a short circuit, which might be due to the high shear modulus of the Mg metal.[88]

3.2.2 Aluminium Batteries

Rechargeable aluminium batteries possess two different operation modes. The first one is an Al-ion battery. This is a rocking-chair type battery, where Al is deposited

on the anode and Al^{3+} is intercalated in the cathode. However, the small size and high charge of the Al^{3+}-ion leads to a strong coulombic interaction with the host material and, therefore, hinders the intercalation of the ion, similar to magnesium.[89] In general, the proposed redox reactions for the Al batteries with cathode active material (AM) are as follows:

At the anode:

$$\mathrm{Al} + 7\,\mathrm{AlCl_4}^- \rightleftharpoons 4\,\mathrm{Al_2Cl_7}^- + 3\,\mathrm{e}^- \tag{3.16}$$

At the cathode:

$$\mathrm{AM} + 4\,\mathrm{xAl_2Cl_7}^- + 3\,\mathrm{xe}^- \rightleftharpoons \mathrm{Al}_x\mathrm{AM} + 7\,\mathrm{xAlCl_4}^- \tag{3.17}$$

The second possible operation mode is a dual-ion battery. Similar to the Al-ion battery, Al is deposited at the anode. However, at the cathode (mostly graphite), $AlCl_4^-$ is intercalated. The operating principle of aluminium dual-ion batteries can be depicted by the following half-reactions:

At the anode:

$$4\,\mathrm{Al_2Cl_7}^- + 3\,\mathrm{e}^- \rightleftharpoons 7\,\mathrm{AlCl_4}^- + \mathrm{Al} \tag{3.18}$$

At the cathode:

$$\mathrm{AM} + \mathrm{xAlCl_4}^- \rightleftharpoons (\mathrm{AlCl_4})_x\mathrm{AM} + \mathrm{xe}^- \tag{3.19}$$

For aluminium dual-ion batteries, it is important to note that three $AlCl_4^-$ are intercalated into the cathode for the electrodeposition of one aluminium atom. Since there is an equilibrium between $AlCl_4^-$ and $Al_2Cl_7^-$ (see 3.20), the plating ends once the $Al_2Cl_7^-$ resources are depleted.[90] This means that the anode does not require the presence of aluminium but needs to be a good current collector with sufficient Al stripping and plating. Therefore, chloroaluminate ionic liquids in aluminium dual-ion batteries must be seen as an anolyte (i.e., liquid anode), which is reduced upon charging in contrast to the electrolyte used in Al-ion batteries.[90]

The commonly used electrolytes for both types of Al-batteries are room-temperature ionic liquids (RTIL). RTILs consist of a Lewis acidic metal salt and a Lewis ba-

sic organic salt, mixed to form weakly coordinated complex ions that become liquid at room temperature.[62] They have the advantage of being non-volatile and non-flammable compared to the electrolyte used in LIBs, making the battery much safer.[91] The most commonly used ionic-liquid is 1-Ethyl-3-methylimidazolium chloride aluminium chloride ([EMImCl]:$AlCl_3$).[62] For the [EMImCl]:$AlCl_3$ electrolyte, the molar ratio of the two components is essential. At a molar ratio of 1:1.5 (an excess of $AlCl_3$), the predominant ions in the ionic liquid are $Al_2Cl_7^-$ and $AlCl_4^-$. At a molar ratio of 1:1, the predominate species is $AlCl_4^-$, and at a molar ratio of 1.5:1 (an excess of [EMImCl]), it is $AlCl_4^-$ and Cl^-. Since Al deposition only works from $Al_2Cl_7^-$, an excess of $AlCl_3$ is crucial for battery performance.[92] Equation 3.20 shows the equilibrium in the ionic liquid. However, the upper-most molar ratio between $AlCl_3$ and [EMImCl] at which a liquid still forms is $\approx$ 2:1.[90]

$$\mathrm{AlCl_3} + \mathrm{AlCl_4^-} \rightleftharpoons \mathrm{Al_2Cl_7^-} \tag{3.20}$$

However, one of the major challenges of [EMImCl]:$AlCl_3$ is its corrosiveness towards the native oxide present on top of the Al anode and other cell parts consisting of stainless steel or copper.[62,93] Another crucial aspect regarding safety is that the electrolyte reacts exothermic when in contact with moisture, leading to hydrochloric acid formation.[94]

For Al-ion batteries, metallic aluminium is the most used anode. However, this material faces drawbacks since its surface is covered with a native oxide layer, blocking ion and electron transport.[95] There are controversies on the exact impact of this layer. Investigations show that this oxide layer increases the electrode/electrolyte interface stability[96] and also restricts the formation of dendrites because it decreases nucleation sites and prevents electrode disintegration.[97] This means that the oxide film can mechanically suppress the growth of irreversible dendritic Al. Electropolished Al electrodes, where the native oxide has been removed, have a higher capacity due to increased active surface area. A higher capacity was also discovered after prolonged contact of the native oxide with a corrosive electrolyte due to the etching of the native oxide and, consequently, the exposure of the bare Al metal to the electrolyte.[98]

A morphology analysis of the deposited Al shows that first, small Al-particles formed, and later, Al is distributed randomly, leading to the formation of dendrites.[69] Fur-

ther, while immersing in a corrosive electrolyte, the native oxide layer gets dissolved, while simultaneously, a new SEI is formed containing the species Al-Cl and Al-O.[69]

Since no aluminium is needed as an anode material for Al-dual-ion batteries, graphite is an ideal alternative. Its advantages are its low cost, high electrical conductivity, low density, and high-temperature resistance. A previous investigation showed that stripping and plating of aluminium from $AlCl_3$:BMImCl 2:1 onto expanded graphite is possible with high reversibility. Further, the plating-stripping charge efficiency was 84%, close to the value obtained for aluminium metal.[99] Despite numerous research on the electrodeposition of metals on HOPG, results on Al are rare. Tu et al. investigated the electrodeposition of Al on graphite from $AlCl_3$–1-butyl-3-methyl-imidazolium chloride ($AlCl_3$:BMImCl).[100] They discovered that the morphology of the deposited Al is dependent on the applied current density with coarse deposits at low current density and a more evenly surface at high current density. In addition, the increase in the current density leads to a decrease in the grain size of the deposited Al. The authors also investigated the crystallographic orientation and discovered that the X-ray diffraction peak intensity of the (200)-plane increases with increasing current density, while it decreases for the (111)-plane. This means that the current density significantly influences the crystallographic orientation of the deposited aluminium.[100] From this observation, they came up with a potential three-step mechanism for the Al deposition. In the first step, a thin, compact Al layer is deposited on the electrode. In the second step, dendrites attach to the thin, compact layer. At high current density, fine-grained particles lead to high aluminium particle density. In contrast, coarse-grained particles result in a relatively high deformation at low current density. This makes it more likely for the foils to form dendrites. As a final step, the dendrites start to grow. Thereby, the growing particles fill up the interstices between the dendrites. This means that the fine-grained morphology at high current density is prone to form compact layers.[100]

In the case of a dual battery, graphite is now also used as a cathode material. However, here, the literature deals mainly with the intercalation of the $AlCl_4^-$ into the graphite host rather than with the interface. Theoretical studies show that the intercalation of $AlCl_4^-$ into graphite is a four-step process and that due to the tetrahedral form of the $AlCl_4^-$, the graphite layers get distorted.[101] The sole investigation of the graphite interface was done by Canever et al. They discovered that an interface layer is formed upon the first cycle due to the decomposition of the electrolyte at po-

tentials lower than 2.45 V (vs. Al/Al^{3+}). The cause for this interface layer are defects in the graphite and heteroatomic functional groups on the graphite's surface.[102]

Combining the graphite anode and graphite cathode leads to a rechargeable dual-carbon battery (RDCB). This concept is already known from lithium and sodium electrolytes.[103,104] Further, it has already been proven experimentally for aluminium.[105,106] Thereby, conductive graphite paper was used as the anode and cathode and the ionic liquids $EMImCl:AlCl_3$ as electrolyte. Due to the high ionic conductivity of the electrolyte, this battery shows a reasonable rate and cycle performance of up to 1000 cycles. The initial discharge capacity is around 70 $mA\,h\,g^{-1}$ at a current density of 200 $mA\,g^{-1}$. The battery also provides a discharge voltage of 2.1 V (vs. Al/Al^{+3}). However, the drawback of this kind of battery is strong self-discharge, with 16.82% h^{-1} in the mentioned publications.[105,106]

3.3 Photoelectrochemical Water Splitting

Solar-water splitting uses sunlight to split water into its elementary forms, oxygen and hydrogen. Two possible ways this could be done are by using a photovoltaic (PV) electrolyzer system or a photoelectrochemical (PEC) system. In a PV electrolyzer system, the sunlight is 'harvested' by a solar cell, which creates electricity that can then be used to power electrolyser, which are used to split water. In a photoelectrochemical (PEC) system, a photoelectrode is placed directly into the water and serves as a light absorber and energy converter.[27] Both approaches are schematically shown in Figure 3.6. The most promising and commonly studied photoelectrode used for the latter are (III-V) semiconductors.[107] For a detailed understanding, it is therefore necessary to investigate the physical basics of semiconductors as well as their behaviour when in contact with an electrolyte.

3.3.1 Fundamentals of Semiconductors

A widely used mode to describe the electronic structure in solids is the band model. The band model is an extension of the molecular orbit model, in which the atomic orbitals are combined into bonding, antibonding and non-bonding molecular orbitals.

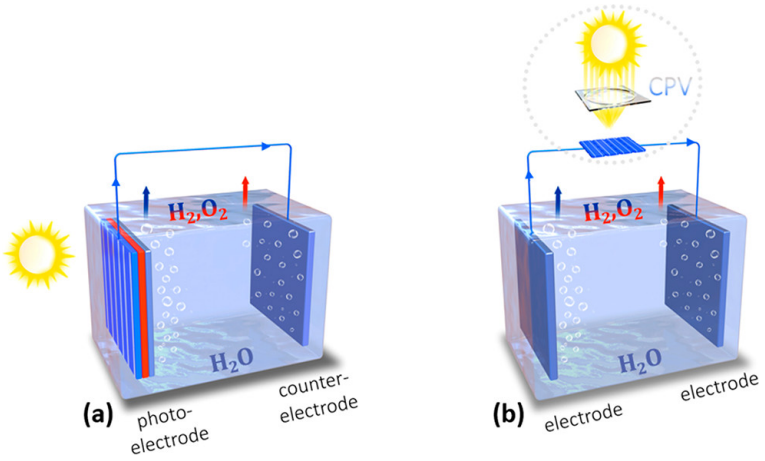

Figure 3.6: Two possible approaches for the hydrogen production: (a) photoelectrochemical (PEC) system and (b) photovoltaic electrolyser system. Reprinted (adapted) with permission from ACS Energy Lett. 2020, 5, 2, 611–622. Copyright 2020 American Chemical Society.[27]

Solids now consist of a large number of 'molecules', each bringing its own molecular orbital. Because these molecular orbitals' energy differences are very small, they are summarised in overlapping and non-overlapping energy bands. The most important of these bands are the valance band (VB), the energetically highest band still occupied by electrons and the conduction band (CB), the energetically lowest empty band. There are now three distinct classes of solids: metals, semiconductors (SC) and insulators. For metals, the CB and the VB overlap, making them electronically conductive. Insulators have a band gap between CB and VB, larger than 5 eV, making them electronic insulators. For semiconductors, the band gap is between 0.1 and 5 eV. This makes them insulators at 0 K, but thermal- or photo-excitation can make them conductive.[108] It is important to note that the definition of the material types via the energy of the band gap is not strict but rather a guide to determine the three classes of solid materials.

For further discussion, it is now essential to introduce the Fermi level (E_F). The Fermi level is the electrochemical potential of the electrons in the solid and the energy at which the probability of an energy level being occupied by electrons is 0.5.[108] Another critical property is the work function (Φ), which describes the energy needed to remove an electron from the solid into the vacuum. Both parameters are shown in the band diagram in Figure 3.7.

The low band gap of semiconductors makes the excitation of an electron from the VB into the CB with a photon of an energy greater than the band gap energy possible. Excess energy is thermalized to the lower edge of the CB. This excitation creates a hole in the VB and an electron in the CB, forming an electron-hole pair. Since the semiconductor is perturbed from its equilibrium state by generating an electron-hole pair, it tends to return to its equilibrium state. This happens by the recombination of the electron and the hole. Thereby, the excess energy is emitted either thermally in the form of heat or radiatively by the emission of a photon. The electron and hole densities in the conduction and valence band are described by a quasi-Fermi level of electrons ($^{*}E_{Fn}$) and a quasi-Fermi level of holes ($^{*}E_{Fp}$), respectively. In general, the density of majority carriers does not significantly increase upon illumination, and the quasi-Fermi level for majority carriers is normally almost the same as the Fermi level at equilibrium. In contrast, the quasi-Fermi level of the minority carriers is significantly reduced compared to the Fermi level. Due to the penetration depth of light, electron-hole pairs occur near the semiconductor surface, which leads to variations in the quasi-Fermi level of minority carriers with the distance from the surface.[108]

The concentration of holes and electrons can not only be generated by exiting electrons from the VB to the CB but also by adding foreign atoms to a semiconductor's lattice structure, which changes its electrical properties. This process, called doping, enables intrinsic semiconductors like silicon, which have a low concentration of free charge carriers, to be electric conductive. There are now two types of doping. The first one is n-type doping. Here, an element with more valance electrons than the intrinsic semiconductor is used, such as As in the case of Si. The energy level of this excess atom is above the VB and close to the CB, making thermal excitation of this electron to the CB possible. So, the electron can contribute to the SC conductivity. In this case, the Fermi level is between the conduction band and the energy level of this excess atom. Here, the electrons act as majority carriers. The second type is p-type doping; here, an element with fewer electrons compared to the lattice is used, like Ga for Si. This creates an acceptor level above the valence band edge and, as a result of the thermal excitation of electrons from the VB, a free hole in the latter. In this case, the positive charges (holes) are the majority carriers, and the Fermi level lies between the valance band and the acceptor level.[108,109]

3.3.2 Semiconductor-Metal and Semiconductor-Electrolyte Interfaces

The most critical part of a semiconductor for PEC water splitting is its interface with the different adjacent media. The following section first describes the case of a semiconductor in contact with a metal before continuing with the semiconductor in contact with an electrolyte — followed by the influence of illumination and external potential.

Semiconductor-Metal Contact

When a metal (M) and a semiconductor (S) are in contact, an interface forms between them. Understanding this interface is crucial for understanding the semiconductor-electrolyte interphase later.

Once a metal is in contact with a semiconductor, as depicted in Figure 3.7, the free electrons will transfer between them due to work function difference. The electrons flow from the solid with the lower work function to the solid with the higher work function. This flow of electrons continues until the two Fermi levels align and an equilibrium is reached. Here, the solid with the higher work function is negatively charged, and the solid with the lower work function is positively charged. In the case of metal, the excess charge is distributed equally over the surface while the bulk is field free. In the case of the semiconductor, the excess carriers stay at a layer near the interface; this area is called the space charge region.

Due to the electric field between the semiconductor and the metal, the edges of the bands in the space charge region are bent. The band bending is thereby dependent on the relation of the work functions between metal and semiconductor.

Upwards band bending toward the interface happens when $\Phi_M > \Phi_S$, while the edges bend downward toward the interface when $\Phi_M < \Phi_S$, as depicted in Figure 3.7. Here, the degree of bending of the energy band of the semiconductor at the interface equals the work function difference between metal and semiconductor.

$$V_{BB} = |\Phi_M - \Phi_S| \tag{3.21}$$

A particular case occurs at an n-type semiconductor when the work function of the metal exceeds that of the semiconductors ($\Phi_M > \Phi_S$). In this case, a Schottky barrier (Φ_{SB}) is formed between the semiconductor and the metal.

$$\Phi_{SB} = \Phi_M - \chi_S \tag{3.22}$$

Here, χ_s is the electron affinity of the semiconductor. No Schottky barrier is formed in the case of an n-type semiconductor when $\Phi_M < \Phi_S$, but rather an ohmic contact between the metal and the semiconductor.[108,110,111]

The band diagrams of the three cases of Metal-semiconductor before contact and after contact with Schottky and ohmic type are displayed in Figure 3.7:

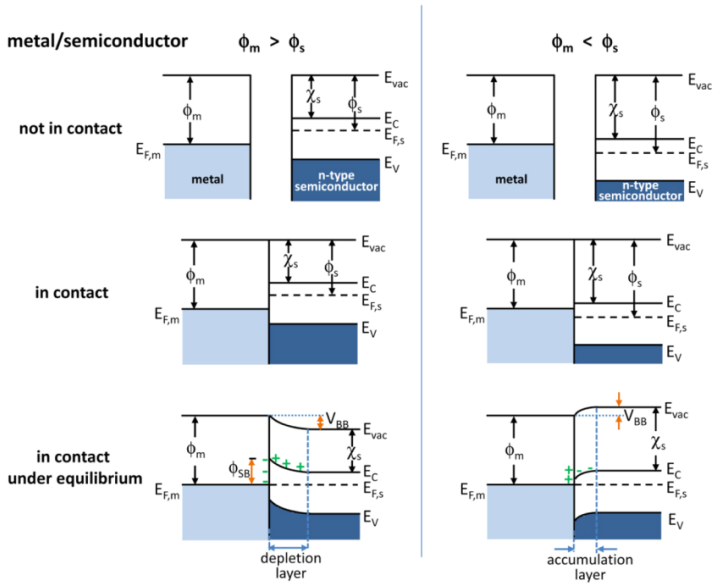

Figure 3.7: Energy band diagrams of metal and n-type semiconductor contacts. E_{vac}, vacuum energy; E_c, energy of conduction band minimum; E_v,energy of valence band maximum; ϕ_m, metal work function; ϕ_s, semiconductor work function; χ_s, electron affinity of the semiconductor. Reprinted (adapted) with permission from Chem. Rev. 2012, 112, 10, 5520–5551. Copyright 2012 American Chemical Society.[110]

Semiconductor-Electrolyte Contact

When a semiconductor is brought in contact with an electrolyte, thermodynamic equilibrium is established on both sides of the interface. Similar to the semiconductor-metal contact, the semiconductor surface's Fermi level and the electrolyte's Fermi level must adjust to achieve an equilibrium. Due to the high number of available states, the Fermi level of the electrolyte is considered nearly constant. The equalization process occurs through electron transfer across the interface, forming a space charge layer at the semiconductor surface. This, in turn, causes band bending in the semiconductor, a phenomenon induced by charge transfer due to different electrochemical potentials between the semiconductor and the electrolyte.

Since there is now an excess amount of charge at the surface of the semiconductor, a double layer occurs inside the electrolyte. The different kinds of double-layer have already been described in the section about battery interfaces (See section 3.2.1 Double-Layer Concepts). Here, the double-layer can be divided into three sections: First, the semiconductor space charge layer, followed by the Helmholtz layer, consists of the IHP, the adsorbed ions (opposite charge to the space charge layer), the OHP (the closest approach of hydrated mobile ions) and finally, the Gouy-Chapman layer, where there is still an excess of one specific type of ion. A schematic illustration of a semiconductor in contact with an electrolyte is shown in Figure 3.8.

Suppose the sample (in the electrolyte) is illuminated with light whose energy exceeds the semiconductor's band gap. This generates electron-hole pairs. Two different mechanisms now occur depending on the semiconductor's type of doping. In the case of an n-doped semiconductor, the generated holes migrate to the surface. In contrast, the electrons migrate to the semiconductor's bulk and the external electric circuit. This creates an anodic photocurrent. In the case of a p-doped semiconductor, the mechanism is reversed, with electrons migrating towards the surface while holes migrate towards the bulk, creating a cathodic photocurrent.

The application of an external potential towards the semiconductor (under illumination in the electrolyte) results in a stronger band bending. The applied potential will be distributed over the space charge and Helmholtz layers. Since the Helmholtz layer's capacity is much larger than the capacity of the space charge layer, any applied potential will fall across the depletion layer of the semiconductor. This would lead to an upward bending of an n-type semiconductor while applying a positive po-

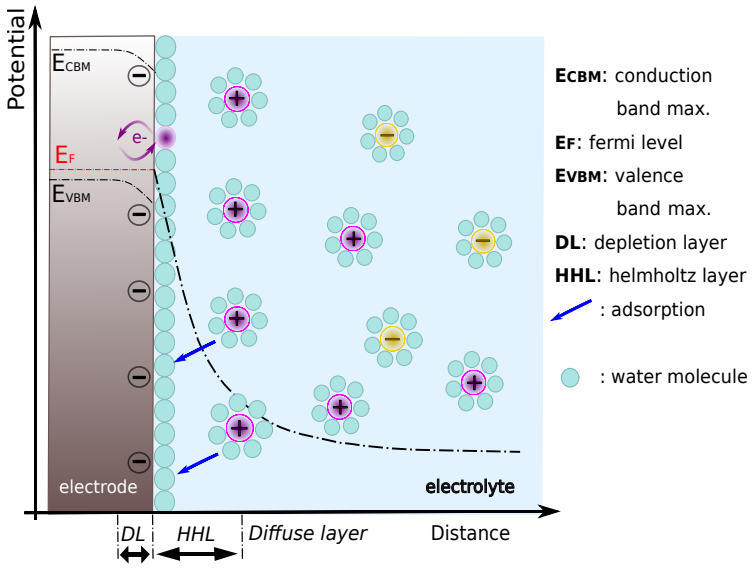

Figure 3.8: Electrochemical interface of a p-type semiconductor with an electrolyte forming a depletion layer in the dark after equilibrium. The positive and negative charges on the electrolyte side account for solvated ions. Taken from [32]. Figure licensed under CC BY 4.0, `https://creativecommons.org/licenses/by/4.0/`

tential and a downwards band bending of a p-type semiconductor with a negative potential. A band diagram of a semiconductor in electrolyte and under illumination is shown in Figure 3.9.

3.3.3 Challenges in PEC Water Splitting

The most crucial part of solar water splitting is the semiconductor-electrolyte interface. However, a dial issue occurs here since most III-V-based photoelectrodes are highly unstable in acidic or alkaline electrolytes, leading to surface corrosion and, ultimately, a reduced device lifetime.[27] A possible way to circumvent this issue is by using an appropriate protective layer. An efficient passivation layer must fulfill four main functions. The passivation layer needs to passivate the absorber surface electronically and chemically, define the energy-converting contact, be transparent

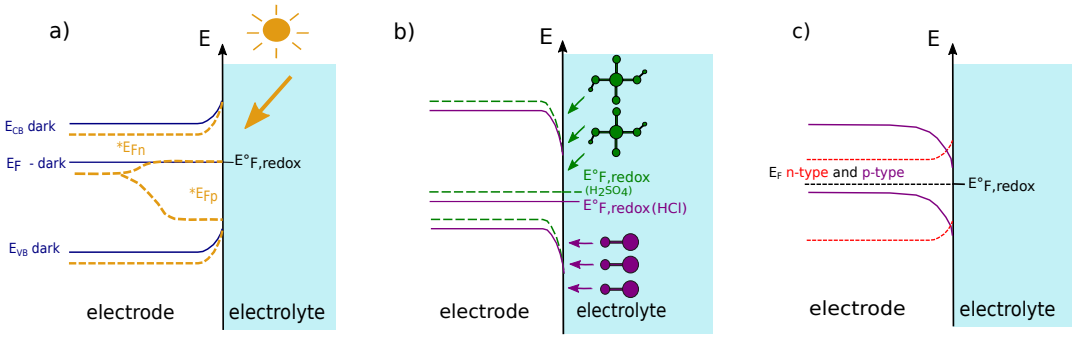

Figure 3.9: Energetic band diagrams showing the influence of the irradiance, the doping type, and the electrolyte on the EDL and the optical properties of an idealized semiconductor-liquid interface (no surface passivation/corrosion). The electrode is considered as photo-cathode for solar water splitting, and H^+/H_2 is the most active redox couple. Interfacial layers and charge-carrier recombination[112] are ignored for the sake of simplicity. a) dark and illuminated (dotted line) EDL of n-type semiconductor. b) EDL of p-type semiconductor influenced by the charging effect of H_2SO_4 (dotted lines) and HCl electrolytes (0.01 M). c) EDL for n and p-type semiconductors. Taken from [32]. Figure licensed under CC BY 4.0, `https://creativecommons.org/licenses/by/4.0/`

and transfer the charge carriers.[107] Furthermore, a passivation layer is also needed to mitigate the influence of electronic defect states in the bandgap that can act as recombination centres and reduce the photocurrent or 'pin' the Fermi level and limit the photovoltage.[107]

Another challenge for PEC water splitting is the high cost of III-V semiconductors. For example, the material costs of single- and dual-junction solar cells are around $30/WDC for and for triple-junction solar cells $53/WDC, constituting 75% of the manufacturing costs.[27]

A further issue in commercialising PEC water splitting is the solar-to-hydrogen (STH) efficiency. Studies have shown that the STH is the most critical factor determining the levelized cost of hydrogen production and the net primary energy balance.[21,22]

Currently, STH efficiencies of up to 19% are reached.[25,113] However, maximum efficiencies well over 25% seem possible for a target operational photovoltage of 1.8 V, the minimum needed to drive the HER and OER at sufficient rates.[107]

4 Characterization Techniques

4.1 Reflection Anisotropy Spectroscopy

Reflection anisotropy spectroscopy (RAS) is a linear, differential optic probe that measures the difference in reflectivity (Δr) of normal incidence plane-polarised light between two orthogonal directions in the surface plane (x, y) normalised to the mean reflectivity (r). Its definition is given in equation 4.1:

$$\text{RAS} = \frac{\Delta r}{r} = 2 \cdot \frac{r_x - r_y}{r_x + r_y} \tag{4.1}$$

Here, r_x and r_y are the Fresnel reflection coefficients along the x and y axes in the surface plane, which have different values at an anisotropic surface.[114] Despite both the real and imaginary parts being measured, only the real part is used in most of the experimental literature.

It is also possible to probe the anisotropy of the reflectance, i.e. the (real) square of the Fresnel reflection amplitude, $R = |r|^2$. This case is then referred to as reflectance anisotropy spectroscopy, where the relation $\mathrm{Re}(\frac{\Delta r}{r}) \approx \frac{1}{2}\frac{\Delta R}{R}$ holds for $\Delta r \ll r$.[115,116]

Figure 4.1 shows the working principle of RAS. The function of the spectrometer will be described in the order of the light path. At the beginning is a Xenon arc lamp, which provides a relatively constant and continuous light output in the range of 1.5 to 6.0 eV. The lamp output is somewhat discontinuous below 1.5 eV, while absorption in air happens above 6.0 eV. In the polariser, the light gets linear polarised. When linearly polarised light is now reflected by an anisotropic crystalline surface, the polarisation becomes elliptic. At the photo-elastic modulator (PEM), due to its birefringent nature, a retardation between the two components of the elliptic polarisation along the x and y surface crystal direction is introduced. This results in a

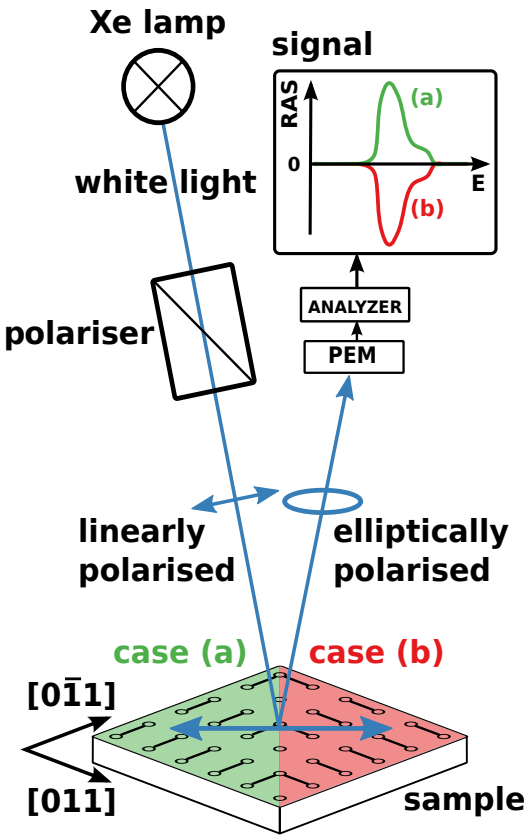

Figure 4.1: General principle of RAS for the case of a dimerised, cubic (100) surface. The rotation of the dimers by 90° (case a, green vs. case b, red) switches the sign of their contribution to the spectrum. Taken from [32]. Figure licensed under CC BY 4.0, `https://creativecommons.org/licenses/by/4.0/`

phase-modulated signal. After passing the analyser, the intensity of the light depends on its polarisation state, the retardation, and the modulation frequency of the PEM. Then, the light passes the monochromator before it is detected by a photomultiplier and demodulated by a lock-in amplifier.[32,114] A more detailed description of the working principle of RAS can be found in the work of Haberland et al.[117]

To reduce the complexity of the signal and to have an adequately high reflectivity, single crystals with very low surface roughness (< 10 nm) and low Miller indices are typically used for RAS. Due to the penetration depth of light, the anisotropy signal

can arise both from the surface and the bulk. To make RAS a surface-sensitive technique, the symmetry of the bulk must be optically isotropic, while the symmetry of the surface must be optically anisotropic. However, two other origins of anisotropy are known. The first is bulk anisotropy, which is found, for instance, in InGaP and caused by ordering effects, and the second is buried heterointerfaces within the penetration depth of the light.[118]

One of the single crystals used for RAS investigation is the (110) surface of fcc (face-centred cubic) crystals. However, the surface and the bulk here contribute to the optical anisotropy.[119,120] Other simple fcc surface structures like (100) and (111) are optically isotropic, meaning that they will not deliver an RA signal. However, these surfaces can undergo surface reconstruction to prevent dangling bonds on the surface. It is reported, that Au(100) can reconstruct into Au(100)-(5 x 20),[121] in some literature also called Au(100)-('hex')[122] and Au(111) can reconstruct into Au(111)-(1 x 23).[121] Since only the topmost surface layer is optical anisotropic in these two cases, the RA signal will only stem from there. An optically isotropic surface also has a further advantage. Since the surface itself does not contribute to the signal, every change in the signal can be attributed to the reactions happening above the surface, like the deposition of a metal on the surface, the adsorption of molecules or the formation of a surface layer. The evolution of the surface reconstruction is also possible to be detected with RAS. Experiments have shown that it is possible to observe the evolution of an Au(110) towards the (1 x 1), (1 x 2) and (1 x 3) surface reconstruction.[123]

In addition to the RAS signal, the plain reflectance signal can be measured. Therefore, no additional optical setup is needed since the reflectance signal is automatically measured using the DC component during the RAS measuring process. In that way, the reflectance measurement can be seen as a by-product of the RAS measurement. The DC signal is thereby proportional to the reflectance of the sample.[118]

Historic Development

RAS was independently developed in the 1980s by Aspnes et al.[124,125] and Safarov et al.[126,127] They used it as an in situ optical probe for layer-by-layer surface control of semiconductors growth by molecular beam epitaxy (MBE)[128] and metal-organic

vapour phase epitaxy (MOVPE).[129] In the upcoming years, RAS has been used mainly to investigate III-V semiconductors, most prominently GaAs. Here it was demonstrated that RAS can be used to control epitaxial growth, the preparation of specific surface reconstructions, and the layer-by-layer removal of GaAs used as a protective cap layer.[130–132] The first study of a semiconductor immersed in a liquid was done by Berkovits et al.[133] They investigated an As-rich GaAs(110) sample immersed in a sodium sulfide solution and discovered that under illumination gallium dimers are created at the expense of arsenic dimers by breaking of chemical bonds between gallium and overlying arsenic atoms.[133] Further etching studies investigated the layer-by-layer etching of Si(100) in an H_2 atmosphere at elevated temperatures[134] and Fabry-Pérot oscillations generated by reactive ion etching of GaAs/AlGaAs multi-layer structures.[135,136] This allowed for the extraction of the etching rate and etch-depth resolution.

The first combination of RAS with electrochemical measurements was done by Sheridan et al. and Mazine et al. in the early 2000s.[119,123,137] They investigated the reconstruction of Au(110) at different applied potentials in a Na_2SO_4-solution and in H_2SO_4. Another system intensively studied with RAS is the adsorption of ions on Cu(110), first in the gas-phase[138,139] and then in an electrochemical environment, where mostly the adsorption of chloride ions in hydrochloric acid was investigated.[120,140] Here, kinetic studies of molecule adsorption and desorption and their memory effect on the surface were investigated. Goletti et al. combined RAS with in situ electrochemical scanning tunnelling microscopy (EC-STM) and low-energy electron diffraction (LEED); this enabled them to identify the two-step process in the anodic and cathodic region of the CV on a Cu(110) surface. Further, they discovered that the adsorption/desorption of two different anions takes place and that chlorine anions are involved in one adsorption/desorption process followed by a surface reconstruction.[120] Based on this work, Vazquez-Miranda et al. fitted RAS transient measurements during the chloride adsorption on Cu(110) with adsorption isotherm models, enabling them to extract kinetic and thermodynamic quantities. Furthermore, correlating the current peaks measured in CV with the derivative of the RAS transients could derive the dependency between applied potential duration and copper/chlorine chemical reactions.[141] The same group combines their RAS results during the potential dependant chloride adsorption on Cu(110) with a singular-value decomposition method. This enabled them to extract three distinct

RAS features that track electrochemical changes.[142]

The in this thesis studies surface of Al(110) has only been studied by Herrmann et al. before. They observed a peak at 1.5 eV, in which the intensity decreases and shifts to lower photon energies upon surface oxidation.[143]

The deposition of metals, which in this thesis is done with aluminium, has also been investigated by RAS before. Two systems were investigated: cobalt and nickel deposition onto Cu(110)[144,145]. These studies monitored the growth in real-time at single photon energy, specifically at 2.1 eV, where a peak characteristic of the clean Cu(110) surface is observed. In both systems, the growth mode on the clean Cu(110) surface involves the formation of islands and results in a rough surface. However, oxygen on the O/Cu(110)-(2×1) surface acts as a surfactant, promoting smooth layer-by-layer growth of cobalt and nickel. In this investigation, RAS provides useful 'fingerprint' spectra characteristic of different stages of the growth processes.

EC-RAS Set-up

Figure 4.2 shows a schematic set-up for electrochemical RAS (EC-RAS) measurements. It consists of the sample of interest at the bottom of the cell, which serves as the working electrode (WE). Above the surface is the electrolyte, where the counter electrode (CE) and an optional reference electrode (RE) are immersed. On top of the cell is an optical quartz glass window. However, this window is not used in every experiment. Compared to a RAS set-up in vacuum, there are additional optical elements in the light path, namely the electrolyte and the optional quartz glass window. Due to different refractive indices of the component, new interfaces occur, either the electrolyte-air interface or the electrolyte-quartz glass window and quartz glass window-air interface. Additionally, mechanical stress applied to the quartz glass window can also alter the light path. These effects can be largely compensated by a baseline correction, which can be done in two ways. The first uses an optical isotropic Si(100) sample, and the second adds two spectra of the sample rotated by 90°. These two methods give the so-called zeroline subtracted from the measured spectrum.

Compared to operando NAPXPS, this set-up has the advantage that up to a few

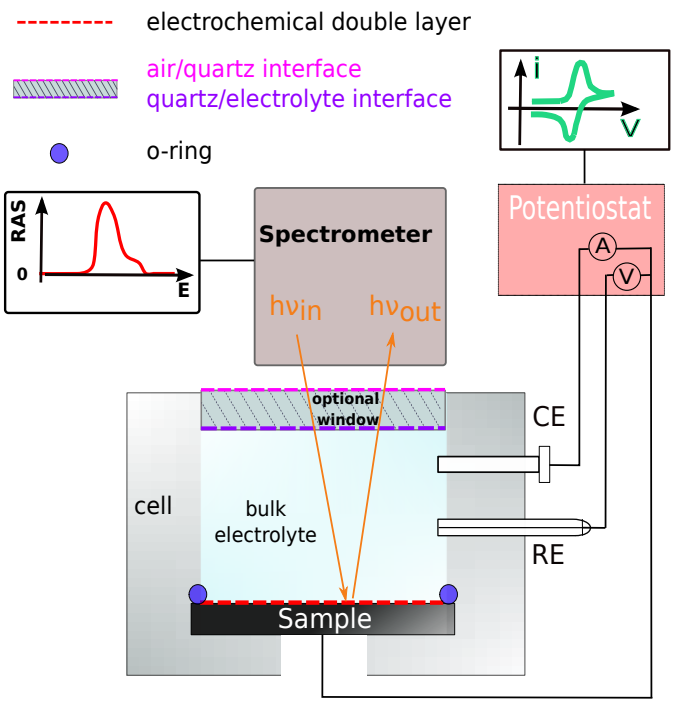

Figure 4.2: Cross-section of a typical cell set-up for electrochemical RAS, with the sample of interest at the bottom and the electrolyte above it. The light shines with near-normal incidence onto the sample. For the electrochemical measurements, a counter (CE) and reference electrode (RE) are needed. Taken from [32]. Figure licensed under CC BY 4.0, `https://creativecommons.org/licenses/by/4.0/`

centimetres of the electrolyte can be used. This allows operando investigation closer to an operando system and prevents issues like small currents and inadequate potential control. Further, the use of ultra-violet to visible light decreases the likelihood of beam damage drastically compared to X-rays.

4.2 Electrochemical Impedance Spectroscopy

Electrochemical impedance spectroscopy (EIS) is a non-invasive and in-situ method for characterising batteries.[146] In EIS, either an alternating current (galvanostatic mode) or voltage (potentiostatic mode) of a defined amplitude and frequency range

(mostly between kHz and mHz) is applied to the cell. Amplitude and phase shift of voltage and current are then measured. EIS is most commonly plotted as a Nyquist plot, where the imaginary part of the impedance is plotted against the real part.

The impedance Z can be written as:

$$Z(\omega) = \frac{\tilde{V}(\omega)}{\tilde{I}(\omega)} = \left|\frac{\tilde{V}(\omega)}{\tilde{I}(\omega)}\right|(\mathrm{cos}\phi(\omega) + j\mathrm{sin}\phi(\omega)) = Z_{Re} + jZ_{Im} \tag{4.2}$$

Here ω is the angular frequency, related to the frequency f by $\omega = 2\pi f$, ϕ is the phase angle between the input and output signals, and j is the imaginary number ($\sqrt{-1}$). The variable $\tilde{V}(\omega)$ is the voltage and $\tilde{I}(\omega)$ is the current. As can be seen in equation 4.2, impedance is a frequency-dependent complex number consisting of a real part (Z_{Re} or Z') and an imaginary part (Z_{Im} or Z").[147,148]

Plotting the negative imaginary part (Z_{Im}) versus the real part (Z_{Re}) of the impedance results in a Nyquist plot. The evaluation of the Nyquist plot is done by fitting it with an equivalent circuit, including resistance, capacitance or inductance, describing the electrochemical behaviour. One of the most straightforward cases is an equivalent circuit consisting of a resistor in parallel to a capacitor (RC), with the complex impedance of this single RC parallel circuit being:

$$Z = \frac{R}{1 + i\omega R} \tag{4.3}$$

This results in a Nyquist plot with a semicircle of the radius $\left(\frac{R}{2}\right)$. In real systems, multiple processes contribute to impedance spectra, such as interfacial layers and charge transfer of ions. In such cases, the impedance spectra can be fitted using several RC elements in series. In the following, a typical Nyquist plot of an electrochemical cell will be investigated.

Figure 4.3 shows a schematic drawing of a typical Nyquist plot of a battery cell. The inductive part at high frequencies stems from the wires connecting the cell to the potentiostat. The high-frequency part, above 1 kHz (marked in blue), contains the intersection of the curve with the real axis corresponding to the internal ohmic resistance of the cell, mostly the electrolyte. The mid-frequency range between 1 kHz and 1 Hz (green area) belongs to electrochemical processes occurring at

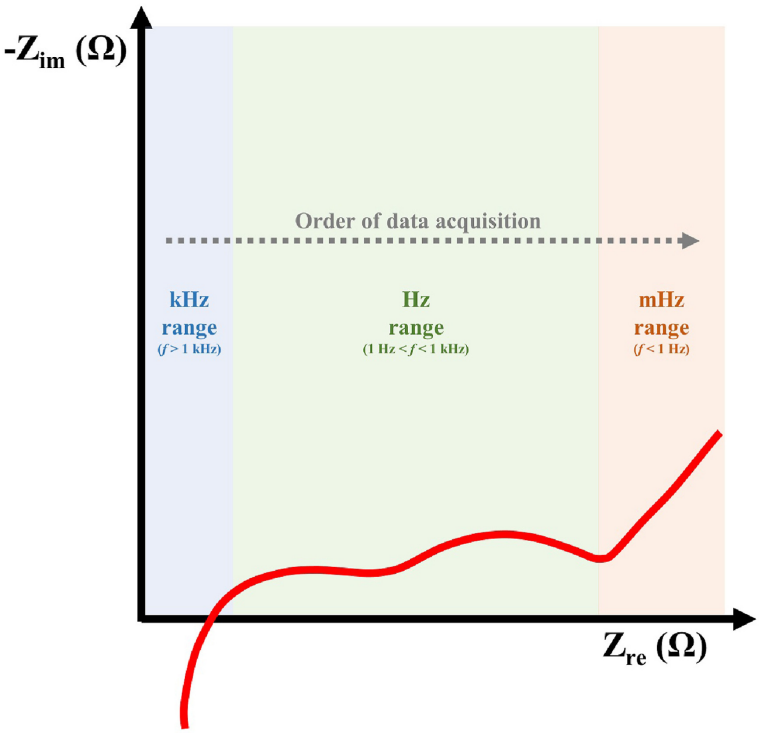

Figure 4.3: Graphical representation of a typical Li-ion cell EIS measurement presented in a complex impedance plot (i.e., Nyquist plot). f is the frequency and, the order of data acquisition refers to the order in which frequencies are typically interrogated. Taken from [146]. Figure licensed under CC BY-NC 4.0, `https://creativecommons.org/licenses/by-nc/4.0/`

the electrode/electrolyte interface. The low-frequency part below 1 Hz (marked in orange) represents the ion diffusion processes within the cell.[146]

4.2.1 The Cation Transference Number (t_+)

The cationic transference number is the fraction of the total electric current carried in an electrolyte by a given ionic species, as defined in equation 4.4.

$$t_+ = \frac{\sigma_+}{\sigma_+ + \sigma_-} = \frac{\sigma_+}{\sigma} = \frac{R}{R_+} \tag{4.4}$$

where R_- is the anion and R_+ cation contributions to the total resistance R_{tot},

respectively, while σ is the conductivity.

The cationic transference number is crucial to determine potential dendrite formation.[43] This is because of two reasons; first, a high cationic transference number prevents salt concentration gradients inside the electrolyte, which could limit the lifetime of the battery and its energy density.[149] Second, the cationic transference number is related to the Sand's time. The Sand's time is the time that predicts the formation of an ion depletion layer near the interface, which then results in the formation of dendrites.[54,150]

The Sand's time is described as:

$$t_{Sand} = \pi D_{salt} \cdot \left(\frac{zC_0F}{2J(1-t_+)} \right) \tag{4.5}$$

Here, C_0 is the bulk electrolyte concentration, F is the Faraday constant, J is the current density, z is the number of the charge and D_{salt} is the ion diffusion coefficient.

Two different methods can be used to determine the cationic transference number. The first is directly from a Nyquist plot of the EIS, and the second is from galvanostatic polarization. Both methods will be described shortly.

Determination of the Cation Transference Number by EIS

The method to extract the cationic transference number directly from a Nyquist plot was developed by Sørensen and Jacobsen.[151] Their technique assumes that first, both the anion and cation transport contribute to the electrolyte resistance (R_{el}), and second that the final impedance from the bulk diffusion at the lowest frequency where Z_{Im}=0 (Z_d(0) (the intersection of the second semicircle with the x-axis) is only dependent on the cation transport.[151] With equation 4.6, it is then possible to calculate the cationic transference number:

$$t_+ = \frac{1}{1 + \frac{Z_d(0)}{R_{el}}} \tag{4.6}$$

Determination of the Cation Transference Number by Galvanostatic Polarization

The polarization method was first established by Hebb and Wagner[152,153] for the separation of ionic and electronic conductivity and popularized by Evans and Bruce for lithium polymer electrolytes.[154] In contrast to the typical Evans and Bruce method, galvanostatic polarisation is used to determine the initial IR response more precisely.[149,155]

Galvanostatic polarisation requires symmetric metal cells, which are reversible for cations but blocking for anions. Here, a constant current (I) is applied, while the changes in voltage are observed over time until the steady state is reached (U_{ss}). Initially, both anions and cations migrate due to the voltage being a driving force. However, the blocking electrode does not support the anion flux and eventually stops the anion flux at the steady state. Forced by electro-neutrality, the cations will flow to compensate for the concentration gradient within the cell, meaning that the steady state voltage solely corresponds to the cation transport. The initial total resistance ($R_{tot,0}$) can be described as followed:

$$R_{tot,0} = R_{SEI,0} + R = \frac{U_0}{I} \tag{4.7}$$

$R_{SEI,0}$ is the initial SEI resistance, R represents the resistance contributed by the migration of anions and cations, and U_0 is the initial voltage.

However, the SEI layer may also grow during the polarization process. Therefore, there is a distinction between $R_{SEI,0}$ (the resistance at the beginning of the galvanostatic polarization) and $R_{SEI,\infty}$ (the value at the steady state).

$$R_{tot,\infty} = R_{SEI,\infty} + R_{+} = \frac{U_\infty}{I} \tag{4.8}$$

Where $R_{SEI,\infty}$ is the final SEI resistance, R_{+} is the resistance contributed by the migration and diffusion of the cations alone and U_∞ is the voltage at a steady state.

Combining equations 4.7 to 4.8 delivers the cationic transference number t_{+}:[148,156]

$$t_{pol} = \frac{I \cdot R_{tot,0} - I \cdot R_{SEI,0}}{U_\infty - I \cdot R_{SEI,\infty}} \tag{4.9}$$

A schematic diagram of a galvanostatic polarization curve and the Nyquist plot with the essential parameters is shown in Figure 4.4.

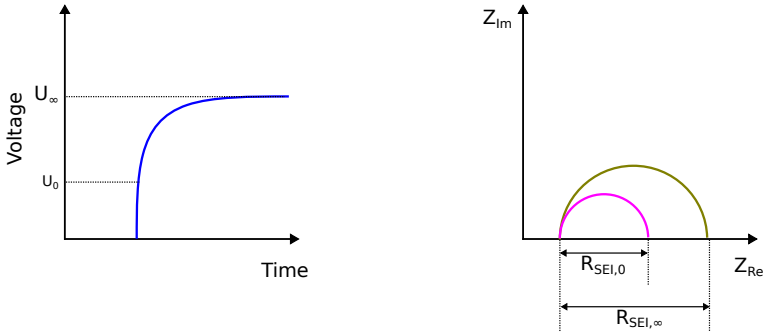

Figure 4.4: Schematic diagram of a galvanostatic polarization curve and Nyquist plots before (pink) and after (olive) the galvanostatic polarization. Inspired by [148, 149, 156].

4.3 Cyclic Voltammetry

Cyclic voltammetry (CV) is an essential potentiodynamic electrochemical analytic technique used to investigate the reduction and oxidation of a given compound. The set-up of a cyclic voltammetry experiment contains three electrodes: The working electrode (WE), which carries out the electrochemical event of interest; the counter electrode (CE), which closes the electric circuit between itself and the WE; and the reference electrode (RE), which is used as a reference point against which the other electrodes' potential can be measured.[157] A three-electrode set-up (with an additional RE) is used because applying a current between the WE and the CE leads to a potential drop-down because of Ohm's law (iR-drop). Therefore, the potential difference between the WE and CE is no longer accurate. The iR-drop can also happen if the reference and working electrodes are too far apart.[158] For measuring a CV, a triangular voltage is applied, and the resulting current response is detected. In a cyclic voltammogram, the potential is then plotted vs the current (density). A crucial parameter in a CV experiment is the scan rate (υ), which determines how fast the applied potential changes with time.

For a deeper understanding of CV, the single-electron transfer reaction is investi-

gated in detail. The investigation begins at open circuit potential, where the reaction is at equilibrium. At this point, the solution is in equilibrium and can be described by the Nernst equation (equation 4.10). It is important to consider that the Nernst equation is only valid when no net current flows through the electrode.[157]

$$E = E^0 + \frac{RT}{zF} \cdot \ln \frac{[O]}{[R]} \tag{4.10}$$

Here, E is the potential of an electrochemical half-cell, and E^0 is the standard potential of a species. [O] and [R] are the concentrations of the oxidized (O) and reduced (R) species in the system at equilibrium, F is Faraday's constant, R is the universal gas constant, z is the number of electrons, and T is the temperature.

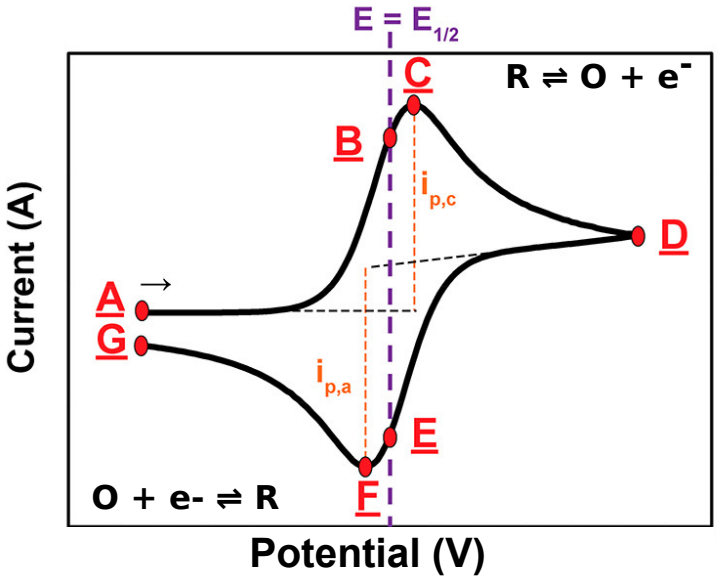

Figure 4.5: Schematic cyclic voltammogram of a reversible reaction. Adapted and modified from [157]. Figure licensed under CC BY-NC 4.0, `https://creativecommons.org/licenses/by-nc/4.0/`

When applying a voltage, two different processes take place at the same time. The first is that increasing the potential increases the concentration gradient at the electrode. This happens because the reduced species' concentration drops to zero at the electrode since it is oxidized. This means the current increases with the potential.[158] This is called heterogeneous charge transport.[159] In the second process,

the diffusion layer, the volume of solution at the surface of the electrode containing the reduced species, increases. This leads to a reduction of the concentration gradient, which means that the current no longer increases that sharply. This happens until the diffusion layer overtakes the concentration gradient, and the current decreases even with growing potential.[158] This is called diffusion-related mass transport.[159]

$$R \rightleftharpoons O + e^- \tag{4.11}$$

Because this might be hard to understand, it is explained in more detail with a general redox-reaction in equation 4.11. Initially, no current flows and only the reduced species R exist in the solution; this is shown by point A in Figure 4.5. By applying a potential, R will be oxidised near the electrode. That means that R's concentration decreases while O's concentration increases, as point B shows. Since more R is oxidised to O as the potential becomes more positive, the current increases, and simultaneously, the concentration of R decreases while the concentration of O increases. Due to the increasing number of species O, a diffusion layer is formed near the electrode. As this diffusion layer grows, it gets increasingly difficult for the R species to reach the electrode by diffusion. At one point, it is so thick that more R is reduced than will migrate to the electrode. This happens at the top of the current peak, represented by point C in Figure 4.5. This means the transport of R to the electrode becomes slower, and therefore, the current decreases again until it reaches the point of the maximal potential, point D in Figure 4.5. The same process occurs, but in reverse order, when the voltage is scanned backwards, where O is reduced towards R.[108,157,158]

In cyclic voltammetry, the Randles-Ševčik equation (equation 4.12) describes the linear increase of the peak current (i_p), which is proportional to the square root of the scan rate (ν).[157]

$$i_p = 0.446 \cdot n \cdot F \cdot A \cdot C^0 \cdot \left(\frac{n \cdot F \cdot \nu \cdot D_0}{R \cdot T}\right)^{1/2} \tag{4.12}$$

Within this equation, n is the number of electrons transferred in the redox event, A is the electrode surface area, D_O is the diffusion coefficient of the oxidised analyte, and C_0 is the bulk concentration of the electrolyte. Equation 4.12, can only

be used for electrochemically reversible electron transfer processes that involve freely diffusing redox species.[157] Furthermore, for reversible electrode processes, under idealised conditions and single electron transfer, the two peak potentials for the cathodic and anodic reactions, E_{pc} and E_{pa}, exhibit a maximum difference of 57 mV.[157]

$$\Delta E_p = |\Delta E_{pc} - \Delta E_{pa}| = \frac{57\text{mV}}{n} \tag{4.13}$$

As additional information of a CV experiment, the amount of transferred charge, Q, can be obtained by integrating a current-time diagram (equation 4.14).

$$Q = \int_{E_1}^{E_2} I \, dt \tag{4.14}$$

4.4 Chronoamperometry

In chronoamperometry (CA), the current of an unstirred solution is recorded over time, while the potential is held constant. Therefore, the current is set from a potential where no reaction occurs to the desired potential. Before the potential step, the oxidized species' concentration is assumed to be equal throughout the solution. As the potential is started, the oxidized species are reduced on the surface of the electrode. This leads to a decline in the concentration of the oxidized species near the electrode and a simultaneous increase in the concentration of the reduced species, leading to a concentration gradient between the electrode and the bulk of the solution. As the solution is not stirred, a diffusion layer is built up with increasing time. This means that the concentration gradient gets smaller over time, and as a result, fewer oxidized species migrate to the electrode, causing the current to decline.[160]

The Cottrell equation describes the curve in Figure 4.6:

$$i(t) = \frac{n \cdot F \cdot A \cdot \sqrt{D} \cdot c}{\sqrt{\pi \cdot t}} \tag{4.15}$$

Here, A is the electrochemically active surface of the electrode, D is the diffusion coefficient, and c is the electrolytes initial concentration.[160]

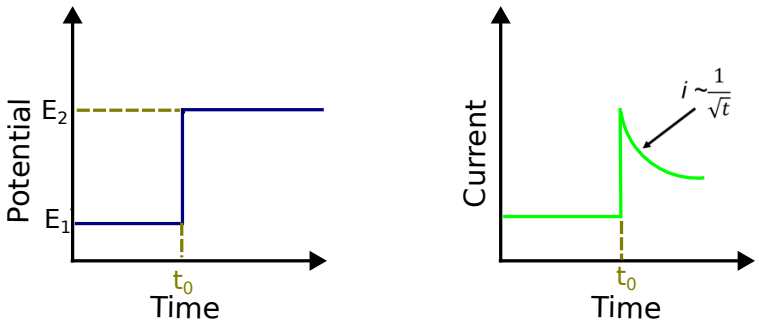

Figure 4.6: a) Timeline of the potential E at chronoamperometry. b) Timeline of the current E at chronoamperometry for a reversible reaction. Inspired by [160].

4.5 Scanning Electron Microscopy

In scanning electron microscopy (SEM), a beam of electrons scans the sample's surface, probing its morphology, 3D microstructure, roughness, cracks, and cavities.

In an optical microscope, the size of an object that can be detected by light of a certain wavelength is given by Abbe's equation:

$$r_d = \frac{\lambda}{n \sin \alpha} \tag{4.16}$$

With r_d as the resolution, λ as the radiation wavelength, α as the aperture angle of the objective lens, and n as the refractive index. This means that with purple light with λ=400 nm, only objects of the size of 200 nm could be detected.

Electrons, however, follow the DeBroglie wavelength, which is correlated to their energy as shown in equation 4.17:

$$\lambda = \frac{h}{m \cdot \nu} \tag{4.17}$$

Where λ is the wavelength, h is the Planck constant, m is the mass of a particle, and ν is the electron's velocity.[108]

By considering the relativistic mass of the electron and the law of energy conservation, the electron wavelength can be calculated as follows:

$$\lambda = \frac{h}{\sqrt{2m_e \cdot e \cdot U \cdot \left(1 + \frac{e \cdot U}{2m_e \cdot c^2}\right)}} \tag{4.18}$$

Here is U, the voltage used to accelerate the electrons, m_e is the mass of the electron, e is the charge of the electron, and c is the speed of light. This will result in an electron wavelength of 12.2 pm when an accelerating voltage of 10 kV is used.[161]

To generate electrons, a high voltage is applied to a filament, resulting in the emission of electrons. As electrons are charged particles, they can be accelerated by a capacitor creating an electric field and directed by electromagnets. Once the electrons hit the sample, they interact with the atoms. This can happen in two different ways. The first is the elastic scattering of the electrons; in this process, they change their direction but keep their energy. The emitted electrons are known as backscattered electrons (BSE). The second interaction mode is inelastic scattering. Here, the electrons change direction and simultaneously transfer energy to the surface. The gained energy leads to the emission of electrons from the surface. These electrons are called secondary electrons (SE) and have a smaller energy, usually below 50 eV. Their different energy is also the reason for their various surface sensitivity. For SE, the surface sensitivity is about 5 nm, while for BSE, it is 100 nm.[161,162]

Two classes of detectors are commonly used for the detection of electrons: an Everhart–Thornley detector and an Inlens detector.

The Everhart–Thornley detector consists of a positively charged grid in front of the detector that attracts the emitted electrons. Behind the grid is the scintillator, which converts the energy of the electrons into photons. The photons then travel to a photomultiplier before being converted into an electric current. This type of detector is typically used for SE but can also be used for BSE.[162]

The Inlens detector uses a diode with a hole in the middle placed directly above the sample to detect the electrons. The hole in the middle serves as a passage for the primary electron beam. In this case, the electrons are not accelerated to a detector. This type of detector is mainly used for BSE but can also be used for SE if a voltage is applied.[162]

In the Inlens detector, the images are generally much sharper than those of the Everhart–Thornley detector. This is because the detector is located directly above

the sample, and thus, the electrons can strike unhindered. The advantage of an Everhart–Thornley detector is its better depiction of the surface topography due to its location beside the sample. For this detector, all emitted electrons feel the attractive force of the positive polarised gird in front of the detector. However, due to surface morphology, only electrons emitted on the same side as the detector can reach it. Electrons emitted on the opposite side get accelerated but then hit the sample and, therefore, do not reach the detector. In comparison, the Inlens detector is located above the sample so that no topographical contrast can arise.

Energy Dispersive X-ray Spectroscopy

Energy dispersive X-ray spectroscopy (EDX) is used to determine the elemental composition of selected areas. In this technique, the beam of electrons hits the core electrons of the atoms near the surface. This causes the emission of these electrons from the atom, leaving behind an electron hole in an energetically lower shell. Now, another electron 'falls' from an energetically higher shell into the hole to restore the energetic minimum. Simultaneously, a photon is emitted whose energy is the energetic difference between the energetically higher shall and the shall containing the hole. The photon energy lies within the X-ray range and is element-specific.

5 Results and Discussion

5.1 The Interfacial Structure of InP(100) in Contact with HCl and H_2SO_4 Studied by Reflection Anisotropy Spectroscopy

The article "The interfacial structure of InP(100) in contact with HCl and H_2SO_4 studied by reflection anisotropy spectroscopy" was submitted to the journal *RSC Advances* in August 2022 and was published as open access in November 2022 (RSC Adv., 2022, 12, 32756) and is distributed under the terms of the Creative Commons Attribution 3.0 Unported Licence. (CC BY 3.0, `https://creativecommons.org/licenses/by/3.0/`).[33]

DOI: 10.1039/d2ra05159a

As a preliminary experiment to establish EC-RAS as a method for investigating interphases in batteries, the evolution of InP immersed in acidic electrolytes during electrochemical cycling was studied. The advantage of starting with InP as substrate was that there were already investigations done on this material[29] and that it is available in wafer form, meaning that a new piece of the wafer was used for every new experiment. This results in a new sample for every experiment and does not require refurbishing, as will be the case of the metal samples in the flowing paragraphs.

The research showed that for both HCl and H_2SO_4 at low electrolyte concentrations (0.01 M), there is a potential-dependent formation of well-ordered InP–electrolyte interfaces. This interface shows a reversible formation and removal of the ultra-thin oxide layer. On the other hand, at high concentrations of HCl and H_2SO_4 (0.5 N), the interface gradually transitions into an unordered state. Additional research on the

stability of the interface formed operando during electrochemical cycling showed that the surfaces prepared at cathodic potential are not stable when the potential returns to OCP.

RSC Advances

PAPER

View Article Online
View Journal | View Issue

Check for updates

Cite this: *RSC Adv.*, 2022, **12**, 32756

The interfacial structure of InP(100) in contact with HCl and H_2SO_4 studied by reflection anisotropy spectroscopy

Mario Löw, †[a] Margot Guidat, †[ab] Jongmin Kim [ab] and Matthias M. May *[ab]

Indium phosphide and derived compound semiconductors are materials often involved in high-efficiency solar water splitting due to their versatile opto-electronic properties. Surface corrosion, however, typically deteriorates the performance of photoelectrochemical solar cells based on this material class. It has been reported that (photo)electrochemical surface functionalisation protects the surface by combining etching and controlled corrosion. Nevertheless, the overall involved process is not fully understood. Therefore, access to the electrochemical interface structure under *operando* conditions is crucial for a more detailed understanding. One approach for gaining structural insight is the use of *operando* reflection anisotropy spectroscopy. This technique allows the time-resolved investigation of the interfacial structure while applying potentials in the electrolyte. In this study, p-doped InP(100) surfaces are cycled between anodic and cathodic potentials in two different electrolytes, hydrochloric acid and sulphuric acid. For low, 10 mM electrolyte concentrations, we observe a reversible processes related to the reduction of a surface oxide phase in the cathodic potential range which is reformed near open-circuit potentials. Higher concentrations of 0.5 N, however, already lead to initial surface corrosion.

Received 17th August 2022
Accepted 9th November 2022

DOI: 10.1039/d2ra05159a

rsc.li/rsc-advances

Open Access Article. Published on 15 November 2022. Downloaded on 11/15/2022 11:04:11 AM.
This article is licensed under a Creative Commons Attribution 3.0 Unported Licence.

1 Introduction

Renewable energies will have to play a significant role in the future energy system. Due to the intermittency of wind or solar power, however, large-scale storage of harvested energy has to be realised, for instance, by electrochemical approaches.[1,2] One of the most significant scientific challenges here is understanding and controlling the electrochemical interface, where charge transfer and chemical reactions occur. The electrochemical interface of semiconductors, which are used in solar water splitting and battery applications, is a topic of intense research.[3–7] Yet while the surface structure under *operando* conditions is decisive for the performance, an atomistic picture of the interface is often not established. The last few years saw an increased effort of the community in the development and use of *in situ* and *operando* techniques to investigate these solid–liquid interfaces. Here, a common theme is that a complementary set of methods is typically required for the desired level of insight.[8–12]

The semiconductor indium phosphide (InP) has been studied intensively for use as a photocathode for solar water splitting,[13,14] but is also involved as a major ingredient in efficient photoelectrochemical multi-junction cells, where the top layer is often formed by an InP-based ternary compound semiconductor.[15,16] One of the main advantages of InP is the possibility to prepare surfaces with surface recombination velocities as low as 170 cm s^{-1}, which leads to an efficient carrier transport across the semiconductor–electrolyte interface and reduces photovoltage losses.[17,18] The versatile opto-electronic properties of InP-based semiconductors also render them platforms for other applications, for instance photonic devices.[19] In photoelectrochemical applications, however, the major challenge for InP is its surface corrosion and instability in aqueous solutions,[17] which then again increases surface charge-carrier recombination.[12] Approaches for surface passivation can, once identified, often be transferred to the more complex ternary compounds.[15,20]

This surface corrosion is best understood by investigating the system under operating conditions in the electrolyte. Ideally, it is then possible to design surface passivation approaches for InP.[14,21–24] Such a passivation layer should block (electro)chemical corrosion and ion transport over the solid–liquid interface while enabling efficient electron transfer. Previous investigations of InP in acidic electrolytes can be summarised as follows:[14,21–23,25] in the cathodic potential range in 0.5 N HCl and H_2SO_4, respectively, InP is reduced towards metallic indium at −0.553 V *vs.* (Ag/AgCl). In the case of HCl, the metallic In reacts further with adsorbed Cl-ions to InCl. An intermediate step that involves $InCl_3$ is also possible, yet unlikely due to its water-solubility. Simultaneously, the phosphorous is reduced to phosphine. In the anodic regions, parts of

[a]*Universität Ulm, Institute of Theoretical Chemistry, Ulm D-89081, Germany*
[b]*Universität Tübingen, Institute of Physical and Theoretical Chemistry, Tübingen D-72076, Germany. E-mail: matthias.may@uni-tuebingen.de*
† These authors contributed equally to this work.

© 2022 The Author(s). Published by the Royal Society of Chemistry

Open Access Article. Published on 15 November 2022. Downloaded on 11/15/2022 11:04:11 AM.
This article is licensed under a Creative Commons Attribution 3.0 Unported Licence.

the InCl are oxidised. However, a significant fraction remains on the surface, which results in the formation of a stable passivation layer after several electrochemical cycles that contains InCl (70 at%), $In(PO_3)_3$ (30 at%) and a layer of adsorbed Cl^- on the surface. In H_2SO_4, on the other hand, InP reacts to metallic indium and phosphine. However, the former is oxidised completely, and no stable passivation layer is observed. A possible way to obtain a stable passivation layer is by intermediate resting periods between the electrochemical cycles.[25] For the passivation layer formed in hydrochloric acid, subsequent Rhodium deposition leads to an efficient photocathode.[14,21] The treatment in an aqueous sodium sulphide solution, on the other hand, results in the removal of the native oxide and the formation of a passivation layer containing In–S and In–OH on the surface after one minute in the solution.[24]

Computational studies have reported on the structure and electronic properties of the pristine and oxidised InP surface using density-functional theory as well as molecular dynamics.[18,26,27] Wood *et al.*[18] investigated the interaction of gas-phase and liquid water with the pristine and oxygen-rich surfaces. Alvarado *et al.*[26,27] changed water coverage adsorbed on InP from single molecules to water film, and they found the OER and HER energetics to be modified due to the adsorption.

Methods used to experimentally study the formation of passivation layers on InP in different electrolytes comprise cyclic voltammetry, X-ray photoelectron spectroscopy (XPS), and on-line electrochemical mass spectrometry (OLEMS).[14,21–23,25] Depending on the conditions, under which surfaces are exposed to water or oxygen, the dominant pathways for surface (oxide) formation can become thermodynamically or kinetically driven.[28] Yet the question of whether these layers are well-ordered and to what extent their formation can be precisely controlled is still open. This knowledge could become instrumental for creating efficient solar water splitting cells.[15,29]

In this work, we study the interface of InP(100) with hydrochloric acid (HCl) and sulphuric acid (H_2SO_4) as electrolytes. Thereby we combine cyclic voltammetry, the standard tool of electrochemistry employed in the studies discussed above,[14,21–23,25] with reflection anisotropy spectroscopy (RAS). The latter is an optical technique sensitive to changes in surface chemistry, surface states, or surface reconstruction.[20,30] RAS enabled the investigation of adsorbates on InP,[20] but also metallic systems were already investigated in electrolytes.[31–33] We hereby show an electrolyte concentration-dependent reversibility of the cycling behaviour in HCl and H_2SO_4.

2 Experimental

Samples were prepared from p-doped InP(100) (Zn-doping of 4×10^{18} cm^{-3}), single-crystalline wafers with an offcut of $(0 \pm 0.5)°$ from CrysTec. The wafers with an epi-ready surface were cleaved and used without further pre-treatment. The samples were then mounted to a photoelectrochemical cell (PECC) from Zahner for the RAS measurement. For the electric contact, samples were back-contacted with a copper wire, fixed with silver resin (Ferro GmbH), and with some drops of GaIn eutectic (Sigma Aldrich). Pt and Ag/AgCl electrodes from Zahner were used as counter and reference electrodes, respectively. The cell was then filled with the desired electrolyte (HCl from VWR Chemicals and H_2SO_4 from Supelco). During measurements, the cell was degassed with argon. For the RA spectroscopy, an EpiRAS from Laytec was employed. The electrochemical measurements were controlled with a Princeton Applied Research VersaSTAT 3F potentiostat. Fig. 1 shows a schematic drawing of the cell.

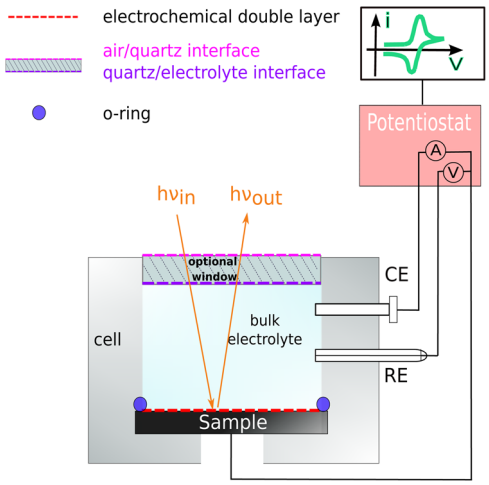

Fig. 1 Cross-section of the photoelectrochemical cell set-up for electrochemical RAS measurement. Here, WE is the InP working electrode, CE is the Pt-wire counter electrode, and RE is the Ag/AgCl reference electrode.

Reflection anisotropy spectroscopy was used here as a spectroelectrochemical method. RAS is a highly surface-sensitive tool that can investigate changes in surface chemistry, surface states, and surface reconstruction with a near-normal-incidence reflection set-up.[34] RAS is also used for controlling the growth during metal–organic chemical vapour deposition (MOCVD). The combination of the two methods allows to create highly ordered surfaces and interfaces with quantitative sub-monolayer control.[4,34–36] Furthermore, RAS is also employed to control layer-by-layer etching of multilayered semiconductors.[37]

For RAS, linearly polarised light impinges at near-normal incidence on the surface. The difference in the reflectivity, Δr, with respect to two orthogonal directions in the surface plane (x, y) is detected by analysis of the polarisation as a function of the photon energy, scaled with the overall reflectivity, r:

$$\mathrm{RAS} := \frac{\Delta r}{r} = \frac{2(r_x - r_y)}{r_x + r_y}; r \in \mathbb{C} \quad (1)$$

In the case of a crystal, where the bulk is optically isotropic – as for the (100) surfaces of zinc blende lattices here – there is no contribution to the signal from the bulk, but only from the (near) surface. Then, RAS becomes highly surface sensitive. This is a significant advantage to most other spectroscopies working with photons as those typically also probe a significant depth of the bulk material.[20,38,39] A baseline correction is applied to all the spectra using the signal of an optically isotropic Si(100) crystal

Open Access Article. Published on 15 November 2022. Downloaded on 11/15/2022 11:04:11 AM.
This article is licensed under a Creative Commons Attribution 3.0 Unported Licence.

in water. This approach for baseline correction allows us to eliminate signals, that do not arise from the sample itself, but from optical components in the light-path that change the polarisation state. Additionally, we have calibrated the signal amplitude of our spectrometer with a Si(110) crystal following the standard procedure for the EpiRAS in a way that the peak at 3.46 eV exhibits an amplitude of 4 RAS units. We obtained a correction factor from this measurement, which we applied to all further measured spectra. No further numerical treatment of the data, such as peak fitting, was employed, we simply took the location of the extrema of the peaks. Cyclic voltammetry measurements were performed between −2 V and +1.5 V (*vs.* Ag/AgCl) with a scan rate of 0.05 V s^{-1}, starting from open circuit potential (OCP) towards the negative terminus for three cycles for low concentration (0.01 M) electrolyte, respectively. For higher-concentration electrolytes (0.5 N), the cyclic voltammogram (CV) was performed between −0.75 V and +0.45 V (*vs.* Ag/AgCl) with a scan rate of 0.05 V s^{-1}, starting from the OCP towards the negative terminus for ten cycles, respectively.

Further on, potentiostatic measurements were performed at the potentials of −2 V, −1 V, 0 V, and +1.5 V *vs.* Ag/AgCl, respectively. Potential step experiments were performed to investigate the stability of the surface at cathodic potentials. In this case, the potential was set to OCP for 10 s, then to −1 V for 30 s, then to OCP for 30 s, to −2 V for 30 s, and finally to OCP for 20 s. This cycle was then repeated two more times. During the electrochemical experiments, RA spectra were recorded continuously, or the anisotropy was measured time-resolved at fixed photon energy (transient mode).

For the computational spectroscopy, density-functional theory (DFT) calculations using the CP2K code[40] were first performed to obtain the relaxed structure of the slabs. The slab consists of 17 layers. To avoid spurious interactions between replica of the slab under 3D-periodic boundary conditions, we set a vacuum spacing of 20 Å between the slabs. Exchange and correlation effects were described by means of the generalised gradient approximation (GGA) using Perdew–Burke–Ernzerhof (PBE) parameterisation.[41] The plane-wave cutoff was set to 800 Ry. We used Goedecker–Teter–Hutter (GTH) pseudopotentials to represent core electrons and valence electrons. After the structural optimisation, the atomic coordinates were transferred to the plane wave/pseudopotential code QUANTUM ESPRESSO.[42] For these calculations, optimised norm-conserving Vanderbilt pseudopotentials were adopted.[43] The Brillouin zone (BZ) was sampled on a 10 × 10 × 1 k-grid with an energy cutoff of 60 Ry. The RAS calculations were performed using the Yambo code.[44,45] We employed the RPA-IP approach for the microscopic dielectric function. To correct the underestimated bandgap calculated by PBE, a scissor shift was adopted. In the RAS calculations, we used an experimental bulk dielectric function.[46]

3 Results & discussion

Fig. 2(a) shows the InP(100) spectra in 0.01 M hydrochloric and 0.01 M sulphuric acid, respectively, at OCP (around 0.2 V *vs.* Ag/AgCl) as well as the epi-ready crystal in air under ambient conditions without any pre-treatment. All three spectra show two positive peaks at 3.25 eV and 4.55 eV due to surface-modified bulk transitions.[20] The presence of electrolytes only slightly influences the RA spectra with an upwards shift in the RAS baseline, which can also arise from imperfect baseline correction. The noise in the high-energy region of the spectra is due to a reduced overall reflectivity from absorption and reflection losses in the electrolyte and at the air–electrolyte interface, respectively.

In the next step, different potentials were applied to investigate their effect on the optical anisotropy and hence the interfacial structure. To this end, we performed potentiostatic measurements at 0 V, −1 V, and −2 V in the cathodic range and +1.5 V in the anodic potential range *vs.* Ag/AgCl, respectively, during the acquisition of RA spectra. The RA spectra in Fig. 2(b) at anodic potentials shift towards more positive anisotropies. In contrast, RA spectra taken at cathodic potentials develop a negative peak for photon energies below 3 eV and the rest of the spectrum shifts to slightly more negative anisotropies. Additionally, the peak at 4.55 eV is much more intensive than at 0 V or OCP. These spectra suggest an ordered surface structure

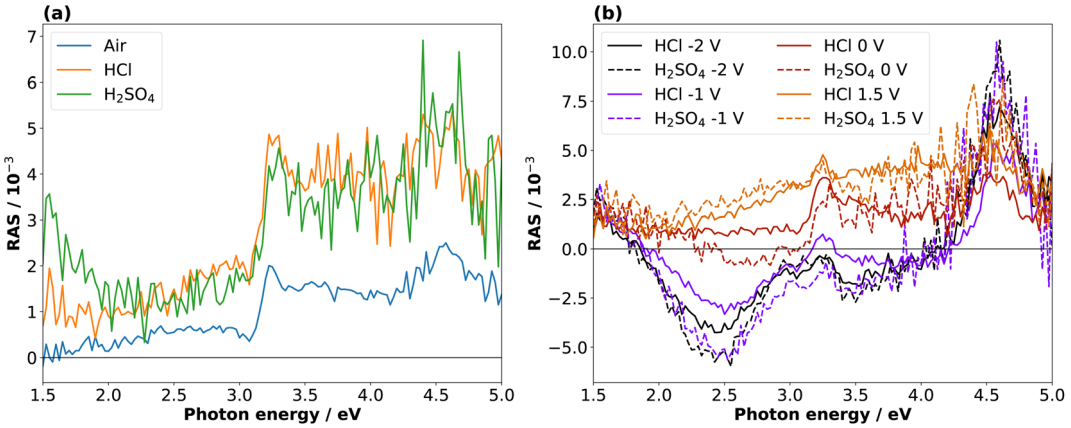

Fig. 2 (a) RA spectra of epi-ready InP(100) in air and immersed in 0.01 M HCl and H_2SO_4 at open-circuit potential. (b) RA spectra at −2 V, −1 V, 0 V and 1.5 V of the InP(100) surface in 0.01 M HCl (solid line) and 0.01 M H_2SO_4 (dashed line) solution.

© 2022 The Author(s). Published by the Royal Society of Chemistry

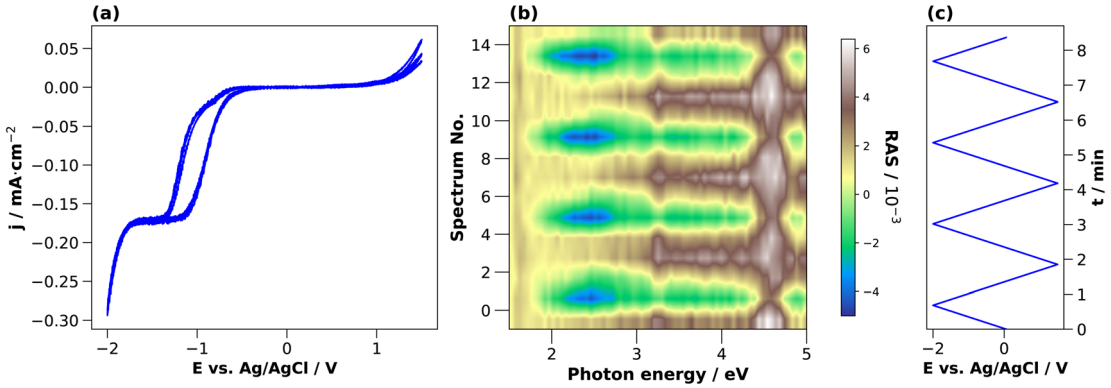

Fig. 3 Cyclic voltammograms of InP in 0.01 M HCl (a) with associated colour plot (b), where the RAS amplitude is colour-coded during continuous acquisition of spectra over time. The evolution of the applied potential over time with aligned *y*-axis is shown in (c). The potential scan from OCP was performed first towards −2 V and then to 1.5 V for 3 cycles, with a scan rate of 0.05 V s^{-1}.

in the cathodic and anodic potential ranges, but with different surface structure or composition. The similarity of the spectra at OCP or 0 V *vs.* Ag/AgCl with the epi-ready oxide indicate a similarity of the interface structure under these conditions.

To investigate the dynamic behaviour of the interface between these states during the cycling in the electrolyte, we changed the potential continuously between two terminals. The CV in 0.01 M HCl is shown in Fig. 3(a). In the cathodic region, the cathodic current density increases from around −0.4 V, reaches a plateau at −1.3 V, and increases further after −1.7 V. This current plateau, observed also for H_2SO_4, corresponds to the photocurrent from the white-light RAS measurement spot. Notable is a small deflection around −0.85 V that occurs only in the forward scan from OCP towards cathodic potentials. In the anodic region, there is an increase in the current density at potentials greater than 1 V. The first cycle shows the highest current density.

During this CV measurement, we continuously recorded RA spectra in the form of a 'colour plot'. The colour-coded signal amplitude during the CV is depicted in Fig. 3(b), showing reversible changes in the RA signal. The comparison with the applied potential in Fig. 3(c) shows that for cathodic potentials, there is a negative anisotropy at around 2.25 eV. In addition, there are significant changes of the optical anisotropy during the potential sweep at the photon energies 3.25 eV and around 4 eV, yet with qualitatively different behaviour. Yet as full spectra are recorded during a colour plot, the time resolution to track one specific spectral feature is relatively low. This can be alleviated by fixing the photon energy and tracking the signal over time with increased time-resolution in the transient mode. Yet before going into detail here, we first discuss the behaviour of InP in H_2SO_4.

The CV for 0.01 M H_2SO_4 in Fig. 4(b) shows that the cathodic current density increases beyond −0.5 V, reaches a plateau at −1.1 V and increases further beyond −1.4 V. In this case, however, the second step after −1.4 V is steeper than for HCl and simultaneously leads to a higher current density value at the potential terminus, where the current is dominated by the hydrogen evolution reaction.[25] For the first forward scan towards cathodic potentials, the cathodic current onset starts at −0.7 V, but at −0.8 V for the subsequent scans. Also here, a small deflection of the cathodic current is observed around −0.6 V. This is in the potential region where, albeit at higher electrolyte concentrations, the reduction of InP towards metallic indium and phosphine was reported at around −0.55 V *vs.* Ag/AgCl.[14,21–23] The cathodic current density at the potential terminus decreases from the first cycle on. Above +1 V, we observe an anodic current, which decreases over the three cycles. In the first cycle, a small oxidation wave can be observed at around +0.3 V, which is absent for the CV taken with HCl. According to the literature, this anodic peak could be due to the formation of indium phosphate.[47]

For higher time-resolution during the CV measurements, transients were recorded *operando* at the energies 2.25 eV, 3.25 eV, and 4.00 eV during a potential sweep with the same settings as for Fig. 3. The photon energies were chosen since changes in the spectra at different potentials in Fig. 2(b) and 3(b) are most pronounced here. These transient measurements enabled us to observe the potential-induced changes on the surface during cycling at higher time-resolution and evaluate the reversibility with respect to the interfacial structure. Fig. 4 shows the periodic changes of the anisotropy in these transients. The minimum of the optical anisotropy occurs under the application of a cathodic potential. In contrast, the maximum is associated with the anodic region. Shape and amplitude of the transients remain virtually constant for HCl, with the exception of the transients at 3.25 and 4 eV, which become more negative from the first cathodic half-scan to the subsequent ones. The case of H_2SO_4 shows distinct differences. Here, the negative extremum of the RA amplitude at 2.25 eV increases from cycle to cycle, yet not for the higher photon energies, which, similar to HCl, only show a slightly less negative amplitude in the first cathodic scan. From these different signal shapes at different potentials and electrolytes, we can try to deduce the reactions on the interface of InP with the respective electrolyte.

At the beginning of the experiment, the epi-ready InP(100) wafer is covered by a thin, well-defined oxide layer. In the presence of an acidic electrolyte, the oxide layer is expected to

Open Access Article. Published on 15 November 2022. Downloaded on 11/15/2022 11:04:11 AM.
This article is licensed under a Creative Commons Attribution 3.0 Unported Licence.

Open Access Article. Published on 15 November 2022. Downloaded on 11/15/2022 11:04:11 AM.
This article is licensed under a Creative Commons Attribution 3.0 Unported Licence.

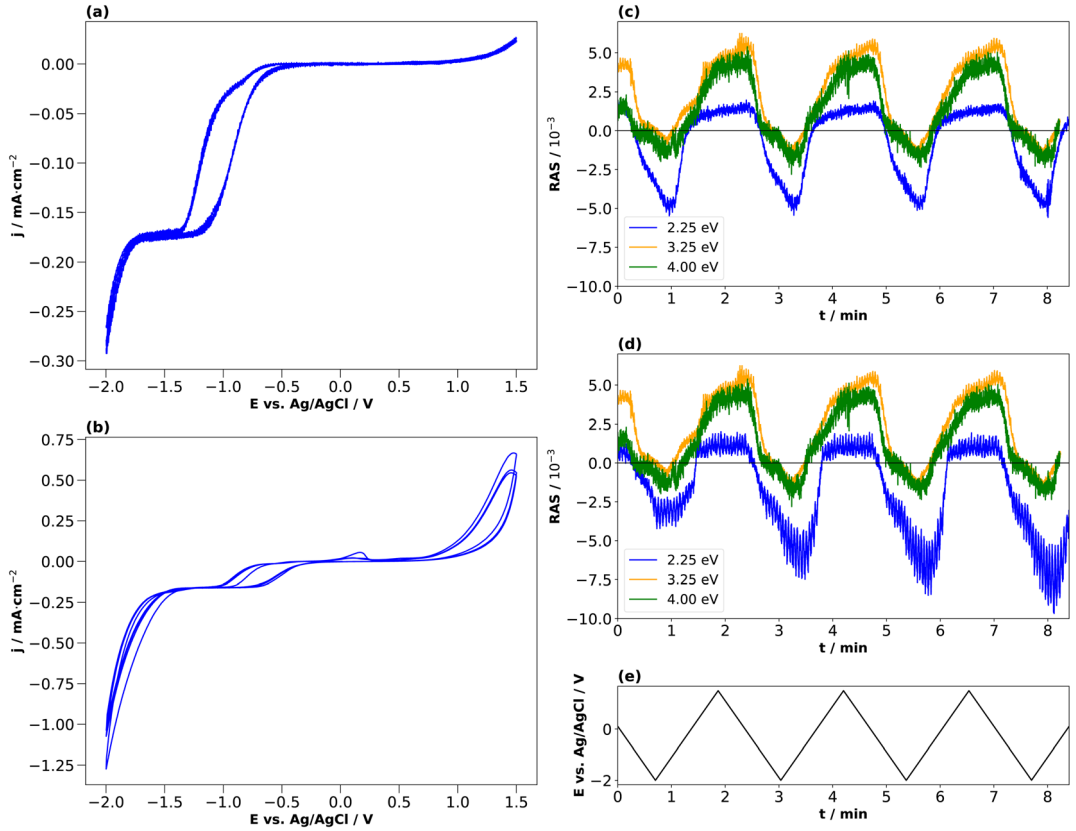

Fig. 4 Cyclic voltammograms of InP in 0.01 M (a) HCl with associated transients (c), and in 0.01 M (b) H_2SO_4 with associated transients (d). (e) Potential plotted against Ag/AgCl. Scan from OCP towards −2 V and than to 1.5 V for 3 cycles, with a scan rate of 0.05 V s^{-1}.

dissolve when scanning the potential from OCP towards the cathodic region.[14,21–23,25] The well-defined, reproducible RA spectrum that we observe at cathodic potentials indicates that this oxide-free layer is well-ordered. Yet the spectral shape does not clearly correspond to one of the main characteristic surface reconstructions of InP(100), the 'P-rich' $p(2 \times 2)/c(4 \times 2)$ reconstruction or the mixed-dimer 'In-rich' (2×4) reconstruction. Both these surfaces exhibit a pronounced negative anisotropy around 1.8–2 eV, associated with surface dimers,[20] while here, the peak observed here is located at 2.5 eV. The strong positive anisotropy around 4.5 eV, however, is a common feature with the In-rich surface.[20,30] Scanning back to OCP or 0 V *vs.* Ag/AgCl, the spectrum is again similar to the epi-ready oxide. This suggests a re-formation of the oxide phase in this potential region for both electrolytes. In both electrolytes, the negative anisotropies are slightly reduced for the first cycle, which could suggest that the re-formed oxide layer is of slightly different nature, possibly with a higher degree of ordering as indicated by the higher transient amplitudes. The observation that both CV and RAS transients remain then constant for HCl indicates a highly reversible process. This would be compatible with the adsorption of chloride on an In-terminated surface, leading to the formation of an InCl surface film starting from −0.55 V (Ag/AgCl),[22] which would also explain the differences at lower photon energies to H_2SO_4. The further change of the anisotropy at cathodic potentials beyond −1.5 V could then be related to the reordering of the (near-)interface water[26] or the adsorption of protons/hydrogen on the surface.

In H_2SO_4, only a fraction of the indium is expected to react with the sulphate ions because of sulphate's weaker interaction with InP compared to the chloride–InP interaction in HCl.[21,23,48] Therefore, metallic indium and $In_x(SO_4)_y$ species would be present at the interface. According to the literature, the metallic Indium and InCl compounds are partially oxidised to In^{3+} in the anodic potential range, forming Indium oxide, and Indium phosphate at high electrolyte concentrations.[22,23] Interestingly, the increasing amplitude of the negative anisotropy with ongoing cycling in the H_2SO_4 electrolyte is associated with a higher overpotential for the hydrogen evolution reaction.

In the literature, conditioning of InP for use as a photocathode was performed typically at higher electrolyte concentrations of 0.5 or 1 N, and these were also the concentrations used to study the resulting surface composition by photoelectron spectroscopy.[22,23] We therefore also applied the same approach to these higher electrolyte concentrations. Fig. 5(a) and (b) show the resulting cyclic voltammograms for both HCl and H_2SO_4. The CV changes its shape from cycle to cycle, effectively reducing the overpotential for the hydrogen evolution reaction, as observed similarly in the literature.[23]

Unlike for the lower concentrations, the amplitudes of the transients at 2.25 eV decrease over the cycles in the cathodic potential region. This occurs continuously for HCl, less so for

© 2022 The Author(s). Published by the Royal Society of Chemistry

Open Access Article. Published on 15 November 2022. Downloaded on 11/15/2022 11:04:11 AM.
This article is licensed under a Creative Commons Attribution 3.0 Unported Licence.

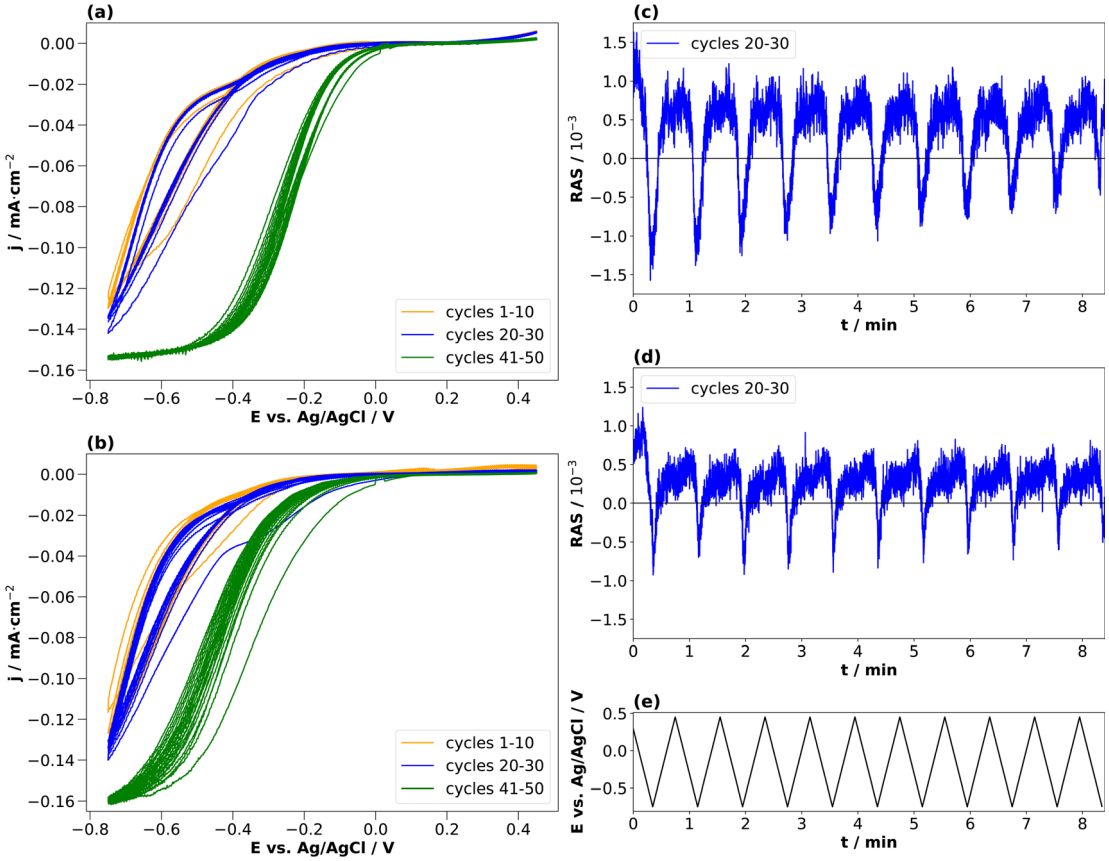

Fig. 5 Cyclic voltammograms of InP (a) HCl (0.5 M) and (b) H_2SO_4 (0.25 M) with corresponding transients at 2.25 eV for cycles 20–30 (c and d) and the applied potentials (e). Potential plotted against Ag/AgCl. Scan from open-circuit potential towards −0.75 V and then to +0.45 V with a scan rate of 0.05 V s^{-1}. The orange curve shows the cycles 1–10, the blue curve shows the cycles 20–30, and the green curve shows the cycles 41–50.

H_2SO_4. This hints towards a decreased interface ordering with ongoing cycles, consistent with inline XPS studies suggesting the formation of a layer of mixed oxides with a thickness in the order of a single or few nanometres.[21–23] Consequently, cycling in higher electrolyte concentrations induces slightly different surface reactions reducing the degree of ordering of the interface. A comparison with the literature on InP(100) in 0.5 M HCl[22,23] shows that the build-up of a passivation layer progressively transforms the surface into a relatively thick, amorphous layer. This lack of reversibility is observed through the evolution of the negative anisotropy in Fig. 5(c) and (d), decreasing from cycle to cycle. In HCl, the passivation layer is composed of InCl, indium phosphate and indium oxide.[22,23] In contrast, the passivation layer from cycling in H_2SO_4 consists of metallic In, $In_x(SO_4)_y$, indium phosphate and indium oxide.

For a more detailed insight, information on the exact surface composition would be instrumental, especially for the structurally well-ordered interface in lower electrolyte concentrations. Alas, in virtually all cases, RAS does not allow to directly derive composition and exact structure from experimental spectra alone, requiring either correlation with other techniques or computational spectroscopy.[49] A straightforward choice for probing the surface/interface composition is X-ray photoelectron spectroscopy. While XPS is almost as surface-sensitive as RAS, it does not probe the surface real-space structure, but rather the electronic structure. Furthermore, the sensitivity of XPS for light elements is strongly reduced, a limitation not found for RAS. With respect to information on the surface structure, the classical surface science method low-energy Electron Diffraction (LEED) could be considered related to RAS, yet the use of LEED is limited to ultra-high vacuum (UHV).

The application of standard XPS for electrochemical systems also requires samples prepared at the desired potential to be transferred from the electrolyte to UHV, which is experimentally challenging. Especially for ultra-thin interface layers, it is important to understand to what extent the surface created at a certain potential will be stable in the absence of applied potential and/or electrolyte. Therefore, we tested the stability of the newly formed interface at cathodic potentials through potential-step experiments during which transients were recorded. This experiment aims to assess the kinetics of formation and disintegration of the interface formed at −2 V and −1 V, respectively. Depending on how fast these changes occur, one can try to assess whether the stability window of the cathodically formed interface is large enough for transfer to UHV. Fig. 6 shows the resulting transients in both electrolytes at 2.25 eV.

Open Access Article. Published on 15 November 2022. Downloaded on 11/15/2022 11:04:11 AM.
This article is licensed under a Creative Commons Attribution 3.0 Unported Licence.

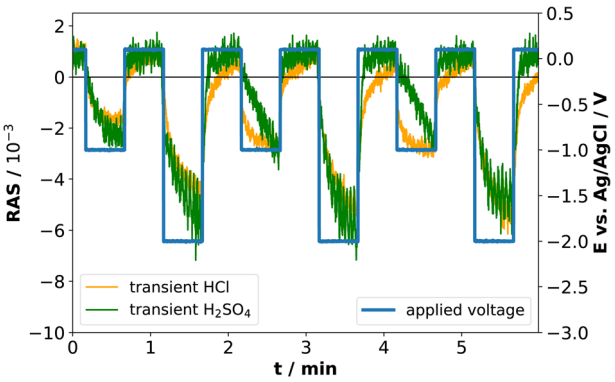

Fig. 6 Potential-step and transient measurements at 2.25 eV in 0.01 M HCl and in 0.01 M H_2SO_4.

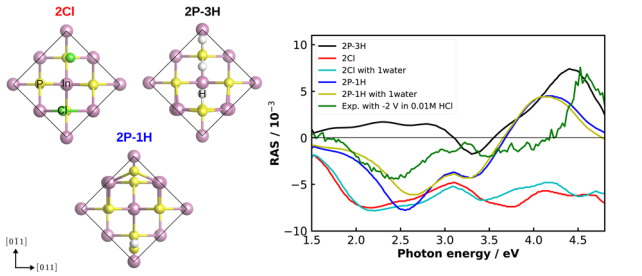

Fig. 7 Left: top view of the fully Cl-covered surface, as well as the surface with one and three adsorbed hydrogen atoms of InP(100) (2Cl, 2P–1H, 2P–3H, respectively). The black line indicates the surface unit cell. Right: computed and experimental (green) RAS of the InP(100) in contact with 0.01 M HCl solution under the applied potential of −2 V.

When the cathodic potential step is applied, the RAS amplitudes of the transient spectrum decrease towards its negative extremum in equilibrium, but with different time-constants. Especially for HCl at −1 V, there appears to be a fast process in addition to a slower signal decrease, while the transient in H_2SO_4 decreases more slowly. After setting the potential back to OCP, the anisotropy in H_2SO_4 changes back to the original value at OCP, while the process is slower in HCl. One of the two processes observed in HCl could be related to the formation and dissolution of the above-mentioned InCl layer, which is not present for the H_2SO_4 case. Yet the time-constants clearly indicate that the time-window for a transfer to XPS is very small and conclusive results would very likely require ambient-pressure XPS similar to ref. [28], but at different applied potentials.

As an alternative to correlation with another experimental method for a more detailed understanding of our experimental RA spectra, we performed computational RAS on structures that could be expected to be relevant for InP(100) in contact with an electrolyte. In Fig. 7, we compare the experimental RA spectrum of InP(100) in 0.01 M HCl at −2 V with calculated spectra. For the latter, we model three systems in which phosphorus atoms at the InP surface are fully substituted with chlorine, forming an InCl layer (termed 2Cl), and one or three hydrogen atoms are adsorbed on the surface (2P–1H and 2P–3H). We further consider adsorption of one water molecule on the 2Cl and 2P–1H structures, as water molecules can significantly alter the RAS signature.[49] When comparing computational to experimental RA spectra, it has to be noted that experimental surfaces would be expected to be not as 'perfect' as the computational structure, where all of the surface is in the same state. This would translate to lower intensities for the experimental spectra. We find that elements of the computed spectra for the 2Cl and 2P–1H, yet also for the 2P–3H surfaces resemble the experimental signature. The calculation for the 2Cl surface reveals a constantly negative anisotropy with negative peaks around 2.2 and 3.8 eV and a shoulder around 2.7 eV, the additional water molecule slightly modifies the spectrum, but the general shape is conserved. A noticeable difference to the experimental RA-signal is that the positive anisotropy at 4.5 eV does not appear in the calculated spectrum. For the case of 2P–1H, two pronounced negative anisotropies around 2.5 eV and 3.3 eV are observed. Unlike the 2Cl surface, the strong positive feature, which also arises in the experimental spectrum, is shown at 4.2 eV. Compared to the experiment, this peak is red-shifted by around 0.35 eV, while the minimum of the anisotropy is slightly blue-shifted and the shift increases with adsorbed water. The 2P–3H structure, on the other hand, displays a rather flat positive anisotropy up to 3 eV, a slight negative peak at 3.3 eV, and a strong positive anisotropy at around 4.4 eV. The latter feature is very similar to the high-energy peak of the experimental spectrum. In general, single water molecules do not play a crucial role for these spectra. Minor discrepancies between the experiment and calculations in terms of the energies would be expected from bandgap errors of the exchange-correlation functional and neglecting defects, oxidation, and domain boundaries on the surface. These initial results suggest a coexistence of H-terminated and Cl-terminated surface, which would lead to a superposition of the spectra of the respective structures. While the computational results give already a first hint towards the real surface structure, a surface phase diagram followed by computational spectroscopy of the – numerous – different structures is required to probe a higher fraction of the chemical space. In addition, multiple water layers and applied potentials might be required.[49] Due to the significant involved computational effort, however, this will have to be left to future work.

To summarise, our results indicate different mechanisms for the two electrolyte concentrations. The transients measurements of InP(100) in low acidic concentrations (0.01 M, Fig. 4) reveal persistently reversible changes in the surface ordering during cycling. Starting from open-circuit potential, a well-ordered, ultra-thin oxide layer appears to be dissolved and, in the case of HCl, replaced by a monolayer of InCl. The spectra found in the cathodic potential range show a strong negative anisotropy around 2.5 eV for both HCl and H_2SO_4, yet with slight differences. Hydrogen adsorption appears to be involved as well for both electrolytes. Setting the potential back to open-circuit, this oxide layer is re-formed and appears to exhibit a higher degree of ordering than the original, epi-ready oxide on the wafer as indicated by a slightly more pronounced spectrum after the first cycle. Also in the anodic potential range,

© 2022 The Author(s). Published by the Royal Society of Chemistry

Open Access Article. Published on 15 November 2022. Downloaded on 11/15/2022 11:04:11 AM. This article is licensed under a Creative Commons Attribution 3.0 Unported Licence.

a spectrum different from OCP is found, but less distinct, which could indicate a lower degree of ordering in this potential range. The reversibility indicates, that potential cycling does not involve further etching of the surface, which is typically accompanied by a gradual loss of interface ordering. Potential cycling in higher electrolyte concentrations of 0.5 N, on the other hand, leads to a gradual change in the shape of the cyclic voltammograms, associated with a gradual loss of interface ordering, when the nm-thick mixture of oxides and phosphates[22,23,47] is formed.

4 Conclusions

Using *operando* electrochemical reflection anisotropy spectroscopy for the study of electrochemical InP(100) interfaces in contact with HCl and H_2SO_4, we find the potential-dependent formation of well-ordered InP–electrolyte interfaces for low electrolyte concentrations. Transient measurements indicate for both electrolytes that there is a reversible formation and removal of ultra-thin oxide layer, yet only in the case of low-concentration (0.01 M) electrolytes. In the case of higher-concentration electrolytes the interface gradually transitions into an unordered state.

Time-resolved potential step measurements show that the surface prepared at cathodic potentials is not stable when the potential is set back to OCP, which hampers the study of the exact chemical nature of this interface state by standard X-ray photoelectron spectroscopy. While initial results from computational RA spectroscopy corroborate the hypothesis that the structures formed in HCl under cathodic potentials involve InCl and adsorbed hydrogen, further computational studies, also under applied potentials, will have to be performed for a more definitive insight.

In summary, our study shows the potential of electrochemical reflection anisotropy spectroscopy for the preparation of well-structured interfaces in the electrolyte. These could then serve as a starting point for subsequent (photo)-electrochemical functionalisation, such as deposition of passivation layers and catalysts, to be used for solar-water-splitting devices.[15] As the process observed here for InP resembles the formation of solid–electrolyte interphases (SEI),[12] electrochemical RAS also has potential as a technique to gain a microscopic, time-resolved insight into SEI processes on battery electrodes.

Conflicts of interest

There are no conflicts to declare.

Acknowledgements

This work was funded by the Deutsche Forschungsgemeinschaft (DFG, German Research Foundation) under Germany's Excellence Strategy – EXC 2154 – project number 390874152 as well as DFG project number 434023472. We acknowledge the state of Baden-Württemberg, through bwHPC, and DFG through grant no. INST 40/575-1 FUGG (JUSTUS 2 cluster) for computational resources. We acknowledge support by the Open Access Publishing Fund of University of Tübingen.

References

1 A. Andrijanovits, H. Hoimoja and D. Vinnikov, *Elektron. Elektrotech.*, 2012, **118**, 21–26.
2 S. Ould Amrouche, D. Rekioua, T. Rekioua and S. Bacha, *Int. J. Hydrogen Energy*, 2016, **41**, 20914–20927.
3 J. Popovic, *Nat. Commun.*, 2021, **12**, 6240.
4 O. Supplie, M. M. May, S. Brückner, N. Brezhneva, T. Hannappel and E. V. Skorb, *Adv. Mater. Interfaces*, 2017, **4**, 1601118.
5 W. A. Smith, I. D. Sharp, N. C. Strandwitz and J. Bisquert, *Energy Environ. Sci.*, 2015, **8**, 2851–2862.
6 H. Gerischer, *Surf. Sci.*, 1969, **18**, 97–122.
7 H. Gerischer, *J. Phys. Chem.*, 1991, **95**, 1356–1359.
8 D. V. Esposito, J. B. Baxter, J. John, N. S. Lewis, T. P. Moffat, T. Ogitsu, G. D. O'Neil, T. A. Pham, A. A. Talin, J. M. Velazquez and B. C. Wood, *Energy Environ. Sci.*, 2015, **8**, 2863–2885.
9 A. M. Tripathi, W.-N. Su and B. J. Hwang, *Chem. Soc. Rev.*, 2018, **47**, 736–851.
10 J. Li and J. Gong, *Energy Environ. Sci.*, 2020, **13**, 3748–3779.
11 G. Gourdin and V. Doan-Nguyen, *Cell Rep. Phys. Sci.*, 2021, **2**, 100660.
12 M. M. May and W. Jaegermann, *Curr. Opin. Electrochem.*, 2022, **34**, 100968.
13 A. Heller, B. Miller, H. J. Lewerenz and K. J. Bachmann, *J. Am. Chem. Soc.*, 1980, **102**, 6555–6556.
14 A. G. Muñoz, C. Heine, H. W. Klemm, T. Hannappel, N. Szabo and H.-J. Lewerenz, *ECS Trans.*, 2011, **35**, 141–150.
15 M. M. May, H.-J. Lewerenz, D. Lackner, F. Dimroth and T. Hannappel, *Nat. Commun.*, 2015, **6**, 8286.
16 J. L. Young, M. A. Steiner, H. Döscher, R. M. France, J. A. Turner and T. G. Deutsch, *Nat. Energy*, 2017, **2**, 17028.
17 J. Tournet, Y. Lee, S. K. Karuturi, H. H. Tan and C. Jagadish, *ACS Energy Lett.*, 2020, **5**, 611–622.
18 B. C. Wood, E. Schwegler, W. I. Choi and T. Ogitsu, *J. Phys. Chem. C*, 2014, **118**, 1062–1070.
19 K. Vyas, D. H. G. Espinosa, D. Hutama, S. K. Jain, R. Mahjoub, E. Mobini, K. M. Awan, J. Lundeen and K. Dolgaleva, *Adv. Phys.: X*, 2022, **7**, 2097020.
20 M. M. May, H.-J. Lewerenz and T. Hannappel, *J. Phys. Chem. C*, 2014, **118**, 19032–19041.
21 A. G. Muñoz, C. Heine, M. Lublow, H. W. Klemm, N. Szabó, T. Hannappel and H.-J. Lewerenz, *ECS J. Solid State Sci. Technol.*, 2013, **2**, Q51–Q58.
22 H. Lewerenz and K. Schulte, *Electrochim. Acta*, 2002, **47**, 2639–2651.
23 K. Schulte and H. Lewerenz, *Electrochim. Acta*, 2002, **47**, 2633–2638.
24 M. V. Lebedev, Y. M. Serov, T. V. Lvova, R. Endo, T. Masuda and I. V. Sedova, *Appl. Surf. Sci.*, 2020, **533**, 147484.
25 A. Goryachev, L. Gao, R. P. J. van Veldhoven, J. E. M. Haverkort, J. P. Hofmann and E. J. M. Hensen, *Phys. Chem. Chem. Phys.*, 2018, **20**, 14242–14250.

© 2022 The Author(s). Published by the Royal Society of Chemistry

Open Access Article. Published on 15 November 2022. Downloaded on 11/15/2022 11:04:11 AM.
This article is licensed under a Creative Commons Attribution 3.0 Unported Licence.

26 R. Alvarado, I. Azahel and W. G. Schmidt, *ACS Omega*, 2022, **7**, 19355–19364.
27 R. Alvarado, I. Azahel, M. Karmo, E. Runge and W. G. Schmidt, *ACS Omega*, 2021, **6**, 6297–6304.
28 X. Zhang, T. A. Pham, T. Ogitsu, B. C. Wood and S. Ptasinska, *J. Phys. Chem. C*, 2020, **124**, 3196–3203.
29 W.-H. Cheng, M. H. Richter, M. M. May, J. Ohlmann, D. Lackner, F. Dimroth, T. Hannappel, H. A. Atwater and H.-J. Lewerenz, *ACS Energy Lett.*, 2018, **3**, 1795–1800.
30 O. Tereshchenko, D. Paget, P. Chiaradia, E. Placidi, J. Bonnet, F. Wiame and A. Taleb-Ibrahimi, *Surf. Sci.*, 2006, **600**, 3160–3166.
31 C. Goletti, G. Bussetti, A. Violante, B. Bonanni, M. Di Giovannantonio, G. Serrano, S. Breuer, K. Gentz and K. Wandelt, *J. Phys. Chem. C*, 2015, **119**, 1782–1790.
32 V. Mazine and Y. Borensztein, *Phys. Rev. Lett.*, 2002, **88**, 147403.
33 B. Sheridan, D. S. Martin, J. R. Power, S. D. Barrett, C. I. Smith, C. A. Lucas, R. J. Nichols and P. Weightman, *Phys. Rev. Lett.*, 2000, **85**, 4618–4621.
34 K. Haberland, P. Kurpas, M. Pristovsek, J.-T. Zettler, M. Weyers and W. Richter, *Appl. Phys. A: Mater. Sci. Process.*, 1999, **68**, 309–313.
35 J.-T. Zettler, K. Haberland, M. Zorn, M. Pristovsek, W. Richter, P. Kurpas and M. Weyers, *J. Cryst. Growth*, 1998, **195**, 151–162.
36 K. Christiansen, M. Luenenbuerger, B. Schineller, M. Heuken and H. Juergensen, *Opto-Electron. Rev.*, 2002, **10**(4), 237–242.
37 G. Sombrio, E. Oliveira, J. Strassner, J. Richter, C. Doering and H. Fouckhardt, *Micromachines*, 2021, **12**, 502.
38 P. Weightman, D. S. Martin, R. J. Cole and T. Farrell, *Rep. Prog. Phys.*, 2005, **68**, 1251–1341.
39 D. S. Martin and P. Weightman, *Surf. Rev. Lett.*, 2000, **07**, 389–397.
40 T. D. Kühne, M. Iannuzzi, M. Del Ben, V. V. Rybkin, P. Seewald, F. Stein, T. Laino, R. Z. Khaliullin, O. Schütt, F. Schiffmann, D. Golze, J. Wilhelm, S. Chulkov, M. H. Bani-Hashemian, V. Weber, U. Borštnik, M. Taillefumier, A. S. Jakobovits, A. Lazzaro, H. Pabst, T. Müller, R. Schade, M. Guidon, S. Andermatt, N. Holmberg, G. K. Schenter, A. Hehn, A. Bussy, F. Belleflamme, G. Tabacchi, A. Glöß, M. Lass, I. Bethune, C. J. Mundy, C. Plessl, M. Watkins, J. VandeVondele, M. Krack and J. Hutter, *J. Chem. Phys.*, 2020, **152**, 194103.
41 J. P. Perdew, K. Burke and M. Ernzerhof, *Phys. Rev. Lett.*, 1996, **77**, 3865–3868.
42 P. Giannozzi, S. Baroni, N. Bonini, M. Calandra, R. Car, C. Cavazzoni, D. Ceresoli, G. L. Chiarotti, M. Cococcioni, I. Dabo, A. D. Corso, S. de Gironcoli, S. Fabris, G. Fratesi, R. Gebauer, U. Gerstmann, C. Gougoussis, A. Kokalj, M. Lazzeri, L. Martin-Samos, N. Marzari, F. Mauri, R. Mazzarello, S. Paolini, A. Pasquarello, L. Paulatto, C. Sbraccia, S. Scandolo, G. Sclauzero, A. P. Seitsonen, A. Smogunov, P. Umari and R. M. Wentzcovitch, *J. Phys.: Condens. Matter*, 2009, **21**, 395502.
43 M. Schlipf and F. Gygi, *Comput. Phys. Commun.*, 2015, **196**, 36–44.
44 A. Marini, C. Hogan, M. Grüning and D. Varsano, *Comput. Phys. Commun.*, 2009, **180**, 1392–1403.
45 D. Sangalli, A. Ferretti, H. Miranda, C. Attaccalite, I. Marri, E. Cannuccia, P. Melo, M. Marsili, F. Paleari, A. Marrazzo, G. Prandini, P. Bonfà, M. O. Atambo, F. Affinito, M. Palummo, A. Molina-Sánchez, C. Hogan, M. Grüning, D. Varsano and A. Marini, *J. Phys.: Condens. Matter*, 2019, **31**, 325902.
46 D. E. Aspnes and A. A. Studna, *Phys. Rev. B: Condens. Matter Mater. Phys.*, 1983, **27**, 985–1009.
47 M. Muthuvel and J. Stickney, *J. Electrochem. Soc.*, 2006, **153**, C67.
48 H. J. Lewerenz, H. Gerischer and M. Lübke, *J. Electrochem. Soc.*, 1984, **131**, 100–104.
49 M. M. May and M. Sprik, *New J. Phys.*, 2018, **20**, 033031.

© 2022 The Author(s). Published by the Royal Society of Chemistry

5.2 In situ Monitoring of the Al(110)-[EMImCl]:$AlCl_3$ Interface by Reflection Anisotropy Spectroscopy

The article "*In situ* monitoring of the Al(110)-[EMImCl]:$AlCl_3$ interface by reflection anisotropy spectroscopy" was submitted to the journal *Batteries & Supercaps* in September 2023 and was published as open access in October 2023 (Batteries & Supercaps 2024, 7, e202300394) and is distributed under the terms of the Creative Commons Attribution 4.0 International. (CC BY 4.0, `https://creativecommons.org/licenses/by/4.0/`). [163]

DOI: 10.1002/batt.202300394

The second project is the first investigation of a battery material with EC-RAS. Here, the knowledge gained from the InP experiments helped in collaboration with another research group within POLiS in getting deeper inside into the interaction between the Al anode and the corrosive [EMImCl]:$AlCl_3$ electrolyte both during OCP and during electrochemical cycling. The study revealed that the natural oxide layer on top of the aluminium deteriorates over time. Post-mortem analysis by SEM and EDX indicated a reduction in the thickness of the passivation layer and the emergence of active sites, leading to an overall increase in surface roughness and inhomogeneities. During the plating and stripping processes, oscillations in the anisotropy were observed at low potentials and correlated to the frequency of the electrochemical cycling by Fournier transformation, indicating an ordered process. Cycling within a potential range where Al plating and stripping in nano-crystalline form predominates was more distinct than cycling in a potential range where Al plating and stripping in microcrystalline form is predominant.

Check for updates

Batteries & Supercaps

Research Article
doi.org/10.1002/batt.202300394

Chemistry Europe
European Chemical Societies Publishing

www.batteries-supercaps.org

Special Collection

In Situ Monitoring of the Al(110)-[EMImCl]:$AlCl_3$ Interface by Reflection Anisotropy Spectroscopy

Margot Guidat[+],*[a] Fatemehsadat Rahide[+],[b] Mario Löw,[c] Jongmin Kim,[a] Helmut Ehrenberg,[b] Sonia Dsoke,[b] and Matthias M. May[a]

Recently, Al-batteries (AlBs) have become promising candidates for post-lithium batteries, with [EMImCl]:$AlCl_3$ (1:1.5) as the most commonly used electrolyte. However, progress in the development of AlBs is currently hindered by the lack of understanding of its solid-electrolyte interface. Monitoring the structure of this interface under operational conditions by complementary spectroscopy could help to identify and overcome bottlenecks of the system. Reflection anisotropy spectroscopy (RAS), an optical *in situ* technique, provides access to physical and chemical properties of electrochemical interfaces on an atomistic level. Herein, we report the first example of RAS as an *in situ* characterization technique for non-aqueous battery systems, investigating an Al(110)-based model system. During chemical pre-treatment in [EMImCl]:$AlCl_3$, the Al(110) surface passivation film is modified. The oxide film is partially etched while an inhomogeneous passivation layer forms, increasing the surface roughness. Upon electrochemical cycling, applied potential-dependent oscillations of the anisotropy are observed and demonstrate the applicability of RAS to monitor phenomena such as plating/stripping and surface passivation in real-time.

Introduction

Al-batteries are a promising class among the post-lithium systems as they provide high specific power and energy.[1–3] Al is abundant, inexpensive, and recyclable, and it can provide a high theoretical volumetric capacity (8046 mAh cm^{-3}), making it a suitable anode material.[3,4] The condition of the Al electrode substrate plays an important role in the performance of rechargeable AlBs.[4] The Al surface is initially covered by a passivation layer consisting of an amorphous, ion/electron blocking oxide (Al_2O_3).[5] Although this oxide layer suppresses dendrite formation[6] and leads to an increased electrode/electrolyte interface stability,[4] it may also hinder the aluminum plating and stripping in non-acidic and non-corrosive $AlCl_3$-free electrolytes, due to the low electronic and ionic conductivities of the latter.[4,7]

The [EMImCl]:$AlCl_3$ Ionic Liquids (IL) remain the most commonly used electrolytes in the field of AlBs. When the ratio of $AlCl_3$ to [EMImCl] is higher than 1, the presence of $Al_2Cl_7^-$ and $AlCl_4^-$ species as well as the Lewis acidity in the electrolyte medium contribute to the corrosivity of the IL. $AlCl_3$ also increases the electrolyte's sensitivity to humidity.[1,8] The replacement of IL electrolytes by non-corrosive electrolytes is therefore crucial and currently constitutes a bottleneck in the field of AlBs since plating and stripping of $AlCl_3$-free electrolytes on Al substrates encounters severe issues such as side reactions and surface passivation.[9–13] It is consequently necessary to modify the electrode/electrolyte interfaces for $AlCl_3$-free electrolytes to partially remove the oxide layer, allowing both the formation of the contact between electrolyte and the Al surface and the prevention of dendrite growth.

Numerous approaches for Al surface pre-treatment and designing the Al-electrolyte interface have, via *in situ* and *ex situ* characterization like *in situ* optical microscopy and X-ray photoelectron spectroscopy (XPS), already shown to improve the cycling stability and hinder dendrite formation.[14–16] The immersion pre-treatment of the Al substrate in IL has been regarded as an efficient strategy to partially remove the inactive oxide layer (Al_2O_3) covering the Al substrate and to activate the Al electrode for subsequent electrochemical cycling in IL electrolytes.[5,17,18] However, the partial removal of the Al_2O_3 layer has not proven to be sufficient to allow subsequent electrochemical cycling in $AlCl_3$-free electrolytes.[19] Several hypotheses could explain the origin of the absence of plating and stripping

[a] M. Guidat,[+] J. Kim, Dr. M. M. May
Institute of Physical and Theoretical Chemistry
Universität Tübingen
Auf der Morgenstelle 15
72076 Tübingen, Germany
E-mail: margot.guidat@uni-tuebingen.de

[b] F. Rahide,[+] Prof. H. Ehrenberg, Dr. S. Dsoke
Institute for Applied Materials (IAM)
Karlsruhe Institute of Technology (KIT)
Hermann-von-Helmholtz-Platz 1
76344 Eggenstein-Leopoldshafen, Germany

[c] M. Löw
Institute of Theoretical Chemistry
Universität Ulm
Lise-Meitner-Str. 16
89081 Ulm, Germany

[+] These authors contributed equally.

Supporting information for this article is available on the WWW under https://doi.org/10.1002/batt.202300394

Special Collection This publication is part of a joint Special Collection dedicated to Post-Lithium Storage, featuring contributions published in Advanced Energy Materials, Batteries & Supercaps, and ChemSusChem.

© 2023 The Authors. Batteries & Supercaps published by Wiley-VCH GmbH. This is an open access article under the terms of the Creative Commons Attribution License, which permits use, distribution and reproduction in any medium, provided the original work is properly cited.

© 2023 The Authors. Batteries & Supercaps published by Wiley-VCH GmbH

in $AlCl_3$-free electrolytes comprising a non-effective pre-treatment in IL, an oxide layer reformation inside the glovebox between pre-treatment and cycling or an oxide layer reformation after immersion in non-corrosive electrolytes.[2,18] Earlier studies have already claimed that the instability and the irregular nature of the Al-IL solid-electrolyte interphase (SEI) render the pre-treatment in IL inefficient.[19]

These findings and hypotheses can, in principle, be probed by *in situ* reflection anisotropy spectroscopy (RAS). Since the latter operates at near normal-incidence reflection, its setup makes it (rather) straightforward to integrate with other techniques.[20,21] RAS, as a non-destructive optical surface analysis can, for instance, provide more insight into the evolution of the surface either during immersion pre-treatment or during electrochemical cycling inside a glovebox. In battery research, RAS has the potential to give insight into SEI formation, metal stripping/plating, as well as ion transport processes. In the working principle of RAS, linearly polarized light impinges at near-normal incidence on a single-crystalline surface.[21,22] The difference in reflectivity, Δr, with respect to two orthogonal directions in the surface plane (x, y) is then measured and scaled with the mean reflectivity, r. The surface's anisotropy can be determined according to Equation (1):

$$\mathrm{RAS}: \ \frac{\Delta r}{r} = 2 \cdot \frac{r_x - r_y}{r_x + r_y} \tag{1}$$

The anisotropy of the signal can arise from both the surface and the bulk of the sample due to the penetration depth of light in the material. In the case of cubic crystals with isotropic bulk, it is possible to exclusively get information about the surface. With such a technique, changes in surface structure and surface chemistry can be studied with a time resolution of about 10 ms. Furthermore, real-time monitoring in an electrochemical environment is possible.[22] Since RAS is restricted to single crystals, the present study focuses on the evolution of Al(110) in the IL electrolyte. Previous work on the corrosion of Al foils in the presence of HCl under galvanostatic conditions has revealed that the evolution of the surface morphology and the evolution of the etching pits depends significantly on the initial morphology of the surface, its impurities and the composition of the surface oxide.[23] Performing experiments with Al single crystals allows working with surfaces that are initially highly pure with a very low surface roughness (<0.1 nm) and a smooth and homogeneous oxide layer on top. For a more detailed understanding of RA-spectra, it is necessary to complement RAS with other surface-sensitive techniques such as XPS and scanning tunneling microscopy (STM), or computational RAS.

In this study, we first establish the experimental and computational spectra of Al(110) surfaces with different surface terminations or in different environments. In a second part, we monitor the evolution of the oxide layer upon pre-treatment in IL (1 : 1.5) by *in situ* RAS and we correlate the results with computational RAS, scanning electron microscopy (SEM) and energy-dispersive X-ray analysis (EDX). The third section investigates the possibility to use *in situ* RAS to study the Al(110)-IL (1 : 1.5) interface during electrochemical cycling. The experimental work presented here provides the first application of RAS on a battery system.

Results and Discussion

Computational and experimental Al(110) reference spectra

A previous study has already investigated RA-spectra of clean Al(110) surfaces prepared in an ultra-high vacuum environment as well as oxygenated Al(110) surfaces.[24] It was found that the characteristic anisotropic peak at about 1.5 eV is related to bulk Al(110) (interband transition), and is weakly affected by surface oxidation. The latter reduces the strength of the peak at 1.5 eV and shifts it to 1.45 eV. After 50 Langmuir of oxygen coverage, the oxide layer becomes amorphous and optically isotropic. Hence, above this amount of coverage, no meaningful changes in the anisotropy intensities can be detected anymore. Due to the strong anisotropy arising from its bulk, studying a (110) crystalline surface by RAS is to some extent reducing its surface-sensitivity because both bulk and surface anisotropy contribute to the RA-spectrum. However, (110) remains the orientation of choice compared to the commonly used (100) and (111) surfaces, where the surface is isotropic and, therefore, does not contribute to the RA-spectrum.

To understand the sensitivity of the RA-spectra to oxygen coverage, we model Al(110) surfaces with different amounts of O atoms on top, i.e., coverage of half a monolayer (0.5 ML) and one monolayer (1 ML). Figure 1a presents the computed RA-spectra of the clean and covered Al(110) surfaces. Similar to the experimental and theoretical results of Herrmann et al., our calculation of the clean surface yields a pronounced peak at 1.48 eV.[24] However, our calculated RA-spectrum is more similar to their experimental spectrum.[24] For instance, we find a negative anisotropy at 1.2 eV, which is also shown in their experimental spectrum, but is not observed in their theoretical result.[24] In principle, we and Herrmann et al. carried out first-principles calculations within the generalized gradient approximation, and also employed the same method for the calculation of the dielectric function, i.e. the IP-RPA approach. The main difference is the number of layers of the Al(110) surface. We and they modeled 21 and 16 layers, respectively. A different study revealed that the thickness of the slab has an effect on the RAS spectrum.[25] In addition, they used a computed bulk dielectric function for the RAS calculation, while an experimental one was adopted in our calculations. Note that by increasing the oxygen coverage, the negative peak at 1.2 eV is slightly shifted to lower energies, while the intensity of the characteristic peak at 1.48 eV is proportionally reduced.

Since the oxygen concentration inside our glovebox is in the order of 0.5 ppm, the Al crystal can, due to its high reactivity, be considered to be passivated with an oxide layer. Thus, it is appropriate to compare an experimental spectrum with a theoretical spectrum corresponding to Al(110) with at least one oxygen monolayer on top.

© 2023 The Authors. Batteries & Supercaps published by Wiley-VCH GmbH

25666223, 2024, 1, Downloaded from https://chemistry-europe.onlinelibrary.wiley.com/doi/10.1002/batt.202300394 by Universitätsbibliothek Tübingen, Wiley Online Library on [07/05/2025]. See the Terms and Conditions (https://onlinelibrary.wiley.com/terms-and-conditions) on Wiley Online Library for rules of use; OA articles are governed by the applicable Creative Commons License

Research Article
doi.org/10.1002/batt.202300394
Chemistry Europe
European Chemical Societies Publishing

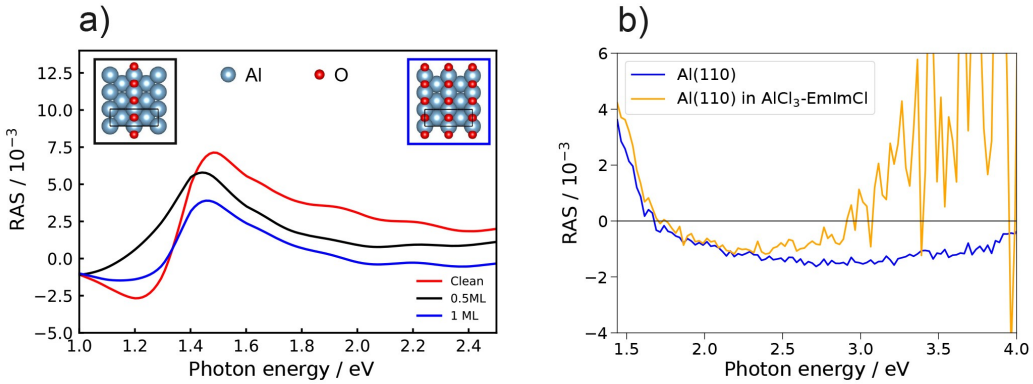

Figure 1. (a) Computed RA-spectra of the clean Al(110) (red), half monolayer (black) and monolayer (blue) coverage of O atoms on the surface. The insets show a top view of the 0.5 ML and 1 ML structures covered with oxygen. Oxygen and Aluminium atoms are depicted in red and light blue, respectively. The unit cells are indicated by the black lines. (b) Reference spectra of the Al(110) surface in Argon atmosphere and of the Al(110)-IL interface directly after immersion.

Figure 1b shows the experimental reference RA-spectra corresponding to the Al(110) surface and the Al(110)-IL interface. The reference spectrum of the as-received Al(110) crystal shows the same characteristics as the theoretical spectrum shown in Figure 1a. The anisotropy intensity is similar to the one of a monolayer oxygen coverage, suggesting that an oxide layer of about one monolayer passivates the Al surface. Since the resolution of the RA-spectra is significantly impacted by the setup, i.e. by the presence of a thick and coloured electrolyte layer, the data presented in this paper have a low signal-to-noise ratio. In particular, the spectrum of Al(110) in the IL suffers from a low signal-to-noise ratio beyond 3.0 eV due to the light absorption from the electrolyte at these energies. Moreover, due to the energy-range limitation of the spectrometer, it is not possible to access energies below 1.44 eV. Therefore, all the following graphics are restricted to an energy range between 1.44 and 2.5 eV, which allows better visibility of the area of interest. Figure 1b exhibits a small anisotropy offset already in the energy range of 1.44–3.0 eV when Al(110) is immersed in IL. Since the bulk electrolyte is not expected to be structured and should, therefore, not contribute to the optical anisotropy in this energy range, the anisotropic offset is expected to originate from an imperfect baseline correction or from a linear electro-optic effect from structured electrolyte molecules acting as dipoles at the near-Al surface. Further explanations are the dependence of the chemical interactions between the surface and the electrolyte, resulting in a modification in the morphology or composition of the surface.

Surface pre-treatment

For the surface pre-treatment, continuous RA-spectra (colourplot) were recorded over the time for 2 h of immersion of the Al crystal C1 in IL and are presented in Figure 2a. On the colourplot (CP), changes related to the peak at 1.5 eV are observed upon immersion. The width of the peak is conserved, but its anisotropy drops in the first phase before increasing

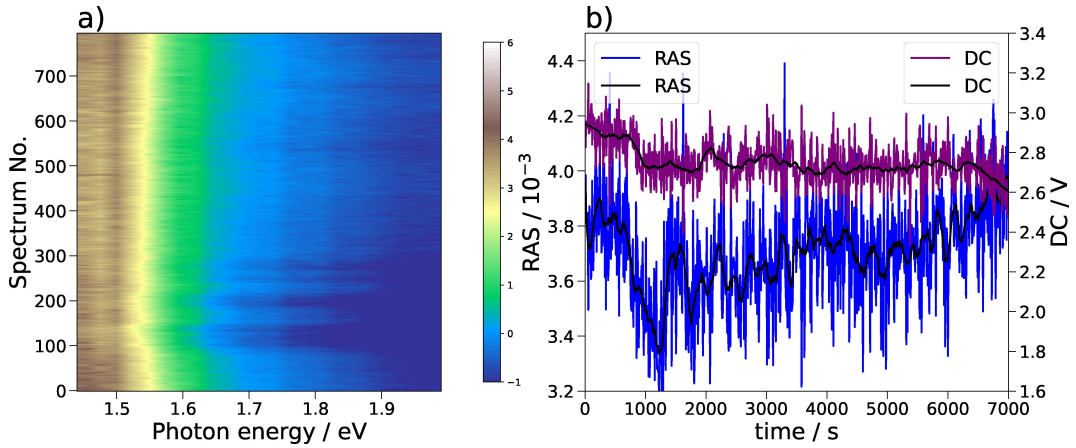

Figure 2. (a) Colourplot (CP) of Al(110) upon immersion in IL for 2 h. (b) Transient at 1.49 eV extracted from the CP. The purple and blue curves correspond to the evolution of the anisotropy and the reflectance over the time, respectively. The black curves correspond to the transients data filtered with a Savitzky–Golay filter.

© 2023 The Authors. Batteries & Supercaps published by Wiley-VCH GmbH

25666223, 2024, 1, Downloaded from https://chemistry-europe.onlinelibrary.wiley.com/doi/10.1002/batt.202300394 by Universitätsbibliothek Tübingen, Wiley Online Library on [07/05/2025]. See the Terms and Conditions (https://onlinelibrary.wiley.com/terms-and-conditions) on Wiley Online Library for rules of use; OA articles are governed by the applicable Creative Commons License

Research Article
doi.org/10.1002/batt.202300394
Chemistry Europe
European Chemical Societies Publishing

slightly above its initial value. For better visibility on the trend of the CP, a transient at 1.49 eV together with the reflectance (proportional to the DC signal) over the time at 1.49 eV are extracted and shown in Figure 2b. Here, the decrease in the anisotropy and the reflectance until the first half hour of the pre-treatment is noticeable, i.e. the interface deteriorates over time. The loss in the interface ordering is expected to originate from partial oxide layer removal and electrolyte decomposition. Previous studies have shown that after immersion or cycling of Al in IL, the Al surface contains a trace amount of chlorine from residual electrolyte that adsorbs on the oxide layer.[26,27] Furthermore, due to trace amounts of water originating from the glovebox atmosphere, $AlCl_3$ undergoes a hydrolysis leading to the formation of $Al(OH)_3$, Al_2O_3, and HCl, which can affect the Al-IL interface.[26] In the second phase, the anisotropy rises until slightly above its initial value at the end of the pre-treatment, meaning that the ordering at the interface. The rupture of the oxide film that partially dissolves in the electrolyte and then leads to the appearance of active sites on the surface would explain the increase of the RA intensity at the end of the pre-treatment. Concerning the DC signal, it progressively decreases until the end of the pre-treatment, confirming that the increase in ordering at the interface does no occur homogeneously over the surface plane and that some areas of the interface keep deteriorating. The formed solid electrolyte interface consisting of the byproducts of the IL electrolyte and repassivated Al_2O_3 oxide film on the Al surface complicates the interpretation of the RA-spectra. Hence, we will in the following refer to the layers present on the Al surface as the passivation layer. To minimize the contribution of the electrolyte film to the spectra, a comparison of spectra and SEM pictures taken before and after pre-treatment (in the absence of electrolyte) is shown in Figure 3.

Figure 3a–b compares the RA-spectra and the DC signals of the Al(110) surface before and after pre-treatment in IL, as well as the relative ratio of the RA-spectrum taken after pre-treatment, divided by the one taken before pre-treatment and the difference between the DC signals. The DC signal is proportional to the reflectance of the Al surface and correlating it with the anisotropy can help understanding the surface evolution. In Figure 1a, apparent changes in the peak at 1.5 eV between non-treated and treated surfaces are displayed. An increase of the anisotropy after pre-treatment is observed. According to the results discussed in Figure 1a, this increase indicates a reduction in oxygen coverage. A comparison of the RA-intensities between the theoretical and experimental spectra suggests that the crystal is initially covered by about one monolayer of oxygen. After pre-treatment, the anisotropy maintains a value between 4 and 5 at 1.5 eV, suggesting that the surface is still partially covered by oxygen after pre-treatment. Taking into account the oxygen content from the glovebox atmosphere, it is to be expected that surfaces re-oxidize after pre-treatment.

For a better understanding, the evolution of the anisotropy is compared to the evolution of the DC signal before and after pre-treatment (Figure 3b). An increase in reflectance and anisotropy implies, according to Figure 1a, a progressive removal of an oxide layer, leaving behind a cleaner surface. However, as depicted in Figure 3a–b, the DC signal decreases after pre-treatment while the RAS signal increases, which is a typical signature of surface roughening. Moreover, it is important to notice that both the RA-spectra ratio and DC signals difference lead to a rather constant value over the whole photon energy range. It suggests that either the surface is getting rougher, rather than its passivation layer reduced or the increase in surface in-homogeneity is more prominent in the evolution of the RA-spectrum than the reduction in the passivation layer thickness. These observations are in agreement with the conclusions from Natishan et al. on the reaction mechanism between chlorine and Al/Al_2O_3 in chlorine-containing electrolytes.[28] They demonstrated that after its adsorption on Al_2O_3, Cl^- is incorporated into the bulk of the oxide and moves towards the oxide/metal interface. Afterwards, Cl^- reaches the oxide/metal interface leading to blister formation and rupture of Al_2O_3 oxide film. The rupture of the oxide film, however, occurs only locally and leads to a heterogeneous, porous oxide layer with pitting corrosion. Assuming a similar mechanism on the oxidized Al(110) surface in the presence of

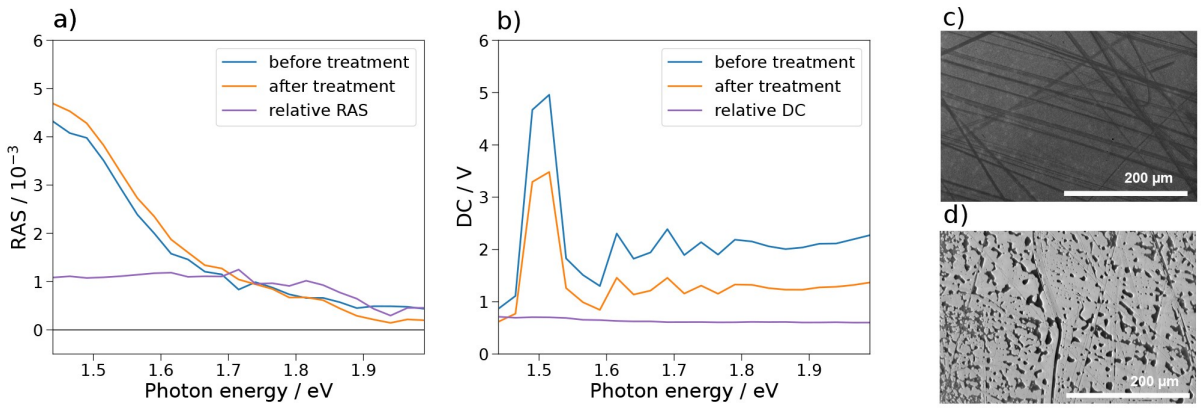

Figure 3. RA-spectra and their ratio (a) and DC signals and their absolute difference (b) of Al(110) surface before and after pre-treatment in IL. (c) and (d) provide the SEM pictures taken before and after pre-treatment, respectively.

© 2023 The Authors. Batteries & Supercaps published by Wiley-VCH GmbH

25666223, 2024, 1, Downloaded from https://chemistry-europe.onlinelibrary.wiley.com/doi/10.1002/batt.202300394 by Universitätsbibliothek Tübingen, Wiley Online Library on [07/05/2025]. See the Terms and Conditions (https://onlinelibrary.wiley.com/terms-and-conditions) on Wiley Online Library for rules of use; OA articles are governed by the applicable Creative Commons License

Research Article
doi.org/10.1002/batt.202300394
Chemistry Europe
European Chemical Societies Publishing

$Al_2Cl_7^-$ and $AlCl_4^-$ species would explain why not only the surface roughness increases, leading to an overall increase in the anisotropy, but also the anisotropy increases at around 1.5 eV due to the appearance of clean Al(110) surface spots. This interpretation implies that the surface is getting inhomogeneous on a microscopic scale.

To complement our findings from the RAS data, SEM pictures and EDX analysis were performed on the Al crystal after it was pre-treated and clean-connect transferred to the SEM chamber. Figure 3c–d compares the SEM pictures of the crystal before (as received from the supplier) and after pre-treatment, respectively. On the picture from Figure 3c, the as-received Al surface presents some scratches from the last polishing steps performed by the supplying company during the surface preparationof the crystal. The surface also contains particles of less than 1 μm in size composed of SiO_2. Since the last polishing step for Al crystals usually involves the use of a SiO_2 particle suspension, the presence of these particles is also attributed to residuals from the surface preparation process.[29] Figure 3d differs considerably from 3c in morphology and composition. The picture taken after pre-treatment shows an inhomogeneous surface made of a gray matrix with dark puddles on top. Displayed on Figures S2, S3 and Table S1, the EDX analysis of the same area indicates that grey matrix is composed almost exclusively of Al with low amounts of C, O and Cl (below 1 atomic weight %), while the dark areas present significant amounts of C (6–7 weight %), O (3–4 weight %), N (2–4 weight %) and Cl (4–5 weight %) and a decrease in Al content. It indicates that the pre-treatment of Al in the IL leads to the emergence of active site areas and areas where the electrolyte decomposes and adds on to the initial surface oxide layer. These results match our RAS interpretation as well as those of earlier studies.[9,19]

The change in anisotropy and reflectance upon surface pre-treatment indicates that RAS is sensitive to the evolution of the Al(110) surface in IL and allows *in situ* access. Yet the formed interface/interphase is very complex and the interpretation of the spectra is not straightforward. Furthermore, since our spectrometer averages over the whole measurement spot of several mm^2, the measurements average over in-plane surface inhomogeneities. Therefore, it is not possible to disentangle if the changes in the anisotropy over the pre-treatment are homogeneously distributed on the surface or are a sum of contributions from inhomogeneous areas on the surface. A parallel *in situ* investigation with reflection anisotropy microscopy (RAM) would provide a better spatial resolution and allow the elucidation of the different contributions. However, it would require, in addition to the spectrometer detector and the UV-visible light source, the inclusion of a camera, an objective lens, and a laser light source. Combining spectroscopy and microscopy is not achievable with our commercially available spectrometer but could, in principle, be implemented in a custom-build reflection anisotropy setup. Although they are currently limited to single-wavelength studies, RAM or 2D-surface optical reflectance (2D-SOR) have already demonstrated surfaces monitoring with spatial resolutions of about 5–10 μm.[30,31]

Electrochemical cycling

In the previous section, the pre-treatment of the Al(110) single crystals in IL monitored by RAS has shown that RAS is sensitive to the Al surface evolution. This suggests that it should be feasible to study *in situ* the Al(110)-IL interface/interphase during plating and stripping with RAS. To compare the electrochemical cycling behaviour of Al single crystals with the one of Al foil – which is commonly used in the AIBs community and shown in Figure S4 – Al(110) crystal number 2 (C2) is cycled in the photoelectrochemical (PEC) cell at a scan rate of 20 mV/s in a potential range allowing full Al stripping. In parallel with the cyclic voltammetry (CV), a CP is recorded at a speed that four spectra are obtained during one full potential cycle. The experimental procedure is illustrated in Figure S1. The CVs depicted in Figure 4 resemble the one with Al-foil taken in similar conditions (Figure S4), indicating that the behaviour of a (110)-oriented Al surface during electrochemical cycling is comparable to a polycrystalline Al surface. The evolution of the surface roughness observed in the RA-spectra over the experimental series can first be understood from the evolution of the CVs. Over the experimental series, the stripping peak on the CV around 0.28 V vs. Al gets more pronounced. This phenomenon is attributed to a progressive Al plating and stripping from a nanocrystalline to microcrystalline form of Al,[32] i.e. the surface is getting rougher. Thus, if the structure of the surface evolves upon cycling with an increasing amount of Al plated and stripped in a microcrystalline form, the plating and stripping occur in a more defined manner, and the variation of the anisotropy is supposed to be higher. However, because of the high scan rate and the large energy range chosen for this set of experiments, the time resolution is too low to observe a trend related to plating and stripping on the CPs recorded in parallel to the CVs (Figure S5).

During the experimental series, the CVs were recorded on both treated and untreated Al(110). As described in the pre-treatment section, when the Al(110) electrode is immersed in IL, the native Al_2O_3 film covering the Al single crystal undergoes a transformation, resulting in a porous film composed of an inner

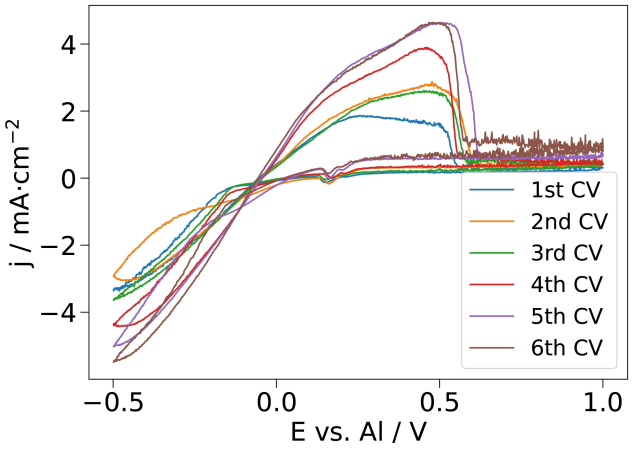

Figure 4. Last cycles of 6 CV experiments measured between −0.5 to 1 V vs. Al at 20 mV/s for 10 cycles.

© 2023 The Authors. Batteries & Supercaps published by Wiley-VCH GmbH

25666223, 2024, 1, Downloaded from https://chemistry-europe.onlinelibrary.wiley.com/doi/10.1002/batt.202300394 by Universitätsbibliothek Tübingen, Wiley Online Library on [07/05/2025]. See the Terms and Conditions (https://onlinelibrary.wiley.com/terms-and-conditions) on Wiley Online Library for rules of use; OA articles are governed by the applicable Creative Commons License

layer enriched with oxides and an outer layer made of both inorganic and organic materials. According to the literature, the partial removal and the reduction in thickness of the Al_2O_3 film makes it easier for charge carriers and ions to move between the Al electrode and the electrolyte.[9,27,33,34] Figure S6 provides insights into the electrochemical behaviour of pre-treated and unpre-treated Al(110) C2 in IL under the same cycling conditions as the one of Figure 4. Specifically, it illustrates notable differences in CVs of these electrodes and their implications for the Al plating and stripping processes.

When examining the CVs of not pre-treated Al(110) in Figure S6a, it is apparent that as the cycle number increases, the current density responsible for Al plating and stripping keeps increasing. This fluctuation indicates an unstable electrode-electrolyte interface, which has a detrimental effect on the plating and stripping processes. This trend aligns with the literature, where it is stated that Al plating and stripping peaks tend to be smaller and less predictable during the initial cycles, but become more reversible with continued cycling, typically around the second or third cycle.[35,36] The native Al_2O_3 film delays the activation of the anode and makes it more challenging to reach a reversible regime, resulting in a significant over-potential.[2,37] Therefore, the result confirms that the presence of the Al_2O_3 film can act as a barrier, limiting the effective interaction between the Al electrode and the electrolyte, and reducing the efficiency of the electrochemical system.[9,36]

In Figure S6b, the maximum of the stripping peaks initially decreases over the first cycles before reaching a stable value. This is an indicator for an efficient modification or removal of the Al_2O_3 oxide layer, which is known to play a crucial role in these electrochemical processes. Hence, the porous surface film formed during the immersion pre-treatment seems to have a beneficial impact on the electrode's performance.[9]

A further set of experiments was performed on a second Al(110) crystal (C3) and was monitored with higher temporal spectroscopic resolution than for C2. In this second experimental series, Al(110) C3 is first pre-treated according to the procedure described in the experimental section. For the cycling performance, the Raman cell from rhd instruments (rhd cell) is used, where a thinner electrolyte layer is present on top of the crystal surface, reducing light absorption from the electrolyte in comparison to the PEC cell. Compared to the previous experiment series (with PEC cell), the cell is cycled at lower scan rates of 2.5 mV/s, and RAS is measured in parallel with higher temporal resolution, as depicted in Figure 5 for a potential range between −0.25 and 0.25 V vs. Al. The potential range of the CV shown in Figure 5a and 5c does not allow for complete Al stripping, but a more detailed *in situ* investigation of the surface during plating and stripping is possible from the spectroscopic side, i. e. about 20 spectra are measured per cycle, as shown in Figure 5b and 5c.

Plotting the applied voltage as a function of the time together with the CP is a systematic way to probe potential direct correlations between the electrochemical and optical measurements. In the case of systems with a high degree of ordering, such as InP in contact with low-concentration acidic electrolytes, there are clear visual correlations between the cyclic potential and the oscillations of the RA-values.[38] For Al in IL, a more complex and less ordered system, plotting the applied voltage with the CP simply helps deducing that they do exhibit a directly apparent correlation and that more extensive analysis of the CP is required. For better visibility of the anisotropy features, transients at 1.49 eV are extracted from the CPs. Figure 6 presents the electrochemical cycling of Al(110) sample C2 between −0.25 to 0.25 V vs. Al (a) and between −0.5 and 0.5 V vs. Al (b), plotted over time together with a transient and a DC-signal extracted from the CP at 1.49 eV.

To reduce the background noise from the transients shown in Figure 6, and to identify if there is a feature correlated to plating and stripping, the transients are filtered by Fast Fourier transform (FFT). The FFT-filtered transient from Figure 6a was extracted from the CP of Figure 5b at 1.49 eV and exhibits an increasing trend in the first cycles. While the anisotropy progressively decreases after the third cycle, small oscillations with a period matching the cycling period of the potential start to appear. The periods of the potential applied during the

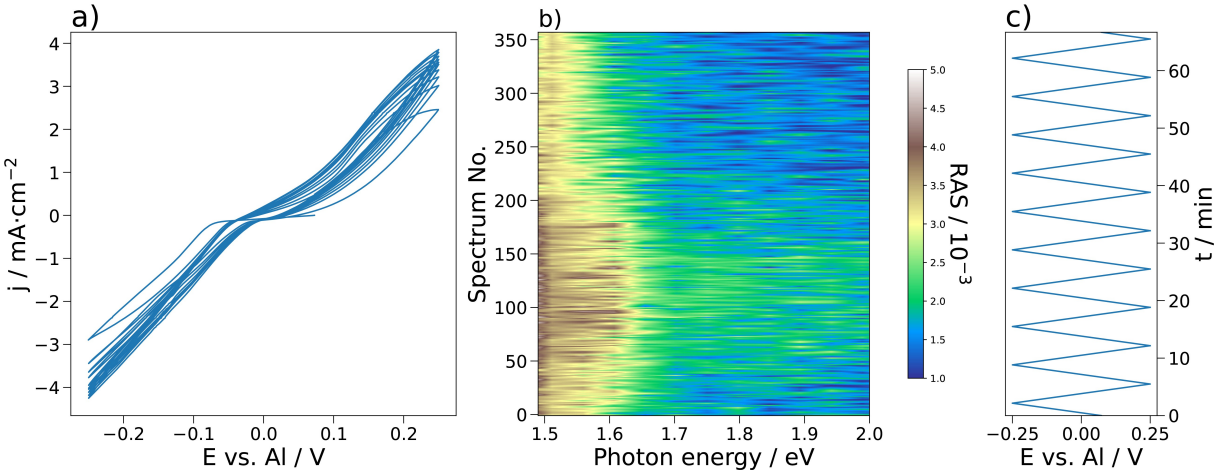

Figure 5. (a) CV between −0.25 and 0.25 V vs. Al for 10 cycles at 2.5 mV/s. (b) CP measured in parallel to CV. (c) applied voltage with respect to the time.

© 2023 The Authors. Batteries & Supercaps published by Wiley-VCH GmbH

25666223, 2024, 1, Downloaded from https://chemistry-europe.onlinelibrary.wiley.com/doi/10.1002/batt.202300394 by Universitätsbibliothek Tübingen, Wiley Online Library on [07/05/2025]. See the Terms and Conditions (https://onlinelibrary.wiley.com/terms-and-conditions) on Wiley Online Library for rules of use; OA articles are governed by the applicable Creative Commons License

Research Article
doi.org/10.1002/batt.202300394
Chemistry Europe
European Chemical Societies Publishing

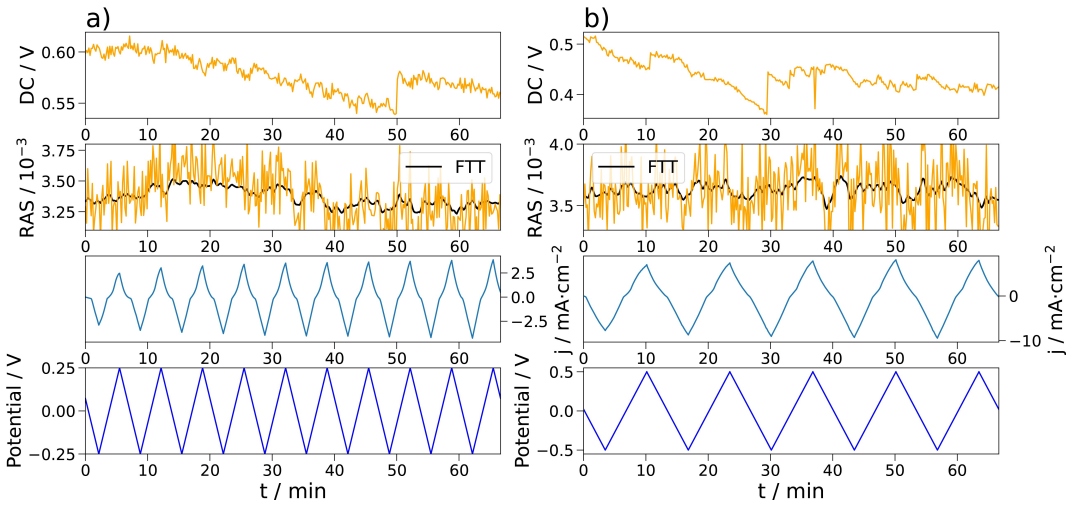

Figure 6. DC signal and transients at 1.49 eV extracted from a CP measured during (a) CV between −0.25 and 0.25 V at a scan speed of 2.5 mV/s for 10 cycles and (b) CV between −0.5 and 0.5 V at 2.5 mV/s for 5 cycles. The black curves correspond to the FFT-filtered transients.

experiments shown in Figure 6a–b are 2.5 and 1.25 mHz, respectively.

Figure 7a shows again the original transient of Figure 6a while its Fourier spectrum is shown in Figure 7b. The DC value at 0 Hz has been discredited due to its high amplitude as compared to the other peaks. The second most dominant peak is observed at 2.5 mHz, which corresponds to the oscillation period of the applied potential. The same conclusion is drawn when examining the FFT of the original transient of Figure 6b: the most prominent peak is observed at 1.25 mHz, i.e. the period of the applied potential (Figure S8).

The presence of these peaks justifies the application of an exponential filter to the data and confirms that the oscillations observed in the transient can be correlated with the applied potential. When correlating the RAS oscillations in Figure 6a with the corresponding CV, the local minima of the oscillations are located shortly after the local maxima in the anodic current. Oscillations of the RAS intensity are also present on the transient from Figure 6b for which the potential range of the CV was broader. However, the period of the oscillations is less well-defined than for the narrower potential range. This indicates that, depending on the potential range in which Al is cycled, the plating and stripping process is more or less ordered. Between −0.25 to 0.25 V, small oscillations emerge with increasing cycle number, meaning that the process is most probably happening homogeneously at the surface and in a layer-by-layer manner.

Between −0.5 and 0.5 V, the build-up and build-down of an anisotropy are less defined, indicating that the process occurs on a larger scale and that the surface is getting rough. The DC signals globally decrease over time, but exhibit some features, i.e. at 50 minutes in Figure 6a and at 10 and 30 minutes in Figure 6b. There are significant changes in the transients at the time of these features, meaning that they are not associated with composition or structural change, but that they can be attributed to surface etching. The progressive surface etching

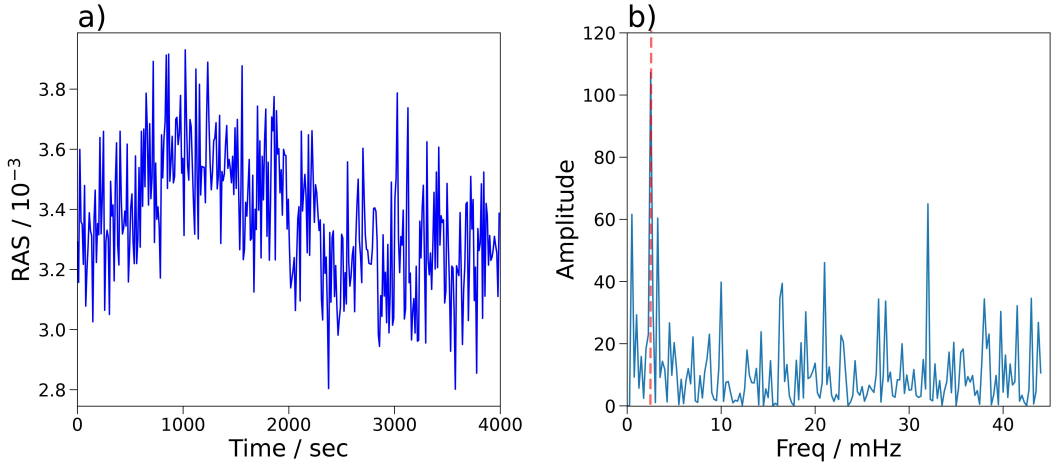

Figure 7. (a) Transient at 1.49 eV extracted from the CP from Figure 6(a) and 6(b). The corresponding Fourier spectrum. The red dashed line marks the predominant frequency of the spectrum at 2.5 mHz.

© 2023 The Authors. Batteries & Supercaps published by Wiley-VCH GmbH

25666223, 2024, 1, Downloaded from https://chemistry-europe.onlinelibrary.wiley.com/doi/10.1002/batt.202300394 by Universitätsbibliothek Tübingen, Wiley Online Library on [07/05/2025]. See the Terms and Conditions (https://onlinelibrary.wiley.com/terms-and-conditions) on Wiley Online Library for rules of use; OA articles are governed by the applicable Creative Commons License

indicates that the stripping/plating is uneven. Al is more stripped than plated, and depending on the potential range used, more or less cycles are needed to fully etch one aluminum layer. Between −0.25 and 0.25 V, only one step-wise increase in the DC signal is observed, while between −0.5 and 0.5 V, 2 step-wise increases can be observed before the process becomes too ill-defined and it is not possible to distinguish features from etching anymore. Hence, the potential range and the scan rate also have an impact on the occurrence of surface etching.

While in this study both single- and poly-crystalline substrates have comparable CVs, using different crystal orientations can result in different cycling performance. This difference in structural form can impact the physical properties of the deposited Al, such as its grain size, grain boundaries, and defect density. This impacts the nucleation and growth of Al deposits, altering the overall electrochemical behaviour. Dendrite formation during Al electrodeposition depends on factors like surface properties of the aluminum substrate, electrolyte, and cycling conditions, and results from inhomogeneous current distribution, ion concentration variations, and defects.[39–41] Single crystals offer defined nucleation sites, promoting or inhibiting dendrite growth based on their surface orientation. As displayed in Figure S7, dendrites were observed on the SEM images of the crystal C2 taken after the experimental series described in Figure S1 was conducted. It means that, depending on the electrochemical conditions, an Al 110-orientation is prone to dendrite growth in a [EMImCl]:$AlCl_3$ (1:1.5) electrolyte. Structural changes from nanocrystalline to microcrystalline aluminum can influence dendrite formation as well. Microcrystalline structures reduce nucleation sites, but may have defects that promote dendrites. Al(110) sample C3 was cycled in smaller potential ranges (where plating/stripping in the nanocrystalline form of Al is predominant) and at lower scan rates than the crystal C2. Unlike for the ones of C3, the SEM images from Figure S7 of C2 present dendrites, meaning that the dendrite growth is favoured by a microcrystalline surface structure.

These findings show that RAS can be used as a probe to study electrochemical interfaces of battery systems comprising stripping/plating, SEI formation, and dendrite growth. Note that since the interfaces of battery systems remain very challenging and are still at an early stage of investigation and comprehension, interpretation and conclusion from RAS investigation should be accompanied by complementary techniques such as XPS, STM, and 2D-SOR. Nevertheless, this study gives a glimpse into the potential of electrochemical RAS as a complementary tool for the study of battery-electrolyte interfaces and interphases. Specifically, it enlightens the etching process and morphological changes at the Al(110)-IL interface during electrochemical conditioning.

Conclusions

In this work, we introduced RAS as an *in situ* technique of the Al(110)-electrolyte interface monitoring for battery applications. We particularly showed that the surface pre-treatment in [EMImCl]:$AlCl_3$ affects the reflectance at the interface and the anisotropic feature of the Al(110) spectrum related to its oxide passivation layer. In the electrolyte, although the Al surface globally deteriorates due to electrolyte decomposition and swelling of the passivation layer, a localized surface ordering progressively rises over the pre-treatment. Comparison of the surface before and after pre-treatment with the computed spectra and with post-mortem SEM/EDX analysis allows deducing a combination of a partial decrease in the passivation layer thickness and the appearance of active sites with an overall increase in surface roughness/inhomogeneities. Al stripping/plating from the [EMImCl]:$AlCl_3$ electrolyte on Al(110) single crystals is comparable to polycrystalline Al foil and evolves from nanocrystalline to a microcrystalline form of Al. The CVs of the pre-treated Al(110) electrode exhibit a faster stabilization of Al plating and stripping peaks compared to those of untreated Al(110). This observation suggests that for an Al crystal with a 110-orientation, the pre-treatment has a positive effect on the Al plating and stripping performances.

The presence of oscillations of the anisotropy during plating and stripping was only observed in a low potential range. It suggests that, depending on the potential range, the stripping and plating process is more or less ordered. Cycling in a potential range, where Al plating and stripping in the nanocrystalline form is predominant, occurs in a more defined manner than cycling in a potential range where Al plating and stripping in the microcrystalline form is preponderant.

Yet the Al-[EMImCl]:$AlCl_3$ interface remains very complex, and the use of [EMImCl]:$AlCl_3$ for a high $AlCl_3$/[EMImCl] ratio is highly corrosive and therefore not sustainable for long-term battery operation. This study emphasizes that RAS is a potential tool to follow the build-up of a conductive and protective film which is required for the implementation of non-acidic, non-aqueous electrolytes.[9] A natural progression of this work is to improve the pre-treatment of noisy signals. As an alternative, focusing on advanced light sources could increase signal-to-noise ratios.

Experimental

Materials and electrolyte preparation

The Al(110) single crystals were purchased from Mateck (purity of 99,999%, diameter of 10 mm, and thickness of 3 mm) and are denoted as C1, C2 and C3. In the study, [EMImCl]:$AlCl_3$ (1:1.5) was prepared by slowly adding aluminum chloride ($AlCl_3$) (Anhydrous, Sigma–Aldrich, 99.99%) to 1-Ethyl-3-methylimidazolium chloride (EMImCl) (Sigma–Aldrich, >95%) while stirring using a magnetic stirring bar at room temperature (28 to 30 C) inside an argon-filled glovebox (MBraun, <0.5 ppm O_2, <0.5 ppm H_2O). Anhydrous Acetonitrile (99.8%) has been purchased from Sigma–Aldrich.

Al surface pre-treatment

All handling and preparation of Al(110) occurred inside an argon-filled glovebox. The Al electrode surface modification has been achieved by immersion for 2 hours in 6 mL of [EMImCl]:$AlCl_3$ (1:1.5)

© 2023 The Authors. Batteries & Supercaps published by Wiley-VCH GmbH

25666223, 2024, 1, Downloaded from https://chemistry-europe.onlinelibrary.wiley.com/doi/10.1002/batt.202300394 by Universitätsbibliothek Tübingen, Wiley Online Library on [07/05/2025]. See the Terms and Conditions (https://onlinelibrary.wiley.com/terms-and-conditions) on Wiley Online Library for rules of use; OA articles are governed by the applicable Creative Commons License

25666223, 2024, 1, Downloaded from https://chemistry-europe.onlinelibrary.wiley.com/doi/10.1002/batt.202300394 by Universitätsbibliothek Tübingen, Wiley Online Library on [07/05/2025]. See the Terms and Conditions (https://onlinelibrary.wiley.com/terms-and-conditions) on Wiley Online Library for rules of use; OA articles are governed by the applicable Creative Commons License

electrolyte. Spectra were taken prior to, during and after surface pre-treatment, in the absence and presence of electrolyte. After each measurement, the Al(110) was cleaned and washed several times with anhydrous acetonitrile inside the glovebox before the RA spectrum was measured.

Electrochemical setup and technique

All electrochemical experiments were performed inside an argon-filled glovebox. For the electrochemical measurement, a photo-electrochemical cell (PEC cell) from Zahner was used for C2 and a Raman cell from rhd instruments was used for C3. For the PEC cell, Al wire as a pseudo reference electrode Alfa Aesar (0.5 mm diameter, 99.9999% purity) and glassy carbon as counter electrode (redox.me) were respectively polished with SiC paper (400 P WS FLEX 16) and 250 nm diamond polishing suspension (rhd instruments) before each electrochemical setup. The PEC and the rhd cell were filled with 9 and 3 ml of [EMImCl]:$AlCl_3$ (1:1.5), respectively. For the RA spectroscopy, an EpiRAS from Laytec was employed. The electrochemical measurements were controlled with a Princeton Applied Research VersaSTAT 3F potentiostat and a Gamry Instruments (Interface 5000E). To perform the measurements, the RA-spectrometer was installed on top of the glovebox. A quartz window placed in the sealing of the glovebox, between the setup and the spectrometer, allowed light transmission. The electrochemical cell was placed under the window on top of a hexapod (Physik Instrumente H-840 Hexapod), which allowed for rotating, inclining, and translating the cell to align it with the lightpath. For the SEM/EDX measurements the Apero 2 from Thermo Fisher Scientific with the clean connect system was used, enabling transport of the sample from the glovebox to the SEM without breaking the inert environment. The SEM/EDX measurements were done with a 10 kV electron beam and a beam current of 26 nA. The experimental series performed with C2 are detailed in Figure S1.

Baseline correction and FFT

A baseline correction was applied to some spectra, using a Si(100) crystal immersed in the electrolyte. The transients from Figure 7 are filtered by Fast Fourier transform (FFT) with an exponential filter of a factor of -0.5.

Computational

To obtain theoretically derived RAS, we firstly performed density-functional theory (DFT) calculations with Quantum Espresso (QE).[42] In the QE, we adopted the optimized norm-conserving Vanderbilt pseudopotentials. The sampling of the Brillouin zone (BZ) was performed with a 40×120×1 **k**-grid for our investigated systems. An energy cutoff of 50 Ry was used. For the exchange-correlation functional, we employed the generalized gradient approximation (GGA) in the Perdew–Burke–Ernzerhof (PBE) parametrization. The subsequent RAS calculations were carried out using the Yambo code.[43,44] Here, we used the IP-RPA method to compute the dielectric function of our investigated slabs.

Supporting Information

The authors have cited additional references within the Supporting Information.[10,46]

Acknowledgements

The authors would like to thank Dr. Marcel Drüschler, Dr. Sebastian Kranz, and Dr. Benedikt Huber from the rhd instruments company for their scientific support and assistance in battery cell setup supplies. We also thank Dr. Holger Euchner for his help in the revision of the manuscript. This work was funded by the Deutsche Forschungsgemeinschaft (DFG, German Research Foundation) under Germany's Excellence Strategy – EXC 2154 – project number 390874152 as well as DFG project number 434023472. We acknowledge the state of Baden-Württemberg, through bwHPC, and DFG through grant no. INST 40/575-1 FUGG (JUSTUS 2 cluster) for computational resources. Open Access funding enabled and organized by Projekt DEAL.

Conflict of Interests

There are no conflicts to declare.

Data Availability Statement

The data that support the findings of this study are openly available on Zenodo at https://doi.org/10.5281/zenodo.10000855, Ref. [45].

Keywords: aluminum · battery · electrochemistry · interfaces · spectroscopy

[1] B. Craig, T. Schoetz, A. Cruden, C. Ponce de Leon, *Renewable Sustainable Energy Rev.* **2020**, *133*, 110100.
[2] Q. Li, N. J. Bjerrum, *J. Power Sources* **2002**, *110*, 1.
[3] E.-S. Lee, S.-H. Huh, S.-H. Lee, S.-H. Yu, *ACS Sustainable Chem. Eng.* **2023**, *11*, 2014.
[4] X. Zhang, R. Lv, W. Tang, G. Li, A. Wang, A. Dong, X. Liu, J. Luo, *Adv. Funct. Mater.* **2020**, *30*, 2004187.
[5] S. K. Das, S. Mahapatra, H. Lahan, *J. Mater. Chem. A* **2017**, *5*, 6347.
[6] C. Schütter, A. Bothe, A. Balducci, *Electrochim. Acta* **2020**, *331*, 135421.
[7] M. Chiku, S. Matsumura, H. Takeda, E. Higuchi, H. Inoue, *J. Electrochem. Soc.* **2017**, *164*, A1841.
[8] J.-K. Chang, S.-Y. Chen, W.-T. Tsai, M.-J. Deng, I.-W. Sun, *Electrochem. Commun.* **2007**, *9*, 1602.
[9] L. C. Loaiza, N. Lindahl, P. Johansson, *J. Electrochem. Soc.* **2023**, *170*, 030512.
[10] T. Mandai, P. Johansson, *J. Mater. Chem. A* **2015**, *3*, 12230.
[11] Z. Slim, E. J. Menke, *Batteries & Supercaps* **2023**, *6*, e202300164.
[12] X. Wen, J. Zhang, H. Luo, J. Shi, C. Tsay, H. Jiang, Y.-H. Lin, M. A. Schroeder, K. Xu, J. Guo, *J. Phys. Chem. Lett.* **2021**, *12*, 5903.
[13] H. Wang, S. Gu, Y. Bai, S. Chen, F. Wu, C. Wu, *ACS Appl. Mater. Interfaces* **2016**, *8*, 27444.
[14] S. Varshney, M. Oded, S. Remennik, V. Gutkin, U. Banin, *Small* **2023**, *19*, 2304478.
[15] R. Tao, H. Fu, C. Gao, L. Fan, E. Xie, W. Lyu, J. Zhou, B. Lu, *Adv. Funct. Mater.* **2023**, 2303072.
[16] S. He, J. Wang, X. Zhang, W. Chu, S. Zhao, D. He, M. Zhu, H. Yu, *J. Mater. Chem. A* **2023**, *11*, 17020.
[17] F. Wu, N. Zhu, Y. Bai, Y. Gao, C. Wu, *Green Energy & Environ.* **2018**, *3*, 71.
[18] H. Wang, S. Gu, Y. Bai, S. Chen, F. Wu, C. Wu, *ACS Appl. Mater. Interfaces* **2016**, *8*, 27444.
[19] T. Dong, K. L. Ng, Y. Wang, O. Voznyy, G. Azimi, *Adv. Energy Mater.* **2021**, *11*, 2100077.

© 2023 The Authors. Batteries & Supercaps published by Wiley-VCH GmbH

[20] K. Haberland, P. Kurpas, M. Pristovsek, J.-T. Zettler, M. Weyers, W. Richter, *Appl. Phys. A Mater. Sci. Process.* **1999**, *68*, 309.
[21] P. Weightman, D. S. Martin, R. J. Cole, T. Farrell, *Rep. Prog. Phys.* **2005**, *68*, 1251.
[22] M. Guidat, M. Löw, M. Kölbach, J. Kim, M. M. May, *ChemElectroChem* **2023**, *10*, e202300027.
[23] J. Scherer, O. Magnussen, T. Ebel, R. Behm, *Corros. Sci.* **1999**, *41*, 35.
[24] T. Herrmann, M. Gensch, M. J. G. Lee, A. I. Shkrebtii, N. Esser, W. Richter, P. Hofmann, *Phys. Rev. B* **2004**, *69*, 165406.
[25] C. Hogan, O. Pulci, P. Gori, F. Bechstedt, D. S. Martin, E. E. Barritt, A. Curcella, G. Prevot, Y. Borensztein, *Phys. Rev. B* **2018**, *97*, 195407.
[26] S. Poetz, P. Handel, G. Fauler, B. Fuchsbichler, M. Schmuck, S. Koller, *RSC Adv.* **2014**, *4*, 6685.
[27] D.-M. She, W.-L. Song, J. He, N. Li, H. Chen, S. Jiao, D. Fang, *J. Electrochem. Soc.* **2020**, *167*, 130530.
[28] P. M. Natishan, W. E. O'Grady, *J. Electrochem. Soc.* **2014**, *161*, C421.
[29] *Buehler Sum Met: The Sum Of Our Experience*, Buehler, Lake Bluff, Il, 4th edition **2018**.
[30] C. Punckt, F. S. Merkt, H. H. Rotermund, *New J. Phys.* **2007**, *9*, 213.
[31] S. Pfaff, A. Larsson, D. Orlov, G. S. Harlow, G. Abbondanza, W. Linpé, L. Rämisch, S. M. Gericke, J. Zetter-berg, E. Lundgren, *ACS Appl. Mater. Interfaces* **2021**, *13*, 19530.
[32] R. Böttcher, S. Mai, A. Ispas, A. Bund, *J. Electrochem. Soc.* **2020**, *167*, 102516.
[33] D. Pradhan, D. Mantha, R. Reddy, *Electrochim. Acta* **2009**, *54*, 6661.
[34] H. Yang, F. Wu, Y. Bai, C. Wu, *J. Energy Chem.* **2020**, *45*, 98.
[35] S. Xia, X. Zhang, K. Huang, Y.-L. Chen, Y. Wu, *J. Electroanal. Chem.* **2015**, *757*.
[36] O. M. Ylivaara, X. Liu, L. Kilpi, J. Lyytinen, D. Schneider, M. Laitinen, J. Julin, S. Ali, S. Sintonen, M. Berdova, E. Haimi, T. Sajavaara, H. Ronkainen, H. Lipsanen, J. Koskinen, S.-P. Hannula, R. L. Puurunen, *Thin Solid Films* **2014**, *552*, 124.
[37] M. Jiang, C. Fu, P. Meng, J. Ren, J. Wang, J. Bu, A. Dong, J. Zhang, W. Xiao, B. Sun, *J. Adv. Mater.* **2022**, *34*, 2102026.
[38] M. Löw, M. Guidat, J. Kim, M. M. May, *RSC Adv.* **2022**, *12*, 32756.
[39] N. Sabi, K. Palanisamy, F. Rahide, S. Daboss, C. Kranz, S. Dsoke, *Batteries & Supercaps* **2023**, *6*, e202300298.
[40] N. Li, D. She, K. Zhang, H.-S. Chen, W.-L. Song, S. Jiao, *ChemSusChem* **2022**, *15*, e202201390.
[41] T. Schoetz, O. Leung, C. P. De Leon, C. Zaleski, I. Efimov, *J. Electrochem. Soc.* **2020**, *167*, 040516.
[42] P. Giannozzi, S. Baroni, N. Bonini, M. Calandra, R. Car, C. Cavazzoni, D. Ceresoli, G. L. Chiarotti, M. Cococcioni, I. Dabo, A. D. Corso, S. de Gironcoli, S. Fabris, G. Fratesi, R. Gebauer, U. Gerstmann, C. Gougoussis, A. Kokalj, M. Lazzeri, L. Martin-Samos, N. Marzari, F. Mauri, R. Mazzarello, S. Paolini, A. Pasquarello, L. Paulatto, C. Sbraccia, S. Scandolo, G. Sclauzero, A. P. Seitsonen, A. Smogunov, P. Umari, R. M. Wentzcovitch, *J. Phys. Condens. Matter* **2009**, *21*, 395502.
[43] A. Marini, C. Hogan, M. Grüning, D. Varsano, *Comput. Phys. Commun.* **2009**, *180*, 1392.
[44] D. Sangalli, A. Ferretti, H. Miranda, C. Attaccalite, I. Marri, E. Cannuccia, P. Melo, M. Marsili, F. Paleari, A. Marrazzo, G. Prandini, P. Bonfà, M. O. Atambo, F. Affinito, M. Palummo, A. Molina-Sánchez, C. Hogan, M. Grüning, D. Varsano, A. Marini, *J. Phys. Condens. Matter* **2019**, *31*, 325902.
[45] M. Guidat, F. Rahide, M. Loew, J. Kim, H. Ehrenberg, S. Dsoke, M. M. May, *Zenodo dataset* **2023**, DOI:10.5281/zenodo.10000854.
[46] F. Rahide, E. Zemlyanushin, G.-M. Bosch, S. Dsoke, *J. Electrochem. Soc.* **2023**, *170*, 030546.

Manuscript received: September 11, 2023
Revised manuscript received: October 10, 2023
Accepted manuscript online: October 13, 2023
Version of record online: November 14, 2023

© 2023 The Authors. Batteries & Supercaps published by Wiley-VCH GmbH

25666223, 2024, 1, Downloaded from https://chemistry-europe.onlinelibrary.wiley.com/doi/10.1002/batt.202300394 by Universitätsbibliothek Tübingen, Wiley Online Library on [07/05/2025]. See the Terms and Conditions (https://onlinelibrary.wiley.com/terms-and-conditions) on Wiley Online Library for rules of use; OA articles are governed by the applicable Creative Commons License

5.3 Operando Investigation of Al Plating Regimes on HOPG in [EMImCl]:$AlCl_3$ by Electrochemical Reflection Anisotropy Spectroscopy

The article "Operando Investigation of Al Plating Regimes on HOPG in [EMImCl]:$AlCl_3$ by Electrochemical Reflection Anisotropy Spectroscopy" was submitted to the journal *Batteries & Supercaps* in September 2024 and was published as open access in October 2024 (Batteries & Supercaps 2024, e202400610) and is distributed under the terms of the Creative Commons Attribution 4.0 International. (CC BY 4.0, `https://creativecommons.org/licenses/by/4.0/`).[164]

DOI: 10.1002/batt.202400610

A deeper study of the morphology during the stripping and plating of aluminium was conducted in the subsequent EC-RAS study. Here, HOPG was used as substrate because it is a potential alternative to aluminium as an anode material in RABs, and the optical contrast between the HOPG substrate and the deposited Al is high, allowing for a more detailed study of the morphology of the deposit. The investigations show that the morphology of electrodeposited Al is highly dependent on the applied potential, with Al-island forming at less cathodic potentials, increasing the surface roughness. On the contrary, a smooth and compact Al layer is deposited during electrodeposition at the high cathodic potential. Further on, the intercalation of $AlCl_4^-$ above 1.8 V (vs. Al pseudo-reference) into the graphite was studied, resulting in the irreversible swelling of the top-most graphite layer as well as the formation of an SEI on top of the graphite.

Check for updates

Batteries & Supercaps

Research Article
doi.org/10.1002/batt.202400610

Chemistry Europe
European Chemical Societies Publishing

www.batteries-supercaps.org

Operando Investigation of Al Plating Regimes on HOPG in [EMImCl]:$AlCl_3$ by Electrochemical Reflection Anisotropy Spectroscopy

Mario Löw*[a] and Matthias M. May[a, b]

Rechargeable aluminium batteries show promise as next-generation systems with a more abundant material base than lithium technology. However, the stable native oxide on top of aluminium metal electrodes leads to poor cell performance. Graphite, on the other hand, is a so far rarely investigated alternative that can be used as both the anode and cathode. Here, metallic aluminium is deposited at the anode, while $AlCl_4^-$ is intercalated at the cathode. For both cases, understanding the electrode–electrolyte interface is crucial for improving the performance of the battery. In this work, we use reflection anisotropy spectroscopy to study the evolution of the interface under applied potentials. We find that the cathode exhibits an irreversible swelling of the topmost graphite layer due to $AlCl_4^-$ intercalation as well as the formation of an SEI during the first voltammetry cycle. On the anode, the electrodeposition of aluminium is initially well-ordered. However, the evolution of the surface morphology depends on the applied potential, with island-like growth at less cathodic potentials, and layer-by-layer growth at more anodic potentials. With the optical *operando* spectroscopy, we can follow these qualitatively different plating and stripping regimes in a time-resolved manner.

Introduction

Rechargeable aluminium batteries (RABs) are a promising material system for the battery market.[1] Their advantages are the inexpensive, abundant, and recyclable aluminium as well as its high theoretical volumetric capacity of 8046 Ah L^{-1},[2] which is four times higher compared to the volumetric capacity of lithium (2062 Ah L^{-1}).[3] Furthermore, its electronegativity is higher compared to other metals used as anode material. This suggests less reactivity and higher safety, meaning it can in principle be handled even when exposed to humid air.[3] However, aluminium metal electrodes face the drawback of being covered with a native oxide layer consisting of the ion- and electron-blocking Al_2O_3.[4] While the oxide layer can enhance the stability of the electrode/electrolyte interface and prevent dendrite formation,[5] it might also impede the plating and stripping of aluminium in non-corrosive and non-acidic electrolytes without $AlCl_3$.[6]

This combination of potential benefits with many remaining challenges for the RAB technology has resulted in significantly increased interest in these systems over the last few years. This includes the development of organic red-ox molecules as cathode material[7] or $AlCl_3$-free electrolytes.[8] Further works targeted aluminium-sulphur,[9] aluminium-selenium[10] and aluminium-air batteries,[11] including aqueous systems.[12]

A promising, but rarely investigated alternative anode material is graphite. Its advantages are its low cost, high electrical conductivity, low density, and high-temperature resistance. A previous investigation showed that stripping and plating of aluminium from $AlCl_3$:BMImCl 2:1 onto expanded graphite is possible with high reversibility. The authors showed that the aluminium can be plated with an overpotential of only −80 mV. In addition, the plating-stripping charge efficiency was 84%, close to the value they obtained for an aluminium metal anode.[13] A further advantage of graphite for RABs is that it can simultaneously be used as an anode and cathode. This is the case since it works with two distinct mechanisms, depending on the polarisation of the electrode. On the cathode side, ions are intercalated/deintercalated into the host lattice. On the anode side, aluminium is stripped and plated onto the graphite. Such a mode of operation also does not require the anode or the cathode to contain Al in the first place. It only needs a material that is an efficient current collector on the anode side and good intercalation material on the cathode side.

Such a kind of battery has already been experimentally demonstrated.[14,15] In these studies, conductive graphite paper was used as the anode and cathode and EMImCl:$AlCl_3$ as the electrolyte. Due to the high ionic conductivity of the electrolyte, this battery shows a reasonable rate and cycle performance of up to 1000 cycles. The initial discharge capacity is around 70 mA h g^{-1} at a current density of 200 mA g^{-1}. The battery also provides a discharge voltage of 2.1 V (vs. Al^{3+}/Al). However, the drawback of this kind of battery is strong self-discharge, with

[a] M. Löw, M. M. May
Institute of Theoretical Chemistry, Universität Ulm, Lise-Meitner-Str. 16, 89081 Ulm, Germany
E-mail: mario.loew@uni-ulm.de

[b] M. M. May
Institute of Physical and Theoretical Chemistry, Universität Tübingen, Auf der Morgenstelle 15, 72076 Tübingen, Germany

Supporting information for this article is available on the WWW under https://doi.org/10.1002/batt.202400610

© 2024 The Author(s). Batteries & Supercaps published by Wiley-VCH GmbH. This is an open access article under the terms of the Creative Commons Attribution License, which permits use, distribution and reproduction in any medium, provided the original work is properly cited.

© 2024 The Author(s). Batteries & Supercaps published by Wiley-VCH GmbH

16.82 %/h in the mentioned publication. Such a system is called a rechargeable dual-carbon battery (RDCB) and the principle is also known for lithium and sodium.[16,17]

Both the cathode as well as the anode have already been investigated before. However, on the cathode side, the focus was the intercalation of the $AlCl_4^-$ into the graphite host.[18] Computational studies show that the intercalation of $AlCl_4^-$ into graphite is a four-step process and that, due to the tetrahedral form of the $AlCl_4^-$, the graphite layers get distorted.[19] The cathode–electrolyte interface has, despite carbon also being used in Al-carbon batteries,[20] only been investigated by Canever et al.[21] The authors discovered that an interfacial layer is formed on the cathode in the first cycle, where the electrolyte decomposes at potentials lower than 2.45 V. The cause for this layer are defects in the graphite and heteroatomic functional groups on the surface of the graphite.

For the anode, the stripping and plating of aluminium from ionic liquids such as [EMImCl]:$AlCl_3$ have been investigated in numerous studies, however mostly with metallic aluminium as substrate.[22–26] The electrodeposition at the anode involves the $Al_2Cl_7^-$ species, which can only be found in the electrolyte if the molar ratio of [EMImCl] and $AlCl_3$ is between 1:1 and 1:2.[27] The electrodeposition mechanism of Al is governed by kinetics with diffusion control at the early stages. Thereby, the activation barrier and the standard equilibrium potential of the (de)chlorination reaction are the most important criteria for the electrodeposition of aluminium.[22] In addition, the Al deposition is a multiple-step process, with either a chemical step ($AlCl_3^- \rightarrow AlCl_2 + Cl^-$) or an electron transfer ($Al^{2+} + e^- \rightarrow Al^+$) being the rate-determining step.[24] Further, the addition of 1,10-phenanthroline anhydrate (OP) to the [EMImCl]:$AlCl_3$ leads to smoother Al deposition.[25]

The highly-oriented pyrolytic graphite (HOPG), that we used in our investigation, has already been studied for the electrodeposition of several metals. This is because electrochemical metal deposition represents a suitable and straightforward approach for local surface structuring and modification and allows the preparation of a surface for the investigation of potential catalysts.[28] Work on Pt showed that the morphology of the deposited Pt nano-particles depends strongly on the applied potential and the current density.[29,30] Further studies were also conducted with Ag,[31] Hg[32] and Pd.[33]

For battery anode materials, there is a large number of *operando*, time-resolved investigations on electrodeposition, investigating potential dendrite formation with a focus on Li.[34] Understanding the evolution of the surface morphology with applied anodic potentials is a crucial step for detecting potential dendrite growth. A smooth surface is less likely to cause short circuits inside the battery. Recent studies on the morphology of Mg electrodeposition show that its morphology is highly dependent on the used electrolyte. The Grignard electrolyte MeMgCl shows unidirectional growth and mossy deposition. $Mg[B(HFIP)_4]_2$, on the other hand, did not show the formation of dendrites, yet the deposition was not smooth, either.[35] An investigation by She et al.[36] on the electrodeposition of aluminium with in situ optical microscopy and transmission electron microscopy showed that the shape of dendritic Al deposits changes as a function of the current density. The deposits have a sharp tip shape at low current densities, while they have a spherical shape at high current densities. This change in morphology is due to the influence of the (local) current density on the movement of ions. When the current density is low, ions move slowly, creating a significant concentration gradient near the tip of dendritic Al. However, ions move more quickly at higher current densities, forming dendritic Al due to increased charge aggregation. A study by Ding et al.[37] showed that high shear modulus metals can form globular dendrites – spherically deposited metal – which can penetrate the separator and cause a short circuit.

Despite numerous research on the electrodeposition of metals on HOPG, results on Al are rare. Tu et al. investigated the electrodeposition of Al on graphite from $AlCl_3^-$ 1-butyl-3-methyl-imidazolium chloride ($AlCl_3^-$[Bmim]Cl).[38] They discovered that the morphology of the deposited Al is dependent on the applied current density with coarse deposits at low current density and a more smooth surface at high current density. In addition, the increase in the current density leads to a decrease in the grain size of the deposited Al. The authors also investigated the crystallographic orientation and discovered that the X-ray diffraction peak intensity of the (200)-plane increases with increasing current density, while it decreases for the (111)-plane. This means that the current density has a significant influence on the crystallographic orientation of the deposited aluminium.[38] Analysis of the electrodeposition was, however, mostly based on ex situ methods or with the mathematical model by Scharifker and Hills.[39]

Operando spectroscopy, on the other hand, is typically preferable for electrochemical systems as it can ideally deliver time-resolved information on the involved processes as a function of the applied potential.[40] For this investigation, we use reflection anisotropy spectroscopy (RAS) as an optical, time-resolved probe of the interfacial structure. RAS is a non-destructive optical light probe that investigates changes on the surface related to surface chemistry, such as adsorption deposition or surface reconstruction, with a near-normal incidence reflection set-up.[41] In previous studies, RAS has already been used for controlling the growth during metal-organic vapour deposition (MOCVD),[42] surface etching and plating and stripping on aluminium[43] and for controlling the layer-by-layer etching of multilayered semiconductors.[44] Though so far rarely used in the battery field, RAS has the potential to provide insight into SEI formation, metal stripping/plating, as well as ion transport processes combining very high interface sensitivity with suitable time resolution. In order to measure RAS, linearly polarized light impinges at near-normal incidence on a single-crystalline surface. Then, the difference in reflectivity (Δr) with respect to the orthogonal directions in the surface plane (x, y) is normalized to the mean reflectivity, r.[41] The surface's optical anisotropy is then defined as follows:

$$\mathrm{RAS} := \Re\left(\frac{\Delta r}{r}\right) = 2 \cdot \frac{r_x - r_y}{r_x + r_y};\ r \in \mathbb{C} \tag{1}$$

© 2024 The Author(s). Batteries & Supercaps published by Wiley-VCH GmbH

25666223, 2025, 5, Downloaded from https://chemistry-europe.onlinelibrary.wiley.com/doi/10.1002/batt.202400610 by Helmholtz-Zentrum Dresden Rossi, Wiley Online Library on [26/03/2026]. See the Terms and Conditions (https://onlinelibrary.wiley.com/terms-and-conditions) on Wiley Online Library for rules of use; OA articles are governed by the applicable Creative Commons License

Research Article
doi.org/10.1002/batt.202400610
Chemistry Europe
European Chemical Societies Publishing

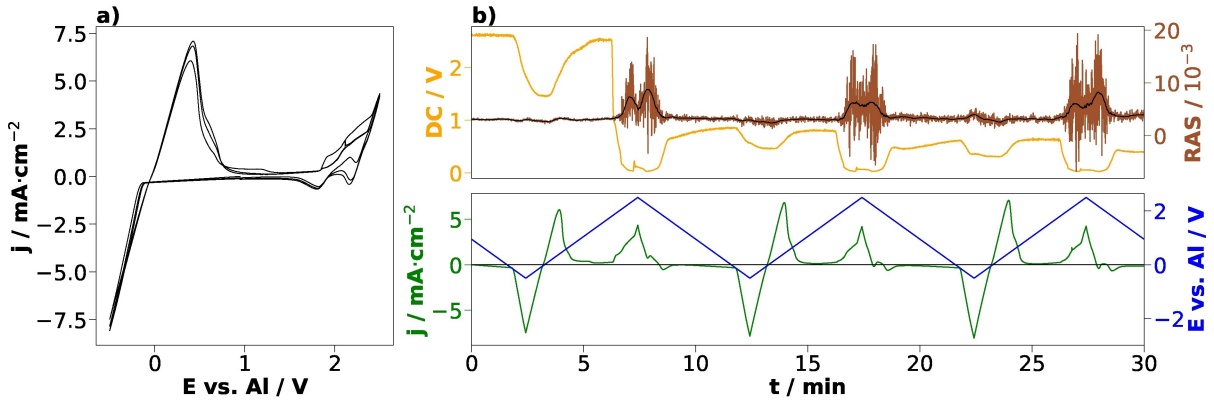

Figure 1. Optical signal during cycling in the full potential window and cyclic voltammogram. a) CV between −0.5 and 2.5 V (vs. Al pseudo-reference), starting form open circuit voltage (OCV) (0.9 V) towards the negative terminus at a scan speed of 10 mV s^{-1} for 3 cycles. b) Upper part: DC signal and transient at 1.5 eV photon energy. The black curve corresponds to the Savitzky–Golay-filtered transient. Lower part: Voltage and current density of the CV in a) plotted against time.

Due to light's penetration depth, both the surface and the bulk contribute to the signal. However, the highly-oriented pyrolytic graphite crystal employed here has the surface orientation (0001), meaning that it is optically isotropic; therefore, only changes on top of the surface contribute to the signal.

In this study, we investigate two different aspects of a dual-graphite battery, namely the interface of the cathode during the interaction of $AlCl_4^-$ into graphite and the electrodeposition of aluminium onto HOPG. To this end, we used one of the most common electrolytes for rechargeable Al batteries, [EMIm-Cl]:$AlCl_3$ (1:1.5). Both intercalation and electrodeposition were first investigated time-dependently with RAS during cyclic voltammetry (CV). Later, the electrodeposition of Al was investigated in depth by chronoamperometry (CA) and chronocoulometry (CC) measurements. The hereby electrodeposited Al is additionally investigated with scanning electron microscopy (SEM) and energy-dispersive X-ray spectroscopy (EDX) for a detailed understanding of the surface morphology. This allows us to observe an irreversible swelling of the topmost graphite layer as well as the formation of an SEI during the intercalation of $AlCl_4^-$ into the graphite structure. Furthermore, we find that the deposition mechanism of Al on HOPG depends on the applied potential and has an ordered nucleation step at the beginning, while the microscopic stripping process depends on the prior plating mechanism.

Results and Discussion

The following section is separated into two parts. In the first one, we investigate the surface during the intercalation of $AlCl_4^-$ into the layers of the HOPG. In the second part, we investigate the stripping and plating of metallic aluminium on top of the HOPG surface.

Intercalation and Deintercalation

Figure 1a shows the CV of HOPG in contact with EMImCl:$AlCl_3$. The CV can be divided into two parts, which represent two different processes. The first part is the stripping and plating of aluminium; this can be found below 1.5 V (vs. Al pseudo-reference). The plating of aluminium is the cathodic process observed below 0 V, while stripping of aluminium is the anodic process above 0 V. The second process is the intercalation and de-intercalation of $AlCl_4^-$ into the layers of the HOPG, occurring above 1.5 V.

Figure 1b shows a transient, which is the time-resolved optical signal at fixed photon energy, in this case recorded at 1.5 eV in parallel to the CV in Figure 1a. The DC signal, proportional to the reflectance, is shown in orange. It shows a decrease in reflectance while plating of aluminium and intercalation of $AlCl_4^-$. The most prominent decrease in reflectivity occurs the first time the potential surpasses 1.8 V. Here, we observe a substantial reduction in reflectance, which subsequently stays significantly below its initial value. This might be caused by the swelling of the topmost layer of graphite due to intercalation of $AlCl_4^-$. An expansion of the natural graphite due to $AlCl_4^-$ intercalation has already been investigated before.[20] Since the reflectance does not return to its original value, it is a clear indicator that this swelling or solid-electrolyte interphase (SEI) formation is irreversible. The following two cycles, in which the voltage surpasses 1.8 V, also show a reduction in reflectance. This time, it is less significant and returns almost to the initial value. This indicates that subsequent intercalation after the first irreversible swelling/SEI formation also changes the surface of the HOPG, either by reversible swelling or adsorption of the solvation shell of the intercalated ions.

The brown curve in Figure 1b shows the RA signal, a measure for the optical anisotropy of the surface, which shows a change in the anisotropy during the intercalation process around the maximum of the associated anodic current. The changes in the RA signal could in principle also arise from the

© 2024 The Author(s). Batteries & Supercaps published by Wiley-VCH GmbH

25666223, 2025, 5, Downloaded from https://chemistry-europe.onlinelibrary.wiley.com/doi/10.1002/batt.202400610 by Helmholtz-Zentrum Dresden Rossi, Wiley Online Library on [26/03/2026]. See the Terms and Conditions (https://onlinelibrary.wiley.com/terms-and-conditions) on Wiley Online Library for rules of use; OA articles are governed by the applicable Creative Commons License

Research Article
doi.org/10.1002/batt.202400610
Chemistry Europe
European Chemical Societies Publishing

relatively low DC signal. However, applying the Savitzky-Golay-Filter to the data shows that two distinct positive peaks arise in all three intercalation steps, with the local minimum located at the turning point of the CV. This suggests that during intercalation of $AlCl_4^-$, an anisotropy is imposed on the interface between HOPG and electrolyte or in the arrangement of the $AlCl_4^-$ underneath the first graphene layer. Theoretical calculations indicate that the bridge 2 position, where Al-anions occupy the bridging position between two non-bonded carbon atoms and the four Cl-atoms nearly occupy the center of the hexagon (C6), is the thermodynamically most stable position.[19] This suggests that most of the intercalated $AlCl_4^-$ went to this position. However, the other possible positions are also favourable, due to their energetic difference between of below 0.02 eV.[19] This could explain the dip in the optical anisotropy at the maximum anodic potential, where sites associated with anisotropy are occupied first and cleared last. Another possible explanation could be an ordered adsorption of $AlCl_4^-$ or its solvation shell on top of the graphite.[21]

Since the anodic current peak above 1.8 V could in principle be either caused by intercalation or graphite oxidation,[20] we performed the same experiment with a glassy carbon electrode, to test our hypothesis. The CV of the glassy carbon still shows the stripping and plating peaks; however, above 1.8 V, no anodic waves are to be found (see SI Figure S1). This suggests that indeed, intercalation takes place above 1.8 V (vs. Al pseudo-reference).

For a more detailed investigation of the surface during intercalation, the HOPG sample was investigated with SEM/EDX after the three intercalation cycles stopped at open-circuit voltage (OCV). The SEM image shows a mosaic-like structure on the surface. Further analysis with EDX shows that this mosaic structure contains carbon, chloride, aluminium, and oxygen species. These either originate from a potential decomposition of the electrolyte or from molecular adsorption on the surface. A similar surface film was also observed by Canever et al.[21] The authors claim that this surface film stems from the decomposition of the electrolyte, which can happen already below 2.5 V, depending on the type of carbon used. However, they also claim that this surface film is more likely to form on carbon surfaces with a high number of defects.[21] HOPG, however, has a quite low number of defects. Similar phenomena are also already known from dual-ion lithium batteries.[45] A mosaically structured SEI on carbon is also detected on the graphite anodes in lithium ion batteries.[46]

For comparison, we cycled only until 1.5 V (vs. Al pseudo-reference) and investigated the resulting surface by means of SEM/EDX. The results are shown in Figure S4 in the SI. To avoid destruction of a potential SEI layer on top of the sample, we did not rinse it with THF (Tetrahydrofuran), as we did for all other samples. This, however, leads to residuals of the electrolyte being present on the surface. Yet still, no SEI can be observed on the surface.

From these results, we can summarize that both, intercalation of $AlCl_4^-$ into graphite, and the irreversible formation of a surface layer are also associated with a distinct optical signature. The strong decrease in reflectance could, therefore, be caused by the irreversible swelling of the graphite layer due to $AlCl_4^-$ intercalation and the irreversible formation of a surface film on top due to a chemical reaction between the carbon and the electrolyte. The ex situ SEM/EDX investigation shows that this layer is stable outside the electrolyte and cannot be removed by washing the electrode in THF. The reduction in reflectance in the following two cycles might be caused by reversible adsorption on top of an already-formed surface layer or reversible intercalation since here, the reflectance returns to its original value. The anisotropy can be caused both by the ordered adsorption of $AlCl_4^-$ (or the remainder of its solvation shell) on top of the surface or by its ordered intercalation. The swelling of the graphite structure and the SEI formation can actually be beneficial for the battery since the literature shows that the swelling of the graphite causes partially turbostratic structures and gradually forms new defects inside the graphite, resulting in the gradual increase of the capacity.[47] The formation of an SEI on the graphite does, on the other hand, lead to a decrease in specific capacity after the first cycle and a simultaneous increase of the coulombic efficiency between the first and the second cycle.[21]

It should be noted that due to our cell set-up, only the topmost layer is in contact with the electrolyte, meaning $AlCl_4^-$ intercalation is only possible through defects in this layer. However, the same experiment with glassy carbon does not show any features in the CV, meaning that no intercalation or (electro)chemical reaction takes place. This could also mean that the formation of the irreversible surface layer requires the intercalation of $AlCl_4^-$ into the graphite.

Stripping and Plating

We now turn to the stripping and plating of aluminium onto HOPG. To this end, we electrochemically cycled the HOPG between −0.5 V and 1.5 V, starting from OCV (1.6 V) towards the negative terminus, with a scan rate of 10 mV s^{-1} for ten cycles, while a transient with a photon energy of 1.5 eV was recorded. The results are shown in Figure 2.

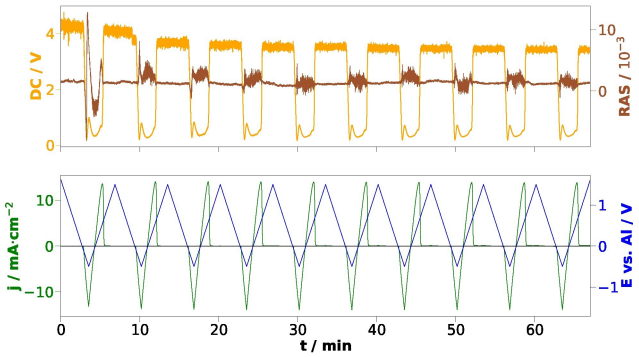

Figure 2. Optical signal during cycling in stripping and plating potential window and cyclic voltammogram. Upper part: DC signal and transients at 1.5 eV photon energy. Lower part: CV between −0.5 and 1.5 V (vs. Al pseudo-reference), starting from OCV (1.6 V) towards the negative terminus, with a scan rate of 10 mV s^{-1} for ten cycles.

© 2024 The Author(s). Batteries & Supercaps published by Wiley-VCH GmbH

25666223, 2025, 5, Downloaded from https://chemistry-europe.onlinelibrary.wiley.com/doi/10.1002/batt.202400610 by Helmholtz-Zentrum Dresden Rossi, Wiley Online Library on [26/03/2026]. See the Terms and Conditions (https://onlinelibrary.wiley.com/terms-and-conditions) on Wiley Online Library for rules of use; OA articles are governed by the applicable Creative Commons License

Research Article
doi.org/10.1002/batt.202400610
Chemistry Europe
European Chemical Societies Publishing

The reflectance (orange curve) shows a similar behaviour as the previous measurement. It decreases upon plating aluminium and increases upon stripping. An interesting observation is a small peak during the plating process, in which the reflectance shortly increases and then decreases again. This peak always occurs at the negative terminus of −0.5 V (vs. Al pseudo-reference), in all of the ten CV cycles. This could indicate a change in how the aluminium is plated. The anisotropy (brown curve) strongly changes in the first cycle. Here, the anisotropy first decreases when the potential is below 0.2 V. During this change, a change in signs from positive to negative occurs. Further, the anisotropy increases again back to positive values; this happens simultaneously with the slight dip observed in the reflectance spectrum. During stripping, the anisotropy has a slight dip in positive direction before it returns to its initial value. This indicates an ordered deposition of the aluminium, taking place over three stages before the aluminium is stripped off again. Changes in the anisotropy also happen in the subsequent cycles; however, there, the changes are much smaller and less pronounced. A potential reason for this might be a decay of the topmost surface layer in contact with the electrolyte, also indicated by the slight decay of the plateau in the reflectance signal with continuous cycling.

For a more detailed view on this presumably ordered nucleation, a chronoamperometry (CA) measurement was performed. For that, the potential was set from OCV towards −0.5 V (vs. Al pseudo-reference) and held for 15 s. Afterwards, the potential was switched back to OCV again. During the whole time, a transient at a photon energy of 1.5 eV was recorded. The results can be seen in Figure 3a.

We observe that upon switching the potential from OCV to 0.5 V, the reflectance and the anisotropy follow instantaneously. In addition, there is a small peak at around 40 s for both, the anisotropy and the reflectance. This might originate from a change in the deposition mechanism of Al, but further investigations are needed to confirm this.

After going back to OCV, the anisotropy and the reflectance stay constant. Figure S5 (Supporting Information) shows RA-spectra of the clean HOPG sample as well as after the Al deposition, both outside of the electrolyte. The spectrum after the deposition is shifted downwards compared to the one with HOPG. In the area between 1.5 eV and 3.0 eV, the downward shift is more pronounced than for the rest of the spectra. This experiment also shows that the deposited Al is stable outside the electrolyte and its surface morphology can be investigated further with ex situ SEM.

Figure 3b and 3c displays an SEM image of the HOPG surface after Al deposition. It shows well-defined, isolated Al-particles spread across the whole surface. The higher magnification in b shows that the particles have a size of around 200–300 nm. Additionally, some of the particles have a triangular shape with flattened corners. The triangular – or, more precisely, truncated octahedral – shape from the top-view of the face-centered cubic (fcc) crystal lattice suggests crystalline nucleation with a predominantly (111) surface,[48,49] an ordering which is detectable by RAS. However, for a precise statement, it should be noted that the triangular-shaped particles also need to have a preferential orientation to contribute to the RAS signal. While initial inspection suggests that there is indeed a preferential orientation of the particles on the graphite substrate, a more quantitative analysis will have to be left to future work. Randomly oriented particles would average out over the optical measurement area of RAS (several mm^2) and would therefore not contribute to the optical anisotropy.

Finding that the initial step of the deposition of aluminium on HOPG at −0.5 V is at least partially ordered, we are now investigating the influence of the different applied potentials on the deposition mechanism. To this end, a series of CA

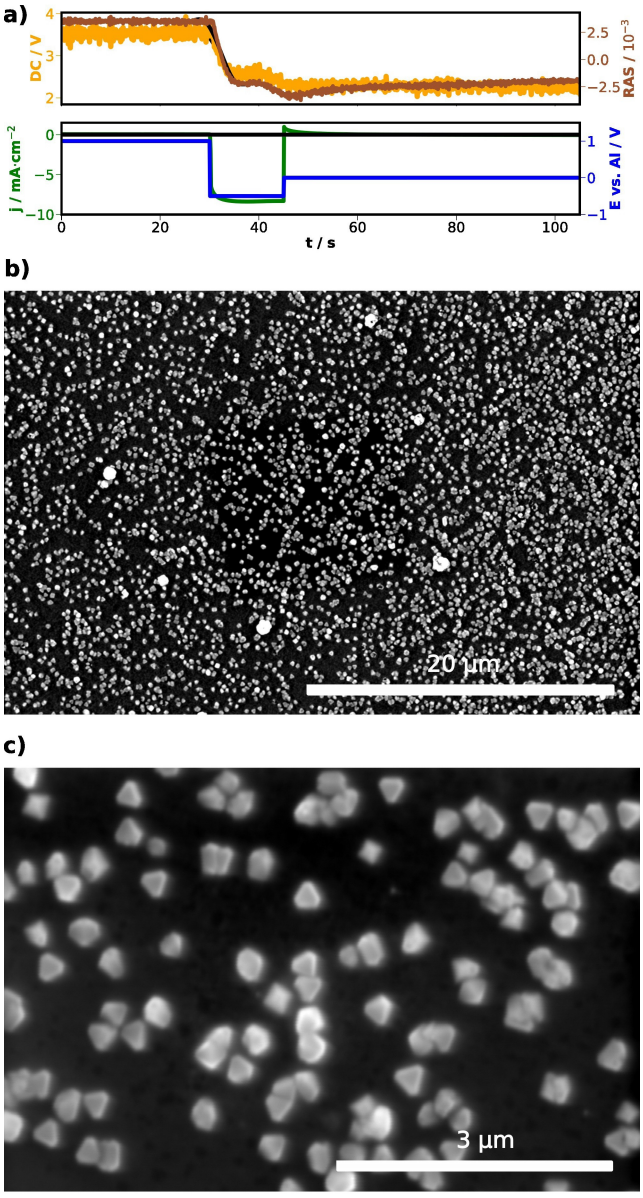

Figure 3. Optical signal during electrodeposition of Al at −0.5 V and ex situ SEM afterwards. a) Upper part: DC and RA transients at 1.5 eV photon energy. Lower part: CA OCV (30 s)→−0.5 V (vs. Al pseudo-reference) (15 s)→OCV. The black curve corresponds to the Savitzky–Golay-filtered transient. SEM of the HOPG sample after Al deposition at b) 5,000x magnification and c) 30,000× magnification.

© 2024 The Author(s). Batteries & Supercaps published by Wiley-VCH GmbH

25666223, 2025, 5, Downloaded from https://chemistry-europe.onlinelibrary.wiley.com/doi/10.1002/batt.202400610 by Helmholtz-Zentrum Dresden Rossi, Wiley Online Library on [26/03/2026]. See the Terms and Conditions (https://onlinelibrary.wiley.com/terms-and-conditions) on Wiley Online Library for rules of use; OA articles are governed by the applicable Creative Commons License

Research Article
doi.org/10.1002/batt.202400610

measurements are performed. In this experimental series, the potential is first held at OCV for 60 s, then a cathodic potential is set for 60 s to observe the plating, followed by another OCV set for 60 s. For the stripping, the potential is set to 0.5 V (vs. Al pseudo-reference) for 90 s to ensure that all the plated Al is removed again from the surface. Finally, a last OCV step for 30 s is done. The cathodic potentials are −0.05 V, −0.075 V, −0.1 V, −0.15 V, −0.2 V, −0.3 V, −0.4 V, and −0.5 V, respectively. The measurements were all done in series, starting from the least to the most cathodic potential. During the CA measurements, anisotropy and reflectance transients were recorded at 1.5 eV. The results are displayed in Figure 4.

Figure 4d shows the DC-signal. Here, we observe three qualitatively different regimes, depending on the applied potential. At the less cathodic potentials (−0.05 V to −0.15 V), the reflectance decreases gradually after the potential is set to the desired voltage and the rate of decreasing reflectance increases with more cathodic potentials. It stays constant during the OCV phase and then increases again back to the initial value when applying the anodic voltage of 0.5 V. For the more cathodic potentials of −0.2 V and −0.3 V, there is an initial dip in the reflectance shortly after setting the potential. After the dip, it stays rather constant before there is again a dip when setting to +0.5 V. These dips are more pronounced for −0.3 V than for −0.2 V, but the reflectance recovers towards the end of the anodic potential step. For −0.4 V and −0.5 V, there is also a slight dip at the beginning, which is, however, less pronounced than for the previous two potentials. After this dip, the reflectance, however, increases and reaches values above the initial value at OCV. When setting the potential to 0.5 V, the reflectance decreases back to its original value, but also in a stepwise fashion with a small dip before reaching the plateau.

Under the assumption, that the reflectance decreases with increased (micro)roughness and vice versa, one can now derive different plating and stripping regimes. For the low cathodic potentials and associated low current densities, surface roughness increases during plating and decreases during stripping, which is in line with Tu et al.[38] This changes qualitatively for intermediate cathodic potentials (plating currents), where an initial phase of increasing roughness (especially for −0.3 V) is followed by a plating regime that then reduces surface roughness, for instance by plating a continuous film over coarse nucleation particles. The reverse is then observed for stripping, where roughness in an initial phase increases again. For the higher current densities then, the initial dip in reflectance again shows the nucleation phase, which is quickly followed a plating regime leading to a significantly enhanced reflectance, which one would expect for a flat, compact Al layer on top of the HOPG.

For the anisotropy (Figure 4c), there is almost no change for the less cathodic potentials of −0.05 V, −0.075 V, and −0.1 V, with only a shallow dip for the latter two potentials. Beyond −0.15 V, however, a pronounced negative anisotropy develops, which is very broad for −0.15 V and becomes more steep and narrow with increasing cathodic potential. After this initial peak, the anisotropy increases again and stays almost constant also during the OCV phase. During the stripping of the aluminium, there are narrow peaks between −0.15 and −0.3 V, a broad and late peak for −0.4 V and finally a very shallow and late peak for the sample plated with −0.5 V. This behaviour again suggests that for high plating current densities, a well-ordered nucleation phase exists, which is less ordered/pronounced at potentials less cathodic than −0.2 V. Though stripped at the same potential, these different plating regimes also translate to different behaviour in the stripping and, as for intermediate potentials, distinct negative peaks in the anisotropy can be observed. This suggests a qualitatively different microstructure

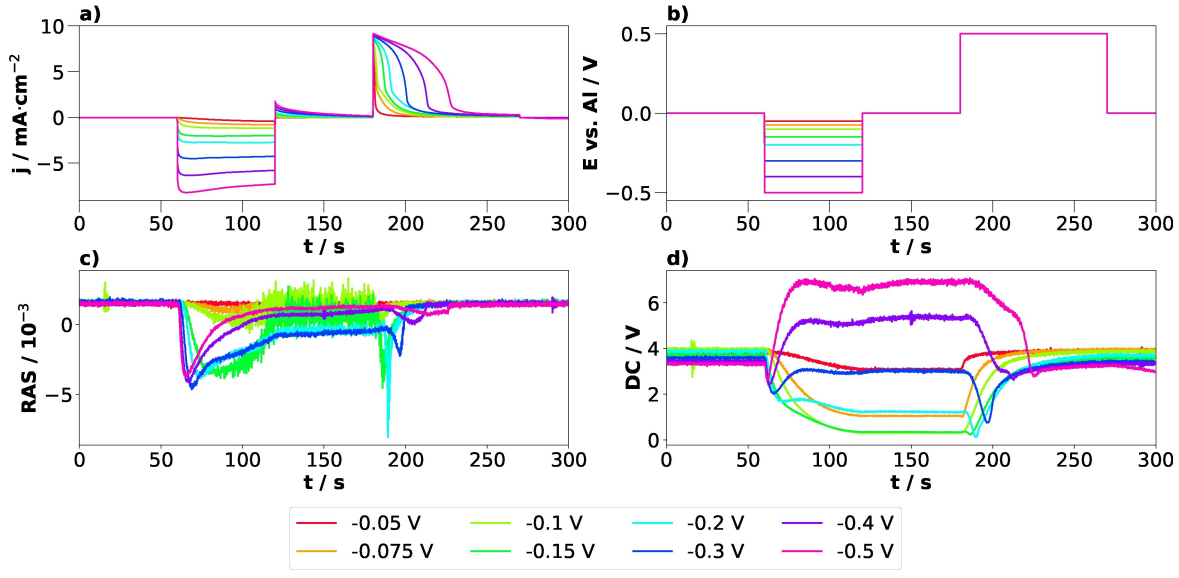

Figure 4. Aluminium deposition at different potentials (vs. Al pseudo-reference) as indicated by the colour code: a) current over time, b) voltage over time, c) RAS over time, d) DC over time. The results of one specific potential were recorded simultaneously. All potentials were recorded in series, starting from the least cathodic potential.

© 2024 The Author(s). Batteries & Supercaps published by Wiley-VCH GmbH

25666223, 2025, 5, Downloaded from https://chemistry-europe.onlinelibrary.wiley.com/doi/10.1002/batt.202400610 by Helmholtz-Zentrum Dresden Rossi, Wiley Online Library on [26/03/2026]. See the Terms and Conditions (https://onlinelibrary.wiley.com/terms-and-conditions) on Wiley Online Library for rules of use; OA articles are governed by the applicable Creative Commons License

Research Article
doi.org/10.1002/batt.202400610
Chemistry Europe
European Chemical Societies Publishing

of the plated Al even in the plating regime at −0.4 V, where already a compact layer with increased reflectance is observed.

The different shapes of the reflectance and anisotropy spectra during aluminium plating and stripping strongly hint at qualitatively different plating and stripping mechanisms for different potentials. For an evaluation of the resulting macroscopic surface morphology, SEM/EDX measurements were performed at two distinct potentials, namely −0.1 V and −0.5 V (Figures 5 and 6). These two potentials were chosen because of their opposite features regarding anisotropy and reflectance. While for −0.1 V, there is a decrease in reflectance during plating and almost no anisotropy peak, −0.5 V shows an increase in reflectance while plating and a pronounced anisotropy peak at the beginning of Al deposition. For a better comparability, the same charge (250 mC) was deposited for both potentials.

Figure 5 shows the SEM/EDX image of the deposition of 250 mC at −0.1 V (23 min deposition time). The SEM image in part a) shows that tiny particles are distributed equally over the surface. In addition, there are also cauliflower-like bigger particles, which lock like agglomerates of the smaller particles. The EDX mapping in Figure 5c confirms that the particles are indeed the deposited Al. The corresponding CC and transient diagram to this measurement can be found in the Supporting Information in Figure S6.

The SEM/EDX images of the Al deposition at −0.5 V (250 mC) (113 s deposition time) can be found in Figure 6. In contrast to the less cathodic potential, the SEM image in part a) now shows that the whole surface is more or less homogeneous, except for some tiny particles. The EDX analysis in parts b) to e) shows that the entire surface is covered with aluminium, which dampens the carbon signal. The corresponding CC and transient measurements are displayed in the Supporting Information in Figure S7.

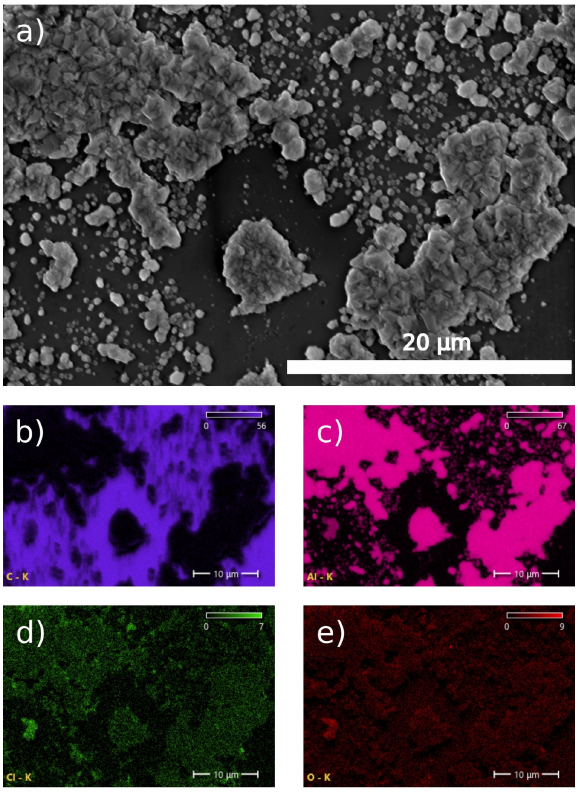

Figure 5. a) SEM images of the HOPG sample after deposition of Al 250 mC at −0.1 V (vs. Al pseudo-reference). EDX maps of b) carbon, c) aluminium, d) chloride, e) oxygen.

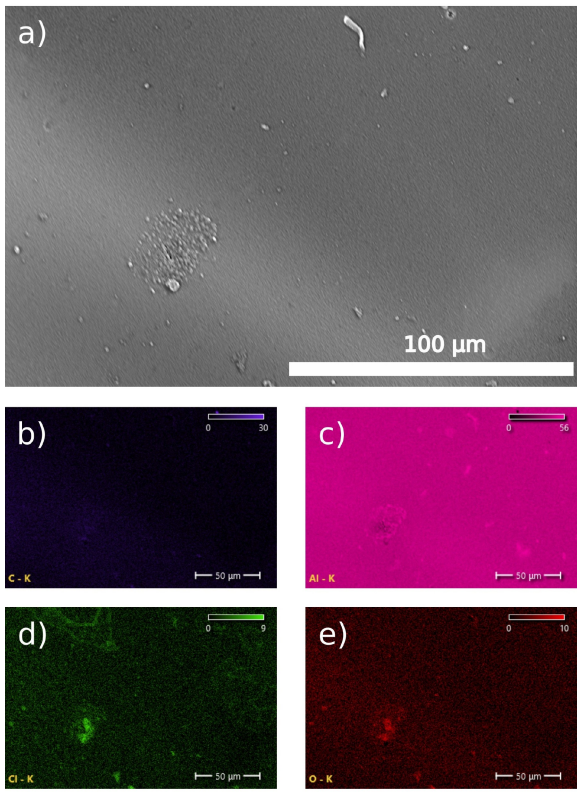

Figure 6. a) SEM images of the HOPG sample after deposition of Al 250 mC at −0.5 V (vs. Al pseudo-reference) EDX map of b) carbon, c) aluminium, d) chloride, e) oxygen.

Evaluating the results of anisotropy and reflectance during Al plating and the ex situ SEM/EDX images, we can now develop a more detailed hypothesis on the involved mechanism. A Volmer-Weber like growth (island growth) predominates at less cathodic potentials (−0.1 V), corroborated by the SEM image showing separate smaller and larger particles on the surface and the decreased reflectivity – increased roughness – during plating. For the more cathodic potentials (−0.5 V), however, Frank-van-der-Merwe like growth (layer-by-layer growth) after a short nucleation stage appears to dominate. This leads to the complete coverage of the HOPG surface with a dense, smooth and therefore optically lustrous Al layer. The optical anisotropy during plating suggests that the initial plating regime at high current densities involves a higher degree of ordering, i.e. well-defined nucleation as shown in Figure 3b, on the surface. This increases the roughness, which in turn leads to a decrease in reflectance. With further charge transferred, the particles – their shape suggests a close-packed (111) surface – start to merge, creating the dense Al layer.

© 2024 The Author(s). Batteries & Supercaps published by Wiley-VCH GmbH

25666223, 2025, 5, Downloaded from https://chemistry-europe.onlinelibrary.wiley.com/doi/10.1002/batt.202400610 by Helmholtz-Zentrum Dresden Rossi, Wiley Online Library on [26/03/2026]. See the Terms and Conditions (https://onlinelibrary.wiley.com/terms-and-conditions) on Wiley Online Library for rules of use; OA articles are governed by the applicable Creative Commons License

Investigations by Tu et al.[38] came to a similar conclusion for the electrodeposition of Al on graphite. The authors discovered that at low current density (16 mA cm^{-2}), the deposited Al becomes coarser, and the particles grow together and agglomerate. At the low current densities, the growth rate of nuclei is higher than the rate of new nuclei formation, leading to a coarse deposition.[38,50] However, with increasing current density, there is a faster formation rate of new nuclei as compared with the growth rate of that, leading to fine-grained deposited particles.[38,51] This leads to a uniform deposition and relatively smooth surface at high current density (32 and 57 mA cm^{-2}).[38] From their findings, the authors proposed a potential mechanism for the Al deposition. This mechanism includes three steps. In the first step, a thin, compact Al layer is deposited on the electrode. In the second step, dendrites attach to the thin, compact layer. At high current density, fine-grained particles lead to high aluminium particle density. In contrast, at low current density, the coarse-grained particles result in a relatively high deformation. This makes it more likely for the foils to form dendrites. As a final step, the dendrites start to grow. Thereby, the growing particles fill up the interstices between the dendrites. This means that the fine-grained morphology at high current density is prone to form compact layers.[38] This mechanism could explain why we see a compact Al layer at a higher cathodic potential (high current density) compared to a lower cathodic potential (low current density). However, we do not observe a film of Al on the surface at low potentials, at which the dendrites start to grow. One potential reason why we do not see a dense film of Al at less cathodic potential is that they used graphite while we used HOPG. This means that they start from surface with higher roughness and, therefore, more potential nucleation spots compared to our HOPG. Another reason could be the different electrolytes: While their study emmployed [Bmim]Cl, we used [EMImCl]$AlCl_3$. The high roughness, Munoz-Torrero et al.[13] discovered during their electrodeposition of Al on expanded graphite, could be explained by the fact that they used expanded graphite compared to HOPG. In addition, their deposition time was 180 min (at −0.5 mA cm^{-2}), much longer than our experiments, which might lead to different morphologies.

Conclusions

We have used *operando* reflection anisotropy spectroscopy to investigate the stripping and plating of aluminium from the ionic liquid [EMImCl]:$AlCl_3$ onto highly-oriented pyrolytic graphite in a time-resolved manner. The approach also allowed us to observe the formation of a stable SEI on HOPG in parallel to the intercalation of $AlCl_4^-$ into the graphite structure. We showed that at less cathodic potentials, there is the formation of Al-islands on the surface, which are, for intermediate potentials, plated over with an Al layer of intermediate roughness. For more cathodic potentials, on the other hand, a compact and smooth Al-layer is formed on the surface after an initial nucleation phase with a high degree of ordering. These different plating regimes also lead to distinct stripping, where the Al layer deposited at −0.5 V appears to feature the most homogeneous stripping behaviour. For the function of the graphite as cathode, we observed that during the first cycle going above 1.8 V, both an irreversible swelling of the topmost layer of the graphic, as well as formation of a stable surface layer, occurs. For subsequent cycles at potentials above 1.8 V, the reversible ad-, desorption or intercalation of $AlCl_4^-$ is associated with distinct optical signatures.

This work shows the potential of electrochemical RAS as an *operando* technique for the investigation of battery interfaces, probing in a time-resolved manner to what extent (fast) charging routines lead to or avoid dendrite formation and, as a consequence of this, cause cell damage. Once a reliable understanding of spectra-structure relationships is formed, models can be developed[52] that enable real-time *operando* control of surface morphologies as a function of electrochemical parameters. With time-resolutions of commercial spectrometers in the range of 10 ms, the approach could also provide valuable insight for the investigation of metal deposition via pulsed current, avoiding dendrite formation.[53]

Further research should also be dedicated to $AlCl_3$-free electrolytes in Al dual-graphite batteries, since $AlCl_3$-based electrolytes are known to be corrosive towards cell parts.[6] While $AlCl_3$-free electrolytes have the disadvantage that plating and stripping onto metal aluminium is challenging,[8,54] the use of graphite as an anode would circumvent this issue and render $AlCl_3$-free electrolytes more promising candidates for Al-based batteries.

Experimental Section

Materials and Electrolyte Preparation

A plate of highly-oriented pyrolytic graphite (HOPG) with the dimensions of of 10 mm×10 mm×1 mm and a mosaic angle of 0.8 ± 0.2 was purchased from Thermo Scientific. For a reproducible surface for each experiment, the topmost layer was removed with adhesive tape from Tesa. For the electrolyte preparation, [EMImCl]:$AlCl_3$ (1:1.5) was prepared by slowly adding aluminium chloride ($AlCl_3$) (Anhydrous, Sigma–Aldrich, 99.99%) to 1-Ethyl-3-methylimidazolium chloride (EMImCl) (Sigma-Aldrich, >95%) while stirring with a magnetic stirring bar at room temperature (28 to 30 C) inside an argon-filled glovebox (MBraun, <1 ppm O_2, <1 ppm H_2O). Anhydrous Tetrahydrofuran (THF) (99.8%) was purchased from Sigma–Aldrich.

Electrochemical Setup

All electrochemical experiments were performed inside an argon-filled glovebox. The electrochemical measurement was conducted using a photo-electrochemical cell (PEC cell) from Zahner. An Al wire from Alfa Aesar (0.5 mm diameter, 99.9999% purity) was used as a pseudo-reference electrode. The cell was filled with 1.5 ml of [EMImCl]:AlCl3 (1:1.5) to ensure HOPG and Al-wire were covered with electrolyte, but the electrolyte layer was thin enough not to cause too much light absorption. The electrochemical measurements were controlled with a Gamry Instruments potentiostat (Interface 5000E). For the deposition experiments, three activating cycles were performed first, between 0.5 V and 1.5 V, starting form OCV towards the negative terminus with a scan rate of 10 mV^{-1}.

© 2024 The Author(s). Batteries & Supercaps published by Wiley-VCH GmbH

25666223, 2025, 5, Downloaded from https://chemistry-europe.onlinelibrary.wiley.com/doi/10.1002/batt.202400610 by Helmholtz-Zentrum Dresden Rossi, Wiley Online Library on [26/03/2026]. See the Terms and Conditions (https://onlinelibrary.wiley.com/terms-and-conditions) on Wiley Online Library for rules of use; OA articles are governed by the applicable Creative Commons License

25666223, 2025, 5, Downloaded from https://chemistry-europe.onlinelibrary.wiley.com/doi/10.1002/batt.202400610 by Helmholtz-Zentrum Dresden Rossi, Wiley Online Library on [26/03/2026]. See the Terms and Conditions (https://onlinelibrary.wiley.com/terms-and-conditions) on Wiley Online Library for rules of use; OA articles are governed by the applicable Creative Commons License

Reflection Anisotropy Measurements

For the RA measurement, an EpiRAS from Laytec was employed. For measurements inside the glovebox, the spectrometer was installed on top of the glovebox with a quartz window placed in the sealing of the glovebox between the setup and the spectrometer, allowing light transmission. The electrochemical cell was placed under the window on top of a hexapod (Physik Instrumente H-840), which allowed for rotating, inclining, and translating the cell to align it with the lightpath. For the SEM/EDX measurements, the Apero 2 from Thermo Fisher Scientific with the clean connect system was utilized. This system facilitated the transfer of the sample from the glovebox to the SEM without compromising the inert environment. For a reproducible orientation of the sample, one edge was marked, allowing for the same orientation of the sample in every experiment. The HOPG had a low reflectivity, in order to measure RAS spectra, the reflected lightpath did not go via the anti-wobble-mirror but directly into the detector. To still obtain correct RAS values, the measured RAS was multiplied by a factor of 2. A baseline correction was applied to all the spectra using an optically isotropic Si(100) sample inside the glovebox. The SEM/EDX measurements were carried out using a 10 kV electron beam and a beam current of 26 nA.

Acknowledgements

This research was funded by the Deutsche Forschungsgemeinschaft (DFG, German Research Foundation) under Germany's Excellence Strategy – EXC 2154 – Project number 390874152 and DFG project 434023472. Open Access funding enabled and organized by Projekt DEAL.

Conflict of Interests

The authors declare no conflict of interest.

Data Availability Statement

The data that support the findings of this study are available at Zenodo at https://doi.org/10.5281/zenodo.13270220.[55]

Keywords: aluminium batteries · electrodeposition · HOPG · solid electrolyte interface · reflection anisotropy spectroscopy

[1] S. K. Gupta, J. Vishwakarma, A. K. Srivastava, C. Dhand, N. Dwivedi, *Energy Storage Mater.* **2024**, *70*, 103538.
[2] X. Zhang, R. Lv, W. Tang, G. Li, A. Wang, A. Dong, X. Liu, J. Luo, *Adv. Funct. Mater.* **2020**, *30*.
[3] J. Tu, W.-L. Song, H. Lei, Z. Yu, L.-L. Chen, M. Wang, S. Jiao, *Chem. Rev.* **2021**, *121*, 4903.
[4] S. K. Das, S. Mahapatra, H. Lahan, *J. Mater. Chem.A* **2017**, *5*, 6347.
[5] H. Chen, H. Xu, B. Zheng, S. Wang, T. Huang, F. Guo, W. Gao, C. Gao, *ACS Appl. Mater. Interfaces.* **2017**, *9*, 22628.
[6] E.-S. Lee, S.-H. Huh, S.-H. Lee, S.-H. Yu, *ACS Sustain. Chem. Eng.* **2023**, *11*, 2014.
[7] G. Studer, A. Schmidt, J. Büttner, M. Schmidt, A. Fischer, I. Krossing, B. Esser, *Energy Environ. Sci.* **2023**, *16*, 3760.
[8] F. Rahide, J. K. Flowers, J. Hao, H. S. Stein, H. Ehrenberg, S. Dsoke, *J. Electrochem. Soc.* **2023**, *170*, 120534.
[9] M. Klimpel, M. V. Kovalenko, K. V. Kravchyk, *Commun. Chem* **2022**, *5*.
[10] X. Huang, Y. Liu, C. Liu, J. Zhang, O. Noonan, C. Yu, *CChem. Sci.* **2018**, *9*, 5178.
[11] R. Buckingham, T. Asset, P. Atanassov, *J. Power Sources* **2021**, *498*, 229762.
[12] R. Tao, H. Fu, C. Gao, L. Fan, E. Xie, W. Lyu, J. Zhou, B. Lu, *Adv. Funct. Mater.* **2023**, *33*.
[13] D. Muñoz-Torrero, P. Leung, E. García-Quismondo, E. Ventosa, M. Anderson, J. Palma, R. Marcilla, *J. Power Sources* **2018**, *374*, 77.
[14] Z. Li, J. Liu, B. Niu, J. Li, F. Kang, *Small* **2018**, *14*.
[15] S. Wang, S. Jiao, W.-L. Song, H.-S. Chen, J. Tu, D. Tian, H. Jiao, C. Fu, D.-N. Fang, *Energy Storage Mater.* **2018**, *12*, 119.
[16] M. Tebyetekerwa, T. T. Duignan, Z. Xu, X. Song Zhao, *Adv. Energy Mater.* **2022**, *12*.
[17] S. Chen, Q. Kuang, H. J. Fan, *Small* **2020**, *16*.
[18] Q. Zhou, Y. Zheng, D. Wang, Y. Lian, C. Ban, J. Zhao, H. Zhang, *Ceram. Int.* **2020**, *46*, 26454.
[19] P. Bhauriyal, A. Mahata, B. Pathak, *Phys. Chem. Chem. Phys.* **2017**, *19*, 7980.
[20] M.-C. Lin, M. Gong, B. Lu, Y. Wu, D.-Y. Wang, M. Guan, M. Angell, C. Chen, J. Yang, B.-J. Hwang, H. Dai, *Nature* **2015**, *520*, 324.
[21] N. Canever, F. R. Hughson, T. Nann, *ACS Appl. Energy Mater.* **2020**, *3*, 3673.
[22] W. A. Appiah, A. Stark, S. Lysgaard, J. Busk, P. Jankowski, J. H. Chang, A. Bhowmik, B. Gollas, J. M. Garcia-Lastra, *Chem. Eng. J.* **2023**, *472*, 144995.
[23] V. Elterman, P. Shevelin, L. Yolshina, A. Borozdin, *Electrochim. Acta* **2021**, *389*, 138715.
[24] R. Böttcher, S. Mai, A. Ispas, A. Bund, *J. Electrochem. Soc.* **2020**, *167*, 102516.
[25] K. Ui, S. Kobayashi, K. Sasaki, T. Takeguchi, T. Tsuda, M. Ueda, J. Nunomura, Y. Honkawa, Y. Kojima, *J. Electrochem. Soc.* **2021**, *168*, 056510.
[26] T. Jiang, M. Chollier Brym, G. Dubé, A. Lasia, G. Brisard, *Surf. Coat. Technol.* **2006**, *201*, 1.
[27] T. Schoetz, O. Leung, C. P. de Leon, C. Zaleski, I. Efimov, *JES* **2020**, *167*, 040516.
[28] T. Brülle, U. Stimming, *J. Electroanal. Chem.* **2009**, *636*, 10.
[29] A. N. Simonov, O. V. Cherstiouk, S. Y. Vassiliev, V. I. Zaikovskii, A. Y. Filatov, N. A. Rudina, E. R. Savinova, G. A. Tsirlina, *Electrochim. Acta* **2014**, *150*, 279.
[30] C. Zhong, W. Hu, Y. Cheng, *J. Power Sources* **2011**, *196*, 8064.
[31] R. Pötzschke, C. Gervasi, S. Vinzelberg, G. Staikov, W. Lorenz, *Electrochim. Acta* **1995**, *40*, 1469.
[32] D. Salinas, E. Cobo, S. Garcia, J. Bessone, *J. Electroanal. Chem.* **1999**, *470*, 120.
[33] M. Kettner, C. Stumm, M. Schwarz, C. Schuschke, J. Libuda, *Surf. Sci.* **2019**, *679*, 64.
[34] J. H. Um, S. Yu, *Adv. Energy Mater.* **2020**, *11*.
[35] L. Leuppert, A. Reupert, T. Diemant, T. Philipp, C. Kranz, Z. Li, M. Fichtner, *RSC Applied Interfaces* **2024**.
[36] D.-M. She, W.-L. Song, J. He, N. Li, H. Chen, S. Jiao, D. Fang, *JES* **2020**, *167*, 130530.
[37] M. S. Ding, T. Diemant, R. J. Behm, S. Passerini, G. A. Giffin, *JES* **2018**, *165*, A1983.
[38] X. Tu, J. Zhang, M. Zhang, Y. Cai, H. Lang, G. Tian, Y. Wang, *RSC Adv.* **2017**, *7*, 14790.
[39] B. Scharifker, G. Hills, *Electrochim. Acta* **1983**, *28*, 879.
[40] M. M. May, W. Jaegermann, *Curr. Opin. Electrochem.* **2022**, *34*, 100968.
[41] M. Guidat, M. Löw, M. Kölbach, J. Kim, M. M. May, *ChemElectroChem* **2023**, *10*, e202300027.
[42] K. Haberland, P. Kurpas, M. Pristovsek, J.-T. Zettler, M. Weyers, W. Richter, *Appl. Phys. A* **1999**, *68*, 309.
[43] M. Guidat, F. Rahide, M. Löw, J. Kim, H. Ehrenberg, S. Dsoke, M. M. May, *Batter. Supercaps* **2024**, *7*, e202300394.
[44] E. A. Schmitt, M. Guidat, M. Nusshör, A.-L. Renz, K. Möller, M. Flieg, D. Lörch, M. Kölbach, M. M. May, *Cell Rep. Phys. Sci.* **2023**, *4*, 101606.
[45] A. Kotronia, H. D. Asfaw, C.-W. Tai, M. Hahlin, D. Brandell, K. Edström, *ACS Appl. Mater. Interfaces.* **2021**, *13*, 3867.
[46] E. Peled, S. Menkin, *J. Electrochem. Soc.* **2017**, *164*, A1703.
[47] J. Zhao, C. Zhao, C. Zou, Y. Wang, W. Wang, Q. Peng, Y. Li, S. Han, L. Zhang, *ChemSusChem* **2023**, *17*.
[48] R. S. Berry, B. M. Smirnov, *J. Chem. Phys* **2000**, *113*, 728.
[49] A. Ishii, *Comput. Mater. Sci.* **2025**, *246*, 113342.
[50] V. Kamavaram, D. Mantha, R. Reddy, *J. Min. Metall. Sect. B.* **2003**, *39*, 43.
[51] Y. Chao-Cheng, *Mater. Chem. Phys.* **1994**, *37*, 355.

© 2024 The Author(s). Batteries & Supercaps published by Wiley-VCH GmbH

[52] E. Oliveira, J. Strassner, C. Doering, H. Fouckhardt, *Appl. Surf. Sci.* **2023**, *611*, 155769.
[53] K. Cicvarić, S. Pohlmann, B. Zhang, F. Rahmanian, L. Merker, M. Gaberšček, H. S. Stein, *Phys. Chem. Chem. Phys.* **2024**, *26*, 14713.
[54] M. Talari, A. Sarapulova, E. Zemlyanushin, N. Sabi, A. Hofmann, V. Trouillet, S. Dsoke, *Batter. Supercaps* **2024**.
[55] M. Löw, M. M. May, Dataset for "Operando investigation of Al plating regimes on HOPG in [EMImCl]:$AlCl_3$ by electrochemical reflection anisotropy spectroscopy" **2024**, https://doi.org/10.5281/zenodo.13270220.

Manuscript received: September 16, 2024
Revised manuscript received: October 21, 2024
Accepted manuscript online: October 22, 2024
Version of record online: November 14, 2024

© 2024 The Author(s). Batteries & Supercaps published by Wiley-VCH GmbH

25666223, 2025, 5, Downloaded from https://chemistry-europe.onlinelibrary.wiley.com/doi/10.1002/batt.202400610 by Helmholtz-Zentrum Dresden Rossi, Wiley Online Library on [26/03/2026]. See the Terms and Conditions (https://onlinelibrary.wiley.com/terms-and-conditions) on Wiley Online Library for rules of use; OA articles are governed by the applicable Creative Commons License

5.4 Magnesium and Aluminum in Contact with Liquid Battery Electrolytes: Ion Transport through Interphases and in the Bulk

The article ”Magnesium and Aluminum in Contact with Liquid Battery Electrolytes: Ion Transport through Interphases and in the Bulk” was submitted to the journal *ACS Materials Letters* in July 2024 and was published as open access in October 2024 (ACS Materials Lett. 2024, 6, 5120-5127) and is distributed under the terms of the Creative Commons Attribution 4.0 International. (CC BY 4.0, `https://creativecommons.org/licenses/by/4.0/`).[165]

DOI: 10.1021/acsmaterialslett.4c01589

EIS was used to gain additional information about the metal interphase studied with EC-RAS. Compared to EC-RAS, EIS can observe the evolution of the interphase over a prolonged period of time and determine transport processes within the interphase. This investigation used symmetric Mg and Al cells with Grignard and [EMImCl]:$AlCl_3$ as respective electrolytes. The research showed that the interphase of Mg is dominated by liquid ion transport pathways. For Al, the interface is dense initially but becomes more porous over time. The determination of the cationic transference number shows a low value (below 0.01) for both the Grignards and the ionic liquid. However, only one CV cycle increased the cationic transference number of the Grignard to over 0.3.

ACS MATERIALS LETTERS

www.acsmaterialsletters.org

Open Access

This article is licensed under CC-BY 4.0

Magnesium and Aluminum in Contact with Liquid Battery Electrolytes: Ion Transport through Interphases and in the Bulk

Published as part of ACS Materials Letters special issue "Post-Lithium Battery Materials".

Mario Löw, Jonas Grill, Matthias M. May, and Jelena Popovic-Neuber*

Cite This: *ACS Materials Lett.* 2024, 6, 5120–5127

Read Online

ACCESS | Metrics & More | Article Recommendations | Supporting Information

ABSTRACT: A significant challenge in improving Mg and Al batteries is the limited understanding of the solid electrolyte interphase (SEI) and its evolution under operating conditions. Additionally, the cationic transference number of related electrolytes is crucial for their performance as well as potential dendrite formation yet it is only rarely determined experimentally. Here, we study Al and Mg systems using Grignards as electrolytes for the Mg case and an ionic liquid electrolyte for the Al case. The activation energies associated with ion transport through the SEI suggest that it initially contains a high contribution from liquid pathways for the Mg case and is dense for the Al case, but becomes fully dominated by liquid pathways after a longer contact with the electrolyte. The initial effective Mg cationic transference number of the Grignards is close to zero and increases significantly after only one cyclic voltammetry cycle.

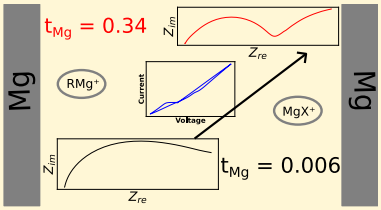

Rechargeable multivalent batteries are promising alternatives to the current lithium-ion batteries.[1−3] For instance, magnesium and aluminum metal batteries could offer a higher volumetric energy density due to their multivalent charge.[3−5] Moreover, these metals are among the most abundant elements on Earth and, therefore, hold the potential for a more sustainable energy storage solution.[6,7] However, understanding and improving the properties of the solid electrolyte interphase (SEI) is crucial for enabling these technologies.[8−10]

For this investigation, we have used two electrolyte systems, including the Gringard electrolytes butylmagnesium chloride (BuMgCl) and ethylmagnesium chloride (EtMgCl), and an ionic liquid doped with aluminum salt, 1-ethyl-3-methylimidazolium chloride-aluminum chloride ([EMImCl]:$AlCl_3$). Grignards are among the first electrolytes used for rechargeable magnesium batteries; they are commercially available and inexpensive.[11,12] Previous electrochemical impedance spectroscopy (EIS) investigations of Grignard electrolytes in symmetric Mg cells showed high total resistances speculated to be related to an adsorption layer present on the Mg anode, containing RMg^+ and RMg· species, stabilized by tetrahydrofuran, as shown by Fourier transform infrared spectroscopy.[11,13,14] Further analysis showed that a native passivation film containing magnesium oxide, magnesium hydroxide, and organic components like carbonates and carboxylates forms on Mg in contact with ambient air.[15,16]

So far, different approaches have been proposed in the recent literature to overcome the ion-blocking passivation layer on top of Mg. One solution is the addition of $LiPF_6$ or $MgBr_2$ to the electrolyte, which was shown to positively affect the SEI formation.[17,18] Another approach is the formation of a so-called artificial SEI. This can be composed of either organic polymers,[19,20] inorganic compounds,[6,21,22] alloys,[23,24] metal−organic frameworks,[25] or 3D scaffolds.[26] Dou et al.[27] investigated the link of the three-dimensional distribution composition to the evolution of the SEI, suggesting that the initial SEI is primarily composed of organic components, leading to electronic leakage, allowing for the decomposition of the electrolyte and continuous growth of a resistive SEI.[27]

[EMImCl]:$AlCl_3$, on the other hand, is a well-established electrolyte for rechargeable aluminium batteries.[28,29] However, it is corrosive to the aluminum, its native oxide, and other components inside the cell.[30−33] For Al metal batteries, the native oxide layer is important since it is dense (Pilling−Bedworth ratio of 1.29)[34] and can suppress the formation of dendrites and confine their existence at the metal/oxide

Received: August 2, 2024
Revised: October 11, 2024
Accepted: October 11, 2024
Published: October 16, 2024



Downloaded via UNIV TUEBINGEN on December 4, 2024 at 13:09:51 (UTC).
See https://pubs.acs.org/sharingguidelines for options on how to legitimately share published articles.

ACS Publications

© 2024 The Authors. Published by American Chemical Society

https://doi.org/10.1021/acsmaterialslett.4c01589
ACS Materials Lett. 2024, 6, 5120−5127

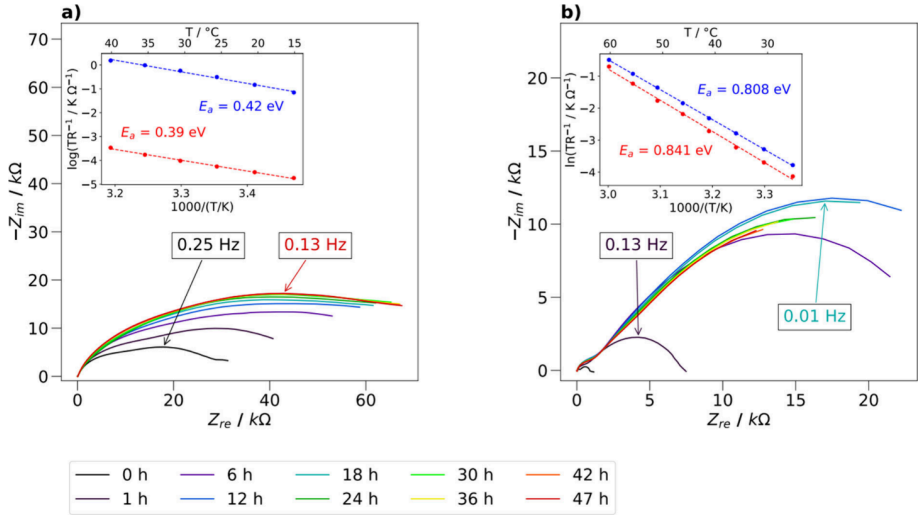

Figure 1. Nyquist plots related to time-dependent EIS measurements of symmetric cells in the 10^7−10^{-2} Hz frequency range: (a) Mg|BuMgCl|Mg and (b) Al|[EMImCl]:$AlCl_3$|Al. Insets: Arrhenius plots and E_a of (a) Mg|BuMgCl|Mg and (b) Al|[EMImCl]:$AlCl_3$|Al. The differently colored Nyquist plots indicate the time in hours from the start of the measurement directly after cell assembly. The red curve shows E_a during increasing temperature; the blue curve shows E_a during decreasing temperature. The activation energy was determined from a freshly assembled cell.

interface.[35−37] Studies of aluminum in contact with [EMIm-Cl]:$AlCl_3$ have shown that the interphase highly depends on the storage conditions and surface properties like roughness and microstructure and may also get dissolved over time.[38,39] However, some corrosion of the native oxide is necessary for adequate cell performance since, otherwise, aluminum cannot be transported over the interface.[35,37] Rahide et al. showed that the presence of Al in an ionic liquid/$AlCl_3$-based electrolyte modifies the surface by creating a beneficial SEI layer containing Al-, Cl-, and N-based compounds.[39]

Further important measurements for insight into the ion transport properties of the electrolyte are related to the determination of the cationic transference numbers and salt diffusion coefficients. This information is essential for understanding dendrite growth and fast charging behavior.[40,41]

The cationic transference number of Grignard electrolytes has yet to be determined. For the related electrolyte C_2H_5MgCl-$((C_2H_5)_2AlCl)_2$/THF, the cationic transference number was determined by potentiometric deposition of Mg in a Hittorf cell. The effective magnesium transference number was found to vary depending on the concentration between 0.19 (0.15 M) and 0.018 (0.4 M).[42] In the case of [EMImCl]:$AlCl_3$, the transference numbers of expected species, $EMIm^+$, $AlCl_4^-$, and Cl^- have already been investigated by Hittorf and other methods, with corresponding effective transference number values of ca. 0.70, 0.30, and 0, respectively.[43−45]

In this letter, we employ in situ EIS to study bulk and interphase ion transport using symmetrical metal cells. This is crucial for the investigation of the SEI since its composition is highly dependent on the environment.[46] This allows us to determine the changes in the electrolyte and SEI resistance over time at conditions as close to open-circuit voltage as possible.[47,48] This type of analysis is well-known in the field of corrosion.[48,49] An ex situ spectroscopy method like X-ray photoelectron spectroscopy would not deliver any necessary information on the morphology of the interphase, while its chemical resolution is also not good enough to determine the distribution of different phases in the SEI, necessary for understanding detailed ion transport properties. Further investigation with operando reflection anisotropy spectroscopy has shown that surfaces created under potential may not be stable and convert within seconds.[50] Furthermore, the analysis of the activation energy of transport (E_a), as well as equivalent circuit development, is essential for elucidating the ion transport in the SEI, especially for determining its possible porosity and dominant liquid conduction pathways.[51] In addition, we use the galvanostatic concentration polarization method combined with EIS to determine the effective cationic transference number and the salt diffusion coefficient.[52] This method coupled with semiblocking electrodes (here, Mg and Al metal) gives access to effective cationic transference numbers of cationic species moving in the direction of positively charged species, which are of relevance for battery performance. For a detailed account of the species that move during galvanostatic polarization with semiblocking electrodes, the reader is directed to consult refs 53−55. Specifically in Grignard electrolytes, Mg does not exist in the form of Mg^{2+} in the electrolyte but only in combination with other ions in the form of RMg^+, RMg; MgX_2, and MgX^+.[13,14,56−58]

For a better understanding of the ionic transport properties of the SEI and the evolution of the surface over time, the E_a of the ionic conduction in the SEI was determined at the start of the experiment, followed by aging of the cell under open-circuit voltage. Figure 1a shows the evolution of the Nyquist plot over time for the Mg|BuMgCl|Mg system upon application of the EIS perturbation potential. We observe that the total resistance of the semicircle increases in the first 24 h but then reaches saturation. The frequency at the vertex of the semicircle is f_{max} = 0.25 Hz for the initial measurement. This clearly shows that the vertex of the semicircle lies within the range of change transfer reaction (<1 Hz).[59] In addition, the semicircle is also longitudinally distorted. Because of this and according to the observed frequencies, we created an equivalent circuit model containing the resistance of the electrolyte, followed by the SEI's capacity and resistance in parallel, and finally, a Randles circuit for the charge-transfer reaction and diffusion in series (Figure S8 in the Supporting

https://doi.org/10.1021/acsmaterialslett.4c01589
ACS Materials Lett. 2024, 6, 5120−5127

Information (SI)). A comparison of the obtained parameters from the fitting shows that the charge-transfer resistance increases in the first 24 h from 20 to over 50 kΩ and then stays constant. Simultaneously, the double-layer capacity decreases from 450 to 200 μF in the first 24 h and stays relatively constant afterward. The SEI capacity doubles in the same time frame from 4 to 70 μF but then drops to 55 μF for the following 24 h. For the SEI resistance, no clear trend can be observed. The E_a of ionic conduction in the SEI lies between 0.39 and 0.42 eV, which is a clear indication of liquid pathways playing an important role in ionic conduction through the SEI (see the SI for details). This can be concluded since the E_a values of ion transport in some of the best inorganic solid Mg conductors are around 1 eV,[60] while the activation energy of ion transport in Grignard electrolyte is expected to be around 0.1 eV.[61] Similar values have been found in the case of SEIs on Li and Na, where the ion transport in the solid state is generally less sluggish than for Mg-ion conductors.[51] In this case, the situation is even more complex since adsorbed species might be present on the surface of the Mg electrode. However, the ion conduction mechanism through adsorbates is not expected to be different than that through inorganic compounds unless they are solvated. In that case, the liquid ion transport pathways may also be due to these, rather than due to the porous nature of the SEI. The scenario has also been speculated upon by Attias et al.[11] The investigation was repeated for the related Grignard electrolyte EtMgCl. The results are shown in Figure S1. Here, the total resistance of the semicircle also increases with time, and its vertex is around 0.1 Hz, except for the very first semicircle, where it is 3.1 Hz. There is also a long tail in the low-frequency range in this semicircle, which does not occur in the following semicircles, possibly an indication of an electrochemical reaction. Despite the outlier in the first semicircle, the same equivalent circuit was also used to fit this data. Here, the SEI resistance is continuously increased from 10 to 60 kΩ. The capacity of the SEI first jumps from 75 to 95 μF in the first hour and then increases further to 105 μF after 12 h, before it drops again to 80 μF after 47 h. The charge-transfer resistance substantially increases in the first 6 h before fluctuating between 30 and 50 kΩ. The increase in SEI resistance and capacity for both Grignards is assigned to the SEI growth on top of the nondense initial oxide.

The equivalent investigation for aluminum with the [EMImCl]:$AlCl_3$ electrolyte is shown in Figure 1b. Here, a strong increase in the total resistance is observed in the first 6 h, followed by a slighter increase up to 18 h, before it decreases again. The data obtained from [EMImCl]:$AlCl_3$-containing cells were fitted with the previously mentioned equivalent circuit (Figure S8). The reasons for using the same equivalent circuit are, first, the existence of a small semicircle below 1 kΩ and the fact that the vertex of the second semicircle lies with the value of 0.12 Hz. The analysis of the fit shows that the SEI resistance increases strongly in the first 6 h from 200 to 1200 Ω. Afterward, it slightly decreases to around 1000 Ω. In the SEI capacity, there is only a jump in the first hour from 140 to 230 μF before it contentiously increases to 350 μF. The charge-transfer resistance increases in the first 12 h from 0.7 to 40 kΩ and stays relatively constant. The activation energy of ionic conduction in the SEI is around 0.8 eV, indicating a relatively dense SEI.

For aluminum in contact with [EMImCl]:$AlCl_3$, the strong increase of the SEI resistance and capacity in the first few hours, as well as the high E_a of ionic conduction in the SEI at the beginning, is a strong indication of corrosion happening at the interface, leading to a partial removal of the native oxide layer on top of the aluminum.[32,62] Since the native oxide layer is partially removed, the double-layer capacity and the charge-transfer resistance change in this time frame. In situ optical measurements by Guidat et al.[32] show that the partial removal of the native oxide already happens within the first hour after immersion into the electrolyte. This couples well with our investigation.

The magnesium used in the previous section exhibited a blackish surface layer. In the following, this surface was mechanically activated by scratching it with a spatula. Figure 2 compares the EIS response of mechanically activated magnesium with that of the pristine one. A comparison shows that the total resistance of the semicircle of the mechanically activated magnesium is larger than that with native oxide. Fits of both plots are available in Figure S15.

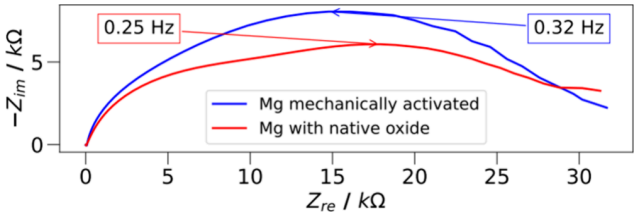

Figure 2. Nyquist plot (10^7–10^{-2} Hz) of Mg with native oxide (red) and mechanically activated Mg (blue) in contact with BuMgCl.

This indicates that the ions face a lower resistance when migrating through the native oxide to the Mg surface than without it. There are two possible explanations for this behavior. A possible explanation could be the change of near-surface composition with exposure to ambient conditions, as the first 10 nm of the Mg surface transform from Mg metal to a mixture of amorphous MgO/OH and then crystalline $Mg(OH)_2$ over a time period of several weeks.[15]

If the crystalline layer performs better with respect to ion transport than the amorphous oxide, its removal by "mechanical activation" would be detrimental to the ion transport through the interphase. This information is crucial for further investigation of magnesium anodes since, in most studies, the native oxide is mechanically removed, expecting improved electrode performance.

The cationic transference numbers for Grignards and the ionic liquid electrolyte were determined by galvanostatic concentration polarization. This type of polarization method was first established[63,64] for the separation of ionic and electronic conductivity and popularized for lithium polymer electrolytes.[65] In contrast to the typical method, we used galvanostatic polarization to determine the initial *IR* response more precisely.[52,66] Therefore, we applied a constant current and recorded the voltage over time until a steady state was reached. In our system, the steady state was reached relatively quickly in under 2 min. The transference number can be calculated via eq 1:

$$t_{pol} = \frac{IR_{tot,0} - IR_{SEI,0}}{U_\infty - IR_{SEI,\infty}} \quad (1)$$

https://doi.org/10.1021/acsmaterialslett.4c01589
ACS Materials Lett. 2024, 6, 5120−5127

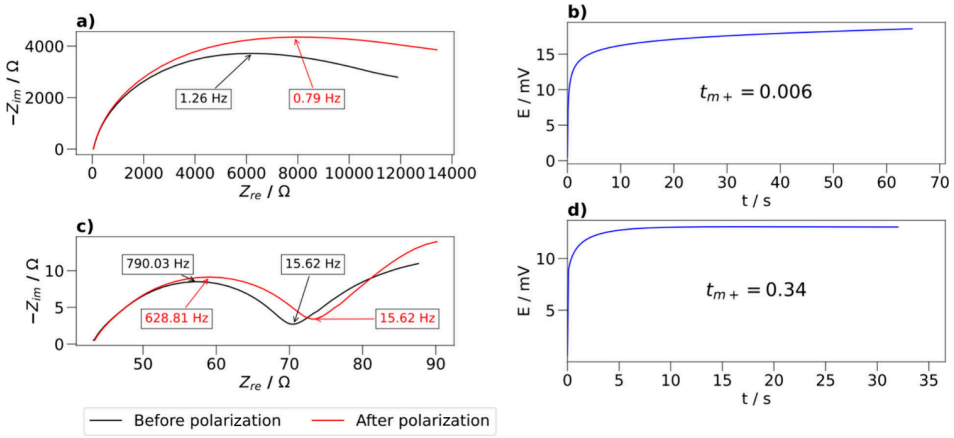

Figure 3. (a) EIS spectra (10^6–10^{-1} Hz) of Mg|BuMgCl|Mg before galvanostatic polarization (black) and after galvanostatic polarization (red). (b) DC polarization curve for $I = 9 \times 10^{-8}$ A. (c) EIS spectra (10^6–10^{-1} Hz) of Mg|BuMgCl|Mg after one CV cycle from −0.5 to 1 V with 10 mV s^{-1} before galvanostatic polarization (black) and after galvanostatic polarization (red). (d) DC polarization curve after the CV cycle for $I = 1 \times 10^{-4}$ A.

where U_∞ is the steady-state voltage, $R_{SEI,0}$ and $R_{SEI,\infty}$ are the resistances of the SEI before and after polarization, respectively, $R_{tot,0}$ is the total resistance before polarization, and I is the applied current during polarization.

In the case of the impedance spectra after cyclic voltammetry (CV), it is also possible to determine the transference number with the low-frequency EIS approach. This considers the electrolyte's resistance (the first intersection between the curve and the x-axis) and the impedance of the polarization (the potential intersection of the right-hand side of the second semicircle):[67]

$$t_{eis} = \frac{1}{1 + \frac{Z_d}{R_{el}}} \tag{2}$$

where Z_d is the impedance of the polarization and R_{el} is the resistance of the electrolyte. In order to obtain the impedance of the polarization from the Nyquist plots in Figure 3, they were fitted with the equivalent circuit described in Figure S8. Before CV, the impedance of the polarization is Z_d = 7625 Ω, and the resistance of the electrolyte is R_{el} = 43.9 Ω; this results in a transference number of $t_{EIS,Mg}$ = 0.0057. After CV, the transference number is $t_{EIS,Mg}$ = 0.37 (Z_d = 72.69 Ω and R_{el} = 43.16 Ω).

Figure 3 shows the Nyquist plot and concentration polarization of BuMgCl in contact with magnesium before and after one CV cycle. The total resistance of the BuMgCl-containing cell is relatively high, over 10 kΩ (Figure 3a). Also, the resulting effective cationic transference number is very small, $t_{Mg,eff}$ = 0.006 (Figure 3b). However, both bulk and interfacial properties change abruptly after only one CV cycle between -0.5 and 1 V (vs Mg). The resistance is significantly reduced to less than 90 Ω, and two semicircles can now be observed. The most striking change, however, is in the cationic transference number, which is significantly increased to $t_{Mg,eff}$ = 0.34. Similar behavior is observed with ethylmagnesium chloride, where the transference number increases from $t_{Mg,eff}$ = 0.004 before CV to 0.41 after CV (see plots in Figure S3). As shown by Benmayza et al.[42] for the C_2H_5MgCl-$((C_2H_5)_2AlCl)_2$ electrolyte, the low t_{Mg} is expected at higher concentrations due to the lower mobility of the Mg dimer ion and the presence of many counter- and non-magnesium ions.[42] The change of $t_{Mg,eff}$ upon the CV run, with values of the same order of magnitude as those of well-performing lithium liquid electrolytes, indicates a drastic change of magnesium speciation or its mobility. We have shown that this is possible in lithium liquid electrolytes with a high concentration of neutral ion pairs.[55] Here, we can speculate that the increase of cationic transference number is again a consequence of the interplay between the existence of a high number of noncharged ion pairs and a smaller amount of magnesium in the positively charged aggregates.

The cationic transference number was also determined for [EMImCl]:$AlCl_3$ (Figure S6). Here, a value of $t_{Al,eff}$ = 0.063 was observed, which aligns well with a previous study showing a nonexistent effective transport of aluminum and dominant aluminum transport in negatively charged species, t_{AlCl^-} = 0.30 ± 0.02.[43] In this case, after one CV cycle, the $t_{Al,eff}$ decreases even further to 0.0004, indicating a nonbeneficial change in speciation/mobility. In addition to the effective transference number values, it is also possible to extract the ambipolar diffusion coefficient of all species, D^δ, from the polarization curve at short polarization times. Therefore, eq 3 was used:

$$D^\delta = \frac{L^2}{\tau^\delta \pi^2} \tag{3}$$

where L is the thickness of the separator and τ^δ is the time constant. The latter can be obtained by plotting the voltage of the chronopotentiometry from the polarization experiment against the square root of the time, with the slope of the linear part being the polarization constant (Figure 4). For BuMgCl, a value of $D^\delta = 1.2 \times 10^{-7}$ cm^2 s^{-1} was obtained, and for

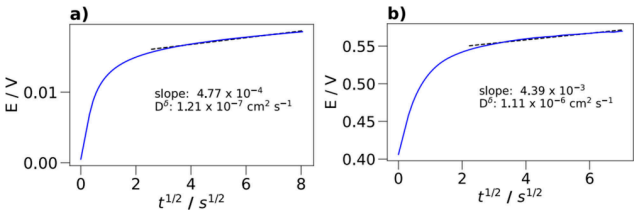

Figure 4. Ambipolar salt diffusion coefficient obtained from the square-root dependence of time vs voltage in the short-time regime of DC polarization for (a) BuMgCl and (b) [EMIm-Cl]:$AlCl_3$.

https://doi.org/10.1021/acsmaterialslett.4c01589
ACS Materials Lett. 2024, 6, 5120−5127

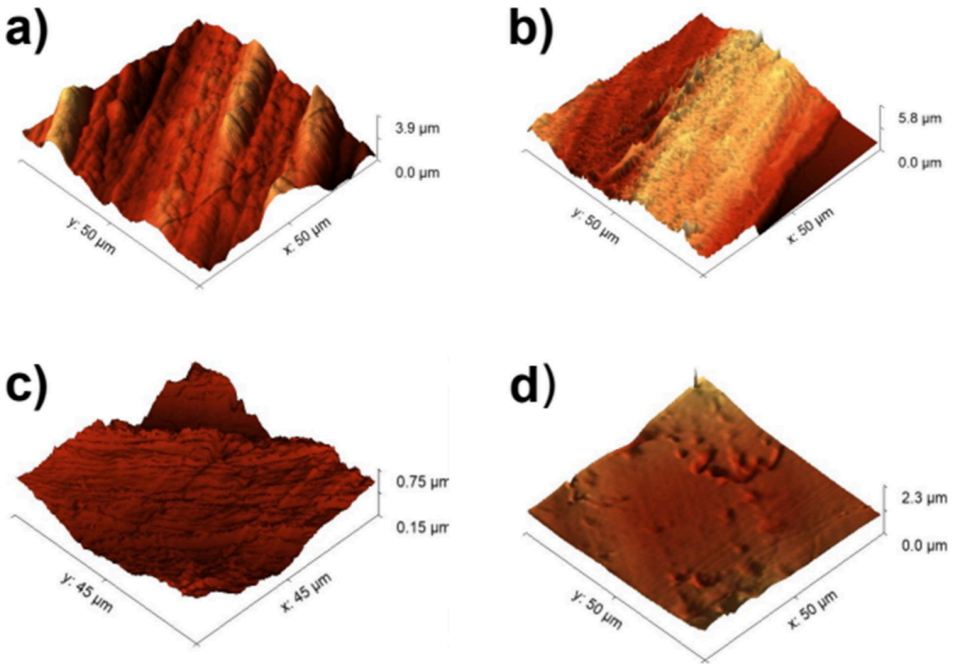

Figure 5. AFM images of the Mg-foil and Al-foil. (a) Fresh Mg-foil with native oxide. (b) Mg-foil with native oxide after prolonged contact with the BuMgCl electrolyte. (c) Fresh Al-foil and (d) Al-foil after prolonged contact with the [EMImCl]:$AlCl_3$ electrolyte.

EtMgCl, a value of $D^{\delta} = 1.0 \times 10^{-7}$ cm^2 s^{-1} was obtained. For [EMImCl]:$AlCl_3$, salt diffusion coefficient of 1.1×10^{-6} cm^2 s^{-1} was observed, which is an order of magnitude higher compared to the literature value.[68]

For a better understanding of the processes taking place at the electrode−electrolyte interphase, both magnesium and aluminum were investigated with atomic force microscopy (AFM) in the pristine state as well as after prolonged contact with their respective electrolyte. The AFM images in Figure 5a,b show that the roughness of the magnesium electrode remained unchanged. The pristine foil displays grooves, likely resulting from the manufacturing process. The small spikes observed on the electrode after contact with the BuMgCl electrolyte are probably scanning artifacts. For Al, Figure 5c,d shows that the surface roughness increases after prolonged contact. Here, two processes take place; first, small Al structures are removed due to the corrosiveness of the electrolyte. Second, pitting of the surface and salt deposition from the electrolyte can also occur, leading to areas with higher differential altitudes and features of several micrometers in height. This results in a smoother surface with some additional larger structures. We also quantitatively assessed the surface roughness of both surfaces. For the pristine Al-foil, the root-mean-square value for the roughness is 197 nm, while it is 309 nm after prolonged contact with the electrolyte. Compared to the research by Sabi et al.,[33] where no effective change was observed after 18 h of exposure, we experience an increase in the surface roughness while immersing the sample in the electrolyte.

In summary, the evolution of the interphase of symmetric Mg and Al cells with Grignard and [EMImCl]:$AlCl_3$ as respective electrolytes was investigated by EIS. The evolution of the shape of the Nyquist plots and the E_a associated with ion transport through the SEI indicates that the interphase of magnesium and aluminum is dominated by liquid ion transport pathways for magnesium and is already dense in the case of aluminum at the beginning. Liquid ion transport pathways remain relevant for both interphases over time. AFM investigations additionally show that the roughness of the magnesium surface stays about the same while immersed in the Grignard. However, the roughness increases for Al due to the electrolyte's corrosiveness. For the Grignards, the cationic transference number increase from $t_{Mg,eff}$ = 0.006 to $t_{Mg,eff}$ = 0.34 after only one CV cycle, indicating a profound change in the transport properties of the electrolyte. For [EMImCl]:$AlCl_3$, the cationic transference number stays relatively low with $t_{Al,eff}$ = 0.063 and does not increase upon electrochemical cycling.

The drastic change in the transference numbers of the Grignard electrolytes after one cycle is related to the change in speciation and/or the related mobility of species. Nuclear magnetic resonance and infrared measurements might be beneficial here. Further, we want to encourage the community of multivalent batteries to do more research on the transference numbers of their electrolytes since they are one of the critical factors for improving electrolytes, as shown by us in this work by a simple setup.

■ ASSOCIATED CONTENT

Data Availability Statement

The data that support the findings of this study are openly available on Zenodo at https://doi.org/10.5281/zenodo.12750755.

Supporting Information

The Supporting Information is available free of charge at https://pubs.acs.org/doi/10.1021/acsmaterialslett.4c01589.

Experimental details, time-dependent Nyquist plots of EtMgCl, transference number measurements of EtMgCl and [EMImCl]:$AlCl_3$, additional CVs, and tables with the fitting values and plots of the Nyquist plots presented in the paper (PDF)

https://doi.org/10.1021/acsmaterialslett.4c01589
ACS Materials Lett. 2024, 6, 5120−5127

AUTHOR INFORMATION

Corresponding Author

Jelena Popovic-Neuber − *University of Stavanger, Faculty of Science and Technology, Department of Energy and Petroleum Engineering, 4021 Stavanger, Norway;* orcid.org/0000-0001-6618-4306; Email: jelena.popovic-neuber@uis.no

Authors

Mario Löw − *Universität Ulm, Institute of Theoretical Chemistry, 89081 Ulm, Germany*

Jonas Grill − *University of Stavanger, Faculty of Science and Technology, Department of Energy and Petroleum Engineering, 4021 Stavanger, Norway*

Matthias M. May − *Universität Tübingen, Institute of Physical and Theoretical Chemistry, 72076 Tübingen, Germany; Universität Ulm, Institute of Theoretical Chemistry, 89081 Ulm, Germany;* orcid.org/0000-0002-1252-806X

Complete contact information is available at: https://pubs.acs.org/10.1021/acsmaterialslett.4c01589

Author Contributions

CRediT: **Mario Löw** conceptualization, data curation, formal analysis, investigation, validation, visualization, writing - original draft, writing - review & editing; **Jonas Grill** conceptualization, data curation, formal analysis, investigation, methodology, validation, writing - original draft, writing - review & editing; **Matthias M. May** conceptualization, data curation, formal analysis, funding acquisition, investigation, resources, supervision, validation, writing - original draft, writing - review & editing; **Jelena Popovic-Neuber** conceptualization, data curation, formal analysis, funding acquisition, investigation, methodology, resources, supervision, validation, visualization, writing - original draft, writing - review & editing.

Notes

The authors declare no competing financial interest.

ACKNOWLEDGMENTS

This work was funded by Deutsche Forschungsgemeinschaft (DFG, German Research Foundation) under Germany's Excellence Strategy - EXC 2154 - Project 390874152, DFG Project 434023472 and institutional funding by University of Stavanger. Mats Ingdal, Dagfinn Sødenaa Sleveland, and Ola Ketil Siqveland are thanked for their laboratory support.

REFERENCES

(1) Liu, F.; Wang, T.; Liu, X.; Fan, L.-Z. Challenges and Recent Progress on Key Materials for Rechargeable Magnesium Batteries. *Adv. Energy Mater.* **2021**, *11*, 2000787.

(2) Elia, G. A.; Kravchyk, K. V.; Kovalenko, M. V.; Chacón, J.; Holland, A.; Wills, R. G. An overview and prospective on Al and Al-ion battery technologies. *J. Power Sources* **2021**, *481*, 228870.

(3) Gupta, S. K.; Vishwakarma, J.; Srivastava, A. K.; Dhand, C.; Dwivedi, N. Aluminum batteries: Opportunities and challenges. *Energy Storage Mater.* **2024**, *70*, 103538.

(4) Faegh, E.; Ng, B.; Hayman, D.; Mustain, W. E. Practical assessment of the performance of aluminium battery technologies. *Nat. Energy* **2021**, *6*, 21−29.

(5) Liang, Y.; Dong, H.; Aurbach, D.; Yao, Y. Current status and future directions of multivalent metal-ion batteries. *Nat. Energy* **2020**, *5*, 646−656.

(6) Zhang, X.; Lv, R.; Tang, W.; Li, G.; Wang, A.; Dong, A.; Liu, X.; Luo, J. Challenges and Opportunities for Multivalent Metal Anodes in Rechargeable Batteries. *Adv. Funct. Mater.* **2020**, *30*, 2004187.

(7) Lee, E.-S.; Huh, S.-H.; Lee, S.-H.; Yu, S.-H. On the Road to Stable Electrochemical Metal Deposition in Multivalent Batteries. *ACS Sustain. Chem. Eng.* **2023**, *11*, 2014−2032.

(8) Popovic, J. In *Nanomaterials for Electrochemical Energy Storage*; Raccichini, R., Ulissi, U., Eds.; Elsevier, 2021; p 327−359.

(9) Liu, X.; Wang, G.; Lv, Z.; Du, A.; Dong, S.; Cui, G. A Perspective on Uniform Plating Behavior of Mg Metal Anode: Diffusion Limited Theory versus Nucleation Theory. *Adv. Mater.* **2023**, *36*, 2306395.

(10) Tang, K.; Du, A.; Dong, S.; Cui, Z.; Liu, X.; Lu, C.; Zhao, J.; Zhou, X.; Cui, G. A Stable Solid Electrolyte Interphase for Magnesium Metal Anode Evolved from a Bulky Anion Lithium Salt. *Adv. Mater.* **2020**, *32*, 1904987.

(11) Attias, R.; Dlugatch, B.; Chae, M. S.; Goffer, Y.; Aurbach, D. Changes in the interfacial charge-transfer resistance of Mg metal electrodes, measured by dynamic electrochemical impedance spectroscopy. *Electrochem. Commun.* **2021**, *124*, 106952.

(12) Lu, Z.; Schechter, A.; Moshkovich, M.; Aurbach, D. On the electrochemical behavior of magnesium electrodes in polar aprotic electrolyte solutions. *J. Electroanal. Chem.* **1999**, *466*, 203−217.

(13) Aurbach, D. Magnesium Deposition and Dissolution Processes in Ethereal Grignard Salt Solutions Using Simultaneous EQCM-EIS and In Situ FTIR Spectroscopy. *Electrochem. Solid-State Lett.* **1999**, *3*, 31.

(14) Aurbach, D.; Turgeman, R.; Chusid, O.; Gofer, Y. Spectroelectrochemical studies of magnesium deposition by in situ FTIR spectroscopy. *Electrochem. Commun.* **2001**, *3*, 252−261.

(15) Fotea, C.; Callaway, J.; Alexander, M. R. Characterisation of the surface chemistry of magnesium exposed to the ambient atmosphere. *Surf. Interface Anal.* **2006**, *38*, 1363−1371.

(16) Newberg, J. T.; Starr, D. E.; Yamamoto, S.; Kaya, S.; Kendelewicz, T.; Mysak, E. R.; Porsgaard, S.; Salmeron, M. B.; Brown, G. E.; Nilsson, A.; Bluhm, H. Formation of hydroxyl and water layers on MgO films studied with ambient pressure XPS. *Surf. Sci.* **2011**, *605*, 89−94.

(17) Xie, Y.; Song, H.; Ye, S.; Tian, F.; Xie, J.; Lei, D.; Wang, C. Hybrid solid electrolyte interphases formed in conventional carbonate electrolyte enable high-voltage and ultrastable magnesium metal batteries. *J. Energy Chem.* **2023**, *78*, 315−324.

(18) Chinnadurai, D.; Lieu, W. Y.; Kumar, S.; Yang, G.; Li, Y.; Seh, Z. W. A Passivation-Free Solid Electrolyte Interface Regulated by Magnesium Bromide Additive for Highly Reversible Magnesium Batteries. *Nano Lett.* **2023**, *23*, 1564−1572.

(19) Häcker, J.; Rommel, T.; Lange, P.; Zhao-Karger, Z.; Morawietz, T.; Biswas, I.; Wag-ner, N.; Nojabaee, M.; Friedrich, K. A. Magnesium Anode Protection by an Organic Artificial Solid Electrolyte Interphase for Magnesium-Sulfur Batteries. *ACS Appl. Mater. Interfaces.* **2023**, *15*, 33013−33027.

(20) Son, S.-B.; Gao, T.; Harvey, S. P.; Steirer, K. X.; Stokes, A.; Norman, A.; Wang, C.; Cresce, A.; Xu, K.; Ban, C. An artificial interphase enables reversible magnesium chemistry in carbonate electrolytes. *Nat. Chem.* **2018**, *10*, 532−539.

(21) Luo, L.; Yang, X.; Gao, Z.; Li, X.; Xu, J.; Zhang, Y.; Deng, R.; Huang, G.; Wang, J.; Pan, F. Overcoming passivation in rechargeable magnesium batteries: Artificial solid electrolyte interface for enhanced anode functionality. *Electrochim. Acta* **2024**, *478*, 143815.

(22) Li, X.; Gao, T.; Han, F.; Ma, Z.; Fan, X.; Hou, S.; Eidson, N.; Li, W.; Wang, C. Reducing Mg Anode Overpotential via Ion Conductive Surface Layer Formation by Iodine Additive. *Adv. Energy Mater.* **2018**, *8*, 1701728.

(23) Wan, B.; Dou, H.; Zhao, X.; Wang, J.; Zhao, W.; Guo, M.; Zhang, Y.; Li, J.; Ma, Z.-F.; Yang, X. Three-Dimensional Magnesiophilic Scaffolds for Reduced Passivation toward High-Rate Mg Metal Anodes in a Noncorrosive Electrolyte. *ACS Appl. Mater. Interfaces.* **2020**, *12*, 28298−28305.

(24) Lv, R.; Guan, X.; Zhang, J.; Xia, Y.; Luo, J. Enabling Mg metal anodes rechargeable in conventional electrolytes by fast ionic transport interphase. *Natl. Sci. Rev.* **2020**, *7*, 333−341.

(25) Zhang, Y.; Li, J.; Zhao, W.; Dou, H.; Zhao, X.; Liu, Y.; Zhang, B.; Yang, X. Defect-Free Metal−Organic Framework Membrane for

Precise Ion/Solvent Separation toward Highly Stable Magnesium Metal Anode. *Adv. Mater.* **2022**, *34*, 2108114.
(26) Song, Z.; Zhang, Z.; Du, A.; Dong, S.; Li, G.; Cui, G. Uniform Magnesium Electrodeposition via Synergistic Coupling of Current Homogenization, Geometric Confinement, and Chemisorption Effect. *Adv. Mater.* **2021**, *33*, 2100224.
(27) Dou, H.; Zhao, X.; Zhang, Y.; Zhao, W.; Yan, Y.; Ma, Z.-F.; Wang, X.; Yang, X. Revisiting the degradation of solid/electrolyte interfaces of magnesium metal anodes: Decisive role of interfacial composition. *Nano Energy* **2021**, *86*, 106087.
(28) Ferrara, C.; Dall'Asta, V.; Berbenni, V.; Quartarone, E.; Mustarelli, P. Physicochemical Characterization of AlCl3−1-Ethyl-3-methylimidazolium Chloride Ionic Liquid Electrolytes for Aluminum Rechargeable Batteries. *J. Phys. Chem. C* **2017**, *121*, 26607−26614.
(29) Borozdin, A.; Elterman, V.; Shevelin, P. Y.; Yolshina, L. Electrochemical behavior of aluminum in 1-ethyl-3-methylimidazolium chloroaluminate ionic liquids. *Electrochim. Acta* **2024**, *490*, 144265.
(30) Craig, B.; Schoetz, T.; Cruden, A.; Ponce de Leon, C. Review of current progress in non-aqueous aluminium batteries. *Renew. Sustain. Energy Rev.* **2020**, *133*, 110100.
(31) Chang, J.-K.; Chen, S.-Y.; Tsai, W.-T.; Deng, M.-J.; Sun, I.-W. Electrodeposition of aluminum on magnesium alloy in aluminum chloride (AlCl3)−1-ethyl-3-methylimidazolium chloride (EMIC) ionic liquid and its corrosion behavior. *Electrochem. Commun.* **2007**, *9*, 1602−1606.
(32) Guidat, M.; Rahide, F.; Löw, M.; Kim, J.; Ehrenberg, H.; Dsoke, S.; May, M. M. In Situ Monitoring of the Al(110)-[EMImCl]: AlCl3 Interface by Reflection Anisotropy Spectroscopy. *Batter. Supercaps* **2024**, *7*, e202300394.
(33) Sabi, N.; Palanisamy, K.; Rahide, F.; Daboss, S.; Kranz, C.; Dsoke, S. Surface Properties-Performance Relationship of Aluminum Foil as Negative Electrode for Rechargeable Aluminum Batteries. *Batter. Supercaps* **2023**, *6*, e202300298.
(34) Xu, C.; Gao, W. Pilling-Bedworth ratio for oxidation of alloys. *Mater. Res. Innov.* **2000**, *3*, 231−235.
(35) Chen, H.; Xu, H.; Zheng, B.; Wang, S.; Huang, T.; Guo, F.; Gao, W.; Gao, C. Oxide Film Efficiently Suppresses Dendrite Growth in Aluminum-Ion Battery. *ACS Appl. Mater. Interfaces.* **2017**, *9*, 22628−22634.
(36) Das, S. K.; Mahapatra, S.; Lahan, H. Aluminium-ion batteries: developments and challenges. *J. Mater. Chem. A* **2017**, *5*, 6347−6367.
(37) Choi, S.; Go, H.; Lee, G.; Tak, Y. Electrochemical properties of an aluminum anode in an ionic liquid electrolyte for rechargeable aluminum-ion batteries. *Phys. Chem. Chem. Phys.* **2017**, *19*, 8653−8656.
(38) Loaiza, L. C.; Lindahl, N.; Johansson, P. Initial Evolution of Passivation Layers in Non-Aqueous Aluminium Batteries. *J. Electrochem. Soc.* **2023**, *170*, No. 030512.
(39) Rahide, F.; Palanisamy, K.; Flowers, J. K.; Hao, J.; Stein, H. S.; Kranz, C.; Ehrenberg, H.; Dsoke, S. Modification of Al Surface via Acidic Treatment and its Impact on Plating and Stripping. *ChemSusChem* **2023**, *17*, e202301142.
(40) Bai, P.; Li, J.; Brushett, F. R.; Bazant, M. Z. Transition of lithium growth mechanisms in liquid electrolytes. *Energy Environ. Sci.* **2016**, *9*, 3221−3229.
(41) Zheng, J.; Engelhard, M. H.; Mei, D.; Jiao, S.; Polzin, B. J.; Zhang, J.-G.; Xu, W. Electrolyte additive enabled fast charging and stable cycling lithium metal batteries. *Nat. Energy* **2017**, *2*, 17012.
(42) Benmayza, A.; Ramanathan, M.; Arthur, T. S.; Matsui, M.; Mizuno, F.; Guo, J.; Glans, P.-A.; Prakash, J. Effect of Electrolytic Properties of a Magnesium Organohaloaluminate Electrolyte on Magnesium Deposition. *J. Phys. Chem. C* **2013**, *117*, 26881−26888.
(43) Dymek, C. J.; King, L. A. Transport Numbers in Molten Aluminum Chloride-1-Methyl-3-Ethylimidazolium Chloride Mixtures. *J. Electrochem. Soc.* **1985**, *132*, 1375−1380.
(44) Hussey, C. L.; Oye, H. A. Transport Numbers in Molten Acidic Aluminum Chloride-1-Methyl-3-Ethylimidazolium Chloride: Their Relationship to EMF Measurements in Chloroaluminate Melts. *J. Electrochem. Soc.* **1984**, *131*, 1621−1625.
(45) Hussey, C. L.; Sanders, J. R.; Oye, H. A. Transport Numbers in the Basic Aluminum Chloride-1-Methyl-3-Ethylimidazolium Chloride Ionic Liquid. *J. Electrochem. Soc.* **1985**, *132*, 2156−2158.
(46) Villevieille, C. Interfaces and Interphases in Batteries: How to Identify and Monitor Them Properly Using Surface Sensitive Characterization Techniques. *Adv. Mater. Interfaces* **2022**, *9*, 2101865.
(47) Nojabaee, M.; Küster, K.; Starke, U.; Popovic, J.; Maier, J. Solid Electrolyte Interphase Evolution on Lithium Metal in Contact with Glyme-Based Electrolytes. *Small* **2020**, *16*, 2000756.
(48) Popovic, J. Solid Electrolyte Interphase Growth on Mg Metal Anode: Case Study of Glyme-Based Electrolytes. *Energy Technol.* **2021**, *9*, 2001056.
(49) Gomes, M. P.; Costa, I.; Pébère, N.; Rossi, J. L.; Tribollet, B.; Vivier, V. On the corrosion mechanism of Mg investigated by electrochemical impedance spectroscopy. *Electrochim. Acta* **2019**, *306*, 61−70.
(50) Löw, M.; Guidat, M.; Kim, J.; May, M. M. The interfacial structure of InP(100) in contact with HCl and H_2SO_4 studied by reflection anisotropy spectroscopy. *RSC Adv.* **2022**, *12*, 32756−32764.
(51) Lim, K.; Fenk, B.; Popovic, J.; Maier, J. Porosity of Solid Electrolyte Interphases on Alkali Metal Electrodes with Liquid Electrolytes. *ACS Appl. Mater. Interfaces.* **2021**, *13*, 51767−51774.
(52) Popovic, J.; Hasegawa, G.; Moudrakovski, I.; Maier, J. Infiltrated porous oxide monoliths as high lithium transference number electrolytes. *J. Mater. Chem. A* **2016**, *4*, 7135−7140.
(53) Maier, J. Concentration Polarization of Salt-Containing Liquid Electrolytes. *Adv. Funct. Mater.* **2011**, *21*, 1448−1455.
(54) Maier, J. Salt concentration polarization of liquid electrolytes and determination of transport properties of cations, anions, ion pairs and ion triples. *Electrochim. Acta* **2014**, *129*, 21−27.
(55) Popovic, J.; Höfler, D.; Melchior, J. P.; Münchinger, A.; List, B.; Maier, J. High Lithium Transference Number Electrolytes Containing Tetratriflylpropene's Lithium Salt. *J. Phys. Chem. Lett.* **2018**, *9*, 5116−5120.
(56) Aurbach, D.; Schechter, A.; Moshkovich, M.; Cohen, Y. On the Mechanisms of Reversible Magnesium Deposition Processes. *J. Electrochem. Soc.* **2001**, *148*, A1004.
(57) Gofer, Y.; Turgeman, R.; Cohen, H.; Aurbach, D. XPS Investigation of Surface Chemistry of Magnesium Electrodes in Contact with Organic Solutions of Organochloroaluminate Complex Salts. *Langmuir* **2003**, *19*, 2344−2348.
(58) Maddegalla, A.; Kumar, Y.; Chakrabarty, S.; Glagovsky, Y.; Schmerling, B.; Fridman, N.; Afri, M.; Aviv, H.; Aurbach, D.; Mukherjee, A.; Bravo-Zhivotovskii, D.; Noked, M. First isolation of solvated $MgCl^+$ species as the sole cations in electrolyte solutions for rechargeable Mg batteries. *Electrochim. Acta* **2023**, *463*, 142869.
(59) Lazanas, A. C.; Prodromidis, M. I. Electrochemical Impedance Spectroscopy-A Tutorial. *ACS Meas. Sci. Au* **2023**, *3*, 162−193.
(60) Roedern, E.; Kühnel, R.-S.; Remhof, A.; Battaglia, C. Magnesium Ethylenediamine Borohydride as Solid-State Electrolyte for Magnesium Batteries. *Sci. Rep.* **2017**, *7*, 46189.
(61) Sheha, E. Ion transport properties of magnesium bromide/dimethyl sulfoxide non-aqueous liquid electrolyte. *J. Adv. Res.* **2016**, *7*, 29−36.
(62) Natishan, P. M.; O'Grady, W. E. Chloride Ion Interactions with Oxide-Covered Aluminum Leading to Pitting Corrosion: A Review. *J. Electrochem. Soc.* **2014**, *161*, C421−C432.
(63) Hebb, M. H. Electrical Conductivity of Silver Sulfide. *J. Chem. Phys.* **1952**, *20*, 185−190.
(64) Wagner, C. Galvanische Zellen mit festen Elektrolyten mit gemischter Stromleitung. *Z. Elektrochem.* **1956**, *60*, 4−7.
(65) Evans, J.; Vincent, C. A.; Bruce, P. G. Electrochemical measurement of transference numbers in polymer electrolytes. *Polymer* **1987**, *28*, 2324−2328.
(66) Popovic, J. Insights into Cationic Transference Number Values and Solid Electrolyte Interphase Growth in Liquid/Solid Electrolytes

https://doi.org/10.1021/acsmaterialslett.4c01589
ACS Materials Lett. 2024, 6, 5120−5127

for Potassium Metal Batteries. *ACS Phys. Chem. Au.* **2022**, *2*, 490−495.
(67) Ravn Sørensen, P.; Jacobsen, T. Conductivity, charge transfer and transport number—an ac-investigation of the polymer electrolyte LiSCN-poly(ethyleneoxide). *Electrochim. Acta* **1982**, *27*, 1671−1675.
(68) Peng, Y.; Shinde, P. S.; Reddy, R. G. Diffusion coefficient and nucleation density studies on electrochemical deposition of aluminum from chloroaluminate ionic liquid electrolytes. *J. Electroanal. Chem.* **2021**, *895*, 115363.

https://doi.org/10.1021/acsmaterialslett.4c01589
ACS Materials Lett. 2024, 6, 5120−5127

5.5 Investigation of the Surface of a Mg Anode in Contact with a Grignard Electrolyte and a Boron-Base Electrolyte with and without Additive by Electrochemical Reflection Anisotropy Spectroscopy

The final section shows the investigation of magnesium single crystals in Grignard electrolytes and the boron-based $Mg[B(HFIP)_4]_2$ with and without an additive by electrochemical reflection anisotropy spectroscopy and the polishing routine to refurbish the crystals after use. The results of the investigation of the boron-based electrolyte will be part of the paper by Chandrappa et al. (B5 in the list of publications). Since the polishing routine was challenging and did not result in crystals that could be used for electrochemistry, only a limited number of results were produced, and the investigation on the Grignard electrolytes was, therefore, not published. I included this section in my thesis since it is important for the further investigation of the interphase of magnesium metal electrodes, and the original topic of my PhD was: "Transient operando studies on electrochemical interfaces in magnesium-based batteries by reflection anisotropy spectroscopy".

RA-Spectra of Magnesium

Figure 5.1 a) shows the reflection anisotropy spectrum of an Mg$(10\bar{1}0)$ single crystal. The spectrum shows a relatively broad peak with a maximum of around 4.7 eV. Since Mg$(10\bar{1}0)$ is an optically isotropic crystal orientation, it should theoretically not deliver an RA-spectrum. However, as shown in Figure 5.1 a), there is a spectrum which deviates from zero. From the literature, it is known that Mg processes a surface consisting of MgO and $Mg(OH)_2$.[166] To check whether the optical anisotropy stems from the magnesium oxide on the surface or not, the RA-spectrum of a MgO(110) single crystal was measured and a computational RA-spectrum of a MgO(110) single crystal was calculated. (The calculation of the computational spectrum was done by Holger Euchner.) The results are presented in Figure 5.1.

All three spectra have roughly the same shape, with an increase of the optical

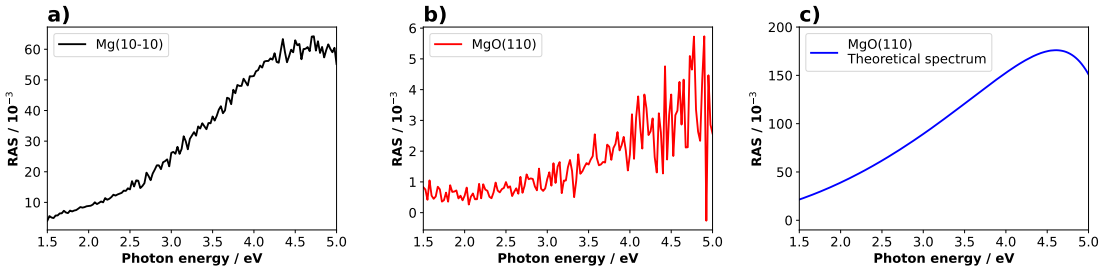

Figure 5.1: Reflection anisotropy spectrum of a) Mg($10\bar{1}0$) b) Mg(110) and c) a computational RAS spectrum of MgO(110)

anisotropy from low to high photon energies with a maximum between 4.5 eV and 5.0 eV. The quantitative difference comes from the different conditions under which these spectra were produced. For the computational spectrum, a perfect defect-free MgO crystal was assumed. Therefore, it has the highest anisotropy values. The MgO layer on top of the Mg crystal is imperfect; therefore, its anisotropy value is smaller than the computational spectrum. The MgO crystal also does not consist of a perfect single crystal. In addition, its surface roughness was relatively large, which resulted in low reflectivity and, therefore, low anisotropy values. The comparison of the three spectra strongly suggests that the anisotropy observed in the Mg($10\bar{1}0$) single crystal originates from an ordered MgO layer on top of the surface.

Operando Investigation of Mg in a Grignard Electrolyte

Figure 5.2 shows the RA- and DC-spectra of pristine Mg($10\bar{1}0$) and the same sample immersed in 1.7 M buthylmagesium chloride (BuMgCl). Figure 5.2 a) shows that the spectra are primarily identical for low photon energies. The sample spectrum inside the electrolyte peaks at around 3.0 eV; afterwards, it declines, and the spectrum becomes quite noisy. The DC-spectrum in Figure 5.2 b) shows that the reflectivity of the sample drops to zero after around 3.3 eV. This is because of the coloured electrolyte, which absorbs the light in this energy range. The non-existent reflectivity also explains why the optical anisotropy displays a high noise signal beyond 3.3 eV.

For the investigation of the Grignard electrolytes, 1.7 M BuMgCl was used as received. A two-electrode set-up was used with the Mg($10\bar{1}0$) single crystal as the

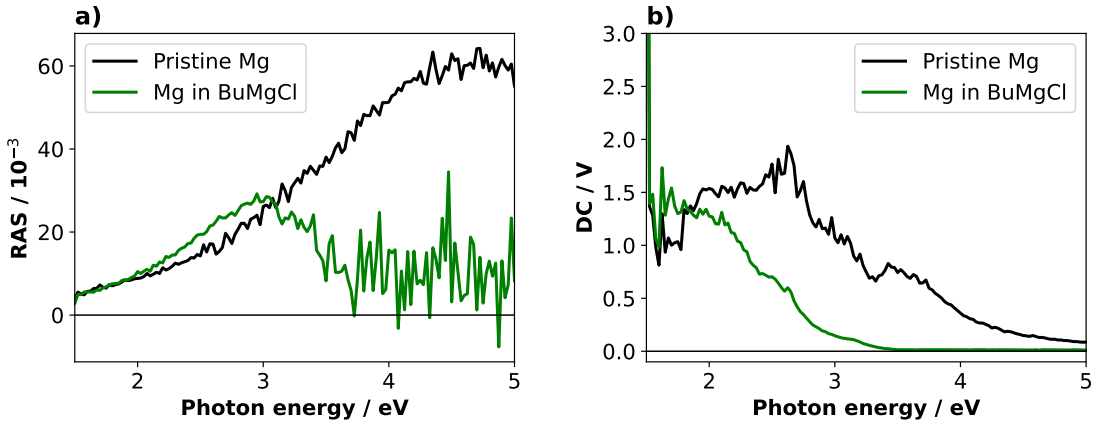

Figure 5.2: a) RA-spectra of pristine Mg and Mg immersed in 1.7 M BuMgCl.
b) DC-spectra of pristine Mg and Mg immersed in 1.7 M BuMgCl.

working electrode and an Mg-wire as a combined counter and the reference electrode. For the investigation, the cell was cycled between -0.5 V and 1 V (vs. Mg pseudo-reference) with a scan rate of 5 mV s^{-1} for two cycles. The results can be found in Figure 5.3.

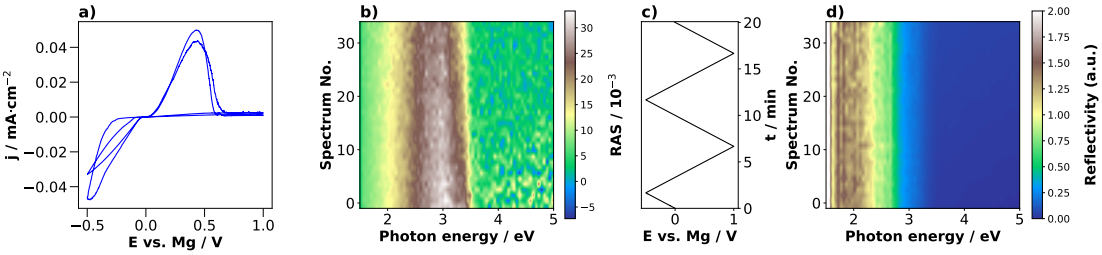

Figure 5.3: Cyclic voltammogram of Mg in contact with 1.7 M BuMgCl (-0.5 V to 1 V 5 mV s^{-1} 2 cycles) and the in parallel run colour plots of the surface b) anisotropy and d) reflectivity.

The CV in part a) shows the stripping and plating of magnesium. In parallel to the CV, a colour plot (the evolution of the RA-spectra over time) was recorded. It shows almost no changes, only slightly narrowing the anisotropy peak over time. Similarly, the sample's reflectivity does not change during the whole CV. There are two possible explanations for this observation. The first one could be that the plating of the deposited Mg happens underneath the MgO layer. This would explain why there are almost no changes in surface anisotropy and reflectivity. However, reports

from literature show that due to their high charge density Mg^{2+}-ions can not migrate through the surface layer formed on Mg-metal.[65] A second possible option could be that the current density is relatively low in comparison to, for example, the deposition of Al on HOPG (Publication B3), which means that also the deposited charge is lower, resulting in less metal being deposited. Therefore, the amount of deposited Mg is below the detection limit of the spectrometer, resulting in no change in the surface's anisotropy and reflectivity.

Due to the electrolyte's colour, the light gets absorbed, and the BuMgCl was diluted with stabilized THF to a concentration of 1.0 M. The same parameters for the CV were used as in the previous experiment, leading to the results shown in Figure 5.4.

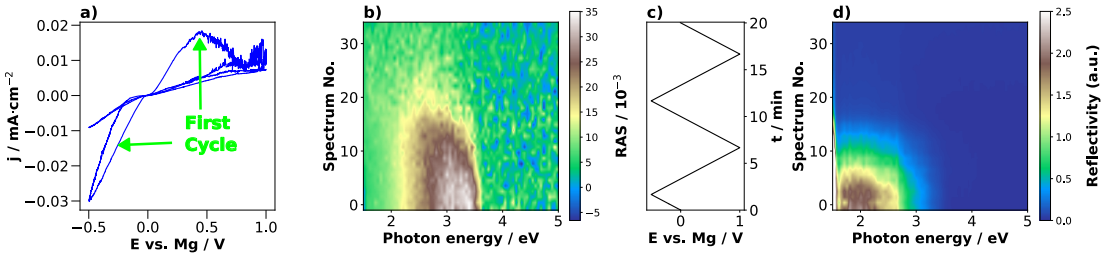

Figure 5.4: Cyclic voltammogram of Mg in contact with 1.0 M BuMgCl diluted with stabilized THF (-0.5 V to 1 V 5 mV s^{-1} 2 cycles) and the in parallel run colour plots of the surface b) anisotropy and d) reflectivity.

The CV in part a) looks more distorted compared to the CV in Figure 5.3. In addition, only the first cycle shows partial stripping and plating, while the second does not. By looking at the anisotropy colour plot, one observes that the peak between 2.5 eV and 3.5 eV is only visible until the middle of the spectrum; after that, it gradually disappears. In the reflectivity spectrum, the peak between 1.5 eV and 2.5 eV disappears in the first third of the colour plot. Combining the optical and chemical results, it is evident that an unordered surface layer forms on top of the Mg sample, blocking the stripping and plating of Mg. Since the only change to the previous experiment is the addition of stabilized THF to the cell, the THF stabilizer Butylhydroxytoluol (BHT) likely causes surface layer formation.[65] A reaction with the THF alone is unlikely since the commercially available Grignard also used THF as a solvent.

Operando Investigation of Mg in $Mg[B(HFIP)_4]_2$ Electrolyte with and without Additive

Research by Chandrappa et al.[167] showed that the addition of 3 wt.% of tris(trimethylsilyl) borate (TMSB) in a typical Cl-free $Mg[B(HFIP)_4]_2$/DME (MgBOR/DME) based non-aqueous electrolyte solution enables a stable Mg | Mo_6S_8 coin cell operation with up to 1000 cycles. The TMBS acts here as a scavenger for the native oxide layer and facilitates the formation of a stable solid electrolyte interphase layer on Mg, resulting in stable long-term electrochemical cycling. EC-RAS was used to uncover the surface reaction during the first few CV cycles. To elucidate the effect of the TMSB, experiments with the pure $Mg[B(HFIP)_4]_2$ and after the addition of the TMBS additive were performed.

As the first step, $Mg[B(HFIP)_4]_2$/DME without additive was investigated. The results are shown in Figure 5.5. Here, the anisotropy increases in the first 30 minutes, stays constant and declines slowly after around 60 minutes. Simultaneously, the DC signal increases from around 100 minutes onward. A possible explanation is the dissolution of the native surface oxide on the magnesium crystal. This is highly likely as the MgO delivers an anisotropy signal, while the Mg metal does not (see Figure 5.1 for comparison). After about 200 minutes, periodic oscillations start to appear in the DC signal and the RA signal. By comparing the dips in reflectance to the applied voltage and current, one can observe that it arises between the maximum of the anodic current and the maximum of the applied anodic potential. These dips in the reflectance indicate that either (mirco)roughening of the electrode surface or the development of an interphase layer occurs. The simultaneous rise of a local optical anisotropy maximum could stem from either an anisotropic (ordered) magnesium stripping or surface roughening and a (re)formation of an oxide layer. The periodic oscillations indicate an almost reversible process, which originates from unhindered and anisotropic metallic stripping and plating or the potential-dependent formation-dissolution of the interphase.

Figure 5.6 shows the same EC-RAS investigation, but this time, after adding 3 wt.% TMSB to the $Mg[B(HFIP)_4]_2$/DME. In this case, there are no significant variations in the optical anisotropy. Nevertheless, the reflectance decreases during the initial three cycles, returning to slightly higher values than the original reflectance after seven cycles. This finding shows the extended pattern of the sample without

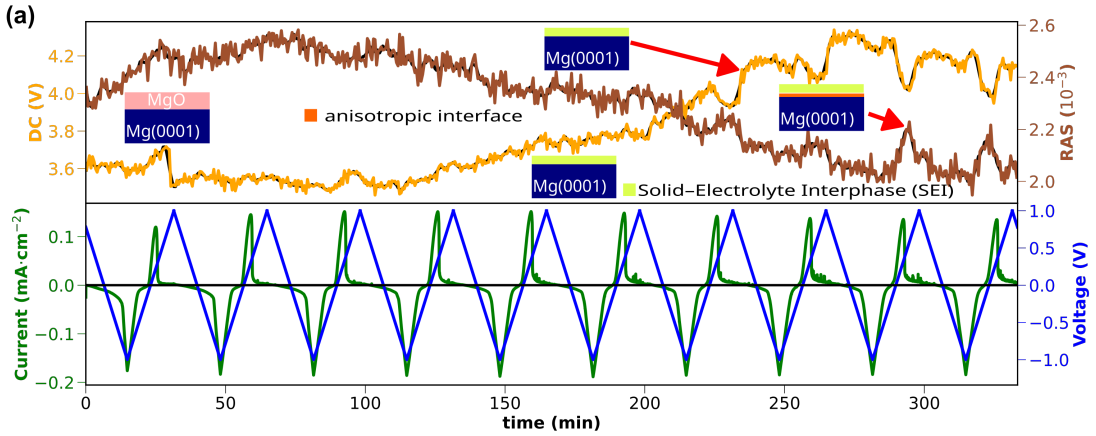

Figure 5.5: Changes in the anisotropy and reflectance during cycling without additive: The upper part shows a transient at 2.64 eV of the real part of the reflective anisotropy (RAS) in borown and the reflectance (proportional to the DC-signal, orange). The graphs were smoothed with a Savitzky-Golay-Filter. The lower part shows the current density (green) and the corresponding applied voltage (blue). CV: -1 V to 1 V (vs. Mg pseudo-reference) 2 mV s^2, 10 cycles. Taken from [167]. Figure licensed under CC BY 4.0, `https://creativecommons.org/licenses/by/4.0/`

additive and provides evidence that an SEI with increased reflectance is formed during these cycles. This makes interpreting the processes at the solid-liquid interphase difficult, as the additive-free electrolyte shows an entirely different behaviour towards the additive's impact on SEI growth, which promotes a more isotropic structure.

Polishing Routine of Mg

For the performance of RA experiments, gleaming single-crystal surfaces are required. However, after several experiments, the magnesium crystal becomes dull, and the RA spectrum becomes very noisy. Mechanical polishing of the Mg crystal was tried to change this. For the polishing, a MiniMet 1000 from Buehler was used. The polishing was done on different polishing cloths with gradually decreasing grain size in the polishing suspension. Table 5.1 displays the polishing routine with the different parameters discovered to obtain the optimal results.[168]

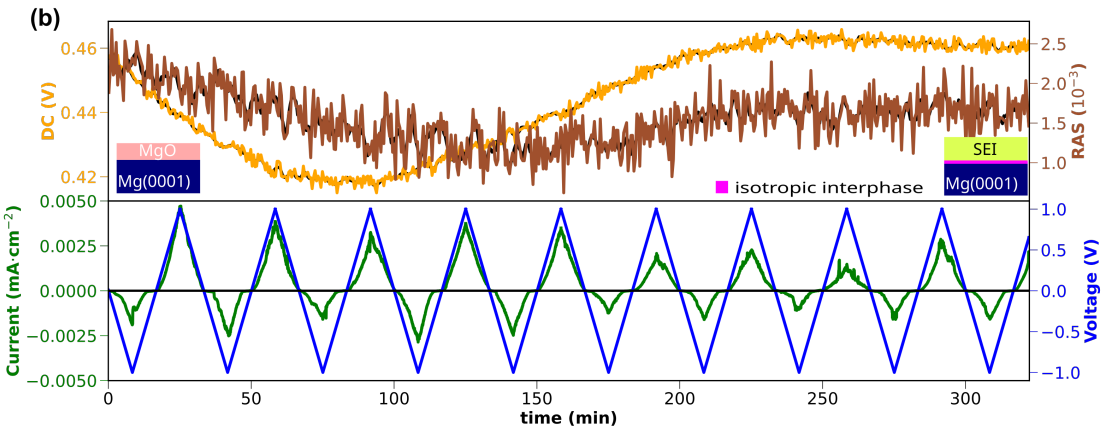

Figure 5.6: Changes in the anisotropy and reflectance during cycling with the additive: The upper part shows a transient at 2.64 eV, the lower part shows the current density and the corresponding applied voltage of the CV: -1 V to 1 V (vs. Mg pseudo-reference) 2 mV s^{-1}, 10 cycles. Taken from [167]. Figure licensed under CC BY 4.0, `https://creativecommons.org/licenses/by/4.0/`

After the polishing, the crystal was cleaned with cotton wool wetted with ethanol, followed by 10 minutes of sonication in a small vial filled with THF.

In the final step, the sample was chemically polished by dipping it in one of two etching solutions for about 5 to 10 seconds. During the chemical etching, bubbles formed on the surface.

The first etching solution contained the following components:[168]

- Ethylene glycol 75 mL
- MilliQ water: 24 mL
- Nitric acid (70%): 1 mL

The second etching solution contains the following compounds:[168]

- Acetic acid: 20 mL
- Nitric acid (70%): 1 mL
- Ethylene glycol: 60 mL
- MilliQ water: 20 mL

Table 5.1: Polishing parameters

Step	Polishing cloth	Polishing suspension	speed [rmp]	pressure [pounds]	time [min]
1	TexMetC	9 µm MetaDi Oil-based Diamond	30	1	10
2	TexMetC	3 µm MetaDi Oil-based Diamond	20	1	6
3	TexMetC	1 µm MetaDi Oil-based Diamond	20	1	5
4	ChemoMet	0.05 µm MasterPolish	20	1	2

Figure 5.7 shows a photo of the surface of the Mg-crystal after usage and the same crystal after the polishing routine. It is observable that during the experiments, the crystal has become dull, and marks of the O-ring have formed. The right-hand side photo (Figure 5.7) shows the crystal after the polishing routine. A mirror-like surface is visible, indicating that the sample has regained its original surface properties.

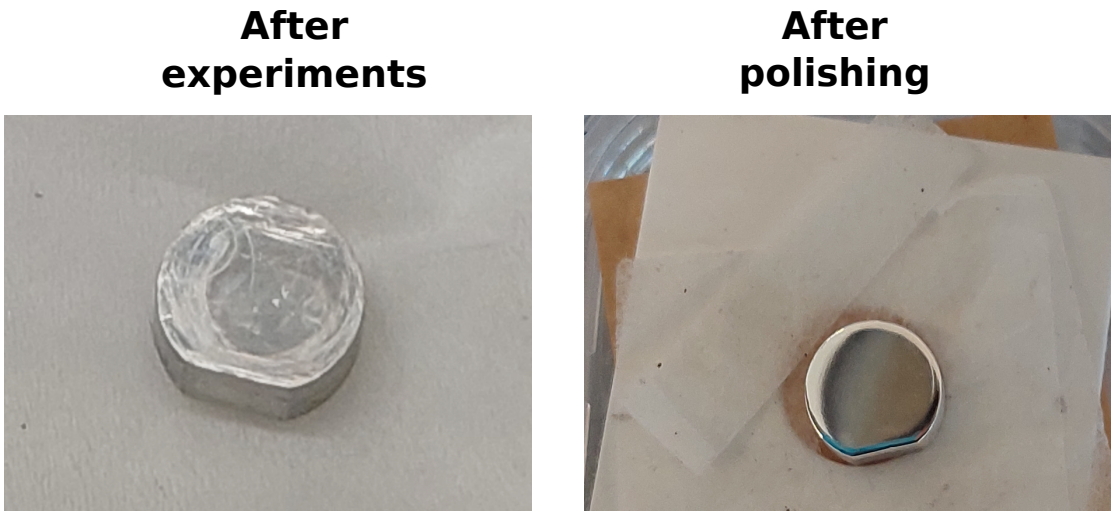

Figure 5.7: Left: Photo of the Mg single-crystal after the experiments. Right: Photo of the Mg single-crystal after the polishing routine.

Comparing the reflection anisotropy and reflectivity spectra (Figure 5.8) of the pristine and polished samples shows that the optical anisotropy of the polished sample has increased compared to the pristine one, hinting towards a higher optical anisotropy and therefore a more ordered sample surface after polishing. In con-

trast, the DC signal decreased between the pristine and polished samples. This means that the polished sample is less reflective than the pristine one.

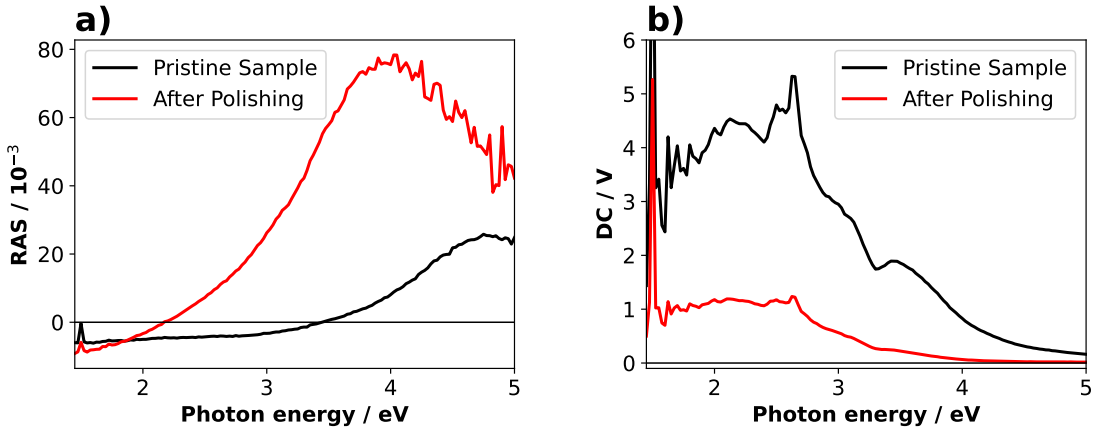

Figure 5.8: Left: RA-spectra of the pristine Mg-crystal and after polishing. Right: DC-spectra of the pristine Mg-crystal after polishing.

As the sample regained its original gleamingness, its electrochemical performance was tested in the next step. Therefore, the polished sample was cycled between -0.5 V and 1 V with a scan rate of 5 mV s^{-1} for ten cycles; 1.7 M BuMgCl was used as electrolyte. Figure 5.9 shows the CV and the corresponding anisotropy and reflectivity colour plots. The CV shows that there is partial plating and stripping. However, the graph is very noisy, and the anodic part looks more like ohmic resistance than actually stripping. This could indicate that a side reaction occurs, which hinders the stripping of the magnesium. This indicates that despite the crystal being optically close to its pristine state, its electrochemical performance is not. A possible explanation could be that a surface film is still present or is formed by the polishing routine on the sample surface, blocking the transport of ions. This cloud also explains the lower reflectivity of the sample after polishing compared to the piste surface. SEM/EDX measurements, however, show no evidence of a surface layer. However, it may be below their detection limit. Several attempts were made to regain the Mg crystal's reflectivity and electrochemical performance. However, all failed to regain both properties. Therefore, only a limited amount of experiments could be performed with Mg single crystals.

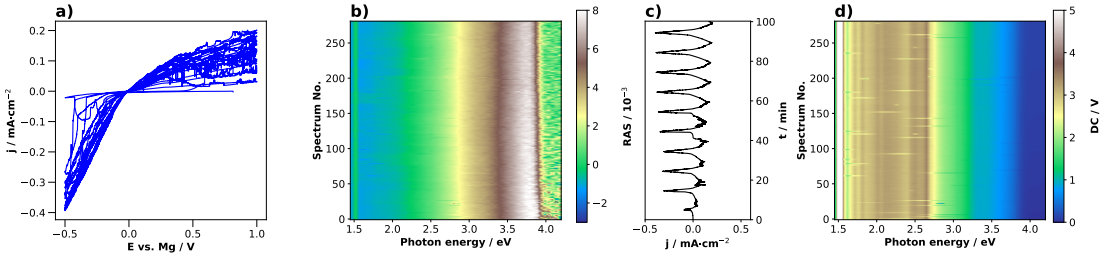

Figure 5.9: Cyclic voltammogram of Mg after polishing in contact with 1.7 M BuMgCl (-0.5 V to 1 V 5 mV s^{-1} 10 cycles) and the in parallel run colour plots of the surface b) anisotropy and d) reflectivity.

Conclusion

The EC-RAS experiments with Mg as a substrate showed that when using Grignard as an electrolyte, almost no changes in the surface anisotropy could be detected during stripping and plating. The dilution of electrolytes with stabilized THF should be avoided, as it leads to the formation of an unordered and ion-blocking surface layer. Control experiments in which unstabilized THF was used to dilute the Grignad could not be performed as, to this point, the sample was already dull and could not be used for further experiments.

The use of the $Mg[B(HFIP)_4]_2$ shows after several cycles oscillation in the anisotropy and reflectivity spectra. This indicates the ordered stripping of the magnesium from the surface as well as the roughening of the surface. When adding TMSB as an additive, this periodic oscillation does not occur, and the spectra hint toward forming an SEI.

The polishing routine regained the gleamiyness of the surface; however, the electrochemical performance failed. A possible explanation is that a thin surface film formed during the polishing, blocking the ion transport. A possible way to regain the original surface and achieve electrochemical performance would be to sputter the surface layer inside an ultra-high vacuum (UHV) chamber followed by an annealing step. However, this approach is quite time-consuming and requires access to a UHV chamber. However, mechanical polishing might be a great way to regain the pristine surface of metals with less reactivity than Mg, which can also not be flame annealed, for example, iron.

6 Conclusion

This thesis investigates the properties of solid-liquid electrolyte interphase using reflection anisotropy spectroscopy (RAS), exploring its novel applications in battery research and electrochemical impedance spectroscopy (EIS). RAS provides operando data on the interface in the electrolyte under applied potential, which many other techniques cannot achieve. The information gathered with RAS are complemented by EIS measurements. EIS is used to gather crucial information for electrochemical systems performance, such as the resistance and capacity of the solid electrolyte interphase (SEI), ion transport properties or the transference number of the electrolyte.

In the first part, the III-V semiconductor InP was investigated in acidic media to elucidate its surface corrosion as a potential material in PEC water splitting. RAS investigations revealed potential-induced anisotropy oscillations in the cathodic region, partly due to the restructuring of the interface and the formation of a thin, well-ordered $InCl_x$ surface film.

For the research on magnesium batteries, Grignards were used as an electrolyte. Here, the EIS measurements showed increased SEI resistance over time. However, one cyclic voltammogram cycle significantly reduced the SEI's resistance and capacity. Additionally, the cationic transference number of the Grignard electrolyte increased by two orders of magnitude after just one CV cycle. Attempts to use RAS on the Grignard system were only partially successful due to the formation of a surface layer on the magnesium single crystal after several experiments. However, it showed that using stabilized THF to dilute the Grignards leads to an unordered blocking layer on the Mg surface. The use of a new crystal enabled the investigation of the boron-based electrolyte $Mg[B(HFIP)_4]_2$ with the additive tris(trimethylsilyl) borate (TMSB). The results revealed a partially ordered interfacial structure between the electrode and electrolyte during the initial stripping and plating without the addi-

tive. Adding TMSB promoted the formation of an altered and more isotropic SEI.

For rechargeable aluminium batteries, the study explored the open-circuit treatment and electroplating/stripping of aluminium in [EMImCl]:$AlCl_3$ (1:1.5). The use of RAS and SEM/EDX analysis allowed the tracking of surface roughness, homogeneity, and oxide layer evolution. EIS measurements showed that the initially dense native oxide layer became porous and more ion-conducting after prolonged contact with the electrolyte. Finally, the electrodeposition of aluminium to HOPG was studied using the [EMImCl]:$AlCl_3$ (1:1.5) electrolyte. The combination of RAS and SEM/EDX revealed that the deposited aluminium morphology strongly depended on the applied potential, with rough islands forming at less cathodic potentials and a flat layer of deposited Al forming at more cathodic potentials. Additionally, significant changes in anisotropy at the beginning of the nucleation step were observed, suggesting an ordered initial step in the aluminium nucleation. Additionally, the formation of an SEI was detected on the HOPG during the interaction of $AlCl_4^-$ into the host structure, with an optical anisotropic first step either due to the swelling of most structures or the initial formation of the SEI. The swelling of the graphite structure and the SEI formation can be beneficial for the battery since the swelling of the graphite causes partially turbostratic structures and gradually forms new defects inside the graphite, resulting in the gradual increase of the capacity.[169] The formation of an SEI on the graphite does, on the other hand, lead to a decrease in specific capacity after the first cycle and a simultaneous increase of the coulombic efficiency between the first and the second cycle.[102]

In further research, reflection anisotropy microscopy (RAM) or two-dimensional surface optical reflectance (2D-SOR) can be utilized to enhance the spatial resolution of battery and PEC water-splitting interface investigations. A recent paper developed a model combining anisotropy and reflectance transients with SEM images, enabling real-time operando control of surface morphologies as a function of electrochemical parameters.[170] This approach could provide more detailed insight into the formation of dendrites and might further improve the investigation of surface morphologies via pulsed current. Using graphite as anode material could be beneficial for using non-corrosive $AlCl_3$-free electrolytes, which currently face the issue of sluggish stripping and plating onto aluminium. Additional information on the behaviour detected during the EIS and the significant changes in cationic transference numbers could help identify the involved species. Further investigation

with Fourier-transform infrared spectroscopy (FTIR) or nuclear magnetic resonance spectroscopy (NMR) could also be beneficial.

7 Acknowledgment

This page has been removed for data protection reasons.

8 List of Symbols and Abbreviations

Symbols

Symbol	Unit	Denotation
A		Arrhenius prefactor
A	m^2	Surface area
a	$mol\,L^{-1}$	Chemical activity
α		Aperture angle of the objective lens
c	$mol\,L^{-1}$	Concentration
c	$299792458\,m\,s^{-1}$	Speed of light
χ_s	$kJ\,mol^{-1}$	Electron affinity
D	$m^2\,s$	Diffusion coefficient
E	V	Potential
E_a	J	Activation energy
E^0	V	Standard potential
e	$-1.60 \cdot 10^{-19}$ C	Charge of electron
f	s^{-1}	Frequency
${}^*E_{Fn}$	eV	Quasi-Fermi level of electrons
${}^*E_{Fp}$	eV	Quasi-Fermi level of protons
η	V	Overpotential
F	$98485\,C\,mol^{-1}$	Faraday constant
γ	$J\,m^{-2}$	Surface energy
h	$6.63 \cdot 10^{-34}\,J\,s$	Planck constant
I	A	Current
I	cd	Light intensity
k_B	$1.38 \times 10^{-23}\,J\,K^{-1}$	Boltzmann constant
λ	m	Wavelength

m	kg	Mass of particle
m_e	$9.11 \cdot 10^{-31}$ kg	Mass of electron
μ	J mol^{-1}	Electrochemical potential
N		Number of atoms
n		Number of electrons
n		Refractive index
ν	V·s^{-1}	Scan rate
ν	m·s^{-1}	Velocity of electron
ω	s^{-1}	Angular frequency
Φ	eV	Work function
Φ_{SB}	eV	Schottky barrier
ϕ	°	Phase angle
Q	C	Charge
R	8.314 J mol^{-1} K^{-1}	Universal gas constant
R	Ω	Resistance
R		Fresnel reflection amplitude
r		Fresnel reflection coefficients
R_{el}	Ω	Electrolyte resistance
$R_{tot,0}$	Ω	Initial total resistance
$R_{SEI,0}$	Ω	Initial SEI resistance
σ	S m^{-1}	Conductivity
T	K	Temperature
t^+		Cationic transference number
U	V	Accelerating voltage of the electron
u	cm^2 V^{-1} s^{-1}	Mobility
U_0	V	Initial voltage
U_∞	V	Steady state voltage
V	V	Voltage
Z	Ω	Impedance
z		Number of electrons
Z_d	Ω	Impedance from the bulk diffusion
Z_{Im}	Ω	Imaginary part of the impedance
Z_{Re}	Ω	Real part of the impedance

Abbreviations and Notations

Abbreviation / Notation	Denotation
2D-SOR	Two-dimensional surface optical reflectance
AFM	Atomic force microscopy
AM	Active material
bcc	Body-centered cubic
BSE	Backscattered electron
BHT	Butylhydroxytoluol
BMImCl	1-Butyl-3-methylimidazoliumchlorid
BuMgCl	Buthylmagesium chloride
C	Capacitor
CA	Chronoamperometry
CB	Conduction band
CE	Counter electrode
CV	Cyclic voltammetry
DC	Direct current (RAS: proportional to the reflectivity)
DME	Dimethoxyethane
EC-RAS	Electrochemical reflection anisotropy spectroscopy
EC-STM	Electrochemical scanning tunnelling microscopy
EDL	Electrochemical double layer
EDX	Energy despersive X-ray spectroscopy
EIS	Electrochemical impedance spectroscopy
EMImCl	1-Ethyl-3-methylimidazolium chloride
fcc	Face-centered cubic
FIB-SEM	Focused ion beam scanning electron microscopy
FTIR	Fourier-transform infrared spectroscopy
GC-MS	Gas chromatography coupled with mass spectrometry
hcp	Hexagonal close-packed
HER	Hydrogen evolution reaction
HFIP	Hexafluoroisopropanol
HOPG	Highly ordered pyrolytic graphite
IHP	Inner Helmholtz plane
InP	Indium phosphide

IR-drop	Ohmic drop
LEED	Low-energy electron diffraction
LFP	Lithium iron phosphate
LIBs	Lithium-ion batteries
MBE	Molecular beam epitaxy
MOVPE	Metal-organic vapour phase epitaxy
NAPXPS	Near ambient pressure X-ray photoelectron spectroscopy
NMC	Lithium-nickel-mangan-cobalt-oxide
NMR	Nuclear magnetic resonance spectroscopy
OCP	Open circuit potential
OER	Oxygen evolution reaction
OHP	Outer Helmholtz plane
P–B ratio	Pilling–Bedworth ratio
PEC	Photoelectrochemical
PEM	Photo-elastic modulator
POLiS	Post Lithium Storage
ppm	parts per million
PV	Photovoltaic
PV-EC	Photovoltaic-Electrochemical
R	Resistor
RA	Reflection anisotropy
RAM	Reflection anisotropy microscopy
RAS	Reflection anisotropy spectroscopy
RABs	Rechargeable aluminium batteries
RDCB	Rechargeable dual-carbon battery
RE	Reference electrode
RMBs	Rechargeable magnesium batteries
RTIL	Room-temperature ionic liquids
SC	Semiconductor
SE	Secondary electrons
SEI	Solid electrolyte interphase
SEM	Scanning electron microscopy
SHE	Standard hydrogen electrode
STH	Solar-to-hydrogen
TEM	Transmission electron microscopy

THF	Tetrahydrofuran
TMSB	Tris(trimethylsilyl) borate
TOF-SIMS	Time-of-flight secondary ion mass spectrometry
UHV	Ultra-high vacuum
VB	Valance band
WE	Working electrode
WDC	Watt direct current
XAS	X-ray absorption spectroscopy
XPS	X-ray photoelectron spectroscopy

9 List of Publications and Conferences Contributions

A. Review Papers and Book Chapters

A1.

Guidat, M.; **Löw, M.**; Kölbach, M.; Kim, J.; May, M. M. Experimental and Computational Aspects of Electrochemical Reflection Anisotropy Spectroscopy: A Review. ChemElectroChem 2023, 10 (8), e202300027.

DOI: 10.1002/celc.202300027

Conceptualization: MMM, MG, and MK. Formal analysis and experiments: **ML(30%)**, MG, JK, and MMM. Writing-Original Draft preparation: MG, JK, **ML(10%)**, and MK. Writing-Review: MG, JK, **ML(20%)**, MK, and MMM. Supervision: MMM.

A2.

Hajduk, A.; Zare Pour, M. A.; Paszuk, A.; Guidat, M.; **Löw, M.**; Ullmann, F.; Moritz, D. C.; Hofmann, J. P.; Krischok, S.; Runge, E.; Schmidt, W. G.; Jaegermann, W.; May, M. M.; Hannappel, T. (Photo-)Electrochemical Reactions on Semiconductor Surfaces, Part B: III-V Surfaces–Atomic and Electronic Structure. In Encyclopedia of Solid-Liquid Interfaces (First Edition); Wandelt, K., Bussetti, G., Eds.; Elsevier: Oxford, 2024; pp 120–156.

DOI: 10.1016/B978-0-323-85669-0.00113-6

Section ”III-V based liquid electrolyte contacts for H_2O splitting”

Research Papers

B1.

Löw, M.; Guidat, M.; Kim, J.; May, M. M. The Interfacial Structure of InP(100) in Contact with HCl and H_2SO_4 Studied by Reflection Anisotropy Spectroscopy. RSC Adv. 2022, 12 (50), 32756–32764.

DOI: 10.1039/d2ra05159a

Conceptualization: MMM, **ML**, and MG. Formal analysis and experiments: **ML**, MG, JK, and MMM. Writing-Original Draft preparation: **ML (60%)**, MG, JK, MMM. Writing-Review: **ML**, MG, JK, and MMM. Supervision: MMM.

B2.

Guidat, M.; Rahide, F.; **Löw, M.**; Kim, J.; Ehrenberg, H.; Dsoke, S.; May, M. M. In Situ Monitoring of the Al(110)-[EMImCl]:$AlCl_3$ Interface by Reflection Anisotropy Spectroscopy. Batteries & Supercaps 2024,7, e202300394.

DOI: 10.1002/batt.202300394

Conceptualization: FR, MG, SD, and MMM. Formal analysis and experiments: MG, FR, **ML**, and JK. Writing-Original Draft preparation: MG, FR, and JK. Writing-Review: MG, FR, **ML**, HE,SD, and MMM. Supervision: SD and MMM.

B3.

Löw, M.; May, M.M.; Operando Investigation of Al Plating Regimes on HOPG in [EMImCl]:$AlCl_3$ by Electrochemical Reflection Anisotropy Spectroscopy. Batteries & Supercaps 2024, e202400610.

DOI: 10.1002/batt.202400610

Conceptualization: **ML** and MMM. Formal analysis and experiments: **ML**. Writing-Original Draft preparation: **ML (70%)** and MMM. Writing-Review: **ML**, and MMM. Supervision: MMM.

B4.

Löw, M.; Grill, J.; May, M.M.; Popovic-Neuber, J. Magnesium and Aluminum in Contact with Liquid Battery Electrolytes: Ion Transport through Interphases and in the Bulk. ACS Materials Lett. 2024, 6, 11, 5120–5127.

DOI: 10.1021/acsmaterialslett.4c01589

Conceptualization: **ML**, JPN and MMM. Formal analysis and experiments: **ML**, JG and JPN. Writing-Original Draft preparation: **ML** and JPN. Writing-Review: **ML**, JPN and MMM. Supervision: JPN and MMM.

B5.

Chandrappa, S. G.; Karkera, G.; **Löw, M.**; Euchner, H.; Panja, S.; Bhattarai, M. K.; May, M.M.; Zhao-Karger, Z.; Fichtner, M. Effect of Silicon-Based Electrolyte Additive on the Solid-Electrolyte Interphase of Rechargeable Mg Batteries. Advanced Science, 2026, 13.2, e10456.

DOI: 10.1002/advs.202510456

Conceptualization: SGC and GK. Formal analysis and experiments: SGC, GK, **ML**, HE, SP and MKB. Writing-Original Draft preparation: SGC, GK; and **ML**, HE and MMM. Supervision: MMM, ZZK and MF.

Papers from previous work

C1.

Löw, M.; Maroni, F.; Zaubitzer, S.; Dongmo, S.; Marinaro, M. Nucleation Mechanisms of Electrodeposited Magnesium on Metal Substrates. Batteries & Supercaps, 2024, 7, e202400250.

DOI: 10.1002/batt.202400250

C2.

Klein, J.; Chesnyak, V.; **Löw, M.**; Schilling, M.; Engstfeld, A. K.; Behm, R. J. Selective Modification and Probing of the Electrocatalytic Activity of Step Sites. Journal of the American Chemical Society, 2020, 142, 1278 - 1286.

DOI: 10.1021/jacs.9b10201

C3.

Engstfeld, A. E.; Forschner, L.; **Löw, M.**; Pithan, L.; Beyer, P.; Jusys, Z.; Bansmann, J.; Behm, R. J.; Drnec, J. Stabilization of Ru-Core Pt-Shell Model Electrodes by Electronic Effects and Electrooxidation Reactions. ChemCatChem, 2025, 17, e202401913.

DOI: 10.1002/cctc.202401913

Conferences Contributions

5. International Symposium on Magnesium Batteries (MagBatt V)
18.09. - 20.09.2024, Ulm, Germany
Poster: Ion transport in the bulk and interphases of Mg/Al liquid battery electrolyte systems
Authors: Mario Löw, Jonas Grill, Matthias M. May and Jelena Popovic-Neuber

Poster: Operando investigation of the interface of rechargeable multivalent batteries by reflection anisotropy spectroscopy
Authors: Mario Löw and Matthias M. May

International Operando Battery Days
12.06. - 14.06.2024 Grenoble, France
Talk: Operando investigation of the interface of rechargeable multivalent batteries with reflection anisotropy spectroscopy
Authors: Mario Löw, Margot Guidat, Fatemehsadat Rahide, Jongmin Kim, Holger Euchner, Helmut Ehrenberg, Sonia Dsoke and Matthias M. May

74th Annual Meeting of the International Society of Electrochemistry
03.09. - 08.09.2023 Lyon, France
Talk: Operando investigation of anodes for rechargeable magnesium metal batteries by reflection anisotropy spectroscopy
Authors: Mario Löw, Holger Euchner and Matthias M. May

DPG-Frühjahrstagung der Sektion Kondensierte Materie (SKM)
26.03. - 31.03.2023 Dresden, Germany
Talk: Investigation of Mg(0001) and Mg(10-10) surfaces in Grignard electrolytes by reflection anisotropy spectroscopy
Authors: Mario Löw, Holger Euchner and Matthias M. May

Electrochemistry 2022 - At the Interface between Chemistry and Physics
27.09. - 30.09.2022 Berlin, Germany
Poster: Investigation of Au(100) and Au(110) surfaces by electrochemical Reflection Anisotropy Spectroscopy in HCl and H_2SO_4
Authors: Mario Löw, Margot Guidat, Florian Keller, Justus Leist, Jongmin Kim and Matthias M. May

4. International Symposium on Magnesium Batteries (MagBatt IV)
06.09. - 08.09.2022, Ulm, Germany
Poster: Investigation of Mg(0001) and Mg(1010) Surfaces in Grignard Electrolyte by Reflection Anisotropy Spectroscopy
Authors: Mario Löw and Matthias M. May

84. Jahrestagung der DPG und DPG-Tagung der Sektion Kondensierte Materie (SKM)
27.09. - 01.10.2021, virtual
Poster: Investigation of Au(100) and Au(110) surfaces in electrolyte by Reflection Anisotropy Spectroscopy (RAS)
Authors: Mario Löw, Margot Guidat, Timothée Gômes, Jongmin Kim and Matthias M. May

Bibliography

[1] M. Roser, *Our World in Data* **2020**, https://ourworldindata.org/cheap-renewables-growth.

[2] H. Ritchie, *Our World in Data* **2021**, https://ourworldindata.org/battery-price-decline.

[3] M. Li, J. Lu, Z. Chen, K. Amine, *Advanced Materials* **2018**, *30*, 1800561.

[4] M. Winter, B. Barnett, K. Xu, *Chemical Reviews* **2018**, *118*, 11433–11456.

[5] D. Larcher, J.-M. Tarascon, *Nature Chemistry* **2014**, *7*, 19–29.

[6] J. B. Goodenough, Y. Kim, *Chemistry of Materials* **2009**, *22*, 587–603.

[7] X. Shi, Y. Qian, S. Yang, *ACS Sustainable Chemistry & Engineering* **2020**, *8*, 7097–7110.

[8] K. Alanne, S. Cao, *Applied Energy* **2019**, *238*, 284–302.

[9] A. M. Oliveira, R. R. Beswick, Y. Yan, *Current Opinion in Chemical Engineering* **2021**, *33*, 100701.

[10] D. W. Rankin, *Crystallography Reviews* **2009**, *15*, 223–224.

[11] C. Grosjean, P. H. Miranda, M. Perrin, P. Poggi, *Renewable and Sustainable Energy Reviews* **2012**, *16*, 1735–1744.

[12] C. Vaalma, D. Buchholz, M. Weil, S. Passerini, *Nature Reviews Materials* **2018**, *3*, 1–11.

[13] W. Pantoja, J. A. Perez-Taborda, A. Avila, *Batteries* **2022**, *8*, 105.

[14] E. A. Olivetti, G. Ceder, G. G. Gaustad, X. Fu, *Joule* **2017**, *1*, 229–243.

[15] J. Tu, W.-L. Song, H. Lei, Z. Yu, L.-L. Chen, M. Wang, S. Jiao, *Chemical Reviews* **2021**, *121*, 4903–4961.

[16] F. Liu, T. Wang, X. Liu, L. Fan, *Advanced Energy Materials* **2020**, *11*, 2000787.

[17] R. Wang, W. Cui, F. Chu, F. Wu, *Journal of Energy Chemistry* **2020**, *48*, 145–159.

[18] L. Truche, E. F. Bazarkina, *E3S Web of Conferences* **2019**, *98*, (Eds.: O. Chudaev, Y. Kharaka, R. Harmon, R. Millot, O. Shouakar-Stash), 03006.

[19] F. Dawood, M. Anda, G. Shafiullah, *International Journal of Hydrogen Energy* **2020**, *45*, 3847–3869.

[20] A. M. Abdalla, S. Hossain, O. B. Nisfindy, A. T. Azad, M. Dawood, A. K. Azad, *Energy Conversion and Management* **2018**, *165*, 602–627.

[21] B. A. Pinaud, J. D. Benck, L. C. Seitz, A. J. Forman, Z. Chen, T. G. Deutsch, B. D. James, K. N. Baum, G. N. Baum, S. Ardo, H. Wang, E. Miller, T. F. Jaramillo, *Energy & Environmental Science* **2013**, *6*, 1983.

[22] H. Song, S. Luo, H. Huang, B. Deng, J. Ye, *ACS Energy Letters* **2022**, *7*, 1043–1065.

[23] A. Heller, B. Miller, H. J. Lewerenz, K. J. Bachmann, *Journal of the American Chemical Society* **1980**, *102*, 6555–6556.

[24] A. G. Muñoz, C. Heine, H. W. Klemm, T. Hannappel, N. Szabo, H.-J. Lewerenz, *ECS Transactions* **2011**, *35*, 141–150.

[25] M. M. May, H.-J. Lewerenz, D. Lackner, F. Dimroth, T. Hannappel, *Nature Communications* **2015**, *6*, 8286.

[26] J. L. Young, M. A. Steiner, H. Döscher, R. M. France, J. A. Turner, T. Deutsch, *Nature Energy* **2017**, *2*, 1–8.

[27] J. Tournet, Y. Lee, S. K. Karuturi, H. H. Tan, C. Jagadish, *ACS Energy Letters* **2020**, *5*, 611–622.

[28] B. C. Wood, E. Schwegler, W. I. Choi, T. Ogitsu, *The Journal of Physical Chemistry C* **2014**, *118*, 1062–1070.

[29] M. M. May, H.-J. Lewerenz, T. Hannappel, *The Journal of Physical Chemistry C* **2014**, *118*, 19032–19041.

[30] L. Carrette, K. A. Friedrich, U. Stimming, *Fuel Cells* **2001**, *1*, 5–39.

[31] J. H. Um, S. Yu, *Advanced Energy Materials* **2020**, *11*, 2003004.

[32] M. Guidat, M. Löw, M. Kölbach, J. Kim, M. M. May, *ChemElectroChem* **2023**, *10*, e202300027.

[33] M. Löw, M. Guidat, J. Kim, M. M. May, *RSC Advances* **2022**, *12*, 32756–32764.

[34] M. Gaberšček, *Nature Communications* **2021**, *12*, 6513.

[35] J. Popovic in *Nanomaterials for Electrochemical Energy Storage - Challenges and Opportunities*, Elsevier, **2021**, pp. 327–359.

[36] M. Winter, R. J. Brodd, *Chemical Reviews* **2004**, *104*, 4245–4270.

[37] *Batteries, Present and future energy storage challenges*, (Eds.: S. Passerini, D. Bresser, A. Moretti, A. Varzi), Besteht aus volume 1 und volume 2, Wiley-VCH Verlag GmbH & Co. KGaA, Weinheim, **2020**, 1896 pp.

[38] *Electrochemical Dictionary*, Springer Berlin Heidelberg, **2008**.

[39] C. Deng, X. Li, R. Chen, K. Ye, J. Lipton, S. A. Maclean, H. Wang, A. D. Taylor, G. Weng, *Energy Storage Materials* **2023**, *60*, 102820.

[40] A. Manthiram, *Nature Communications* **2020**, *11*, 1550.

[41] X.-B. Cheng, R. Zhang, C.-Z. Zhao, Q. Zhang, *Chemical Reviews* **2017**, *117*, 10403–10473.

[42] K. Xu, *Chemical Reviews* **2004**, *104*, 4303–4418.

[43] J. Popovic, *Nature Communications* **2021**, *12*, 6240.

[44] H. Helmholtz, *Annalen der Physik* **1879**, *243*, 337–382.

[45] G. Wedler, H.-J. Freund, *Lehrbuch der physikalischen Chemie*, 6., vollst. überarb. und aktualisierte Aufl., Wiley-VCH, Weinheim, **2012**, 1141 pp.

[46] K. Jackowska, *Applied Electrochemistry, Aspects in Material and Environmental Science*, 2nd Edition, expanded and amended, (Ed.: P. Krysiński), De Gruyter, Berlin, **2024**, 1390 pp.

[47] L. L. Zhang, X. S. Zhao, *Chemical Society Reviews* **2009**, *38*, 2520.

[48] H. Du, K. Song, M. Yang, P. Huang, W. Chen, *ChemSusChem* **2023**, *16*, e202300708.

[49] R. Bedworth, N. Pilling, *J Inst Met* **1923**, *29*, 529 –582.

[50] C. Xu, W. Gao, *Materials Research Innovations* **2000**, *3*, 231–235.

[51] E. McCafferty in *Introduction to Corrosion Science*, Springer New York, New York, NY, **2010**, pp. 209–262.

[52] P. Peljo, H. H. Girault, *Energy & Environmental Science* **2018**, *11*, 2306–2309.

[53] M. L. Meyerson, J. K. Sheavly, A. Dolocan, M. P. Griffin, A. H. Pandit, R. Rodriguez, R. M. Stephens, D. A. Vanden Bout, A. Heller, C. B. Mullins, *Journal of Materials Chemistry A* **2019**, *7*, 14882–14894.

[54] P. Bai, J. Li, F. R. Brushett, M. Z. Bazant, *Energy & Environmental Science* **2016**, *9*, 3221–3229.

[55] W. Schmickler, E. Santos, *Interfacial Electrochemistry*, Springer Berlin Heidelberg, **2010**.

[56] E. R. Cooper, M. Li, I. Gentle, Q. Xia, R. Knibbe, *Angewandte Chemie International Edition* **2023**, *62*, e202309247.

[57] M. Paunovic, *Fundamentals of electrochemical deposition*, 2nd ed, (Ed.: M. Schlesinger), Includes bibliographical references and index, Wiley, Hoboken, N.J, **2006**, 1373 pp.

[58] A. M. Tripathi, W.-N. Su, B. J. Hwang, *Chemical Society Reviews* **2018**, *47*, 736–851.

[59] I. Källquist, R. Le Ruyet, H. Liu, R. Mogensen, M.-T. Lee, K. Edström, A. J. Naylor, *Journal of Materials Chemistry A* **2022**, *10*, 19466–19505.

[60] E. J. Crumlin, Z. Liu, H. Bluhm, W. Yang, J. Guo, Z. Hussain, *Journal of Electron Spectroscopy and Related Phenomena* **2015**, *200*, 264–273.

[61] M Salmeron, R Schlögel, *Surface Science Reports* **2008**, *63*, 169–199.

[62] M. R. Palacin, P. Johansson, R. Dominko, B. Dlugatch, D. Aurbach, Z. Li, M. Fichtner, O. Lužanin, J. Bitenc, Z. Wei, C. Glaser, J. Janek, A. Fernández-Barquín, A. R. Mainar, O. Leonet, I. Urdampilleta, J. A. Blázquez, D. S. Tchitchekova, A. Ponrouch, P. Canepa, G. S. Gautam, R. S. R. G. Casilda, C. S. Martinez-Cisneros, N. U. Torres, A. Varez, J.-Y. Sanchez, K. V. Kravchyk, M. V. Kovalenko, A. A. Teck, H. Shiel, I. E. L. Stephens, M. P. Ryan, E. Zemlyanushin, S. Dsoke, R. Grieco, N. Patil, R. Marcilla, X. Gao, C. J. Carmalt, G. He, M.-M. Titirici, *Journal of Physics: Energy* **2024**, *6*, 031501.

[63] D. Sharon, M. Salama, R. Attias, D. Aurbach, *The Electrochemical Society Interface* **2019**, *28*, 71–77.

[64] A. Ponrouch, M. R. Palacín, *Philosophical Transactions of the Royal Society A: Mathematical Physical and Engineering Sciences* **2019**, *377*, 20180297.

[65] R. Attias, M. Salama, B. Hirsch, Y. Goffer, D. Aurbach, *Joule* **2019**, *3*, 27–52.

[66] Q. Sun, S. Luo, R. Huang, S. Yan, X. Lin, *Coordination Chemistry Reviews* **2024**, *515*, 215956.

[67] M. Smith, W. Becker, *Tetrahedron* **1967**, *23*, 4215–4227.

[68] D. Aurbach, A. Schechter, M. Moshkovich, Y. Cohen, *Journal of The Electrochemical Society* **2001**, *148*, A1004.

[69] E.-S. Lee, S.-H. Huh, S.-H. Lee, S.-H. Yu, *ACS Sustainable Chemistry & Engineering* **2023**, *11*, 2014–2032.

[70] Z. Lu, A. Schechter, M. Moshkovich, D. Aurbach, *Journal of Electroanalytical Chemistry* **1999**, *466*, 203–217.

[71] D. Aurbach, Y. Cohen, M. Moshkovich, *Electrochemical and Solid-State Letters* **2001**, *4*, A113.

[72] D. Aurbach, R. Turgeman, O. Chusid, Y. Gofer, *Electrochemistry Communications* **2001**, *3*, 252–261.

[73] S. F. Amalraj, D. Aurbach, *Journal of Solid State Electrochemistry* **2011**, *15*, 877–890.

[74] Z. Zhao-Karger, M. E. Gil Bardaji, O. Fuhr, M. Fichtner, *Journal of Materials Chemistry A* **2017**, *5*, 10815–10820.

[75] Z. Zhao-Karger, R. Liu, W. Dai, Z. Li, T. Diemant, B. P. Vinayan, C. Bonatto Minella, X. Yu, A. Manthiram, R. J. Behm, M. Ruben, M. Fichtner, *ACS Energy Letters* **2018**, *3*, 2005–2013.

[76] B. Dlugatch, M. Mohankumar, R. Attias, B. M. Krishna, Y. Elias, Y. Gofer, D. Zitoun, D. Aurbach, *ACS Applied Materials & Interfaces* **2021**, *13*, 54894–54905.

[77] Z. Li, T. Diemant, Z. Meng, Y. Xiu, A. Reupert, L. Wang, M. Fichtner, Z. Zhao-Karger, *ACS Applied Materials & Interfaces* **2021**, *13*, 33123–33132.

[78] Z. Meng, Z. Li, L. Wang, T. Diemant, D. Bosubabu, Y. Tang, R. Berthelot, Z. Zhao-Karger, M. Fichtner, *ACS Applied Materials & Interfaces* **2021**, *13*, 37044–37051.

[79] L. Leuppert, A. Reupert, T. Diemant, T. Philipp, C. Kranz, Z. Li, M. Fichtner, *RSC Applied Interfaces* **2024**, *1*, 1142–1155.

[80] Y. Liang, H. Dong, D. Aurbach, Y. Yao, *Nature Energy* **2020**, *5*, 646–656.

[81] M. Jäckle, A. Groß, *The Journal of Chemical Physics* **2014**, *141*, 174710.

[82] M. Jäckle, K. Helmbrecht, M. Smits, D. Stottmeister, A. Groß, *Energy & Environmental Science* **2018**, *11*, 3400–3407.

[83] I. T. Røe, S. M. Selbach, S. K. Schnell, *The Journal of Physical Chemistry Letters* **2020**, *11*, 2891–2895.

[84] A. Kopač Lautar, D. Kopač, T. Rejec, T. Bančič, R. Dominko, *Physical Chemistry Chemical Physics* **2019**, *21*, 2434–2442.

[85] R. Davidson, A. Verma, D. Santos, F. Hao, C. Fincher, S. Xiang, J. Van Buskirk, K. Xie, M. Pharr, P. P. Mukherjee, S. Banerjee, *ACS Energy Letters* **2018**, *4*, 375–376.

[86] R. Davidson, A. Verma, D. Santos, F. Hao, C. D. Fincher, D. Zhao, V. Attari, P. Schofield, J. Van Buskirk, A. Fraticelli-Cartagena, T. E. G. Alivio, R. Arroyave, K. Xie, M. Pharr, P. P. Mukherjee, S. Banerjee, *Materials Horizons* **2020**, *7*, 843–854.

[87] J. H. Kwak, Y. Jeoun, S. H. Oh, S. Yu, J.-H. Lim, Y.-E. Sung, S.-H. Yu, H.-D. Lim, *ACS Energy Letters* **2021**, *7*, 162–170.

[88] M. S. Ding, T. Diemant, R. J. Behm, S. Passerini, G. A. Giffin, *Journal of The Electrochemical Society* **2018**, *165*, A1983–A1990.

[89] E. Levi, M. D. Levi, O. Chasid, D. Aurbach, *Journal of Electroceramics* **2007**, *22*, 13–19.

[90] K. V. Kravchyk, M. V. Kovalenko, *Advanced Energy Materials* **2020**, *10*, 2002151.

[91] H. Yang, H. Li, J. Li, Z. Sun, K. He, H. Cheng, F. Li, *Angewandte Chemie International Edition* **2019**, *58*, 11978–11996.

[92] T. Schoetz, O. Leung, C. P. de Leon, C. Zaleski, I. Efimov, *Journal of The Electrochemical Society* **2020**, *167*, 040516.

[93] S. Wang, Z. Yu, J. Tu, J. Wang, D. Tian, Y. Liu, S. Jiao, *Advanced Energy Materials* **2016**, *6*, 1600137.

[94] F. Endres, *ChemPhysChem* **2002**, *3*, 144–154.

[95] S. K. Das, S. Mahapatra, H. Lahan, *Journal of Materials Chemistry A* **2017**, *5*, 6347–6367.

[96] X. Zhang, R. Lv, W. Tang, G. Li, A. Wang, A. Dong, X. Liu, J. Luo, *Advanced Functional Materials* **2020**, *30*, 2004187.

[97] H. Chen, H. Xu, B. Zheng, S. Wang, T. Huang, F. Guo, W. Gao, C. Gao, *ACS Applied Materials & Interfaces* **2017**, *9*, 22628–22634.

[98] S. Choi, H. Go, G. Lee, Y. Tak, *Physical Chemistry Chemical Physics* **2017**, *19*, 8653–8656.

[99] D. Muñoz-Torrero, P. Leung, E. García-Quismondo, E. Ventosa, M. Anderson, J. Palma, R. Marcilla, *J. Power Sources* **2018**, *374*, 77–83.

[100] X. Tu, J. Zhang, M. Zhang, Y. Cai, H. Lang, G. Tian, Y. Wang, *RSC Adv.* **2017**, *7*, 14790–14796.

[101] P. Bhauriyal, A. Mahata, B. Pathak, *Phys. Chem. Chem. Phys.* **2017**, *19*, 7980–7989.

[102] N. Canever, F. R. Hughson, T. Nann, *ACS Appl. Energy Mater.* **2020**, *3*, 3673–3683.

[103] M. Tebyetekerwa, T. T. Duignan, Z. Xu, X. Song Zhao, *Advanced Energy Materials* **2022**, *12*, 2202450.

[104] S. Chen, Q. Kuang, H. J. Fan, *Small* **2020**, *16*, 2002803.

[105] Z. Li, J. Liu, B. Niu, J. Li, F. Kang, *Small* **2018**, *14*, 1800745.

[106] S. Wang, S. Jiao, W.-L. Song, H.-S. Chen, J. Tu, D. Tian, H. Jiao, C. Fu, D.-N. Fang, *Energy Storage Mater.* **2018**, *12*, 119–127.

[107] T. Hannappel, S. Shekarabi, W. Jaegermann, E. Runge, J. P. Hofmann, R. van de Krol, M. M. May, A. Paszuk, F. Hess, A. Bergmann, A. Bund, C. Cierpka, C. Dreßler, F. Dionigi, D. Friedrich, M. Favaro, S. Krischok, M. Kurniawan, K. Lüdge, Y. Lei, B. Roldán Cuenya, P. Schaaf, R. Schmidt-Grund, W. G. Schmidt, P. Strasser, E. Unger, M. F. Vasquez Montoya, D. Wang, H. Zhang, *Solar RRL* **2024**, *8*, 2301047.

[108] G. Wittstock, *Lehrbuch der Elektrochemie, Grundlagen, Methoden, Materialien, Anwendungen*, (Eds.: B. Speiser, J. Witt), Literaturangaben, Wiley, Weinheim, **2023**, 11036 pp.

[109] R. V. de Krol, *Photoelectrochemical Hydrogen Production*, (Ed.: M. Grätzel), Springer US, Boston, MA, **2012**, 321124 pp.

[110] Z. Zhang, J. T. Yates, *Chemical Reviews* **2012**, *112*, 5520–5551.

[111] R. Memming, *Semiconductor electrochemistry*, Second edition, Previous edition: 2000, Wiley-VCH, Weinheim, **2015**, 11 pp.

[112] M. M. May, W. Jaegermann, *Current Opinion in Electrochemistry* **2022**, *34*, 100968.

[113] W.-H. Cheng, M. H. Richter, M. M. May, J. Ohlmann, D. Lackner, F. Dimroth, T. Hannappel, H. A. Atwater, H.-J. Lewerenz, *ACS Energy Letters* **2018**, *3*, 1795–1800.

[114] P Weightman, D. S. Martin, R. J. Cole, T Farrell, *Reports on Progress in Physics* **2005**, *68*, 1251–1341.

[115] O. Supplie, M. M. May, S. Brückner, N. Brezhneva, T. Hannappel, E. V. Skorb, *Advanced Materials Interfaces* **2017**, *4*, 1601118.

[116] W. G. Schmidt, *physica status solidi (b)* **2005**, *242*, 2751–2764.

[117] K. Haberland, P. Kurpas, M. Pristovsek, J.-T. Zettler, M. Weyers, W. Richter, *Applied Physics A: Materials Science & Processing* **1999**, *68*, 309–313.

[118] K. Haberland, PhD thesis, Technischen Universität Berlin, **2002**.

[119] V. Mazine, Y. Borensztein, *Physical Review Letters* **2002**, *88*, 147403.

[120] C. Goletti, G. Bussetti, A. Violante, B. Bonanni, M. Di Giovannantonio, G. Serrano, S. Breuer, K. Gentz, K. Wandelt, *The Journal of Physical Chemistry C* **2015**, *119*, 1782–1790.

[121] D. Kolb, J. Schneider, *Electrochimica Acta* **1986**, *31*, 929–936.

[122] O. Magnussen, J. Hotlos, R. Behm, N. Batina, D. Kolb, *Surface Science* **1993**, *296*, 310–332.

[123] V. Mazine, Y. Borensztein, L. Cagnon, P. Allongue, *physica status solidi (a)* **1999**, *175*, 311–316.

[124] D. E. Aspnes, A. A. Studna, *Applied Physics Letters* **1985**, *46*, 1071–1073.

[125] D. E. Aspnes, *Journal of Vacuum Science & Technology B: Microelectronics Processing and Phenomena* **1985**, *3*, 1498–1506.

[126] V. Berkovits, V. Kiselev, V. Safarov, *Surface Science* **1989**, *211–212*, 489–502.

[127] V. I. Safarov, *Il Nuovo Cimento D* **1998**, *20*, 1047–1054.

[128] B. A. Joyce, *Reports on Progress in Physics* **1985**, *48*, 1637–1697.

[129] M. Behet, R. Hövel, A. Kohl, A. Küsters, B. Opitz, K. Heime, *Microelectronics Journal* **1996**, *27*, 297–334.

[130] Z. Sobiesierski, D. I. Westwood, M. Elliott, *Physical Review B* **1997**, *56*, 15277–15281.

[131] J. Ortega-Gallegos, L. Guevara-Macías, A. Ariza-Flores, R. Castro-García, L. Lastras-Martínez, R. Balderas-Navarro, R. López-Estopier, A. Lastras-Martínez, *Applied Surface Science* **2018**, *439*, 963–967.

[132] G. Hughes, C. Springer, U. Resch, N. Esser, W. Richter, *Journal of Applied Physics* **1995**, *78*, 1948–1952.

[133] V. L. Berkovits, A. O. Gusev, V. M. Lantratov, T. V. L'vova, A. B. Pushnyi, V. P. Ulin, D. Paget, *Physical Review B* **1996**, *54*, R8369–R8372.

[134] S. Brückner, P. Kleinschmidt, O. Supplie, H. Döscher, T. Hannappel, *New Journal of Physics* **2013**, *15*, 113049.

[135] G. Sombrio, E. Oliveira, J. Strassner, C. Doering, H. Fouckhardt, *Journal of Vacuum Science & Technology B Nanotechnology and Microelectronics: Materials Processing Measurement and Phenomena* **2021**, *39*, 052204.

[136] E. A. Schmitt, M. Guidat, M. Nusshör, A.-L. Renz, K. Möller, M. Flieg, D. Lörch, M. Kölbach, M. M. May, *Cell Rep. Phys.Sci.* **2023**, *4*, 101606.

[137] B. Sheridan, D. S. Martin, J. R. Power, S. D. Barrett, C. I. Smith, C. A. Lucas, R. J. Nichols, P. Weightman, *Physical Review Letters* **2000**, *85*, 4618–4621.

[138] L. Sun, M. Hohage, P. Zeppenfeld, R. Balderas-Navarro, K. Hingerl, *Physical Review Letters* **2003**, *90*, 106104.

[139] X. F. Jin, M. Y. Mao, S. Ko, Y. R. Shen, *Physical Review B* **1996**, *54*, 7701–7704.

[140] G. Barati, V. Solokha, K. Wandelt, K. Hingerl, C. Cobet, *Langmuir* **2014**, *30*, 14486–14493.

[141] S. Vazquez-Miranda, V. Solokha, R. E. Balderas-Navarro, K. Hingerl, C. Cobet, *The Journal of Physical Chemistry C* **2020**, *124*, 5204–5212.

[142] S. Vazquez-Miranda, L. Guevara-Macías, J. Ortega-Gallegos, K. Hingerl, C. Cobet, R. Balderas-Navarro, *Applied Surface Science* **2024**, *669*, 160511.

[143] T. Herrmann, M. Gensch, M. J. G. Lee, A. I. Shkrebtii, N. Esser, W. Richter, P. Hofmann, *Physical Review B* **2004**, *69*, 165406.

[144] T. Herrmann, K. Lüdge, W. Richter, N. Esser, P. Poulopoulos, J. Lindner, K. Baberschke, *Physical Review B* **2001**, *64*, 184424.

[145] M. Wahl, T. Herrmann, N. Esser, W. Richter, *physica status solidi (c)* **2003**, 3002–3006.

[146] N. Meddings, M. Heinrich, F. Overney, J.-S. Lee, V. Ruiz, E. Napolitano, S. Seitz, G. Hinds, R. Raccichini, M. Gaberšček, J. Park, *Journal of Power Sources* **2020**, *480*, 228742.

[147] S. Wang, J. Zhang, O. Gharbi, V. Vivier, M. Gao, M. E. Orazem, *Nature Reviews Methods Primers* **2021**, *1*, 41.

[148] K. Lim, PhD thesis, Universität Stuttgart, **2022**.

[149] J. Popovic, G. Hasegawa, I. Moudrakovski, J. Maier, *Journal of Materials Chemistry A* **2016**, *4*, 7135–7140.

[150] X. Liu, G. Wang, Z. Lv, A. Du, S. Dong, G. Cui, *Advanced Materials* **2023**, *36*, DOI 10.1002/adma.202306395.

[151] P. Ravn Sørensen, T. Jacobsen, *Electrochimica Acta* **1982**, *27*, 1671–1675.

[152] M. H. Hebb, *J. Chem. Phys.* **1952**, *20*, 185–190.

[153] C. Wagner, *Z. Elektrochem.* **1956**, *60*, 4–7.

[154] J. Evans, C. A. Vincent, P. G. Bruce, *Polymer* **1987**, *28*, 2324–2328.

[155] J. Popovic, *ACS Phys. Chem. Au.* **2022**, *2*, 490–495.

[156] S. M. Nojabaee, PhD thesis, Universität Stuttgart, **2018**.

[157] N. Elgrishi, K. J. Rountree, B. D. McCarthy, E. S. Rountree, T. T. Eisenhart, J. L. Dempsey, *Journal of Chemical Education* **2017**, *95*, 197–206.

[158] B. Speiser, *Chemie in unserer Zeit* **1981**, *15*, 62–67.

[159] J. Heinze, *Angewandte Chemie* **1984**, *96*, 823–840.

[160] B. Speiser, *Chemie in unserer Zeit* **1981**, *15*, 21–26.

[161] L. Reimer, *Scanning Electron Microscopy, Physics of Image Formation and Microanalysis*, Second Completely Revised and Updated Edition, Springer Berlin Heidelberg, Berlin, Heidelberg, **1998**, 529 pp.

[162] G. Dehm, *In-Situ Electron Microscopy, Applications in Physics, Chemistry and Materials Science*, 1st ed., (Eds.: J. M. Howe, J. Zweck), Description based on publisher supplied metadata and other sources., John Wiley & Sons, Incorporated, Weinheim, **2012**, 1428 pp.

[163] M. Guidat, F. Rahide, M. Löw, J. Kim, H. Ehrenberg, S. Dsoke, M. M. May, *Batteries & Supercaps* **2023**, *7*, e202300394.

[164] M. Löw, M. M. May, *Batteries & Supercaps* **2024**, e202400610.

[165] M. Löw, J. Grill, M. M. May, J. Popovic-Neuber, *ACS Materials Letters* **2024**, *6*, 5120–5127.

[166] Y. Gofer, R. Turgeman, H. Cohen, D. Aurbach, *Langmuir* **2003**, *19*, 2344–2348.

[167] S. Guddehalli Chandrappa, G. Karkera, S. Dinda, M. Löw, H. Euchner, A. Reupert, S. Panja, M. K. Bhattarai, M. M. May, Z. Zhao-Karger, M. Fichtner, *Advanced Science* **2026**, *13*, e10456.

[168] G. Vander Voort, *Buehler Tech-Notes* **2015**, *4*, 1–7.

[169] J. Zhao, C. Zhao, C. Zou, Y. Wang, W. Wang, Q. Peng, Y. Li, S. Han, L. Zhang, *ChemSusChem* **2023**, *17*, e202301109.

[170] E. Oliveira, J. Strassner, C. Doering, H. Fouckhardt, *Appl. Surf. Sci.* **2023**, *611*, 155769.

Curriculum Vitae

Personal Details:

Name: Mario Löw
Date of Birth: 1996
Place of Birth: Laichignen, Germany

Education:

04/2021 – 05/2025
Ph.D. in chemistry; Ulm University, Germany.
Supervisor: Dr. Matthias M. May

10/2018 – 12/2020
Master of science chemistry; Ulm University, Germany.

09/2015 – 03/2019
Bachelor of science chemistry; Ulm University, Germany.

09/2007 – 7/2015
High school diploma (Abitur); Albert-Schweizer-Gymnasium Laichingen, Germany.

Working Experience:

01/2026 - now
Postdoc, Helmholtz-Zentrum Dresden-Rossendorf, Germany;
Spectroelectrochemical investigation of Tc-complexes.

11/2024 - 01/2025
Scientific employee, University of Tübingen, Germany;
Task: Investigation of the interfaces of III-V semiconductors with reflection anisotropy spectroscopy.

02/2024 – 05/2024
Research abroad, University of Stavanger, Norway;
Task: Investigation of the interfaces of magnesium and aluminium batteries with electrochemical impedance spectroscopy.

04/2021 – 10/2024
Scientific employee, Ulm University, Germany;
Task: Investigation of the interfaces in rechargeable multivalent batteries with reflection anisotropy spectroscopy.

03/2020 – 12/2020
Student assistants, Zentrum für Sonnenenergie- und Wasserstoff-Forschung (ZSW), Ulm, Germany;
Task: Investigation of the nucleation of magnesium during electrodeposition.

11/2019 – 12/2019
Student assistant, Helmholtz-Institut Ulm (HIU), Germany
Task: Synthesis of an electrolyte for magnesium batteries.

07/2018 – 12/2018
Student assistants, Ulm University, Germany;
Task: Organic syntheses.

Activities:

12/2022 – 12/2024
Elected affiliates representative of the Post Lithium Storage (POLiS) Cluster of Excellence.

04/2021 – 05/2025
Participation in the Graduate School Electrochemical Energy Storage (GS-EES) of the Center for Electrochemical Energy Storage Ulm and Karlsruhe (CELEST).

Appendix

This review from our group discusses the fundamentals and implementation of electrochemical reflection anisotropy spectroscopy (EC-RAS).

The article ”Experimental and Computational Aspects of Electrochemical Reflection Anisotropy Spectroscopy: A Review” was submitted to the journal ChemElectroChem in January 2023 and was acppected in March 2023 as open access in (ChemElectroChem2023, 10, e202300027) and is distributed under the terms of the Creative Commons Attribution 4.0 Unported Licence. (CC BY 4.0, `https://creativecommons.org/licenses/by/4.0/`.[32]

DOI: 10.1002/celc.202300027

ChemElectroChem

Review
doi.org/10.1002/celc.202300027

Chemistry Europe
European Chemical Societies Publishing

www.chemelectrochem.org

Special Collection

Experimental and Computational Aspects of Electrochemical Reflection Anisotropy Spectroscopy: A Review

Margot Guidat,[a, b] Mario Löw,[b] Moritz Kölbach,[a] Jongmin Kim,[a, b] and Matthias M. May*[a, b]

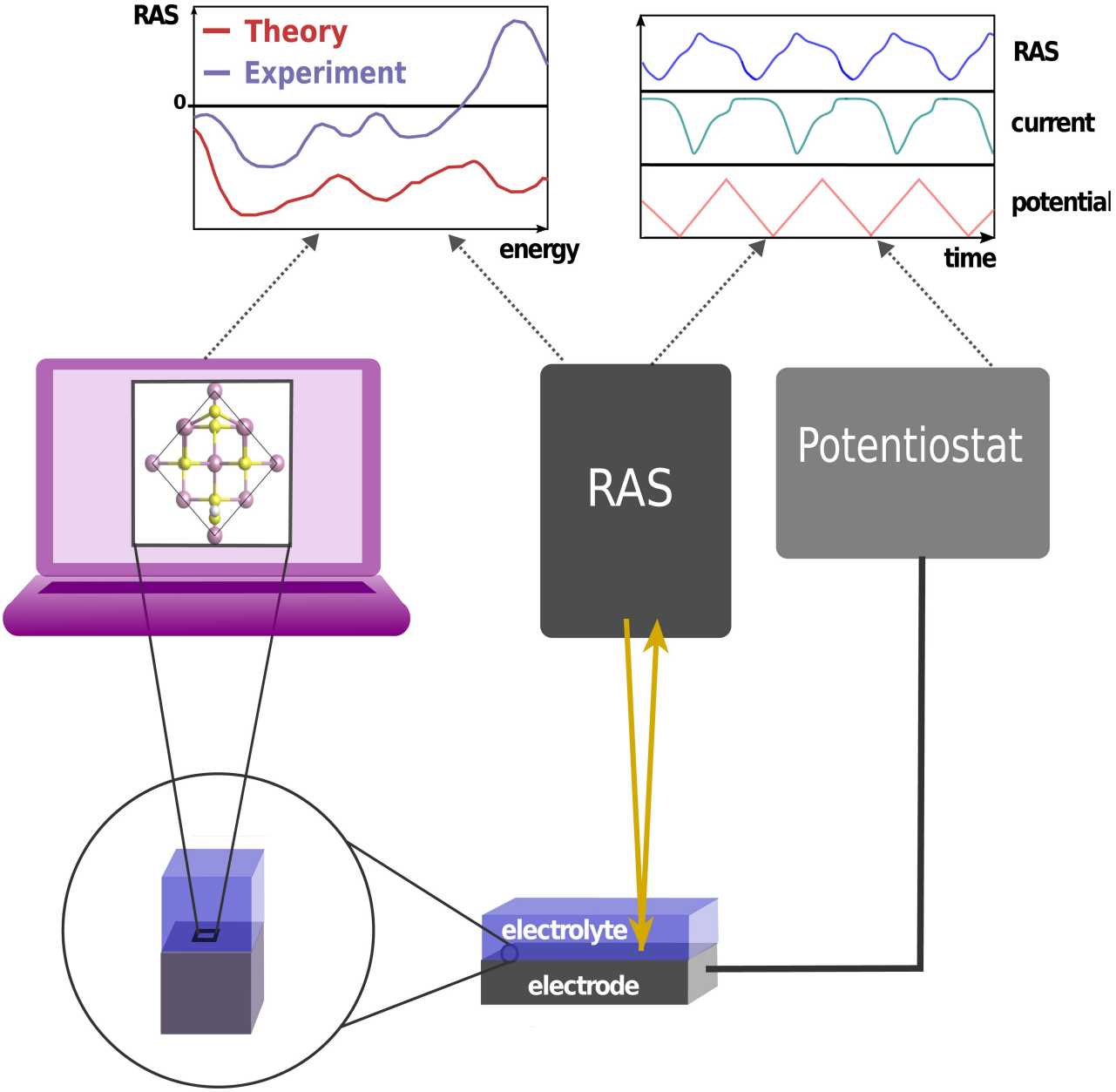

© 2023 The Authors. ChemElectroChem published by Wiley-VCH GmbH

21960216, 2023, 8, Downloaded from https://chemistry-europe.onlinelibrary.wiley.com/doi/10.1002/celc.202300027 by KIZ der Universitat Ulm, Wiley Online Library on [03/05/2023]. See the Terms and Conditions (https://onlinelibrary.wiley.com/terms-and-conditions) on Wiley Online Library for rules of use; OA articles are governed by the applicable Creative Commons License

Electrode/electrolyte interfaces play a crucial role in many electrochemical energy conversion and storage technologies. Hence, a deep understanding of the interfacial structure, energetic alignment and processes is of high relevance and has triggered the development of a number of in situ and operando techniques. One approach for gaining information about the change in surface chemistry and structure on an atomic scale is reflection anisotropy spectroscopy (RAS). This review presents and discusses the continuing effort to develop RAS as an in situ optical probe for solid-liquid interfaces under applied potentials. Experimental and computational basic principles are presented and key challenges of electrochemical RAS are highlighted. Furthermore, we exemplarily demonstrate the potential of the method for spectroelectrochemistry, focusing on indium phosphide- and gold-aqueous electrolyte interfaces as exemplary case studies, and outline research directions for battery systems.

1. Introduction

Electrochemical energy conversion and storage is expected to play a crucial role in a global sustainable energy system based on renewable energy. Potential applications are for example electrolyzers,[1] photoelectrochemical (PEC)[2] as well as photocatalytic water splitting,[3] batteries[4], supercapacitors,[5] and carbon dioxide removal.[6] At the heart of any of such electrochemical energy conversion and storage systems is the electrode/electrolyte interface. Even though this interface is an essential aspect of improving these devices, the physical and chemical processes occurring at electrochemical interfaces still lack fundamental understanding for most systems.[7] Changes in the chemistry, morphology and homogeneity of the surface structure of electrodes caused by corrosion, oxidation, and ion ad-/desorption processes can hinder the efficiency and the durability of electrochemical devices.[8] A microscopic understanding and ultimately controlling and designing the relevant interfaces of (photo)electrodes are hence of particular importance.

Interface and surface phenomena have been widely investigated in ultra-high vacuum (UHV), with techniques such as ex situ X-ray photoelectron spectroscopy (XPS)[9] and ex situ secondary ion mass spectrometry (SIMS).[10] However, these methods fail to account for the electrochemical environment and the applied potential at the electrode. An intermediate approach towards a realistic electrochemical environment are emersion-type experiments, where electrodes are exposed to an electrolyte or water film under inert gas conditions, which has to be removed before transfer to an adjacent analysis chamber.[11] Although recent efforts are focused to further close these gaps by developing techniques such as near-ambient pressure XPS and in situ SIMS,[12,13] significant challenges remain. Specifically, the short inelastic path of photoelectrons in the electrolyte limits studies to thin film of electrolyte in the case of ambient pressure XPS, while the utilization of a traditional time-of-flight mass analyzer in SIMS limits the mass resolution.[14] A deep understanding of the interfacial structure, energetics and processes, however, requires analysis with (close-to) atomic resolution in realistic environments, i.e. with the presence of a thick electrolyte allowing sufficient mass transport for the (photo)currents of a working device.[15]

The electrochemical double layer (EDL), i.e. the charge distribution at the electrode/electrolyte interface, plays a key role in designing efficient electrodes for electrochemical energy conversion devices. Gaining insight into the EDL requires electrochemical characterization methods with both high time (100 ms or better) and spatial (Å-nm) resolution. The limitation of several techniques with respect to their resolution and the type of information they can provide is described by Esposito et al. in detail.[8] In short, most experimental methods fall into the two categories of scanning probe measurements (SPM) and pump-probe techniques. The former allow high spatial resolution, but are restricted in temporal resolution. Scanning photocurrent microscopy[16] and optical spectroscopies (Raman,[17] Infrared,[18] UV-visible) are hindered by their optical diffraction resolution ranges and their long acquisition time. The techniques with a higher spatial resolution, i.e. with atomic resolution, are also limited by long acquisition times and by the nature of the interaction, physical by the contact of a tip for atomic force miscroscopy (AFM)[19–21] and electrical by the applied voltages for electrochemical scanning tunneling microscopy (ECSTM).[22] These interactions can alter the surface and hence decrease the reliability of the obtained data. Nevertheless, the time acquisition of scanning probe microscopy techniques can be extended to the millisecond range with video-rate measurements.[23] Pump-probe techniques consist of ultrafast spectroscopic techniques with a fs-ns time scale for the investigation of electronic processes such as interfacial transfer of charge carriers and lifetimes of electronic and vibrational states.[24,25] Such techniques show high temporal resolution, but the information is typically non-local.

Another category of techniques that is worth to be mentioned are synchrotron-based X-ray techniques, where the in situ evolution of structural changes of electrodes can be monitored.[26–28] In addition to be non-destructive, and to have high penetration depth of hard X-rays into liquid electrolytes, surface resonant X-ray diffraction (SRXRD) has the advantage to access the atomic structure of both the electrode and the adsorbate adlayers with a reasonable temporal resolution. Combining these diffraction techniques with additional spec-

[a] M. Guidat, Dr. M. Kölbach, J. Kim, Dr. M. M. May
Institute of Physical and Theoretical Chemistry, Tübingen D-72076, Germany
E-mail: matthias.may@uni-tuebingen.de
[b] M. Guidat, M. Löw, J. Kim, Dr. M. M. May
Universität Ulm, Institute of Theoretical Chemistry, Ulm D-89081, Germany

Special Collection An invited contribution to the Electrochemical Nibbles for Computational Chemists Special Collection

© 2023 The Authors. ChemElectroChem published by Wiley-VCH GmbH. This is an open access article under the terms of the Creative Commons Attribution License, which permits use, distribution and reproduction in any medium, provided the original work is properly cited.

troscopies can give further insight into chemical composition and charge distribution at the electrochemical interface. However, the need to set wavelength and/or polarization state of the X-rays at sufficiently high intensities requires a synchrotron facility. In this review, however, we will focus on lab-based techniques that at least have the potential for a higher sample-throughput and refer the reader to the extensive literature in this field.[26,27]

In addition to the methods mentioned above, reflection anisotropy spectroscopy (RAS) is a surface-sensitive method that has the potential to help understanding the structure and the fundamental properties of electrochemical interfaces at an atomistic level with an adequate time resolution (down to a few milliseconds).[29] In short, RAS probes the difference in reflectivity of broad band light at near-normal incidence between two orthogonal directions of a single-crystal surface plane, scaled with the overall reflectivity. An adequate interpretation of experimental RAS data does, however, require both experimental and theoretical considerations to derive a comprehensive understanding of the structure-property relationship of solid-liquid interfaces. To compute the surface optical properties, the surface dielectric function determined from density-functional theory (DFT) is considered.[30] Some previous studies[31–33] have already determined the surface optical properties from first principles for the study of surface structure and surface reconstruction in vacuum. In particular, Schmidt et al. have performed many RAS investigations on III–V(100) surfaces in vacuum with quantitative and qualitative analysis.[34–38] From an electrochemical perspective, however, this approach neglects effects from the solid surfaces in contact with molecules from a realistic bulk electrolyte.[39] It is challenging to accurately calculate theoretically derived RAS, since DFT for the underlying ground-state does, in a purely surface-science approach involving vacuum, not necessarily describe the electrode-electrolyte interaction comprehensively. One fundamental challenge consists in including the polarization generated by mobile ions to preserve electric boundary condition from the supercell to the ionic solution.[40] The main constraints are the simulation of applied electric field and the simulation of realistic electrolyte, limited at best to a mono-layer for large supercells. Model systems with simplified, few-monolayer approximations for electrolytes can, however, be a bridge towards more realistic electrochemical systems.[39]

In this review, we present and discuss the technique of RAS, with a focus on its development towards an in situ/operando spectroscopy in electrochemical environments. In this regard, the need of method development from an experimental and a computational point of view using well-defined reference systems is highlighted. As case studies, we demonstrate the application of electrochemical RAS for aqueous electrolyte systems with the interfacial structures of indium phosphide and gold in contact with acidic electrolytes. Moreover, we discuss potential applications of RAS to investigate the solid-electrolyte interphase in battery systems.



Margot Guidat is currently a PhD student in physical chemistry at Tübingen University. She received her M.Sc. in chemical engineering from ENSCR at Rennes university in 2020. Her research interests include in situ/operando spectroscopic techniques for elucidating electrochemical processes at solid-liquid interfaces of both solar-water-splitting and aluminum battery systems.

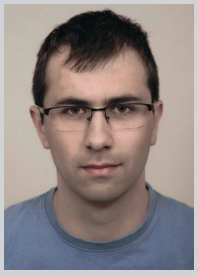

Mario Löw is currently a PhD student at Ulm University. He received his M.Sc. in chemistry from Ulm University in 2021. His research interests include the operando investigation of the interface in rechargeable magnesium batteries.



Jongmin Kim did his PhD studies Humboldt-University of Berlin. He currently holds a postdoctoral position at Tübingen University, where his research focuses on computational investigation of electrochemical interfaces in water–splitting devices as well as further method development within density-functional theory.



Matthias M. May studied physics in Stuttgart, Grenoble, and Berlin, with a focus on condensed matter and computational physics. His PhD studies (2011–2015) at Humboldt-Universität zu Berlin and Helmholtz-Zentrum Berlin targeted III–V semiconductors for solar water splitting. He spent two years as postdoctoral fellow at the Chemistry Department of the University of Cambridge, funded by the German Academy of Sciences Leopoldina. He leads an Emmy-Noether group at the Institute of Physical and Theoretical Chemistry at Tübingen University. His scientific interests lie in the area of photoelectrochemical energy conversion and solid-liquid interfaces.

© 2023 The Authors. ChemElectroChem published by Wiley-VCH GmbH

21960216, 2023, 8, Downloaded from https://chemistry-europe.onlinelibrary.wiley.com/doi/10.1002/celc.202300027 by KIZ der Universitat Ulm, Wiley Online Library on [03/05/2023]. See the Terms and Conditions (https://onlinelibrary.wiley.com/terms-and-conditions) on Wiley Online Library for rules of use; OA articles are governed by the applicable Creative Commons License

2. From epitaxial growth to electrochemical interface monitoring

RAS is a linear, differential optic probe that measures the difference in reflectivity of normal incident light between two orthogonal directions of the surface normalized by the overall reflectivity. The definition of the RAS signal is given in equation 1. r_x and r_y are the complex eigenvalues of the Fresnel reflection coefficient tensor along the two axes x and y in the surface plane. In case of an anisotropic surface, r_x and r_y have different values and their difference normalized by the average reflectivity represents the optical anisotropy of the sample.[41] While both real and imaginary parts are measured, experimental literature typically refers to the real part, a convention that we will also employ for the spectra displayed in the following sections.

$$\mathrm{RAS} = \frac{\Delta r}{r} = 2 \cdot \frac{r_x - r_y}{r_x + r_y} \tag{1}$$

It is noteworthy to mention that one can also probe the anisotropy of the reflectance, i.e. the (real) square of the Fresnel reflection amplitude, $R = |r|^2$. This case is then referred to as reflectance anisotropy spectroscopy, where the relation $\mathrm{Re}\left(\frac{\Delta r}{r}\right) \approx \frac{1}{2}\frac{\Delta R}{R}$ holds true for $\Delta r \ll r$.[42,43]

2.1. Experimental realization

The basic working principle of RAS and the configuration used in this study are illustrated in Figure 1. For a more detailed description of the working principle of RAS, we refer the reader to the work of Haberland et al.[45] When linearly polarized light in the UV-visible range is reflected by an anisotropic crystalline surface, the polarization becomes elliptic and reaches the photoelastic modulator (PEM) of the spectrometer. Due to its birefringent property, the PEM induces a retardation between the two components of the elliptic polarization along the x and y surface crystal direction, resulting in an oscillating signal. After the modulated polarized light has passed through an analyzer, its intensity (I) now depends on the polarization state of the light, the retardation, and the modulation frequency ω of the PEM. This is then detected by a photomultiplier and demodulated by a lock-in amplifier. The intensity, given in equation 2, is thus proportional to the optical ratio shown in the equation 1.[41]

$$\mathrm{Re}\left(\frac{\Delta r}{r}\right) = \frac{\sqrt{2} I_{2\omega}}{I_0} \tag{2}$$

To allow sufficiently high reflectivity and to limit the complexity of the anisotropic signal, RAS is restricted to single crystals with very low surface roughness (< 10 nm). The anisotropy of the signal can arise from both the surface and the bulk of the sample due to the relatively large penetration depth

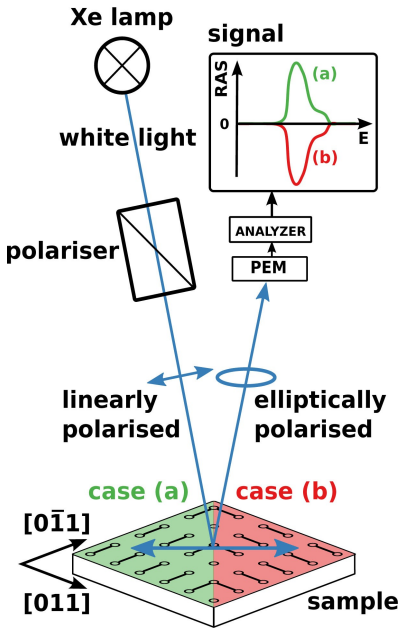

Figure 1. General principle of RAS for the case of a dimerized, cubic (100) surface. The rotation of the dimers by 90 (case a, green vs. case b, red) switches the sign of their contribution to the spectrum. Adapted from Ref. [44] with permission from the ACS. Further re-use subject to permission by ACS.

of light. To get a signal exclusively from the surface, the symmetry of the bulk in the plane of the surface must be isotropic whereas the symmetry of the surface must be anisotropic. Cubic systems with (100) and (111) surfaces orientation have isotropic symmetry and in principle should give a zero RAS signal. However, they can undergo a surface reconstruction. For example, annealing Au(100) allows obtaining a pseudo hexagonal reconstructed Au(100)-(5 × 20) surface which breaks the symmetry between the bulk and the surface and gives a RAS signal exclusively from the surface. For alloys like InP, their surface typically reconstruct in dimer-rich surfaces which present some anisotropy. For cubic systems with (110) surfaces, the RAS signal is more complex because the signal is also arising from the bulk. However, a break in the symmetry between the bulk and the surface gives different contribution to the RAS signal and surface evolution can be monitored. For instance, it is possible to distinguish a (1 × 2) from a (1 × 1) or (1 × 3) reconstruction of Au(110). Yet for example in the case of cubic (100) surfaces, whose bulk is isotropic, it is possible to exclusively get information about the surface.

Several related optical methods currently exist for the study of surface structure and chemistry with a sub-nanometer surface sensitivity. Table 1 shows a summary of the most common of these techniques to distinguish and clarify their differences and similarities with RAS. Surface differential reflectivity (SDR) is very similar, also by name to RAS because the information extracted from both measurements are very similar. However, SDR is applicable for both isotropic and anisotropic surfaces. Since the technique consists of measuring the reflectivity of a sample's surface before and after exposure

© 2023 The Authors. ChemElectroChem published by Wiley-VCH GmbH

21960216, 2023, 8, Downloaded from https://chemistry-europe.onlinelibrary.wiley.com/doi/10.1002/celc.202300027 by KIZ der Universitat Ulm, Wiley Online Library on [03/05/2023]. See the Terms and Conditions (https://onlinelibrary.wiley.com/terms-and-conditions) on Wiley Online Library for rules of use; OA articles are governed by the applicable Creative Commons License

21960216, 2023, 8, Downloaded from https://chemistry-europe.onlinelibrary.wiley.com/doi/10.1002/celc.202300027 by KIZ der Universitat Ulm, Wiley Online Library on [03/05/2023]. See the Terms and Conditions (https://onlinelibrary.wiley.com/terms-and-conditions) on Wiley Online Library for rules of use; OA articles are governed by the applicable Creative Commons License

Table 1. Main differences between RAS and other related spectroscopic techniques.

Method	RAS	SE[a]	SDR[b]	ER[c]	RAIRS[d]
Principle	$2 \cdot \frac{r_x - r_y}{r_x + r_y}$	$\frac{r_p}{r_s}$	$\frac{R_{clean}(E) - R_{ox}(E)}{R_{ox}(E)}$	$a\Delta\varepsilon' + b\Delta\varepsilon''$	$\int_\nu \ln\left(\frac{R_0}{R_{adsorbates}}\right) d\nu$
Time resolution	few ms	few fs	few ms	few ms	< 1 s
sample type	single-crystal with anisotropic surface	thin film	single-crystal	thin film	single-crystal
typical energy range (eV)	1.5–5	1–6	0.5–5	0.5–5	0.05–0.5
1 or 2 step measurement ?	1 step	1 step	2 steps	2 steps	2 steps

[a] spectroscopic ellipsometry. [b] surface differential reflectivity. [c] electroreflectance. [d] reflection-absorption infrared spectroscopy.

(E) to an external gas (here oxygen as an example in Table 1), the acquisition of one spectrum requires two different experimental conditions. The variation in reflectivity between clean surface and surface after exposure can arise from surface electronic states, electric fields, or optical properties of the growing oxide layer.[46] Note that although SDR resembles RAS, the type of provided information is different, i.e. SDR allows learning about molecular adsorption, but not about surface ordering and reconstructions.

Spectroscopic ellipsometry (SE) is based on the same principle as RAS. It measures the change of polarization state between the incident and reflected light on a surface. However, while RAS is operating at near-normal incidence, SE is measured at oblique incidence. Therefore, the polarized light is composed of components parallel (rp) and perpendicular (rs) to the plane of incidence. Since the set-up is commonly oriented at 45 from the incidence plane, a signal is emerging from measurements also for isotropic surfaces.[47,48] This technique is mainly used to determine the dielectric function and the thickness of thin films.[49]

First introduced by Seraphin,[50] electroreflectance (ER) is used for the determination of internal parameters of thin-film solar cells such as the internal electric field and the band gaps of the different junctions.[51] RAS, on the other hand, is a "static" reflection technique which allows accessing the real part of the optical response. While in ER spectroscopy, in addition to the set-up illustrated in Figure 1, an external AC voltage is applied between the backside and the front side of the p-n junction. This applied AC voltage allows accessing both real and imaginary parts of the optical response of the interface, respectively, represented by the real and imaginary part ε' and ε'' of the dielectric function in Table 1. Thus, the AC voltage "modulates" the reflection, amplifying the response generated by the electric field and suppressing the constant background of reflection.

Finally, reflection-absorption infrared spectroscopy (RAIRS) measures the difference in reflectivity of the surface with ($R_{adsorbates}$) and without (R_0) adsorbed molecules.[52,53] Studying adsorbed monolayer and submonolayer on metal surfaces by RAIRS allows accessing information about their molecular structure, their chemical identity and adsorption site.

2.2. Computational aspects

The great challenge for RAS is that, without correlation to other complementary experimental methods, it is not a straightforward quantitative technique. Yet this correlation with other techniques is certainly time-consuming, but sometimes not possible at all. For this reason, complimentary computational efforts are a viable alternative. The following section is not an in-depth picture as can be found in references [41] and [43], but gives a first overview of computational RAS.

Reflection anisotropy is associated with the dielectric response function of a semi-infinite system. According to the three-phase model devised by McIntyre and Aspnes,[54] the dielectric response function can be described by dielectric functions of bulk and vacuum layers and a surface layer with thickness *d*.

Equation 1 can be rewritten in the following manner.[41,43]

$$\frac{\Delta R}{R} = \frac{4\pi d}{\lambda} \mathrm{Im}\left[\frac{\Delta\varepsilon_s}{\varepsilon_b - 1}\right], \tag{3}$$

where $\boldsymbol{\varepsilon}_s$ and $\boldsymbol{\varepsilon}_b$ represent complex dielectric functions ($\varepsilon = \varepsilon' + i\varepsilon''$) of the surface and bulk, respectively, and λ is the wavelength of the light. When the first energy derivative of $\boldsymbol{\varepsilon}_b$ is employed in this model, it yields to the subsequent equations:

$$\frac{\Delta R}{R} = \frac{4\pi d}{\lambda}\left[A\Delta\varepsilon_s{}'' - B\Delta\varepsilon_s{}'\right], \tag{4}$$

where

$$A = \frac{\varepsilon_b{}' - 1}{(1 - \varepsilon_b{}')^2 + (\varepsilon_b{}'')^2}, \tag{5}$$

and

$$B = \frac{\varepsilon_b{}''}{(1 - \varepsilon_b{}')^2 + (\varepsilon_b{}'')^2}. \tag{6}$$

By using the half-slab polarizability α^{hs}, equation 3 transforms into[55,56]

© 2023 The Authors. ChemElectroChem published by Wiley-VCH GmbH

$$\frac{\Delta R}{R}(\omega) = \frac{4\omega}{c}\mathrm{Im}\left[\frac{4\pi(\alpha_{xx}^{\mathrm{hs}}(\omega) - \alpha_{yy}^{\mathrm{hs}}(\omega))}{\varepsilon_b(\omega) - 1}\right]. \quad (7)$$

Likewise, the half-slab polarizability can be applied to equation 4.

For a symmetric slab, α^{hs} can be calculated within the independent-particle random phase approximation (IP-RPA) that neglects the local field effect:[31]

$$\mathrm{Im}\left[4\pi\,\alpha_{xx}^{\mathrm{hs}}(\omega)\right] = \frac{4\pi^2 e^2}{m^2\omega^2 A}\sum_{\mathbf{k}}\sum_{v,c}|P^x_{v\mathbf{k},c\mathbf{k}}|^2 \times\delta(E_{c\mathbf{k}} - E_{v\mathbf{k}} - \hbar\omega). \quad (8)$$

In equation 8, $P_{v,c}$ is the transition matrix element of the momentum operator, and A is the surface area. Calculating this polarizability requires the Kohn-Sham (KS) single-particle eigenvalues and wave-functions. The eigenvalues and wave-functions need to be calculated from DFT or other quantum chemistry methods to be used as an input in the IP-RPA scheme. Unfortunately, this IP-RPA scheme underestimates excitation energies due to the underestimated KS eigenvalues, since the unphysical self-interaction and the derivative discontinuity in the exchange-correlation functional result in an incorrect band gap for semiconductors or insulators. A simple way for correcting this limitation is to consider a scissors shift operator.[31] This technique is useful for semiconductors or insulators. However, it does not apply to materials where many-body effects are crucial, such as metallic and low-dimensional systems or oxides.

If the slab is nonsymmetric, a real-space cutoff approach to capture the actual surface response is needed. By considering the cutoff θ, modified matrix elements are constructed as follows[31]

$$\tilde{P}^x_{v\mathbf{k},c\mathbf{k}} = -i\int d\mathbf{r}\psi^*_{v\mathbf{k}}(\mathbf{r})\theta(z)\frac{\partial}{\partial r_x}\psi_{c\mathbf{k}}(\mathbf{r}), \quad (9)$$

and the corresponding polarizability becomes

$$\mathrm{Im}\left[4\pi\alpha_{xx}^{\mathrm{hs}}(\omega)\right] = \frac{8\pi^2 e^2}{m^2 w^2 A}\sum_{\mathbf{k}}\sum_{\mathrm{v,c}}\left[P^x_{v\mathbf{k},c\mathbf{k}}\right]^*\tilde{P}^x_{v\mathbf{k},c\mathbf{k}} \times\delta(E_{c\mathbf{k}} - E_{v\mathbf{k}} - \hbar\omega)\,. \quad (10)$$

A typical computational workflow to compute equation 7 using equations 9 and 10, which was for instance employed in Refs. [39] and [57], is to start with the structural optimizations of slabs on a DFT level, for instance with the CP2K code,[58] using the generalized gradient approximation as parameterized by Perdew-Burke-Ernzerhof for the exchange-correlation functional.[59] The Yambo code[60,61] readily provides a module for computational RAS in the IP-RPA approach, providing the reflectance, i.e. $\Delta R/R$. Underestimated bandgaps for semiconductors can be corrected by a scissor operator. Using Yambo does, however, require a ground-state calculation in QUANTUM ESPRESSO[62] as an intermediate step. For the bulk dielectric function, either experimental or computational input can be employed.

2.3. Application of RAS in surface science

RAS was first developed by Aspnes et al. in the 1980s[63] to establish an in situ optical probe to achieve a layer-by-layer surface control in III–V semiconductor growth systems as for example molecular beam epitaxy (MBE)[64] or metal-organic vapor phase epitaxy (MOVPE).[65] Since then, the technique has been widely used for the study of semiconductor surfaces and interfaces in growth environments. In particular, RAS studies on GaAs have not only demonstrated how the spectroscopy can be used to control epitaxial growth and the preparation of specific surface reconstructions, but also the possibility to investigate layer-by-layer removal of GaAs as a protective cap layer for the preparation of fresh surfaces was shown.[66–68] More recently, Sombiro et al. have pointed out the utilization of RAS to extract etching rate and etch-depth resolution from the analysis of Fabry-Pérot oscillations generated by reactive ion etching of GaAs/AlGaAs multi-layer structures.[69] Also dry etching in hydrogen ambient was studied by Brückner et al.,[70] who report that RAS reveals a layer-by-layer removal from Si(100) single-crystals in H_2 atmosphere at elevated temperatures. This study suggests that RAS is a relevant tool for the development of direct growth processes of III–V/Si solar cells, since well-defined monolayer etching allows single domain preparation. In principle, the fitting methods used to determine growth rate, etching rate, and etch-depth resolution from transients in dry processes can be adapted for transients measured during electrochemical processes.

Investigations on the adsorption of constituents of an electrolyte – typically water – can serve as an intermediate step between UHV and gas-phase studies on the one side and the full electrochemical environment with the solid/liquid phase boundary on the other side.[44,71–74] The great advantage of such a type of study is that the surface stays in inert gas or vacuum conditions prior to and after water adsorption, which allows to precisely characterize and control the initial surface configuration by standard surface science tools. This can help to understand, for instance, the impact of step edges on the reactivity of a given surface[74] or derive activation energies.[71] The downside of such a type of experiment is that the comparability with the realistic electrochemical environment is limited at best. Low-temperature water adsorption from the gas phase[73] allows to adsorb multi-layer water (ice) on a surface, but reactivity of the interface might be qualitatively different from the ambient temperatures of a typical electrochemical experiment. Adsorption at ambient temperatures, on the other hand, limits the maximum water layer thickness typically to a sub-monolayer.[44,72] For comprehensive overviews about the application of RAS in a number of fields during the past decades, we refer the reader to the reviews by Weigthman et al.[41] and Supplie et al.[42] which focus mainly on applications in surface science.

© 2023 The Authors. ChemElectroChem published by Wiley-VCH GmbH

21960216, 2023, 8, Downloaded from https://chemistry-europe.onlinelibrary.wiley.com/doi/10.1002/celc.202300027 by KIZ der Universitat Ulm, Wiley Online Library on [03/05/2023]. See the Terms and Conditions (https://onlinelibrary.wiley.com/terms-and-conditions) on Wiley Online Library for rules of use; OA articles are governed by the applicable Creative Commons License

3. Emergence, principles, and application of electrochemical RAS

Implementing (photo)electrochemical surface conditioning for photoelectrodes could enable novel process routes at potentially low costs, but the understanding and control of the related interface (electro)chemistry is so far limited.[75] Nevertheless, such surface functionalization approaches already demonstrated their use for achieving highest solar-to-hydrogen efficiencies by effective surface protection against corrosion.[75,76] In this regard, with its straightforward set-up operating at near-normal incidence configuration (Figure 2), RAS represents a potential tool for the in situ/operando monitoring of (photo)electrochemical surface passivation with a sub-nanometer control of surface modifications.

More generally, RAS can be developed as probe of the electrochemical double layer and can easily be coupled with intrinsically electrochemical characterization methods such as chronoamperometry (CA) or cyclic voltammetry (CV). The correlation between RA spectra and cyclic voltammogramms can complement the understanding of electrochemical processes from CV by providing access to charge, potentials, and chemical species with a sub-nanometer spatial resolution in the surface normal. For instance, some surface reconstructions are not distinguishable on the cyclic voltammogramm, because they involve non-Faradic processes with very small change in capacitance of the EDL (see Figure 3) and therefore very small charging currents. Thanks to RAS, the different surface reconstructions and surface steps are observable and distinguishable.[77] In this regard, since the first RAS implementation, there has been a rapid growth of the field and RAS was used on metallic systems in electrochemical environments or molecular films on metals.

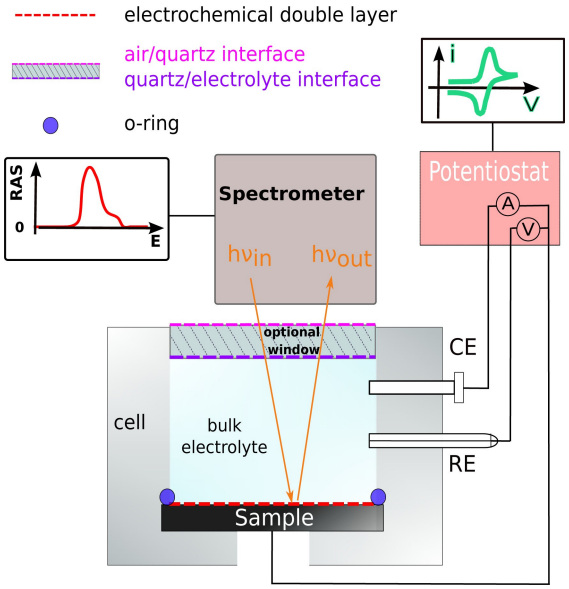

Figure 2. Cross-section of a typical cell setup for electrochemical RAS. CE and RE refer to counter and reference electrode, respectively. Adapted from Ref. [57] with permission from the Royal Society of Chemistry.

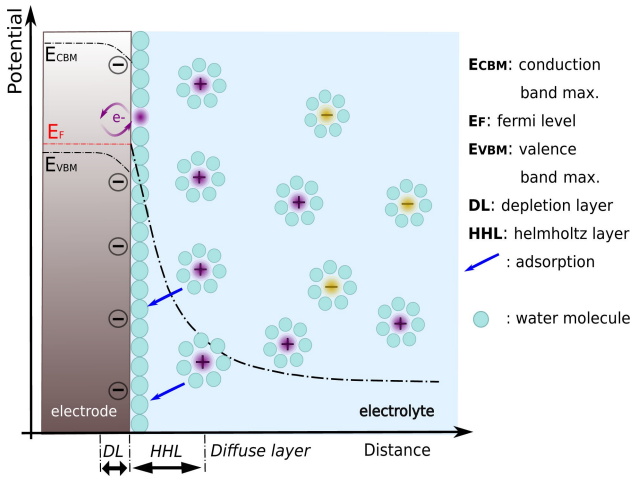

Figure 3. Electrochemical interface of a p-type semiconductor with an electrolyte forming a depletion layer in the dark after equilibrium. The positive and negative charge on the electrolyte side account for solvated ions. Inspired by Gerischer.[78]

3.1. Application of RAS in electrochemistry

Here, we now follow the literature on first "electrochemical RAS" (EC-RAS) applications, i.e. RAS applied in electrochemical environments. First applications of EC-RAS were dedicated to the study of different gold single-crystalline surfaces in aqueous electrolytes. These studies have outlined the relationship between surface charge and reconstruction by measuring RA spectra for interfaces between Au(110) and aqueous electrolytes while potentials were applied to Au(110).[79,80] Yet, their investigation focused exclusively on experimental EC-RAS and were corroborating previous findings evidenced by STM. Similarly, Sheridan et al. have combined experimental RAS with the modelling of the surface optical response – not full ab initio computational spectroscopy – to investigate the impact of surface phases transition and surface roughening of Au(110) in sulfuric acid under applied voltage on the electronic structure.[81] Again, to support their findings, the authors refer to results from other studies on the same system, for instance with EC-STM and ex situ low-energy electron diffraction (LEED).[82,83] This emphasizes that RAS, at least in the initial phase of system exploration, is not a high-throughput technique and that it in principle needs to be supplemented by other surface-sensitive techniques. In such an exploratory phase, it is typically not possible to identify chemical species directly from the spectra. After correlation with complementary experimental techniques or computational spectroscopy, however, an assignment of spectral features to chemical species is often possible.

Mazine et al. combined experimental and computational RAS – the latter for a slab in vacuum – with EC-STM in their study on interfaces of gold with aqueous electrolytes.[84,85] Correlating STM images and RA spectra show the relationship between surface charge and surface reconstruction and steps, while attempts on including local field effects on theoretical

© 2023 The Authors. ChemElectroChem published by Wiley-VCH GmbH

21960216, 2023, 8, Downloaded from https://chemistry-europe.onlinelibrary.wiley.com/doi/10.1002/celc.202300027 by KIZ der Universitat Ulm, Wiley Online Library on [03/05/2023]. See the Terms and Conditions (https://onlinelibrary.wiley.com/terms-and-conditions) on Wiley Online Library for rules of use; OA articles are governed by the applicable Creative Commons License

21960216, 2023, 8, Downloaded from https://chemistry-europe.onlinelibrary.wiley.com/doi/10.1002/celc.202300027 by KIZ der Universitat Ulm, Wiley Online Library on [03/05/2023]. See the Terms and Conditions (https://onlinelibrary.wiley.com/terms-and-conditions) on Wiley Online Library for rules of use; OA articles are governed by the applicable Creative Commons License

RAS are made to enlighten the origin of the transitions obtained for the different reconstructions.

In addition to the determination of surface states, surface roughness and surface phase transitions, it is possible to deeply investigate surface transformations, ion adsorption, and solid electrolyte interphase formation processes by evaluating the spectral features during the transition from clean to adsorbate-covered cubic surfaces in both liquid and non-liquid environments. Extensive research on the Cu(110) surface has shown the sensitivity of RAS to molecular adsorbate orientation,[86,87] and its potential as a surface analytic tool for kinetic studies of molecule adsorption and desorption, as well as their memory effect on the surface.[88–90] Later on, the study of ad/desorption of molecules in the gas phase on Cu(110) has been extended to electrochemical environments.[91–93] All studies have mainly investigated chlorine ion adsorption on Cu(110) in hydrochloric acid. Goletti et al. used EC-RAS together with EC-STM and ex situ LEED to identify the two-step process in the anodic and cathodic region of the CV.[92] They have ruled out the adsorption (desorption) of two different anions and have demonstrated that chlorine anions are involved in one adsorption (desorption) process followed by a surface reconstruction (deconstruction). The latter study on copper has performed EC-RAS on the same system with slightly different potential range and also show together with EC-STM the reversible formation of stripes and channels induced by chlorine ad/desorption.[93] Very often, specific spectral features of RAS are directly correlated with the surface coverage. By fitting transient measurements with adsorption isotherm models, it is then possible to access some kinetic and thermodynamic quantities.[74,93] Vazquez-Miranda et al. have particularly demonstrated the extraction of the formation energy of adsorption of chlorine ions and lateral interaction parameter from a transient by fitting it with Frumkin-type isotherms.[93,94] Furthermore, by correlating the current peaks measured in CV with the derivative of the RAS-transients, they could derive the dependency between applied potential duration and copper/chlorine chemical reactions.

Recently, the use of RAS in combination with AFM and CV has unraveled the mechanism responsible for porphyrin dissolution in acidic media,[95] a more complex system involving organic molecules. In their approach, several types of porphyrin nanocrystals were vacuum-deposited on graphite substrates and cycled in sulfuric acid. The correlation of RAS with the current density revealed that the single electron transfer involved in the oxidation of porphyrin in a more cationic form is the precursor of its dissolution. The study of porphyrin-liquid interfaces is relevant for energy-storage systems such as post-lithium batteries, where battery based on an alkyne-substituted-porphyrin complex are under development.[96]

3.2. EC-RAS setup

Figure 2 shows a typical electrochemical RAS setup, where the single-crystal is in contact with the liquid electrolyte. The sample of interest (working electrode) is mounted together with a counter electrode and an optional reference electrode in a photoelectrochemical cell filled with an electrolyte. Compared to conventional RAS setups, additional potential measurement artefacts in the RA spectrum have to be carefully considered in this configuration, e.g. artefacts from the liquid medium, as the setup now comprises media of at least three different refractive indices, as opposed to two for a vacuum or gas-phase setup. If a quartz window is present in the photoelectrochemical cell, as indicated in Figure 2, it affects the refraction angle of the light at the air-quartz and quartz-electrolyte interfaces due the different refractive indexes of the media. Hence, the optical path between the spectrometer and the sample has to be carefully adjusted. Furthermore, if non-homogeneous mechanical stress is applied to the window, its dielectric tensor is no longer scalar, leading to a stress-induced contribution of the window to the signal. In principle, the photoelectrochemical cell can also be used without a quartz window. The air-electrolyte interface, however, still changes the refraction angle of the light and hence modifies the light focal point. Also vibration damping might be needed in this case, as vibrations disturb the electrolyte surface and hence the optical path. Baseline effects can be largely compensated by adequate baseline correction using an optically isotropic standard such as an oxidized Si(100) sample, a reference of well-defined anisotropy such as Si(110), or the sum of two spectra where the sample has been rotated by 90 in between.

3.3. Important aspects of the EDL

Literature on electrochemical RAS has so far mainly been limited to metallic systems. This is most likely due to the additional complexity introduced by semiconductor-electrolyte contacts. One factor is almost certainly the reduced structural stability against electrochemical corrosion of most semiconductors when compared to many (noble) metals. Furthermore, the interfacial energetics are altered, as semiconductor-electrolyte interfaces have additional potential drops compared to metal-electrolyte interfaces whose potential drop region is limited (mainly) to the Helmholtz layer (HHL). Figure 3 illustrates a simple case of the electrochemical double layer of solid-liquid interfaces for a semiconductor electrode in the dark. When the semiconductor is in contact with an electrolyte, the charges in the solid need to be redistributed to reach equilibrium due to the Fermi level E_F differences between solution and electrode. The E_F of the semiconductor aligns with the E_F of the red-ox species resulting in a band bending of the conduction and valence band energies (respectively denoted E_{CB} and E_{VB}) forming in this case with a downward band-bending of a p-type semiconductor a depletion layer. Therefore, it is not possible to neglect the tunneling process as for metal electrodes.[98,99] As sketched in Figure 4, the band bending, which depends on the externally applied voltage/irradiation, the red-ox potential from the electrolyte, and the doping level of the substrate, can shift electronic states of the surface across E_F. Thus, charge transfer between the electrode and the ions adsorbed at the surface can occur via conduction/valence band and via surface states.[97]

© 2023 The Authors. ChemElectroChem published by Wiley-VCH GmbH

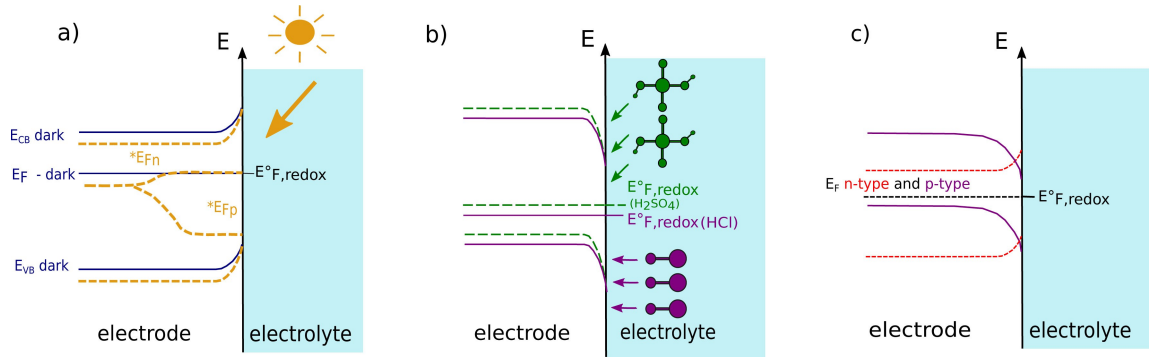

Figure 4. Energetic band diagrams showing the influence of the irradiance, the doping type, and the electrolyte on the EDL and the optical properties of an idealized semiconductor-liquid interface (no surface passivation/corrosion). The electrode is considered as photo-cathode for solar water splitting, and H^+/H_2 is the most active redox couple. Interfacial layers and charge-carrier recombination[97] are ignored for the sake of simplicity. a) dark and illuminated (dotted line) EDL of n-type semiconductor. b) EDL of p-type semiconductor influenced by the charging effect of H_2SO_4 (dotted lines) and HCl electrolytes (0.01 M). c) EDL for n and p-type semiconductors.

Band bending arises from an electric charge exchange between the bulk and the surface (states) of the semiconductor. The resulting electric field modifies the dielectric function of such a material and therefore contributes to the anisotropy of the associated RA spectrum, making it an indirect probe of interfacial electric fields.[100] This effect, called the linear electro-optic effect, may have different origins. On the electrode side, the electric field is influenced by the doping level of the substrate, while in the space-charge layer on the electrolyte side, it depends on molecular dipoles and their orientation with respect to the surface, but also on the ion distribution. An electric dipole within an adsorbed molecular film can also affect the integrated electric field. External parameters that impact the electric field are certainly the applied voltage, but also the irradiation of the system. The development of an illumination-induced photovoltage adds another layer of complexity. At a given light intensity, the photovoltage also depends on the charge-carrier recombination, which can, and in most cases will, change upon corrosion or potential-induced restructuring of the interface.[97] Yet as RAS is an optical technique, a minimum level of illumination by the measurement spot cannot be avoided.

Investigating these different contributions of the electric field by RAS can help elucidate surface reconstructions during molecular chemisorption processes and study preferential adsorption sites from the evidence of adsorbed molecular films.[101] Taken together, these specifics of the EDL of the semiconductor-electrolyte system show that these interfaces can be more complex than for metals, which also impacts spectroelectrochemistry. Figure 5 compares their different impact on the EDL and on the optical properties of semiconductors. The orange and red spectra, respectively corresponding to n-type with and without additionnal illumination, are almost identical. It indicates that additional illumination, in the considered situation, has hardly no influence on the optical properties of the interface. In this case, n-type InP is acting as a photo-cathode for the reduction of protons. Hence, as showed on Figure 4 (a), the redox potential aligns with the the quasi-Fermi level of the electrons (*E_{Fn}), resulting in a minor increase

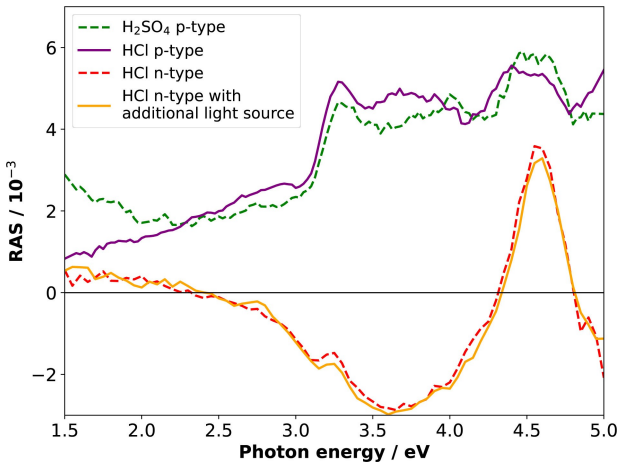

Figure 5. RA spectra of InP(100) for the different conditions a), b) and, c) illustrated on Figure 4. Here, the doping shows a major effect, the electrolyte a minor effect, and the bias illumination essentially none.

of the photovoltage. Similarly to the spectra with and without additional illumination, the spectra associated to p-InP-HCl and p-InP-H_2SO_4 interfaces (purple and green spectra, respectively) resemble each other. The electrolytes have the same concentration, but different pH, which influence the redox potential of H^+/H_2 and therefore modify the position of the Fermi level and the band bending (see Figure 4 (b)). For this reason, the type of electrolyte has a minor effect on the related RA spectra. The most noticeable changes between the RA spectra provided by Figure 5 are in fact due to a difference in doping levels. Since E_{CB}, E_{VB} and E_F depend on the charge carriers concentrations, the doping level strongly impacts the electronic structure and therefore the optical properties at the interface.

3.4. Aqueous electrolyte systems I: InP(100)

As a first example for the application of electrochemical RAS, we present an investigation of the interfacial structure of InP(100) in contact with 0.01 M hydrochloric acid (HCl). Such

© 2023 The Authors. ChemElectroChem published by Wiley-VCH GmbH

21960216, 2023, 8, Downloaded from https://chemistry-europe.onlinelibrary.wiley.com/doi/10.1002/celc.202300027 by KIZ der Universitat Ulm, Wiley Online Library on [03/05/2023]. See the Terms and Conditions (https://onlinelibrary.wiley.com/terms-and-conditions) on Wiley Online Library for rules of use; OA articles are governed by the applicable Creative Commons License

III–V semiconductor/electrolyte interfaces play a crucial role in high-efficiency direct PEC solar water-splitting devices. These systems produce hydrogen via combining water electrolysis and solar energy harvesting in a single process and have been shown to achieve highest solar-to-hydrogen efficiencies.[75] However, even though significant progress has been made in improving the stability of III–V semiconductors in aqueous electrolytes, corrosion is still preventing practical applications.[76] Hence, a detailed understanding of the processes at the solid/electrolyte interface is crucial for the realization of a viable solar-water splitting technology based on III–V semiconductors. Therefore, we have chosen InP(100) as a first case study for an electrochemical RAS analysis, as it is available in high single-crystalline quality, but also subject to rapid electrochemical corrosion. A more detailed investigation with experimental details can be found in our recent publication.[57]

Figure 6 (a) presents a 2D color-coded graphic (colorplot) showing continuously acquired RA spectra in situ under CV conditions. The starting point were samples prepared from *epi-ready* InP(100) wafers, but without pre-treatment of the surface prior to immersion into the electrolyte. The corresponding applied potential as a function of time, and the cyclic voltammogramm are shown on the right-hand side of Figure 6 (a) and in Figure 6 (b), respectively. Note that a baseline correction is applied to all the spectra using the signal of an optically isotropic Si(100) crystal in water. Such a continuous type of measurement is helpful for the exploration of a novel system, giving a broad spectral overview at the expense of temporal resolution.

In Figure (b), the cathodic current for the corresponding CV in the voltage range between −0.4 V to −1.3 V can be ascribed to the reduction of InP into phosphine and metallic In. The latter can then further react with HCl to form an InCl interfacial film starting from potentials lower than −0.4 V vs. (Ag/AgCl).[57] The cathodic current density starting from around −0.4 V and reaching a plateau at −1.3 V is associated with the hydrogen evolution reaction. Here, the current density is limited in rate by the low overall photocurrent from the incident light of the spectrometer, while below −1.7 V, the hydrogen production is no longer photo-current limited.[57] This highlights again the challenge that for a semiconductor, the optical probe can impact the photoelectrochemical response of the system under investigation.

The formation and disintegration of the InCl film strongly depends on the electrolyte concentration. The literature shows that for high HCl concentration (0.5 M), in the anodic region,

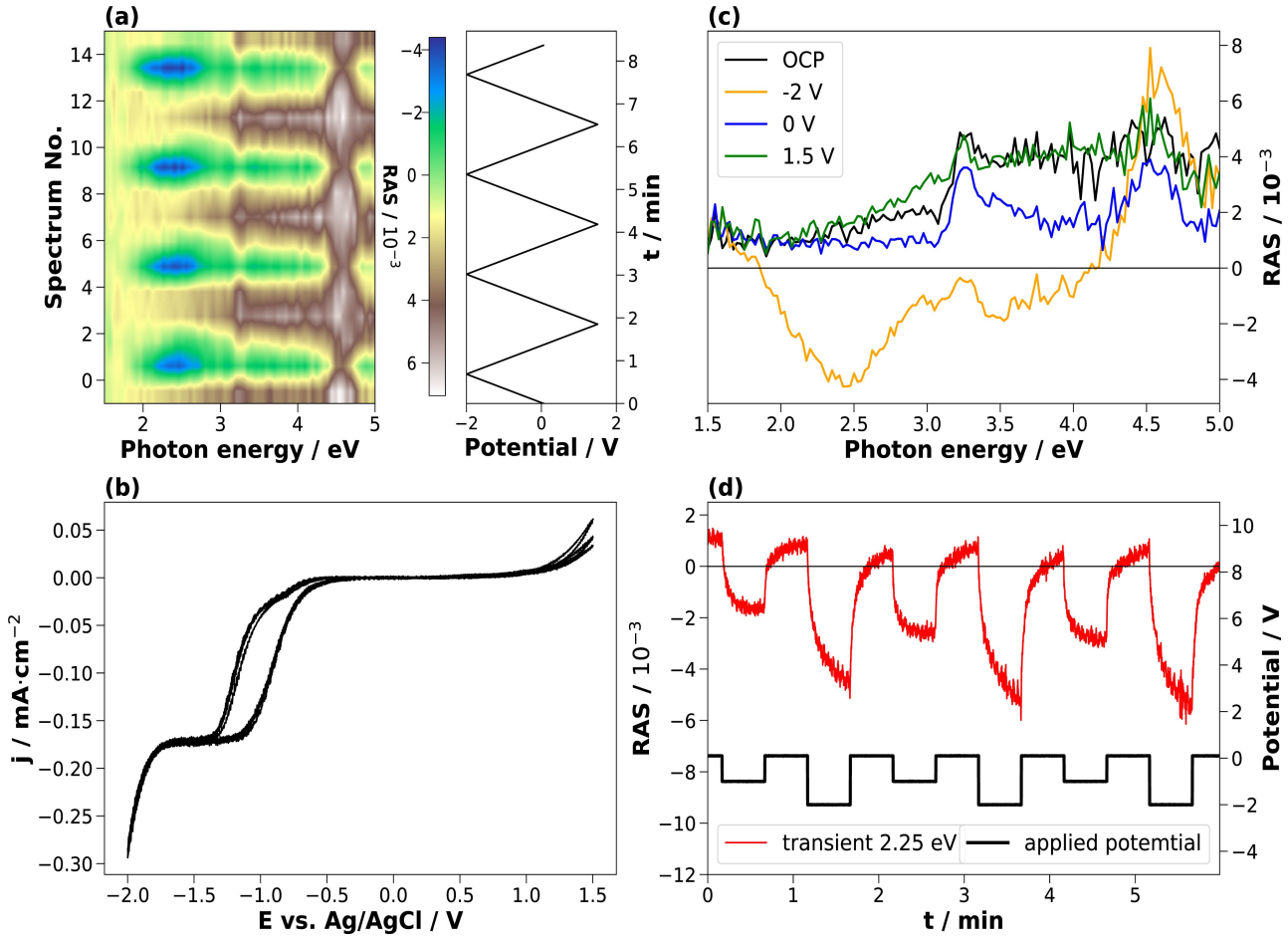

Figure 6. P-type InP(100) in contact with 0.01 M HCl. Left: Colorplot (a) of the InP(100) surface in contact with the electrolyte under cyclic voltammetry conditions (b), scan from open-circuit potential (OCP) towards −2 V and then to 1.5 V for 3 cycles, with a scan rate of 50 mV s^{-1}. Right: RA spectra in the electrolyte (c) at OCP and during chronoamperometry, and transient at 2.25 eV (d) acquired while potential steps are applied.

© 2023 The Authors. ChemElectroChem published by Wiley-VCH GmbH

21960216, 2023, 8, Downloaded from https://chemistry-europe.onlinelibrary.wiley.com/doi/10.1002/celc.202300027 by KIZ der Universitat Ulm, Wiley Online Library on [03/05/2023]. See the Terms and Conditions (https://onlinelibrary.wiley.com/terms-and-conditions) on Wiley Online Library for rules of use; OA articles are governed by the applicable Creative Commons License

21960216, 2023, 8, Downloaded from https://chemistry-europe.onlinelibrary.wiley.com/doi/10.1002/celc.202300027 by KIZ der Universitat Ulm, Wiley Online Library on [03/05/2023]. See the Terms and Conditions (https://onlinelibrary.wiley.com/terms-and-conditions) on Wiley Online Library for rules of use; OA articles are governed by the applicable Creative Commons License

InCl then only partially dissolves into In^{3+} and Cl^- at −0.3 V vs. (Ag/AgCl). Therefore, the formation of InCl is non-reversible, and a several nm-thick passivation layer builds up over the cycles.[102–104]

In the case of 0.01 M HCl, however, the CV shows, in terms of the interfacial structure, fully reversible cathodic and anodic processes. The reversibility of the processes is also observed on the colorplot (CP) by a reversible build-up of characteristic anisotropies in the cathodic and anodic potential ranges. The strong anisotropic features shown in Figure 6 (c) indicate well-ordered interfacial structures. A reference spectrum acquired at OCP (around 0.2 V vs. Ag/AgCl) in the electrolyte is plotted together with three spectra measured in 0.01 M HCl at different constant applied potentials. The spectral signature of the reference spectrum exhibits two peaks at around 3.25 and 4.55 eV, respectively, due to surface-modified bulk transitions.[44] The strong features at about 2.25 and 4.5 eV at −2 V indicate that when scanning to negative potentials, the epi-ready oxide layer present on the epi-ready InP(100) wafer dissolves in the acidic electrolyte, leading to a well-ordered, oxide-free layer. At 0 V and anodic potentials, the spectra are again very similar to the one at OCP, suggesting the re-formation of an oxide layer very similar to the initial epi-ready oxide, accompanied by chlorine-InP interactions.[103,104] To better understand the involved interfacial structure and chemistry, computational RAS is performed.

Computational RA spectroscopy first requires setting up an adequate selection of structural models for the system under investigation. In this case, the ingredients In, P, O, Cl, and H span a large parameter space of potential structures. Our starting point here was guided by the findings discussed above. For a comparison of computed RA spectra with the experimental spectrum of InP(100) in 0.01 M HCl under the applied potential of −2 V, we consider three structures: the fully Cl^- covered InP(100) surface in which an InCl layer is formed (2Cl), and one and three hydrogen atoms adsorbed on the InP(100) surface (2P-1H and 2P-3H, respectively). Furthermore, we investigate how sensitive the calculated spectrum is to the adsorption of one and two water molecules on the 2Cl and 2P-1H surfaces. Figure 7 displays the computed spectra of all investigated systems as well as the experimental spectrum. Our calculations reveal that the theoretically derived RA spectra of the 2Cl, 2P-1H, and 2P-3H surfaces are similar to the experimental spectrum. In the 2Cl case, two main negative peaks around 2.2 and 3.8 eV are revealed. The positions of these peaks are slightly changed when the additional one water molecule is adsorbed. The spectral shape, however, remains conserved. The spectrum for two water adsorbed 2Cl surface is considerably up-shifted compared to that of one water adsorbed surface. Interestingly, a positive anisotropy at 4.5 eV, which is observed in the experiment, is not shown. This suggests that the real interface is more complex than a simplified model with a highly ordered supercell and in the absence of oxygen molecules. Similar to the 2Cl structure, we can find the two notable negative anisotropies around 2.5 eV and 3.3 eV in the calculated spectrum of 2P-1H. In contrast to 2Cl, the 2P-1H surface exhibits a strong positive feature at 4.0 eV. This shows a redshift of around 0.55 eV compared to the main positive peak shown in the experiment. The adsorption of water molecules results in a slight blueshift and an increase in the minimum peak. Our calculation of the 2P-3H surface displays a constantly positive feature until 3 eV, a negative anisotropy, and a pronounced positive anisotropy at 3.4 and 4.4 eV, respectively. The corresponding maximum anisotropy in the computed spectrum is similar to that in the experiment. Based on these results, we can anticipate that H-terminated and Cl-terminated surfaces coexist. This hypothesis will have to be tested in future work where applied potentials and more structures are be considered.

While the results from computational RAS already help to form a first atomistic picture of the studied electrochemical system, they do not yet show the high degree of quantitative agreement with experiment as often established for many vacuum-based systems. This demonstrates the above-mentioned challenges of the large chemical parameter space resulting in many structures to be considered as well as the

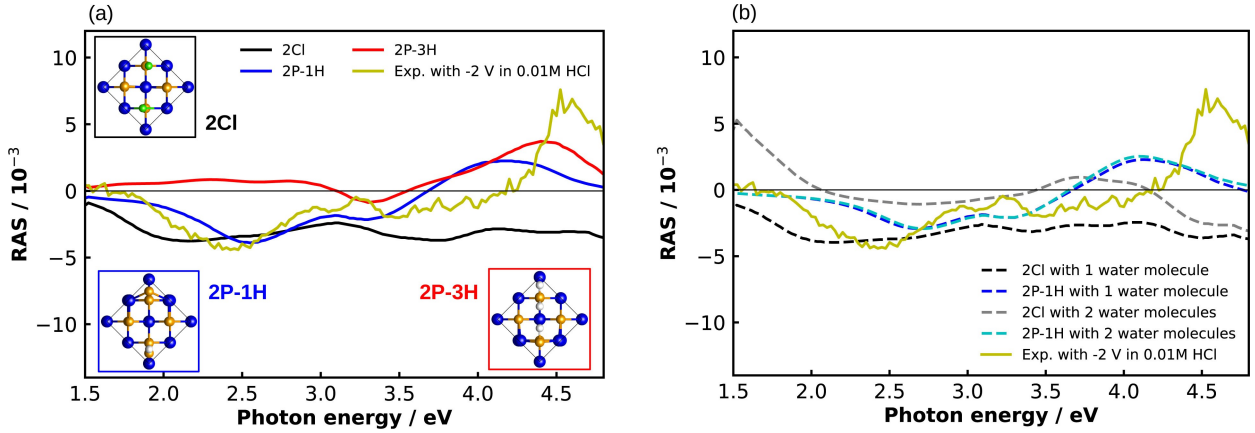

Figure 7. (a) Calculated and experimental (yellow) RA spectra of the InP(100) surface covered with Cl atoms and adsorbed with one and three H atoms. The injects are the top view of corresponding structures. Green-, blue-, orange-, and white-colored balls represent Cl, P, In, and H atoms, respectively. (b) Computed RA spectra of one water molecule adsorbed on 2Cl and 2P-1H.

© 2023 The Authors. ChemElectroChem published by Wiley-VCH GmbH

methodological uncertainty on how to best treat applied potentials in a bulk electrolyte.

Further testing of the validity of the structural model derived from the data above should, in principle, be enabled by complementary XPS, probing the chemical composition of the surface. Yet such an analysis requires the transfer to ultra-high vacuum, where the electrolyte layer has to be removed before the measurement. Yet here, the question arises, if the interfacial layer persists under this change of external conditions. Time-resolved measurements that assess the kinetic stability of a given interface can help to estimate the experimentally available time-window between breaking of the potential control and establishing a dry surface in UHV. Figure 6 (d) shows a transient, where the optical anisotropy is acquired at a fixed photon energy of 2.25 eV, while potential steps at −1 V and −2 V are applied. The fast and reversible change in the anisotropy suggests that if a thin InCl layer builds up in the cathodic region, it immediately dissolves when setting the potential back to OCP. Therefore, at low HCl concentration, the hypothetically formed InCl is unstable and unlikely to be accessible for further analysis by other techniques, where no potential can be applied in an electrolyte, such as XPS in vacuum.

To summarize, in situ electrochemical RAS enabled to identify electrochemical conditions with respect to potentials and electrolyte concentration, under which highly ordered InP-electrolyte interfaces can be prepared. Alas, the observed surface layer generated is not stable when the applied voltage is set back to OCP, which renders complementary analysis for the identification of the exact chemical composition by XPS challenging. The results clearly demonstrate the potential of electrochemical RAS for the monitoring of well-defined (photo)electrochemical etching or layer deposition for III–V semiconductors, especially relevant for solar water splitting applications. In order to computationally identify the real surface structure formed by different potentials, complex surface phase diagram of various surface structures have to be investigated. To do so, molecular dynamics and calculations with applied potentials, followed by excited state calculations can be performed, but the computational effort is significant.

3.5. Aqueous systems II: Au(110)

Understanding electrochemical interfaces implies the ability to distinguish between chemical and physical processes occurring between the electrode surface and the electrolyte. Noble metals such as gold, inert in most acidic and alkaline media, allow focusing on the physical and chemical adsorption of molecules from the electrolyte on the metal surface by preventing or at least – compared to semiconductors – reducing chemical side reactions. Changes in the interaction between the electrolyte's dipoles and electrode surface under applied potentials can also lead to surface structural changes. Insights from these processes on gold can then be ideally transferred to more complex electrochemical systems.

The interfacial structure of gold single-crystals in contact with electrolytes has been experimentally widely investigated by STM, CV, and RAS.[105,106] Additionally, ex-situ RHEED and LEED have been used in UHV to verify the surface reconstruction after annealing prior to electrochemical cycling.[107] In particular, Mazine et al. have reported on the reconstruction of Au(110) in sulfuric acid under different applied potentials observed by RAS.[84] Initially possessing a reconstructed annealed Au(110)(1 × 2) surface, the crystal adopts an unreconstructed (1 × 1) surface upon immersion in H_2SO_4. Starting from an Au(110)(1 × 1) surface in H_2SO_4 at OCP, RAS measurements trace the electrochemically induced surface reconstruction below 0.05 V vs. SCE (0.018 V vs. Ag/AgCl) reference corresponding to a (1 × 2) missing row. The charge-distribution organization at the electrode surface depends on the applied potential. Hence, tuning the applied potential modifies surface-ion interactions, which play an essential role in the reconstruction/deconstruction.

At room temperature, the unreconstructed Au surface is in a metastable state. Applying a negative electrode potential with respect to the potential of zero charge (pzc) reduces the activation barrier for the reconstruction,[108] and therefore allows the transition from the (1 × 1) to the (1 × 2) surface. When applying potentials above 0.25 V vs. SCE (0.218 V vs. Ag/AgCl), the electrode is charged positively. Adsorption of the anions of the electrolyte (sulfate ions) on the Au surface lifts the reconstruction and the unreconstructed (1 × 1) surface is restored.

Here, we show typical electrochemical RAS experiments with Au(110) in low concentrations of both sulfuric and hydrochloric acid. Prior to the electrochemical RAS experiment, the crystal is flame-annealed to prepare a reconstructed (1 × 2) surface.[79,81,84,108] A baseline correction is applied to all the spectra using the spectrum of Au(110) in the electrolyte at OCP and its inverted spectrum, which was obtained by rotating the sample by 90 . The RA spectra obtained in H_2SO_4 and HCl are presented in Figure 8 (a) and (b), respectively. After annealing, Au(110) RA spectra exhibit a "W"- like shape. Contributions to the complex dieletric function arise both from the bulk and the surface. The slight differences between the spectra are due to different interband transitions from different Fermi level positions.[80] In general, the results in sulfuric acid (H_2SO_4) agree with those of Mazine et al.[84] The blue curve was recorded under open-circuit potential and shows a characteristic RA spectrum of well-ordered unreconstructed (1 × 1) Au(110) in an acidic environment.[84] The spectra obtained under applied potentials exhibit similar features as the spectrum measured in H_2SO_4. Below OCP, an Au(110) (1 × 2) reconstruction (−0.15 V, orange spectra) is observed with a pronounced shoulder at about 2 eV. In the range from OCP to 0.6 V, an Au(110) (1 × 1) unreconstructed (0.3 V, green spectra) surface is existent. This shows that the different surface reconstructions are associated with distinct optical signatures, hence at this stage providing a similar type of information as the diffraction patterns from LEED, which is limited to UHV.

Interestingly, when increasing the potential to values higher than 0.6 V, a positive anisotropic peak develops around 2.3 eV

© 2023 The Authors. ChemElectroChem published by Wiley-VCH GmbH

21960216, 2023, 8, Downloaded from https://chemistry-europe.onlinelibrary.wiley.com/doi/10.1002/celc.202300027 by KIZ der Universitat Ulm, Wiley Online Library on [03/05/2023]. See the Terms and Conditions (https://onlinelibrary.wiley.com/terms-and-conditions) on Wiley Online Library for rules of use; OA articles are governed by the applicable Creative Commons License

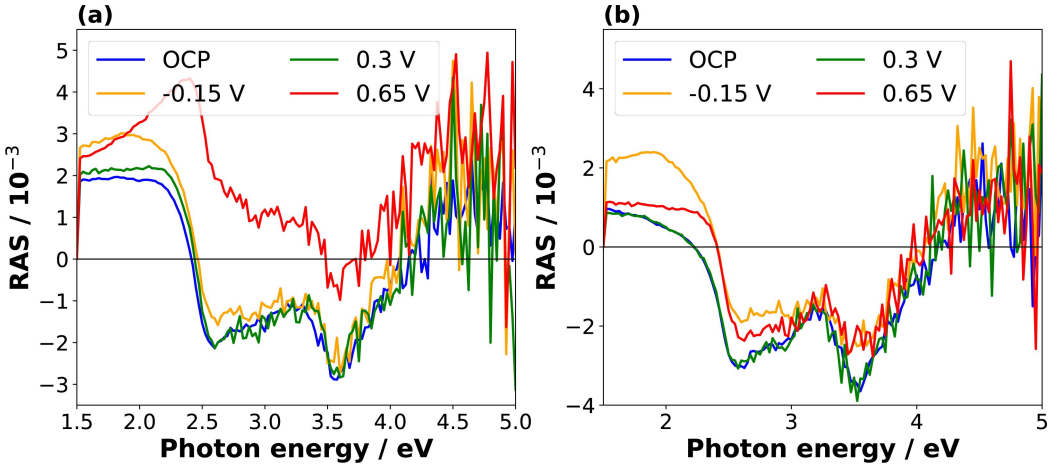

Figure 8. RA spectra of annealed Au(110) in different electrolytes under applied potentials. (a) in 0.1 M HCl and (b) in 0.1 M H_2SO_4 under different applied potentials vs. Ag/AgCl and at OCP. At the beginning of the experiments, the OCP values of Au(110) in 0.1 M HCl in 0.1 M H_2SO_4 were 164 mV and 367 mV, respectively. The orange spectra correspond to the Au(110) (1×2) reconstruction while the green spectra correspond to the unreconstructed Au(110) (1×1) surface.

in HCl (0.65 V, red spectrum). This peak was not observed in the spectrum measured in H_2SO_4 (see Figure 8 a) and, to the best of our knowledge, has not been reported in the literature. With no computational spectroscopy available at this point, the interpretation of this spectral feature has to rely on literature data. Yet for a metal, this task should be, due to the absence of a photovoltage adding uncertainty to actual potential at the surface as discussed above, a more reliable undertaking.

Some previous studies of gold/acidic electrolyte interfaces have shown that the screening of anions depends on the charge of the surface.[77,109–111] In particular, Shi et al. have reported that applying a potential above 0.7 V vs. SCE (0.668 V vs. Ag/AgCl) to the Au(111)/HCl interface leads to a change in the polarity of the chemisorption bond between gold and chloride, forming an ordered ($p \times \sqrt{3}$) overlayer of adsorbed chloride.[111] A polarity drop between Cl-anions and the gold surface could generate a linear electro-optic effect at the Au(110)/HCl interface and could explain the presence of the shoulder on the RA spectrum at 2.3 eV. Furthermore, the formation of an ordered overlayer could explain why the optical anisotropy of the interface is significantly increased. The observed optical anisotropy could therefore be the signature of an ordered Cl^- overlayer, formed in the anodic region above 0.7 V vs. SCE (0.668 V vs. Ag/AgCl).

The distinction between anisotropic features responsible for surface reconstructions and electrode/electrolyte electrostatic interactions and the reversibility of these processes can be readily observed in the transient illustrated in Figure 9 (a). The transient corresponds to Au(110) in 0.1 M HCl under CV conditions. Here, the transient was recorded at 2.3 eV because at this energy both features responsible for surface reconstruction/deconstruction and adsorbed anions overlayer are present. The CV, illustrated in Figure 9 (c), was performed between −0.25 V and +0.6 V (vs. Ag/AgCl) with a scan rate of 20 mV/s, starting from −0.25 V for 4 cycles. The current density and the potential from the CV are plotted separately as function of the

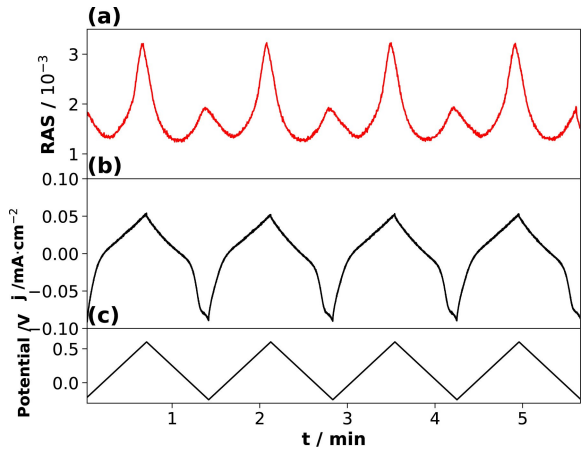

Figure 9. Time-resolved correlation between RAS and CV for Au(110). (a) Transient of Au(110) in 0.1 M HCl at 2.3 eV after annealing, during cycling voltammetry conditions (−0.25 to 0.6 V vs. Ag/AgCl reference electrode for 4 cycles with 20 mV/s scan rate.) (b) and (c) respectively correspond to the current and the voltage as function of the time from the CV.

time on Figure 9 (b) and (c), respectively. Such a plot type allows easier correlation between faradaic processes and changes in optical properties at the interface. The small time shift between the maxima of the current density and the transient is, in this case, an artifact from imperfect temporal alignment of CV and RAS measurements.

Figure 9 (a) shows the first maximum anisotropic peak corresponding to a voltage of 0.6 V and is a signature of the change in chloride adsorption. The second maximum anisotropic peak corresponds to a voltage of −0.25 V and indicates the reconstruction. On the CV, the reconstruction is associated with a progressive decline of the current density from 0.6 to −0.25 V marked by a shoulder at around 0.018 V (vs. Ag/AgCl). Whereas in the same potential range, the anisotropy first decreases until it reaches a minimum at around 0.2 V (beginning of the anion adsorption) and then rises again. The reverse

© 2023 The Authors. ChemElectroChem published by Wiley-VCH GmbH

21960216, 2023, 8, Downloaded from https://chemistry-europe.onlinelibrary.wiley.com/doi/10.1002/celc.202300027 by KIZ der Universitat Ulm, Wiley Online Library on [03/05/2023]. See the Terms and Conditions (https://onlinelibrary.wiley.com/terms-and-conditions) on Wiley Online Library for rules of use; OA articles are governed by the applicable Creative Commons License

21960216, 2023, 8, Downloaded from https://chemistry-europe.onlinelibrary.wiley.com/doi/10.1002/celc.202300027 by KIZ der Universitat Ulm, Wiley Online Library on [03/05/2023]. See the Terms and Conditions (https://onlinelibrary.wiley.com/terms-and-conditions) on Wiley Online Library for rules of use; OA articles are governed by the applicable Creative Commons License

trend is observed during the deconstruction. Yet, while the transient peaks are almost symmetric around the extrema of the applied potential, the current cycles from the CV show a pronounced asymmetry around the cathodic extremum. After the formation of the reconstruction (below 0.018 V), the slope of the current decrease is reduced towards −0.2 V. This could be attributed either to the onset of a (1×3) surface reconstruction[112] or a change of the charging current of the EDL. A more detailed analysis of transients during potential steps, also including isotherms[94] would be needed to clarify this.

In summary, we showed that the well-known, potential-dependent re-ordering of the Au-electrolyte interface is associated with distinct optical anisotropies and can therefore be monitored in a time-resolved manner by electrochemical RAS. This demonstrates how RAS can complement CV, in which the distinction between surface reconstruction and chemical processes is not straightforward. Although electrochemical RAS is more developed for metallic systems than for III–V semiconductors systems – or semiconductors in general – mentioned in the previous section, it still needs significant input to become a well-establish method. In this regard, RAS represents an excellent complementary method to scanning tunneling measurements (STM) when investigating single-crystalline metals at different potentials.[107] It could also be used in the currently field of battery research, especially for metal-anode batteries, as we will briefly discuss in the following.

3.6. Outlook for battery systems

Metal electrodes like magnesium or aluminium are expected to play an essential role in next-generation battery technologies.[113] Especially for novel material combinations and novel electrolytes, often very little is known about the electrode-electrolyte interface's atomistic structure at operation conditions. Nevertheless, this knowledge is crucial for developing and benchmarking new and sustainable batteries. From this, RAS can potentially be used for battery research on the anode and the cathode, as outlined in the following.

Two aspects are crucial for the investigation of the anode: the solid-electrolyte interphase (SEI) and stripping and plating. For alkali and alkaline earth metals anode batteries, an SEI is formed on the battery's anode in contact with the liquid electrolyte's salts, solvents, additives, or impurities, consisting of different components in either a mosaic, homogeneous or even artificially created form.[4,114] In addition to the already existing ex situ and in situ/operando techniques for interfaces in batteries,[115] RAS could be highly beneficial when creating an artificial SEI because it allows controlling the growth process in the same way it monitors the growth process of semiconductors.[48] The other point worth considering on the anode side is stripping and plating. Here RAS can investigate changes in the surface anisotropy during metal deposition in analogy to epitaxial growth studies in gas-phase ambient.[48] The technique should also allow the detection of nuclei that lead to dendrite formation. Such investigations are especially relevant for lithium metal batteries. However, they should also be addressed for multivalent metal batteries (e.g. Al and Mg batteries).[116]

For the cathode, RAS also promises to benefit battery research: despite a large number of cathode materials for rechargeable magnesium batteries being investigated,[117] only little is known about the cathode-electrolyte interface (CEI). This is because mostly the intercalation into the cathode is investigated rather than the interphase.[118] RAS could close the knowledge gap and help develop high-performance batteries by highlighting an often overlooked topic.

However, there are also some challenges when investigating metal electrodes for batteries with RAS, both from an experimental and computational perspective. The first challenge comes with the electrolyte used in batteries, which might be, as in the case of Grignard, optically active.[119] The consequence is that the probing light is absorbed, which leads to a low signal-to-noise ratio in the RA spectra. Furthermore the surface preparation is quite challenging as alkali and earth-alkaline metals are highly reactive with oxygen and water. Therefore polishing and annealing must be done in a glove box.[120] This, however, allows for the direct observation of the crystal surface quality without transfer to UHV.

For theoretical investigations, battery electrolytes are also challenging because the number of atoms increases compared to aqueous electrolytes by a factor of ten when using highly advanced electrolytes like $Mg[B(hfip)_4]_2$ for magnesium batteries.[121] Furthermore, for metallic systems, a higher number of **k**-points are generally demanded to describe partially occupied bands of the systems. These combined effects lead to high computational costs.

As we have outlined, electrochemical RAS for battery applications will be a significant challenge; however, it can open up a new way to investigate the anode and cathode surface operando with a reduced or even without the requirement of correlation with other experimental techniques.

4. Conclusion and Outlook

The present review outlined the potential and current state of RAS as an emerging optical technique for exploring electrochemical interfaces. Probing the polarization state of light reflected at crystalline surfaces, EC-RAS detects changes in the surface structure and surface chemistry of electrochemical systems in situ/operando with a sub-monolayer resolution and on a reasonably fast time scale with standard light sources. The use of more advanced light sources with higher luminosity, hitherto barely explored, could further improve time resolution to the μs range.

Outlining the theory behind computational RAS, we briefly showed that standard DFT on a PBE level together with IP-RPA for the excited states can already provide reasonable, quantitative results for some systems. While in general, the computational method is relatively well-established for semiconductors, it remains challenging for metallic systems, whereas for electrochemical experiments, the study of metals dominates. Further-

© 2023 The Authors. ChemElectroChem published by Wiley-VCH GmbH

21960216, 2023, 8, Downloaded from https://chemistry-europe.onlinelibrary.wiley.com/doi/10.1002/celc.202300027 by KIZ der Universitat Ulm, Wiley Online Library on [03/05/2023]. See the Terms and Conditions (https://onlinelibrary.wiley.com/terms-and-conditions) on Wiley Online Library for rules of use; OA articles are governed by the applicable Creative Commons License

more, the exploration of best practices for computational RAS of electrochemical systems has just begun. This explains why most EC-RAS applications on metallic systems in the literature combined their studies with other experimental techniques such as STM, but none used computational RAS.

We presented typical experimental approaches and results for the metallic system Au(110) and the semiconductor InP(100). For the former, RA spectra under applied potentials show that RAS is a powerful tool to visualize changes in surface reconstruction and in ions adsorption at the interface. For the latter, we also show first steps for the interpretation of experimental signatures aided by computational spectra derived from a DFT ground-state structure. This already allowed to determine experimental parameters with respect to applied potential and electrolyte composition, at which ordered surfaces of InP can be stabilized in the electrolyte, providing a starting position for further (photo)electrochemical surface processing. Yet the many constituents of the interface in addition to the requirement to apply an electrode potential in a realistic manner renders the configuration space to be probed by DFT large and the overall computational effort significant.

Time-resolved potential steps measurements allow to quantify the time-window available between breaking of the potential control and complete removal of the electrolyte for transfer to complementary UHV-based analysis. This is highly relevant to assess the transferability decoupled electrochemical experiments followed by surface science analysis in vacuum. Furthermore, fitting time-resolved measurements with adsorption isotherm models gives more quantitative insights into interfacial processes by the determination of kinetic and thermodynamic parameters. Also quantitative measures for the surface quality prior to or during an electrochemical experiment can be derived. When comparing a specific spectrum with a reference spectrum for the same surface, it is possible to quantitatively assess the quality of a given surface, i.e. which fraction of the surface actually shows a given reconstruction. Similarly, the quantity of a specific chemical species or ion on a well-ordered interface can be assessed, as soon as the corresponding spectral signature has been identified from complementary experiments or computational spectroscopy. Finally, RAS also has the potential to make an impact in battery research, giving insides into SEI formation, metal stripping and plating, as well as ion transport processes.

Experimental Section

InP samples were prepared from p-doped InP(100) (Zn-doping of $4 \cdot 10^{18}$ cm^{-3}), single-crystalline wafers with an offcut of (0 ± 0.5) from CrysTec. The wafers with an epi-ready surface were cleaved and used without further pre-treatment. For the RAS measurement, the InP samples were mounted into a photoelectrochemical cell (PECC) from Zahner without an optical window. The back-side of the samples were contacted with a copper wire, fixed with a silver paste (Ferro GmbH), and with GaIn eutectic (Sigma Aldrich). Pt and Ag/AgCl electrodes were used as counter and reference electrodes, respectively.

A gold single crystal was purchased from Mateck (purity 99,999 %), polished on one side to a roughness below 0.01 μm and an orientation accuracy better than 0.1 . Before electrochemical RAS measurements, the crystal was flame-annealed with the following procedure. The crystal was placed on a ceramic plate and flamed annealed with a bunsen burner gun to about 100 C below the melting temperature for about 5 minutes until the edge of the crystal turned red. The crystal was cooled down under Argon flow for about 10 min.[122] The annealed crystal was then transferred to the PECC equiped with an optical window. Pt and Ag/AgCl electrodes were used as counter and reference electrodes, respectively.

The PECC was filled with the HCl and H_2SO_4 electrolytes (VWR Chemicals, reagent grade). The RA spectra were measured with an RA-Spectrometer (EpiRAS from Laytec) equipped with a Xenon light source. The electrochemical measurements were done with a potentiostat (Versa STAT 3F from AMETEK). Further details of the experimental procedure can be found elsewhere.[57]

For structural optimizations of slabs of the electronic structure model, DFT calculations were performed using the CP2K code.[58] The code employs the gaussian and plane waves scheme. The generalized gradient approximation (GGA) as parameterized by Perdew-Burke-Ernzerhof (PBE) for the exchange-correlation functional was used.[59] A plane-wave cutoff of 800 Ry was set. We adopted Goedecker-Teter-Hutter (GTH) pseudopotentials. Ground-state properties were computed with QUANTUM ESPRESSO.[62] Here, we employed optimized norm-conserving vanderbilt pseudopotentials.[123] The sampling of Brillouin zone (BZ) was carried out with a $10 \times 10 \times 1$ **k**-grid, and an energy cutoff was set to 60 Ry. For computational RAS, we used the IP-RPA approach implemented in Yambo.[60,61] We applied a scissor operator to correct the underestimated band gap.

Acknowledgements

The following organizations are thanked for financial support: DFG (Deutsche Forschungsgemeinschaft) under Germany's Excellence Strategy – EXC 2154 – Project number 390874152 as well as DFG project number 434023472. Computational resources were provided by the state of Baden-Württemberg, through bwHPC, and DFG through grant no. INST 40/575-1 FUGG (JUSTUS 2 cluster). We thank Krishnaveni Palanisamy for discussions on the experimental approach to anneal the gold crystals.

Conflict of Interest

The authors declare no conflict of interest.

Data Availability Statement

The data used to generate the plots for this review (section 3) are openly available on Zenodo[124] and the NOMAD Repository.[125]

Keywords: electrochemistry · interfaces · time-resolved spectroscopy · computational chemistry · surface chemistry

© 2023 The Authors. ChemElectroChem published by Wiley-VCH GmbH

[1] M. Chatenet, B. G. Pollet, D. R. Dekel, F. Dionigi, J. Deseure, P. Millet, R. D. Braatz, M. Z. Bazant, M. Eikerling, I. Staffell, P. Balcombe, Y. Shao-Horn, H. Schäfer, *Chem. Soc. Rev.* **2022**, *51*, 4583.
[2] K. Sivula, R. van de Krol, *Nat. Rev. Mater.* **2016**, *1*, 15010.
[3] Q. Wang, K. Domen, *Chem. Rev.* **2020**, *120*, 919.
[4] J. Popovic, *Nat. Commun.* **2021**, *12*, 6240.
[5] J. Sun, B. Luo, H. Li, *Adv. Sustainable Syst.* **2022**, *3*, 2100191.
[6] M. M. May, K. Rehfeld, *Adv. Energy Mater.* **2022**, *12*, 2103801.
[7] M. Wang, Z. Feng, *Chem. Commun.* **2021**, *57*, 10453.
[8] D. V. Esposito, J. B. Baxter, J. John, N. S. Lewis, T. P. Moffat, T. Ogitsu, G. D. O'Neil, T. A. Pham, A. A. Talin, J. M. Velazquez, B. C. Wood, *Energy Environ. Sci.* **2015**, *8*, 2863.
[9] M. Bozorgchenani, F. Buchner, K. Forster-Tonigold, J. Kim, A. Groß, R. J. Behm, *Langmuir* **2018**, *34*, 8451.
[10] C. R. Brundle, Ultra-High Vacuum Techniques of Surface Characterization, in *Industrial Applications of Surface Analysis*, volume 199 of *ACS Symposium Series*, pages 13–32, American Chemical Society **1982**.
[11] A. Hajduk, M. V. Lebedev, B. Kaiser, W. Jaegermann, *Phys. Chem. Chem. Phys.* **2018**, *20*, 21144.
[12] D. M. Itkis, J. J. Velasco-Velez, A. Knop-Gericke, A. Vyalikh, M. V. Avdeev, L. V. Yashina, *ChemElectroChem* **2015**, *2*, 1427.
[13] Z. Wang, Y. Zhang, B. Liu, K. Wu, S. Thevuthasan, D. R. Baer, Z. Zhu, X.-Y. Yu, F. Wang, *Anal. Chem.* **2016**, *89*, 960.
[14] M. Favaro, B. Jeong, P. N. Ross, J. Yano, Z. Hussain, Z. Liu, E. J. Crumlin, *Nat. Commun.* **2016**, *7*, 12695.
[15] S. Axnanda, E. J. Crumlin, B. Mao, S. Rani, R. Chang, P. G. Karlsson, M. O. M. Edwards, M. Lundqvist, R. Moberg, P. Ross, Z. Hussain, Z. Liu, *Sci. Rep.* **2015**, *5*, 9788.
[16] D. V. Lang, C. H. Henry, *Solid-State Electron.* **1978**, *21*, 1519.
[17] R. Paul, G. Safa, G. Dina, *J. Raman Spectrosc.* **2016**, *6*, 16.
[18] W. S. Lau, *Infrared Characterization for Microelectronics*, World Scientific **1999**.
[19] D. Cao, Y. Song, J. Peng, R. Ma, J. Guo, J. Chen, X. Li, Y. Jiang, E. Wang, L. Xu, *Front. Chem.* **2019**, *7*, 626.
[20] Y. Gan, G. V. Franks, *J. Phys. Chem. B* **2005**, *109*, 12474.
[21] A. Jarzembski, C. Shaskey, K. Park, *Front. Energy* **2018**, *12*, 43.
[22] M. Aliofkhazraei, *Modern Electrochemical Methods in Nano, Surface and Corrosion Science*, IntechOpen, Rijeka **2014**.
[23] O. M. Magnussen, *Chem. Eur. J.* **2019**, *25*, 12865.
[24] M. Maiuri, M. Garavelli, G. Cerullo, *J. Am. Chem. Soc.* **2020**, *142*, 3.
[25] T. Elsaesser, *Chem. Rev.* **2017**, *117*, 10621.
[26] H. Khan, A. S. Yerramilli, A. D'Oliveira, T. L. Alford, D. C. Boffito, G. S. Patience, *The Canadian Journal of Chemical Engineering* **2020**, *98*, 1255.
[27] B. F. Baggio, Y. Gründer, *Annual Rev. Anal. Chem.* **2021**, *14*, 87.
[28] K. A. Stoerzinger, W. T. Hong, E. J. Crumlin, H. Bluhm, Y. Shao-Horn, *Acc. Chem. Res.* **2015**, *48*, 2976.
[29] R. J. Gale (Editor), *Spectroelectrochemistry*, Springer US **1988**.
[30] A. Groß, *Theoretical Surface Science*, Springer, Berlin, Heidelberg **2009**.
[31] C. Hogan, R. Del Sole, G. Onida, *Phys. Rev. B* **2003**, *68*, 035405.
[32] C. Hogan, E. Ferraro, N. McAlinden, J. F. McGilp, *Phys. Rev. Lett.* **2013**, *111*, 087401.
[33] C. Hogan, R. Magri, R. Del Sole, *Phys. Rev. B* **2011**, *83*, 155421.
[34] W. G. Schmidt, K. Seino, P. H. Hahn, F. Bechstedt, W. Lu, S. Wang, J. Bernholc, *Thin Solid Films* **2004**, *455–456*, 764.
[35] W. G. Schmidt, J. L. Fattebert, J. Bernholc, F. Bechstedt, *Surf. Rev. Lett.* **1999**, *06*, 1159.
[36] W. G. Schmidt, A. Hermann, F. Fuchs, M. Preuss, *Large-Scale Simulations for Understanding Surface Optical Spectra*, Springer-Verlag **2006**.
[37] W. G. Schmidt, F. Bechstedt, J. Bernholc, *J. Vac. Sci. Technol. B* **2000**, *18*, 2215.
[38] W. G. Schmidt, N. Esser, A. M. Frisch, P. Vogt, J. Bernholc, F. Bechstedt, M. Zorn, T. Hannappel, S. Visbeck, F. Willig, W. Richter, *Phys. Rev. B* **2000**, *61*, R16335.
[39] M. M. May, M. Sprik, *New J. Phys.* **2018**, *20*, 033031.
[40] C. Zhang, T. Sayer, J. Hutter, M. Sprik, *J. Phys. E* **2020**, *2*, 032005.
[41] P. Weightman, D. S. Martin, R. J. Cole, T. Farrell, *Rep. Prog. Phys.* **2005**, *68*, 1251.
[42] O. Supplie, M. M. May, S. Brückner, N. Brezhneva, T. Hannappel, E. V. Skorb, *Adv. Mater. Interfaces* **2017**, *4*, 1601118.
[43] W. G. Schmidt, *Phys. Status Solidi B* **2005**, *242*, 2751.
[44] M. M. May, H.-J. Lewerenz, T. Hannappel, *J. Phys. Chem. C* **2014**, *118*, 19032.
[45] K. Haberland, P. Kurpas, M. Pristovsek, J.-T. Zettler, M. Weyers, W. Richter, *Appl. Phys. A* **1999**, *68*, 309.
[46] A. Cricenti, *J. Phys. Condens. Matter* **2004**, *16*, S4243.
[47] A. Rothen, *Rev. Sci. Instrum.* **1945**, *16*, 26.
[48] J.-T. Zettler, *Prog. Cryst. Growth Charact. Mater.* **1997**, *35*, 27.
[49] S. Richter, O. Herrfurth, S. Espinoza, M. Rebarz, M. Kloz, J. A. Leveillee, A. Schleife, S. Zollner, M. Grundmann, J. Andreasson, R. Schmidt-Grund, *New J. Phys.* **2020**, *22*, 083066.
[50] B. O. Seraphin, *Optical Properties of Solids: Papers from the NATO Advanced Study Institute on Optical Properties of Solids*, Springer US **1969**.
[51] C. Huber, C. Krämmer, D. Sperber, A. Magin, H. Kalt, M. Hetterich, *Phys. Rev. B* **2015**, *92*, 075201.
[52] P. Hollins, *Infrared Reflection–Absorption Spectroscopy*, John Wiley & Sons, Ltd, Chichester, UK **2006**.
[53] K. Mudiyanselage, D. J. Stacchiola, *In-situ Infrared Spectroscopy on Model Catalysts*, John Wiley and Sons, Inc. **2013**.
[54] J. McIntyre, D. Aspnes, *Surf. Sci.* **1971**, *24*, 417.
[55] R. del Sole, *Solid State Commun.* **1981**, *37*, 537.
[56] F. Manghi, R. Del Sole, A. Selloni, E. Molinari, *Phys. Rev. B* **1990**, *41*, 9935.
[57] M. Löw, M. Guidat, J. Kim, M. M. May, *RSC Adv.* **2022**, *12*, 32756.
[58] T. D. Kühne, M. Iannuzzi, M. D. Ben, V. V. Rybkin, P. Seewald, F. Stein, T. Laino, R. Z. Khaliullin, O. Schütt, F. Schiffmann, D. Golze, J. Wilhelm, S. Chulkov, M. H. Bani-Hashemian, V. Weber, U. Borštnik, M. Taillefumier, A. S. Jakobovits, A. Lazzaro, H. Pabst, T. Müller, R. Schade, M. Guidon, S. Andermatt, N. Holmberg, G. K. Schenter, A. Hehn, A. Bussy, F. Belleflamme, G. Tabacchi, A. Glöß, M. Lass, I. Bethune, C. J. Mundy, C. Plessl, M. Watkins, J. VandeVondele, M. Krack, J. Hutter, *J. Chem. Phys.* **2020**, *152*, 194103.
[59] J. P. Perdew, K. Burke, M. Ernzerhof, *Phys. Rev. Lett.* **1996**, *77*, 3865.
[60] A. Marini, C. Hogan, M. Grüning, D. Varsano, *Comput. Phys. Commun.* **2009**, *180*, 1392.
[61] D. Sangalli, A. Ferretti, H. Miranda, C. Attaccalite, I. Marri, E. Cannuccia, P. Melo, M. Marsili, F. Paleari, A. Marrazzo, G. Prandini, P. Bonfà, M. O. Atambo, F. Affinito, M. Palummo, A. Molina-Sánchez, C. Hogan, M. Grüning, D. Varsano, A. Marini, *J. Condens. Matter Phys.* **2019**, *31*, 325902.
[62] P. Giannozzi, S. Baroni, N. Bonini, M. Calandra, R. Car, C. Cavazzoni, D. Ceresoli, G. L. Chiarotti, M. Cococcioni, I. Dabo, A. D. Corso, S. de Gironcoli, S. Fabris, G. Fratesi, R. Gebauer, U. Gerstmann, C. Gougoussis, A. Kokalj, M. Lazzeri, L. Martin-Samos, N. Marzari, F. Mauri, R. Mazzarello, S. Paolini, A. Pasquarello, L. Paulatto, C. Sbraccia, S. Scandolo, G. Sclauzero, A. P. Seitsonen, A. Smogunov, P. Umari, R. M. Wentzcovitch, *J. Phys. Condens. Matter* **2009**, *21*, 395502.
[63] D. E. Aspnes, A. A. Studna, *Phys. Rev. Lett.* **1985**, *54*, 4.
[64] B. A. Joyce, *Rep. Prog. Phys.* **1985**.
[65] M. Behet, R. Hövel, A. Kohl, A. M. Küsters, B. Opitz, K. Heime, *Microelectronics J* **1996**, *27*, 297.
[66] Z. Sobiesierski, D. I. Westwood, M. Elliott, *Phys. Rev. B* **1997**, *56*, 15277.
[67] J. Ortega-Gallegos, L. Guevara-Macías, A. Ariza-Flores, R. Castro-García, L. Lastras-Martínez, R. Balderas-Navarro, R. López-Estopier, A. Lastras-Martínez, *Appl. Surf. Sci.* **2018**, *439*, 963.
[68] G. Hughes, C. Springer, U. Resch, N. Esser, W. Richter, *J. Appl. Phys.* **1995**, *78*, 1948.
[69] G. Sombrio, E. Oliveira, J. Strassner, C. Doering, H. Fouckhardt, *J. Vac. Sci. Technol.* **2021**, *39*, 052204.
[70] S. Brückner, P. Kleinschmidt, O. Supplie, H. Döscher, T. Hannappel, *New J. Phys.* **2013**, *15*, 113049.
[71] N. Witkowski, R. Coustel, O. Pluchery, Y. Borensztein, *Surf. Sci.* **2006**, *600*, 5142.
[72] M. M. May, O. Supplie, C. Höhn, R. van de Krol, H.-J. Lewerenz, T. Hannappel, *New J. Phys.* **2013**, *15*, 103003.
[73] A. Baghbanpourasl, W. G. Schmidt, M. Denk, C. Cobet, M. Hohage, P. Zeppenfeld, K. Hingerl, *Surf. Sci.* **2015**, *641*, 231.
[74] M. M. May, H. Stange, J. Weinrich, T. Hannappel, O. Supplie, *SciPost Phys.* **2019**, *6*, 58.
[75] M. M. May, H.-J. Lewerenz, D. Lackner, F. Dimroth, T. Hannappel, *Nat. Commun.* **2015**, *6*, 8286.
[76] B. L. Pearce, S. J. Wilkins, T. Paskova, A. Ivanisevic, *J. Mater. Res.* **2015**, *30*, 2859.
[77] C. I. Smith, N. J. Almond, P. Weightman, *J. Electrochem. Soc.* **2007**, *154*, F90.
[78] H. Gerischer, *Electrochim. Acta* **1990**, *35*, 1677.
[79] C. I. Smith, P. Harrison, T. Farrell, P. Weightman, *J. Phys. Condens. Matter* **2012**, *24*, 482002.
[80] P. Harrison, C. I. Smith, Y. Gründer, C. A. Lucas, S. D. Barrett, P. Weightman, *Phys. Chem. Chem. Phys.* **2016**, *18*, 24396.

© 2023 The Authors. ChemElectroChem published by Wiley-VCH GmbH

21960216, 2023, 8, Downloaded from https://chemistry-europe.onlinelibrary.wiley.com/doi/10.1002/celc.202300027 by KIZ der Universitat Ulm, Wiley Online Library on [03/05/2023]. See the Terms and Conditions (https://onlinelibrary.wiley.com/terms-and-conditions) on Wiley Online Library for rules of use; OA articles are governed by the applicable Creative Commons License

[81] B. Sheridan, D. S. Martin, J. R. Power, S. D. Barrett, C. I. Smith, C. A. Lucas, R. J. Nichols, P. Weightman, *Phys. Rev. Lett.* **2000**, *85*, 4.
[82] O. Magnussen, J. Wiechers, R. Behm, *Surf. Sci.* **1993**, *289*, 139.
[83] R. Michaelis, D. Kolb, *Surf. Sci.* **1990**, *234*, L281.
[84] V. Mazine, Y. Borensztein, *Phys. Rev. Lett.* **2002**, *88*, 147403.
[85] V. Mazine, *Phys. Status Solidi* **1999**, *6*.
[86] T. Yamada, K. Shirasaka, A. Takano, M. Kawai, *Surf. Sci.* **2004**, *561*, 233.
[87] P. D. Lane, G. E. Isted, R. J. Cole, *Phys. Status Solidi B* **2010**, *247*, 1969.
[88] X. F. Jin, M. Y. Mao, S. Ko, Y. R. Shen, *Phys. Rev. B* **1996**, *54*, 7701.
[89] L. Sun, M. Hohage, P. Zeppenfeld, R. Balderas-Navarro, K. Hingerl, *Phys. Rev. Lett.* **2003**, *90*, 106104.
[90] C. Punckt, F. S. Merkt, H. H. Rotermund, *New J. Phys.* **2007**, *9*, 213.
[91] G. Barati, V. Solokha, K. Wandelt, K. Hingerl, C. Cobet, *Langmuir* **2014**, *30*, 14486.
[92] C. Goletti, G. Bussetti, A. Violante, B. Bonanni, M. Di Giovannantonio, G. Serrano, S. Breuer, K. Gentz, K. Wandelt, *J. Phys. Chem. C* **2015**, *119*, 1782.
[93] S. Vazquez-Miranda, V. Solokha, R. E. Balderas-Navarro, K. Hingerl, C. Cobet, *J. Phys. Chem. C* **2020**, *124*, 5204.
[94] G. Jerkiewicz, *Electrocatal* **2010**, *1*, 179.
[95] R. Yivlialin, C. Filoni, F. Goto, A. Calloni, L. Duò, F. Ciccacci, G. Bussetti, *Molecules* **2022**, *27*, 8010.
[96] Z. Chen, P. Gao, W. Wang, S. Klyatskaya, Z. Zhao-Karger, D. Wang, C. Kübel, O. Fuhr, M. Fichtner, M. Ruben, *ChemSusChem* **2019**, *12*, 3737.
[97] M. M. May, W. Jaegermann, *Curr. Opin. Electrochem.* **2022**, *34*, 100968.
[98] P. P. Notten, *Electrochemical study of the etching of III–V semiconductors*, Technische Universiteit Eindhoven **1989**.
[99] H.-J. Lewerenz, I. D. Sharp, *Chapter 1. Concepts of Photoelectrochemical Energy Conversion and Fuel Generation*, Royal Society of Chemistry **2018**.
[100] S. E. Acosta-Ortiz, A. Lastras-Martínez, *Phys. Rev. B* **1989**, *40*, 1426.
[101] T. Bruhn, B.-O. Fimland, M. Kneissl, N. Esser, P. Vogt, *Phys. Rev. B* **2011**, *83*, 045307.
[102] A. Goryachev, L. Gao, R. P. J. van Veldhoven, J. E. M. Haverkort, J. P. Hofmann, E. J. M. Hensen, *Phys. Chem. Chem. Phys.* **2018**, *20*, 14242.
[103] K. Schulte, H. Lewerenz, *Electrochim. Acta* **2002**, *47*, 2633.
[104] H. Lewerenz, K. Schulte, *Electrochim. Acta* **2002**, *47*, 2639.
[105] C. I. Smith, P. Harrison, C. A. Lucas, Y. Grunder, S. D. Barrett, P. Weightman, *J. Phys. Condens. Matter* **2016**, *28*, 015005.
[106] B. M. Ocko, A. Gibaud, J. Wang, *J. Vac. Sci. Technol.* **1992**, *10*, 3019.
[107] D. M. Kolb, J. Schneider, *Electrochim. Acta* **1986**, *31*, 929.
[108] D. Kolb, *Prog. Surf. Sci.* **1996**, *51*, 109.
[109] I. R. de Moraes, F. C. Nart, *J. Electroanal. Chem.* **1999**, *461*, 110.
[110] O. M. Magnussen, J. Hageböck, J. Hotlos, R. J. Behm, *Faraday Discuss.* **1992**, *94*, 10.
[111] Z. Shi, J. Lipkowski, *J. Electroanal. Chem.* **1996**, *403*, 225.
[112] C. I. Smith, A. Bowfield, N. J. Almond, C. P. Mansley, J. H. Convery, P. Weightman, *J. Phys. Condens. Matter* **2010**, *22*, 392001.
[113] A. El Kharbachi, O. Zavorotynska, M. Latroche, F. Cuevas, V. Yartys, M. Fichtner, *J. Alloys Compd.* **2020**, *817*, 153261.
[114] Q. Zhao, S. Stalin, L. A. Archer, *Joule* **2021**, *5*, 1119.
[115] A. M. Tripathi, W.-N. Su, B. J. Hwang, *Chem. Soc. Rev.* **2018**, *47*, 736.
[116] Y. Liang, H. Dong, D. Aurbach, Y. Yao, *Nat. Energy* **2020**, *5*, 646.
[117] F. Maroni, S. Dongmo, C. Gauckler, M. Marinaro, M. Wohlfahrt-Mehrens, *Batteries & Supercaps* **2021**, *4*, 1221.
[118] J. Shi, J. Zhang, J. Guo, J. Lu, *Nanoscale Horiz.* **2020**, *5*, 1467.
[119] Z. Lu, A. Schechter, M. Moshkovich, D. Aurbach, *J. Electroanal. Chem.* **1999**, *466*, 203.
[120] B. E. Hayden, E. Schweizer, R. Kötz, A. M. Bradshaw, *Surf. Sci.* **1981**, *111*, 26.
[121] Z. Zhao-Karger, M. E. G. Bardaji, O. Fuhr, M. Fichtner, *J. Mater. Chem. A* **2017**, *5*, 10815.
[122] L. A. Kibler, *Int. S. of Electrochem.* **2003**.
[123] M. Schlipf, F. Gygi, *Comput. Phys. Commun.* **2015**, *196*, 36.
[124] M. Löw, M. Guidat, J. Kim, M. M. May, Zenodo dataset for "The interfacial structure of InP(100) in contact with HCl and H2SO4 studied by reflection anisotropy spectroscopy" **2022**, DOI: 10.5281/zenodo.7410144.
[125] J. Kim, NOMAD dataset: RAS InP100 with Cl and H **2023**, DOI: 10.17172/NOMAD/2023.01.16-1.

Manuscript received: January 20, 2023
Revised manuscript received: February 23, 2023
Version of record online: March 22, 2023

© 2023 The Authors. ChemElectroChem published by Wiley-VCH GmbH

21960216, 2023, 8, Downloaded from https://chemistry-europe.onlinelibrary.wiley.com/doi/10.1002/celc.202300027 by KIZ der Universitat Ulm, Wiley Online Library on [03/05/2023]. See the Terms and Conditions (https://onlinelibrary.wiley.com/terms-and-conditions) on Wiley Online Library for rules of use; OA articles are governed by the applicable Creative Commons License

Name: Mario Löw

Erklärung

Ich erkläre, dass ich die Arbeit selbständig verfasst und keine anderen als die angegebenen Quellen und Hilfsmittel verwendet habe.

Ulm, den .....

Mario Löw